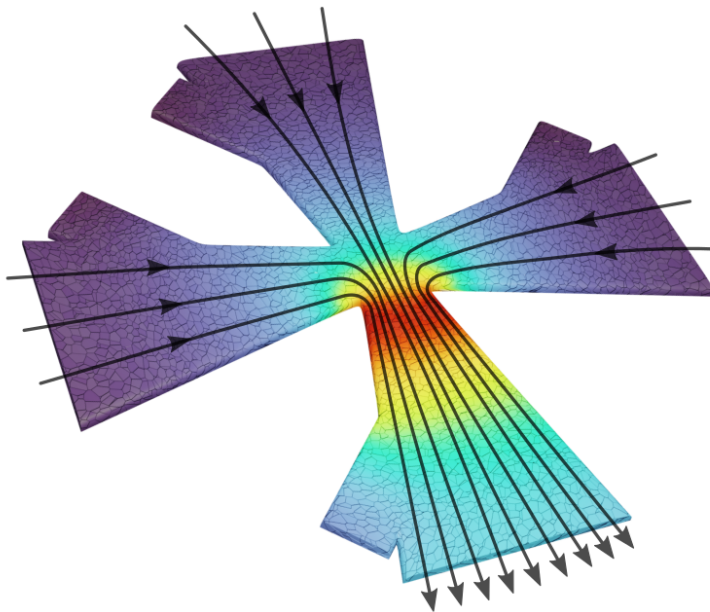




FACULTY OF SCIENCES
CESAM RESEARCH UNIT, Q-MAT CENTER
EXPERIMENTAL PHYSICS OF NANOSTRUCTURED MATERIALS



Electroannealing as a nanofabrication tool for Nb-based superconducting circuits

Simon COLLIERNE

Academic year 2022-2023

Ph.D. thesis committee:

- Prof. Dr. M. Verstraete, University of Liège (Chairman)
- Assoc. Prof. S. Dorbolo, University of Liège (Secretary)
- Prof. Dr. B. Vanderheyden, University of Liège
- Prof. Dr. J. Van den Vondel, KULeuven
- Prof. Dr. C. B. Winkelmann, Université Grenoble Alpes
- Prof. Dr. A. V. Silhanek (Supervisor)

Dissertation presented in partial fulfillment of the requirements for the degree of Doctor of Science by **Simon Collienne**.

© Copyright by Université de Liège - Faculté des Sciences, Place du 20-Août, 7, B-4000 Liège, Belgium.

Tous droits réservés. Aucune partie de ce document ne peut être reproduite sous forme d'imprimé, photocopie ou par n'importe quel autre moyen, sans l'autorisation écrite de l'auteur ou du promoteur.

All rights reserved. No part of this publication may be reproduced in any form by print, photo print or any other means without permission in writing from the author or the advisor.

To Adèle, my greatest discovery.

Abstract

Since the advent of nanotechnologies, the sustained increase in accuracy and resolution of fabrication procedures currently allows the design of electronic circuits with a precision of a few nm. The diversity of fabrication techniques such as overlay lithography, shadow evaporation, or multilayer systems offer a large palette of possibilities in the design and realization of sophisticated devices. However, these techniques present the disadvantage of increased complexity associated to multi-step processing and require sophisticated top-notch equipment within the reach of only few labs worldwide. In the context of this thesis, we demonstrate how the application of a high current density stimulating atom migration (electromigration) combined with localized annealing (electroannealing) allows for the modification of properties in superconducting Nb-based nano-circuits of several geometries.

Foremost, we propose an alternative and scalable approach to fabricate SNS junctions with tailored properties by electroannealing. This technique enables targeted modifications of the superconducting properties of each individual constrictions. This is illustrated in monolithic Y-shaped Nb on sapphire samples (Chapter 3), for which we demonstrate the modification of the superconducting critical temperature, normal resistance and critical current at a preselected junction without affecting the neighbouring terminals. We further observe the gradual appearance of Fraunhofer-like critical current oscillations with magnetic field which indicates the gradual modification of a superconducting weak link. The high loci-selectivity evidenced by atomic force microscope imaging evidences the potential of the electroannealing technique as an important tool toward all-electric control of multiterminal Josephson junctions.

In Chapter 4, we explore the effects of mild current pulses (electropulsing) on Nb/Al multiterminal devices for which the changes in resistance are bound to few percent of the initial value. We demonstrate that the affected region remains invisible to both scanning electron microscopy SE2 detector and atomic force microscopy, although surprisingly it becomes apparent through SE1 in-lens detectors and Kelvin probe force microscopy. This fact suggests a sizable decrease of the work function and an increase of electron yield in those regions. Comparing the spread and shape of the affected area with thermal maps computed through finite element modelling we are able to conclude that temperatures above ~ 435 K are necessary to induce materials' properties changes. In addition, we show that the extension of the affected volume can be controlled by the junction's geometry. These findings provide

further insights on the subtle modifications produced by gentle electroannealing of Nb/Al microstructures and represent a step forward towards mastering this emerging nanofabrication technique.

Chapter 5 is devoted to the controlled modifications of the Josephson-junction properties of a bridge-type Nb nanoSQUID by electroannealing process, allowing us to tune and tailor the response of a single device. We report on a highly nontrivial evolution of the material properties when performing subsequent electroannealing steps. As the current density is increased, an initial stage characterized by a modest improvement of the superconducting critical temperature and normal-state conductivity of the bridges, is observed. This is followed by a rapid deterioration of the junction properties, i.e., decrease of critical temperature and conductivity. Strikingly, further electroannealing leads to a noteworthy recovery before irreversible damage is produced. Within the electroannealing regime where this remarkable resurrection of the superconducting properties is observed, the nanoSQUID can be operated in nonhysteretic mode in the whole temperature range and without compromising the critical temperature of the device. As for the previous chapters, the proposed postprocessing is particularly appealing in view of its simplicity and robustness.

In chapter 6 we introduce a numerical model able to predict the modifications on the superconducting and normal properties of a multiterminal junctions produced by controlled electroannealing. In particular, it is possible to reveal the distribution of local superconducting temperature $T_c(x, y)$ and resistivity $\rho(x, y)$ in Nb-based thin film devices with multibranching or multiply-connected structures. The proposed method offers a new toolbox for understanding the modifications introduced in superconducting weak link, SQUIDs, multiterminal Josephson junctions, and filters by the electroannealing process. Furthermore, the electroannealed states exhibit a rich evolution of their transport properties depending on the two independent perpendicular currents. In particular, the critical current contour (CCC), which defines the transition to the normal state in the current space, changes from an initial ellipsoidal shape to a non-monotonic curve after the second electroannealing step. Numerical simulations solving the Ginzburg-Landau equations, considering the sample's geometry, faithfully reproduce the CCC of the virgin state and should be a valuable tool in understanding the transport properties for electroannealed states of multiterminal devices.

Overall, this thesis showcases the promising perspectives of the electroannealing technique for tailoring to a certain extent Nb superconducting junctions. The findings contribute to the advancement of superconducting nano-circuits and may offer valuable insights for the development of Nb-based devices for quantum computing, resonators, or single photon detectors.

Résumé

Depuis l'avènement des nanotechnologies, l'augmentation constante de la précision et de la résolution des procédures de fabrication permet aujourd'hui la conception de circuits électroniques avec une précision de quelques nm. La diversité des techniques de fabrication telles que la lithographie par overlay, l'évaporation par ombrage ou les systèmes multicouches offrent une large palette de possibilités dans la conception et la réalisation de dispositifs sophistiqués. Ces techniques présentent cependant l'inconvénient d'une complexité accrue liée au traitement en plusieurs étapes et nécessitent des équipements sophistiqués accessibles uniquement à quelques laboratoires dans le monde. Dans le cadre de cette thèse, nous démontrons comment l'application d'une densité de courant élevée induisant une migration atomique (électromigration) combinée à un recuit local (électro-annealing) permet de modifier les propriétés de nano-circuits supraconducteurs à base de Nb présentant des géométries complexes.

Dans un premier temps, nous proposons une approche alternative et évolutive pour concevoir des jonctions SNS avec des propriétés contrôlées par électro-annealing. Cette technique permet des modifications ciblées des propriétés supraconductrices de chaque constriction individuelle. Cela est mis en évidence dans des échantillons monolithiques en forme de Y en Nb sur substrat de saphir, pour lesquels nous démontrons la modification de la température critique, de la résistance normale et du courant critique au niveau d'une jonction présélectionnée sans affecter les terminaux voisins. Nous observons également l'apparition progressive d'oscillations du courant critique avec le champ magnétique de type Fraunhofer, ce qui indique la création progressive d'un weak link supraconducteur. La haute sélectivité mise en évidence par l'imagerie au microscope à force atomique démontre le potentiel de la technique d'électro-annealing en tant que moyen de prédilection vers le contrôle des jonctions Josephson multi-terminales.

Dans le Chapitre 4, nous explorons les effets des faibles impulsions de courant (électropulsations) sur les dispositifs multi-terminaux Nb/Al, pour lesquels les variations de résistance sont de l'ordre de quelques pourcents de la valeur initiale. Nous démontrons que la région affectée reste invisible à la fois aux détecteurs à balayage SE2 et à la microscopie à force atomique, bien qu'elle devienne apparente grâce aux détecteurs "In lens" SE1 et à la microscopie à sonde de Kelvin. Ce fait suggère une diminution notable du travail d'extraction (work function) et une augmentation du rendement des électrons dans ces régions. En comparant la propagation et la forme de la zone affectée avec les répartitions de température calculées par modélisation

par éléments finis, nous pouvons conclure que des températures supérieures à environ 435 K sont nécessaires pour induire des modifications des propriétés des matériaux. De plus, nous montrons que l'extension de la zone affectée peut être contrôlée par la géométrie de la jonction. Ces résultats fournissent de nouvelles informations sur les modifications subtiles produites par des étapes douces d'électro-annealing sur des microstructures Nb/Al et représentent une avancée vers la maîtrise de cette nouvelle technique de nanofabrication.

Le Chapitre 5 est consacré aux modifications par le processus d'électro-annealing des propriétés des jonctions Josephson de type constriction (Dayem bridge) d'un nanoSQUID à base de Nb, nous permettant ainsi d'ajuster la réponse d'un même dispositif. Nous rapportons une évolution hautement non triviale des propriétés des jonctions lorsque des étapes d'électro-annealing successives sont effectuées. À mesure que la densité de courant augmente, on observe une première étape caractérisée par une amélioration modeste de la température critique et de la conductivité à l'état normal des jonctions. Cela est suivi par une détérioration rapide des propriétés de la jonction, c'est-à-dire une diminution de la température critique et de la conductivité. De manière surprenante, une nouvelle étape d'électro-annealing entraîne un remarquable rétablissement des propriétés supraconductrices avant que des dommages irréversibles ne se produisent. Dans la plage d'électro-annealing où cette résurrection remarquable des propriétés supraconductrices est observée, le nanoSQUID peut être utilisé en mode non hystérétique dans toute la plage de température sans compromettre la température critique du dispositif. Comme pour les chapitres précédents, le post-traitement proposé par électro-annealing est particulièrement attractif en raison de sa simplicité et de sa robustesse.

Dans le chapitre 6, nous présentons un modèle numérique capable de déduire les modifications des propriétés supraconductrices et de résistivité de jonctions multi-terminales produites par électro-annealing. En particulier, il est possible de révéler la distribution de la température critique locale $T_c(x, y)$ et de la résistivité $\rho(x, y)$ dans des dispositifs à films minces à base de Nb présentant des structures à branches multiples ou connectées de manière multiple. La méthode proposée offre un nouvel outil pour comprendre les modifications introduites dans les weak links supraconducteurs, les SQUIDs, les jonctions Josephson multi-terminales et les filtres par le processus d'électro-annealing. De plus, les états électro-annealés montrent une évolution riche de leurs propriétés de transport en fonction des deux courants perpendiculaires indépendants. En particulier, le contour du courant critique (CCC), qui définit la transition vers l'état normal dans l'espace des courants, passe d'une forme initiale ellipsoïdale à une courbe non monotone après la deuxième étape d'électro-annealing. Les simulations numériques résolvant les équations de Ginzburg-Landau, en prenant en compte la géométrie de l'échantillon, reproduisent fidèlement le CCC de l'état initial et devraient être un outil précieux pour comprendre les propriétés de transport des états électro-annealés des dispositifs multi-terminaux.

Dans l'ensemble, cette thèse met en valeur les perspectives prometteuses de la technique d'électro-annealing pour personnaliser à volonté les jonctions supracon-

ductrices en Nb. Les résultats contribuent à l'avancement des nano-circuits supra-conducteurs et pourraient offrir des informations précieuses pour le développement de dispositifs à base de Nb pour l'informatique quantique, les résonateurs ou les détecteurs de photons uniques.

Acknowledgments

From my perspective, completing a thesis involves many factors that are beyond one's control. While motivation and perseverance are undoubtedly crucial qualities, I believe there are three essential points that significantly contribute to successfully finishing the work.

Undoubtedly, the first crucial aspect is the choice of supervisor. It is only natural that I express my gratitude to Prof. Alejandro Silhanek, who made this thesis possible. Right from the beginning, he believed in me and welcomed me into the EPNM group, assuring me with a phrase that remains etched in my memory to this day: "For my part, I can promise you a thesis." And true to his word, he didn't shy away from hard work. By maintaining a discipline as demanding as that expected from his doctoral students, he constantly guided, motivated, reviewed, and imparted a fraction of his knowledge to me. He served as the foundational pillar without whom this thesis would not have been possible. For all these reasons, I am immensely grateful.

Secondly, the research topic is of tremendous importance. Working in the field of superconductivity, I have discovered a rich domain where the qualities of experimenters and theorists can be highlighted. When combined with the technique of electromigration, the possibilities of superconductivity become endless, limited only by our imagination. The countless hours of reading and the liters of sweat were more than compensated for by the joy and satisfaction of partially lifting the veil on these wonderful topics.

Lastly, having a supportive and high-quality environment is essential, both professionally and personally. I have been incredibly fortunate in this regard, and I have a long list of people to whom I would like to express my heartfelt gratitude.

First, I have been fortunate to be part of an exceptional working environment at EPNM-SPIN. I am grateful to Prof. Duy Nguyen for his early-morning croissants and his characteristic kindness. Furthermore, I would like to extend my appreciation to my current colleagues: Stefan, Emile, Nicolas, Amaury, Francisco, and Hugo, as well as my former colleagues: Sylvain, Jérémy, Joseph, Obaid, Sunil, Suraj, Elijah, Davi, Sarah, Antoine, Justine, Clémentine, Caroline, Arnaud, and Charles. Our lunchtime discussions were always a source of joy and rejuvenation, providing the necessary motivation to carry on with the day. Thank you all for your invaluable contributions. I would like to dedicate a special mention to Thomas, whose un-

derstanding extended far beyond our experiences in Sart Tilman during our shared journeys. I will miss those mornings, sometimes in the cold, when we cycled together before reaching the office. And of course, Xavier, thank you for everything you have done for me.

I would also like to express my deep gratitude to my colleagues at KULeuven and Prof. Joris Van de Vondel, who always welcomed me warmly to the other half of our beautiful country. Special thanks to Bart and Wout, who taught me how to handle a cryostat for the first time, and to Heleen and Lukas, who were always available and greeted me with a smile when it was time to recharge the cryostat. Vyacheslav, thank you for your assistance in learning the electromigration software.

This thesis also provided me with the opportunity to explore new horizons. I extend my thanks to Prof. Dieter Kölle and Julian Linek for their hospitality during my internship at the University of Tuebingen, and of course, Prof. Clemens Winkelmann during my month of measurements at the Institut Néel in Grenoble. I would like to offer a special acknowledgment to Danial and his wife Tabassom, whose exceptional kindness and benevolence will always be remembered.

Last but not least, I cannot overlook Dr. Zeljko Zelic, who responded to my numerous emails and patiently addressed my countless inquiries regarding the tdGL simulations. His invaluable assistance was absolutely indispensable. Thank you.

Il y avait ceux de l'université et puis les autres. Peu de personnes peuvent se vanter de pouvoir compter sur le soutien sans faille de leurs parents. Maman, Papa, votre fils est conscient de la chance qu'il a de vous avoir pour parents.

Et puis bien sûr à toi Florence pour ton soutien et la venue de notre Adèle qui a changé ma vie. Les raisons de se lever le matin ne furent plus jamais les mêmes.

Contents

Abstract	5
Résumé	7
Acknowledgments	11
List of symbols	17
List of acronyms	21
Introduction	23
1 Theoretical background	27
1.1 Historical perspective	27
1.2 Theories of superconductivity	28
1.2.1 London equations	28
1.2.1.1 A macroscopic quantum phenomenon	29
1.2.1.2 Generalization of the second London equation	30
1.2.1.3 Flux quantization	31
1.2.2 Ginzburg-Landau approach	32
1.2.2.1 The thermodynamics of superconductors	32
1.2.2.2 Ginzburg-Landau equations	34
1.2.2.3 Type I versus type II superconductors	37
1.2.3 BCS theory	39
1.3 The Josephson effect	41
1.3.1 Different kinds of weak links	43
1.3.1.1 What is a weak link?	43
1.3.1.2 Point contacts	45
1.3.1.3 Long junctions	47
1.3.1.4 Weak link regimes	48
1.3.2 The voltage state	49
1.3.3 Weak link in a magnetic field	51
1.3.4 The SQUID sensor	52
1.3.4.1 Asymmetric model for SIS junctions	54
1.3.4.2 SQUID with linear CPR	59

1.3.4.3	The voltage state	62
1.3.4.4	Applications of SQUIDs	64
2	Experimental techniques	65
2.1	Sample fabrication	65
2.2	Physical Property Measurement System	66
2.3	Electromigration	67
2.3.1	Historical perspective	68
2.3.2	Electron wind force theory and mass transport	68
2.3.3	The grains structure	71
2.3.4	Controlled electromigration	72
2.3.5	EM software	73
2.4	Imaging techniques	75
2.4.1	In-situ Atomic Force Microscopy	76
2.4.2	Kelvin Probe Force Microscopy	77
3	Targeted modifications of monolithic multiterminal superconducting weak-links	79
3.1	Introduction	80
3.2	Results	82
3.3	Atomic force microscopy imaging of the targeted structural modification	86
3.4	Fabrication details	86
3.5	Finite elements model	87
3.6	Conclusion	88
4	Effect of moderated electropulsing on Nb multiterminal transport bridges	89
4.1	Introduction	90
4.2	Experimental details	91
4.3	Electropulsing protocol and methodology	92
4.4	Visualization of the eletropulsing-induced junction's modification . .	93
4.5	Finite element modelling	95
4.6	Atomic force microscopy profile	98
4.7	Superconducting transition of each junction after electropulsing . . .	99
4.8	Kelvin-probe Force Microscopy	99
4.9	Conclusion	99
5	Nb-Based Nanoscale Superconducting Quantum Interference Devices Tuned by Electroannealing	101
5.1	Introduction	102
5.2	Methods	103
5.2.1	Controlled EA	103
5.2.2	Cryogenic transport measurements	103
5.2.3	<i>In situ</i> SEM transport measurements	103
5.3	Properties of the pristine Nb nanoSQUIDs	104

5.3.1	Fabrication and electrical characterization	104
5.3.2	Magnetic field dependence of the critical current	105
5.4	Electroannealed devices	108
5.4.1	Targeted damage at the weak links	108
5.4.2	Characterization of the superconducting properties of the weak links after EA	110
5.4.3	Critical current vs magnetic field oscillations after EA	112
5.4.4	Thermal regimes and retrapping	114
5.4.5	Finite Element Method simulation	116
5.4.6	<i>In situ</i> atomic force microscopy	117
5.4.7	Coherence length evolution over EA	118
5.4.8	Dynamic thermal model	119
5.5	Conclusion	122
6	Electroannealed four-branches devices	123
6.1	Introduction	123
6.2	Electromigration of nanodevices	124
6.3	Finite elements modeling	125
6.4	Transport properties	132
6.5	Ginzburg-Landau simulations	137
6.6	Conclusion	142
	Conclusions and perspectives	143
	Appendices	147
A	CPR of point contacts	148
A.1	Ambegaokar-Baratoff (AB)	148
A.2	Aslamazov-Larkin (AL)	148
A.3	Kulik-Omelyanchuk - dirty limit (KO-1)	148
A.4	Kulik-Omelyanchuk - clean limit (KO-2)	149
A.5	Haberkorn (H)	149
A.6	Beenakeer (B)	150
B	The SQUID dynamics in the zero voltage state	151
B.1	Newton-Raphson method	151
B.2	Current bellow critical current	152
B.3	Critical current oscillations	152
C	Supplemental Material of chapter 6	154
C.1	In situ scanning electron microscopy of sample S2	155
C.2	Weak links superconducting properties	156
	Bibliography	157
	Curriculum Vitae	173

List of symbols

Roman

A	magnetic vector potential	F	force
A_{eff}	effective loop area	F_E	electrical force
b	parameter of GL boundary condition	F_w	wind force
B	magnetic flux density	g	Gibbs free energy density
B_0	external applied magnetic flux density	g^{cond}	condensation energy density
B_{c2}	second critical magnetic flux density	g^{magn}	magnetic energy density
B_{max}	magnetic flux density shift	g_n	Gibbs free energy density in normal state
C	capacitance	g_s	Gibbs free energy density in superconducting state
\mathcal{C}	dimensionless heat capacity	G	conductance
C_H	specific heat at constant H	G_j	junction conductance
C_n^{el}	electronic specific heat in normal state	G_j^{Thr}	threshold junction conductance
C_s^{el}	electronic specific heat in superconducting state	$G(\epsilon)$	energy dependent density of state
d	weak-link length	G^{surf}	surface energy
d_{eff}	effective weak-link length	G^{vortex}	surface energy for a vortex creation
\bar{d}	normalized weak-link length	h	Planck constant
\bar{d}_c	critical normalized weak-link length	\hbar	reduced Planck constant
D	diffusivity	\mathcal{H}	heat loss coefficient
e	proton charge	H	magnetic field
$e(t)$	time dependent error	H_c	critical magnetic field
E	electric field	H_{c1}	first critical magnetic field
E_a	activation energy	H_{c2}	second critical magnetic field
E_K	kinetic energy	i	normalized current
f	frequency	i_{cav}	normalized averaged critical current
f_{PID}	PID response	i_r	normalized retrapping current
f_{nl}	non linear response	i_s	normalized supercurrent
f_R	vacancy relaxation factor	I	current
		I_{av}	averaged current

I_c	critical current	$Q_{GL}(0)$	dimensionless GL vector potential
I_{cav}	averaged critical current	R	resistance
I_D	displacement current	R_j	junction resistance
I_F	noise current	R_L	lead resistance
I_N	normal current	R_{max}	maximum resistance
I_s	supercurrent	R_{min}	minimum resistance
I_{th}	threshold current	R_N	normal resistance
I_ϕ	circular current	R_w	wire resistance
J_a	atomic flux	R_{therm}	thermal resistance
J_c	critical current density	s	entropy density
$J_{GL}(0)$	dimensionless GL current density	s_n	entropy density in normal state
J_n	normal current density	s_s	entropy density in superconducting state
J_P	probability current density	t	sample thickness
J_s	supercurrent density	T	temperature
k	wave number	T_{amb}	ambient temperature
k_B	Boltzmann constant	T_b	bath temperature
K	dimensionless thermal conductivity	T_{bound}	temperature at the boundary
l	mean free path	T_c	critical temperature
L	inductance	T'_c	weak-link critical temperature
L_G	geometric inductance	T_h	temperature to reach the reversible regime
L_h	latent heat	u	internal energy density
L_K	kinetic inductance	\bar{u}	ratio of the relaxation times for the magnitude and the phase of the order parameter
m_q	mass of Cooper pair	v	normalized voltage
m_e	mass of an electron	$\langle v \rangle$	time averaged normalized voltage
M	magnetization	v_a	atomic drift velocity
n_a	atomic density	V_0	applied voltage
n_p	density of Cooper pairs	V_{BCS}	attractive BCS potential
n_s	density of super electrons	\hat{V}	BCS potential operator
n	winding number	w	junction width
p	control variable	Z	valence number
p_{setp}	setpoint control variable	Z_w	associated wind force valence number
p_{joule}	Joule heating power density	Z^*	effective valence number
p_{subst}	evacuating power density		
q	heat flux		
q_{int}	heat flux at the interface		
q_p	charge of a Cooper pair		
Q	thermal source density		

Greek

α	thermal coefficient	κ_{GL}	GL parameter
α_{Stekly}	Stekly parameter	λ_L	London penetration depth
α_I	critical current asymmetry parameter	μ	mobility
$\alpha(T)$	first coefficient of GL expansion	μ_0	magnetic permeability of vacuum
$\beta(T)$	second coefficient of GL expansion	$\xi(T)$	temperature dependent coherence length
β_c	Stewart-McCumber parameter	ξ_N	proximity effect characteristic length
β_{DTM}	dynamic thermal model parameter	ξ_0	BCS coherence length
β_L	inductance parameter	ρ	electrical resistivity
γ	critical phase asymmetry parameter	ρ_m	density
Γ	inelastic scattering parameter	σ	mechanical stress
$\delta_{a \rightarrow b}$	phase variation along $a \rightarrow b$ path	$\sigma^{(0)}$	dimensionless normal conductivity
δT_c	critical temperature variation	τ	junction dimensionless time
$\Delta(T)$	temperature dependent superconducting gap	τ_c	junction characteristic time
ϵ_{coll}	mean electron energy at collision	$\tau_{GL}(0)$	dimensionless GL time
ϵ_F	Fermi energy	ϕ	dimensionless magnetic flux
ϵ_K	electron energy of wave number k	φ	scalar potential
η	order parameter	$\varphi_{GL}(0)$	dimensionless GL scalar potential
η_L	indctance asymmetry parameter	Φ	magnetic flux
θ	phase of the macroscopic wave function	Φ_{ext}	external applied magnetic flux
Θ	jauge invariant phase difference	Φ_W	work function
Θ_c	critical jauge invariant phase difference	Φ_0	flux quantum
Θ_{cav}	averaged critical jauge invariant phase difference	ψ	dimensionless GL order parameter
κ	thermal conductivity	$\psi_{GL}(0)$	dimensionless GL order parameter
		Ψ	macroscopic wave function
		Ψ_0	global minimum of GL expansion
		ω_D	Debye frequency
		Ω_D	atomic volume

List of acronyms

AB	Ambegaokar-Baratoff	149
AC	alternative current	42
AFM	Atomic Force Microscopy	65
AL	Aslamasov-Larkin	45
B	Beenakeer	45
BCS	Bardeen-Cooper-Schrieffer	28
CCC	Critical Current Contour	133
CPR	current phase relationship	42
DC	direct current	42
EA	Electroannealing	81
EBL	Electron Beam Lithography	65
EM	Electromigration	65
EP	Electropulsing	90
ET	Everhart-Thornley	93
FBL	Flux Blocked Loop	63
FEM	Finite Element Method	95
gTDGL	generalized time-dependent Ginzburg-Landau	137
GL	Ginzburg-Landau	36
GPIB	General Purpose Interface Bus	77
H	Haberkorn	45
KO	Kulik-Omelyanchuk	45
KO-1	First Kulik-Omelyanchuk model	45
KO-2	Second Kulik-Omelyanchuk model	45
KPFM	Kelvin Probe Force Microscopy	65
KULeuven	Katholieke Universiteit Leuven	65

MBB	Make Before Break	77
MTF	Median Time to Failure	68
ODSEE	One Dimension Structure with Electrodes in Equilibrium	47
PID	Proportional-Integral-Derivative	73
PMMA	Poly(methyl methacrylate)	65
PPMS	Physical Property Measurements System	65
RCSJ	Resistively and Capacitively Shunted Junction	49
RF	Radio Frequency	90
RIE	Reactive Ion Etching	65
RMS	Root Mean square	74
RRR	Residual resistivity ration	105
SCS	Superconductor-Constriction-Superconductor	41
SS'S	Superconductor-weaker superconductor-Superconductor	88
SE2	Secondary Electron	93
SEM	Scanning Electron Microscopy	65
SThM	Scanning Thermal Microscopy	142
SIS	Superconductor-Insulator-Superconductor	41
SNS	Superconductor-Normal metal-Superconductor	44
SQUID	Superconducting QUantum Interference Device	47
STEM	Scanning Transmission Electron Microscopy	75
UHV	Ultra High Vacuum	86
WL	Weak-link	43
YBCO	Yttrium Baryum Copper Oxide	75
2DEG	2D Electron Gas	123

Introduction

Superconductivity, discovered by Kamerlingh Onnes in the early 20th century, continues to fascinate with its remarkable properties. Aside from its well-known applications such as levitating trains and lossless electric current transmission, superconductivity constitutes the basis of the Josephson effect. This phenomenon, predicted by Brian Josephson in 1962, describes how the superposition of the superconducting condensate in a weak link between two superconducting electrodes can give rise to a non-dissipative current through the weak link separating them. While Josephson junctions were initially designed with an insulating layer, they can in general be created introducing a region with a lower critical current. Examples of weak links include simple constrictions (Dayem bridge), normal metals, ferromagnets or lower critical temperature superconductors. Josephson junctions are vital components in superconducting electronics and find applications in areas such as frequency-voltage conversion for metrology, single-photon detectors, superconducting single-electron detectors, quantum computing with artificial atoms, and SQUID sensors. SQUIDs, consisting of two Josephson junctions integrated into a superconducting loop, are currently among the most sensitive magnetic flux sensors. The geometry and properties of the junctions play a crucial role in these devices, highlighting the significance of nanofabrication techniques in their production.

An innovative nanofabrication technique is investigated in this thesis through the electromigration procedure. Initially discovered in the late 1960s during the trend of circuit miniaturization, electromigration emerged as a challenge when devices utilizing such circuits failed after a few weeks of use. Electron microscopy revealed that the increasingly smaller cross-sections resulted in current densities that caused wire breaks. Although naturally considered detrimental to the electronics industry and an obstacle to circuit miniaturization, electromigration can also be regarded as a nanofabrication tool that allows modification of materials on a scale beyond conventional techniques. Currently, nanofabrication methods, such as lithography using light or charged particles, achieve resolutions of less than 10 nm, which are exceptional and suitable for industrial processes but fall short when designing structures at atomic scale. However, by employing constricted geometries, the electromigration technique enables the precise determination of the region with the highest current density where induced changes occur. Over the past few decades, extensive research has been conducted on this technique, successfully reducing junction widths down to a few atoms and creating sub 10 nm nanogaps. The examples mentioned above

typically involve simple junctions with constrictions where the current has only one possible pathway. This thesis extends the electromigration technique to geometries with $N > 2$ terminals. By carefully selecting input and output current polarities, a particular junction can be preferentially targeted to increase the current density and induce changes, having the other junctions unaffected.

The objective of this thesis is to master the electromigration process in order to address and control superconducting junctions in niobium-based multi-terminal and SQUID circuits.

To that end, it will be essential to seize the relevance of several intertwined physical mechanisms at play during this complex process, including stress-migration, thermal annealing, grain growth, etc.

This thesis is structured as follows:

Chapter 1 provides the necessary theoretical background to comprehend the thesis content. It begins with a brief historical overview and then delves into the generalized London equations and the Ginzburg-Landau equations. Special emphasis is placed on understanding the Josephson effect and various weak-link variants relevant to the thesis. The chapter concludes with a discussion on the theory of dc-SQUIDs.

Chapter 2 presents an overview of the experimental techniques used. It includes a brief description of the sample fabrication technique, a detailed account of the cryostat employed for low-temperature measurements, an explanation of the electromigration technique, and a description of the in-house software used for its control. The chapter concludes with an overview of the imaging techniques utilized in the thesis.

Chapter 3 presents the results of selective electromigration on a niobium-based three-terminal sample. It demonstrates that careful selection of input and output current polarities enables targeted modification of specific junctions through electromigration.

Chapter 4 focuses on the effect of moderate electromigration on a multi-terminal niobium sample. It reveals that even mild electromigration of a junction, where no structural modifications can be observed through SEM or AFM imaging, results in changes in electrical properties that can be measured through resistance or work function analysis using Kelvin probe force microscopy (KPFM). A finite-element study determines the temperature threshold at which these modifications occur.

Chapter 5 investigates the electromigration of parallel junctions in a niobium-based SQUID. It demonstrates that successive electromigration steps progressively modify the SQUID from an irreversible state dominated by the formation of hot spots to a reversible state exhibiting voltage oscillations as a function of magnetic field. Additionally, a peculiar evolution of superconducting properties is observed, characterized by a sudden resurrection of the critical temperature and normal resistance after a long period of progressive deterioration.

Chapter 6 proposes a model for estimating the modifications induced in a four-terminal device by attempting to reproduce the $R(T)$ characteristic of the junctions after successive electromigration steps. Preliminary results of the transport properties of the device are investigated using time-dependent Ginzburg-Landau equations.

Chapter 1

Theoretical background

1.1 Historical perspective

The history of superconductivity² is closely related to the fierce competition for gas liquefaction that animated the physics laboratories at the beginning of the 20th century [1, 2]. At the time, oxygen had just been liquefied by James Dewar, enabling to reach a temperature of 20 K. However, one last element resisted liquefaction: helium, the lightest element on the periodic table. Aware of this immense challenge, Heike Kamerlingh Onnes, a Dutch physicist born in 1853, surrounded himself with the best technicians to be the first to succeed in liquefying a few liters of helium in 1908. As the only person in the world who could reach a temperature as low as 1 K, he tackled the question of the behavior of conductivity of metal close to 0 K, for which esteemed physicists such as Matthiessen, Dewar and Lord Kelvin had very different theories [3–5]. In 1911 Gilles Holst, Onnes’ student, was in charge of measuring the resistivity of a sample of mercury and obtained an unexpected result shown in the left panel of Fig. 1.1: a total disappearance of the resistance below the so-called *critical temperature* $T_c \sim 4.2\text{ K}$ [6]. This property of *zero resistivity* marked the discovery of superconductivity. Shortly after, it turned out that an increase in temperature was not the only way to break the superconducting state. Indeed, the application of a magnetic field, called *critical magnetic field* H_c , of a few mT is sufficient to transition into the normal state.³ An empirical relation describes the link between T and H_c [7]:

$$H_c(T) = H_c(0) \left[1 - \left(\frac{T}{T_c} \right)^2 \right], \quad (1.1)$$

²This first two sections brings together the basic elements of superconductivity theory as I would have liked to be introduced to it. Some sections like the one related to the thermodynamics of superconductors are introduced only for pedagogical purposes. The informed reader can skip this section and move on directly to more specialized topic as the Josephson effect 1.3.

³Note that we limit ourselves for the moment to the so-called type I superconductors for which the critical field is very low. All the pure elements of the periodic table are of type I except Nb which is of type II. More details will be given in section 1.2.2.

and is shown in the right panel of Fig. 1.1. It was not until about two decades later that another crucial property of superconductors was revealed. In 1933, Walther Meissner and Robert Ochsenfeld conducted experiments on the magnetic behavior of superconductors and showed that the magnetic field is expelled from the volume of the material below T_c [8]. As a result, a superconductor behaves like a *perfect diamagnet*:

$$\mathbf{B} = \mathbf{0}. \quad (1.2)$$

If the infinite conductance of a superconductor can be explained by a perfect conductor model, *i.e.* a material with zero resistivity, it does not explain the Meissner-Ochsenfeld effect. Indeed, Maxwell's equations predict that for a perfect conductor $\partial \mathbf{B} / \partial t = \mathbf{0}$, *i.e.* the magnetic field cannot vary in time within the perfect conductor and consequently the value of \mathbf{B} for $T < T_c$ will be equal to the applied field at the time of the transition. On the other hand, the experiment shows that $\mathbf{B} = \mathbf{0}$ whatever the history of the applied field for a superconductor. This result reveals the fundamental importance of the Meissner-Ochsenfeld effect which must be the foundation in any theory of superconductivity [1] (see section 1.2.2.1).

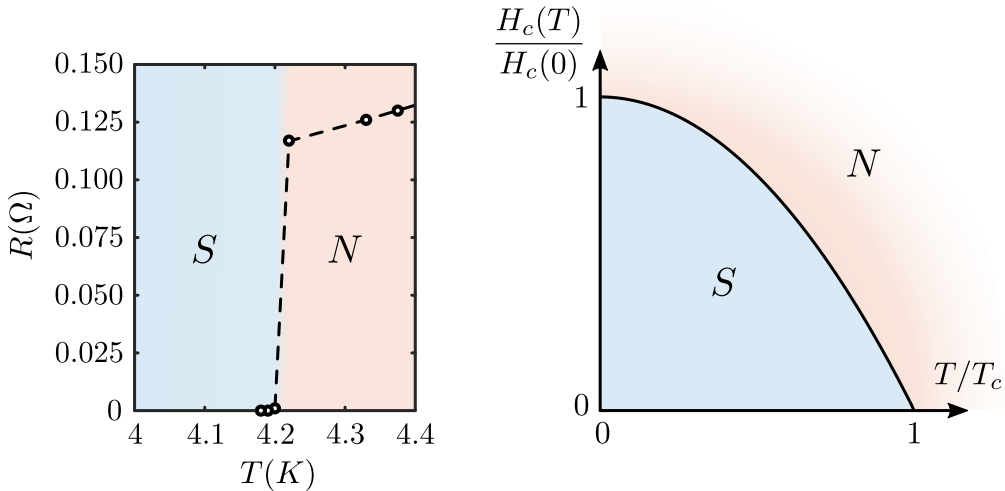


Figure 1.1 – First observation of the transition between the normal state N and the superconducting state S . Below the critical temperature $T_c \sim 4.2$ K, the resistivity of mercury drops abruptly to zero (left panel, adapted from [6]). Temperature dependence of the critical field H_c according to (1.1) for a type I superconductor (right panel).

1.2 Theories of superconductivity

1.2.1 London equations

Before the microscopic Bardeen-Cooper-Schrieffer (BCS) theory of superconductivity¹, physicists rely on *phenomenological theories* of the superconducting state. In

¹See section 1.2.3.

opposition to most models that focus on the analogy with a perfect conductor, the Fritz and Heinz London brothers understood the importance of the Meissner-Ochsenfeld effect by postulating the two *ad hoc* London equations [9]:

$$\frac{\partial \mathbf{J}_s}{\partial t} = \frac{1}{\mu_0 \lambda_L^2} \mathbf{E}, \quad (1.3)$$

$$\nabla \times \mathbf{J}_s = -\frac{1}{\mu_0 \lambda_L^2} \mathbf{B}, \quad (1.4)$$

where \mathbf{J}_s is the superconducting current density and

$$\lambda_L = \sqrt{m_e / (\mu_0 n_s e^2)}, \quad (1.5)$$

is the *London penetration depth*¹. Equation (1.3) implies that an electric field \mathbf{E} is only necessary to *vary* the current density and that once a given current is reached, it can flow indefinitely without voltage source. Put it in another way, this means that a constant current can flow without dissipation. The second London equation (1.4) accounts for the Meissner-Ochsenfeld effect and shows that an external field \mathbf{B}_0 applied to the interface of a superconductor decreases according to $\mathbf{B} = \mathbf{B}_0 \exp(-r/\lambda_L)$, with r the distance towards the interior of the material. The physical meaning of λ_L is then straightforward: it is the characteristic length over which the external magnetic field is expelled from the superconductor. Finally, let us note that the London equations are linear which means that their validity is restricted to the case of weak electric and magnetic fields and a uniform superconducting charge carriers density n_s [11].

1.2.1.1 A macroscopic quantum phenomenon

Back in 1935 Fritz London was already aware that a purely classical explanation of superconductivity would be incomplete. Subsequently, the London brothers hypothesized that a superconductor is a *macroscopic quantum system*, *i.e.* the microscopic phenomena are intrinsically governed by quantum mechanics whose effects are observable on a macroscopic scale due to the coherence of the superelectrons over large distances. From now on, we will assume the existence of a *macroscopic wave function*

$$\Psi(\mathbf{r}, t) = |\Psi(\mathbf{r}, t)| e^{i\theta(\mathbf{r}, t)}, \quad (1.6)$$

that describes all superelectrons in a superconductor. The variable $\theta(\mathbf{r}, t)$ being the *phase* of the wave function and $|\Psi(\mathbf{r}, t)|$ its *amplitude*. $\Psi(\mathbf{r}, t)$ can vary in space and time but ensures that the superelectrons are always locally coherent while the local density of superconducting charge carriers is given by:

$$\frac{n_s(\mathbf{r}, t)}{2} = |\Psi(\mathbf{r}, t)|^2 = \Psi^*(\mathbf{r}, t) \Psi(\mathbf{r}, t), \quad (1.7)$$

¹The subscript s refers to the superconducting electrons. According to the two-fluids model of Gorter and Casimir [10], the total electronic density n is divided into a sum of superconducting electrons n_s and normal electrons n_n . The conservation of current implies $\mathbf{J} = \mathbf{J}_s + \mathbf{J}_n$. The equations (1.3) and (1.4) govern only the behavior of the superconducting electrons.

where $n_s(\mathbf{r}, t)$ is the density of superelectrons. The $1/2$ factor will be explained shortly after. The macroscopic quantum hypothesis provides no explanation concerning the microscopic origin of superconductivity. Its only interest is to assert that electrons can be described according to (1.6). It was not until 1957 with the advent of the BCS theory [12] that a complete microscopic explanation validated this hypothesis for *conventional superconductors*, also called *low critical temperature superconductors*.

1.2.1.2 Generalization of the second London equation

In order to treat the motion of superelectrons in a quantum manner, it is essential to start from the Schrödinger equation which takes into account the magnetic field. A particle of mass m and charge q in magnetic field, the wave function must obey [13, 14]:

$$i\hbar \frac{\partial \Psi(\mathbf{r}, t)}{\partial t} = \frac{1}{2m} \left(\frac{\hbar}{i} \nabla - q\mathbf{A}(\mathbf{r}, t) \right)^2 \Psi(\mathbf{r}, t) + q\varphi(\mathbf{r}, t)\Psi(\mathbf{r}, t), \quad (1.8)$$

where \mathbf{A} is the vector potential and φ the scalar potential¹. The probability current which describes the flow of a quantum object subjected to the equation (1.8) is given by:

$$\mathbf{J}_P = \frac{1}{2} \left[\left(\frac{\frac{\hbar}{i} \nabla - q\mathbf{A}}{m} \Psi \right)^* \Psi + \Psi^* \left(\frac{\frac{\hbar}{i} \nabla - q\mathbf{A}}{m} \Psi \right) \right]. \quad (1.9)$$

It will be shown in the section 1.2.3 that the charge carriers responsible for superconductivity are in fact pairs of electrons called *Cooper pairs* whose density is related to those of the superelectrons by the simple relation $n_p(\mathbf{r}, t) = n_s(\mathbf{r}, t)/2$, justifying at the same time the factor $1/2$ in the formula (1.7). To ensure maximum consistency, we will use the Cooper pair density $n_p(\mathbf{r}, t)$ in the rest of the manuscript. Combining (1.6) and (1.8), we can obtain the expression of the supercurrent by multiplying the charge of a Cooper pair $q_p = -2e$ with (1.9) to obtain:

$$\mathbf{J}_s(\mathbf{r}, t) = \frac{q_p^2 n_p(\mathbf{r}, t)}{m_p} \left[\frac{\hbar}{q_p} \nabla \theta(\mathbf{r}, t) - \mathbf{A}(\mathbf{r}, t) \right], \quad (1.10)$$

which can be rewritten with (1.5):

$$\mathbf{J}_s(\mathbf{r}, t) = -\frac{1}{\mu_0 \lambda_L^2} \left[\frac{\Phi_0}{2\pi} \nabla \theta(\mathbf{r}, t) + \mathbf{A}(\mathbf{r}, t) \right], \quad (1.11)$$

where

$$\Phi_0 = h/2e \sim 2.068 \times 10^{-15} \text{ Wb}, \quad (1.12)$$

is the flux quantum. The second term of (1.11) is identical to the equation (1.4) if we take into account that $\mathbf{B} = \nabla \times \mathbf{A}$, while the first term constitutes the contribution of quantum mechanics and thus generalizes the second London equation.

¹The electric and magnetic fields being related to the potentials by $\mathbf{E} = -\frac{\partial \mathbf{A}}{\partial t} - \nabla \varphi$ and $\mathbf{B} = \nabla \times \mathbf{A}$.

1.2.1.3 Flux quantization

Another property emerging from the generalization of the second London equation is the *fluxoid quantization* [15, 16]. Consider a multiply connected superconducting material immersed in a magnetic field as sketched in Fig. 1.2. According to London's equations, screening currents at the interfaces of the superconductor will expel the magnetic field from its volume. As recalled in section 1.2.1.1, only the amplitude of Ψ is directly related to the local density of Cooper pairs via (1.7). Although the phase θ is not directly measurable, it must verify an important property. Indeed, we notice that the wave function (1.6) is not modified if we add a quantity $2\pi n$ to its phase, n being an integer. This implies that the variation of the phase along a closed path Γ_1 (see Fig. 1.2) has to be as a general rule equal to $2\pi n$:

$$\oint_{\Gamma_1} \nabla\theta \cdot d\mathbf{l} = 2\pi n. \quad (1.13)$$

By isolating the phase gradient from the equation of the supercurrent (1.11), the equation (1.13) takes the following more intuitive form:

$$\mu_0\lambda_L^2 \oint_{\Gamma_1} \mathbf{J}_s \cdot d\mathbf{l} + \int_S \mathbf{B} \cdot d\mathbf{S} = n\Phi_0, \quad (1.14)$$

where S is the area enclosed by Γ_1 . The left-hand side of (1.14) is called the *fluxoid* and takes into account the magnetic flux generated from the supercurrent and the magnetic field. The quantization of the fluxoid is a direct consequence of the quantum generalization of the second London equation. If the path Γ_1 is chosen to be further than a few λ_L from the edges, (1.14) imposes that the magnetic flux that passes through any surface can only be an integer of quantum flux: $\int_S \mathbf{B} \cdot d\mathbf{S} = n\Phi_0$. If the integral is done on another path Γ_2 that occupies a simply connected region of the superconductor, the two terms on the left are zero given the absence of magnetic

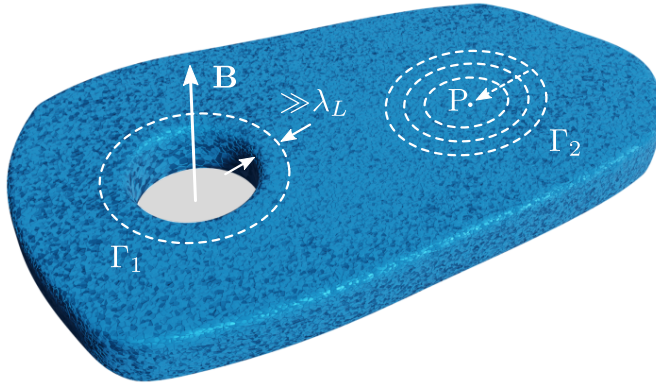


Figure 1.2 – Superconductor immersed in a magnetic field. The two paths Γ_1 and Γ_2 are enclosing multiply connected and simply connected regions respectively.

field and supercurrent. We have:

$$\oint_{\Gamma_2} \nabla \theta \cdot d\mathbf{l} = 0. \quad (1.15)$$

Considering a smaller and smaller path Γ_2 , up to the limit of a point P , (1.15) implies that $\theta(\mathbf{r}_P, \text{end}) - \theta(\mathbf{r}_P, \text{start}) = 0$ and therefore the phase $\theta(\mathbf{r})$ is unambiguously defined for a simply connected superconductor.

1.2.2 Ginzburg-Landau approach

1.2.2.1 The thermodynamics of superconductors

A key point of superconductivity is to understand that the superconducting transition can be interpreted as an actual *phase transition*, in the thermodynamic sense of the term, between the normal and superconducting states. We can therefore associate a state function to them¹. For the superconducting state, the Meissner-Ochsenfeld effect (1.2) implies²:

$$\mathbf{M} = -\mathbf{H}, \quad (1.16)$$

while the magnetization is zero for the normal state:

$$\mathbf{M} = 0, \quad (1.17)$$

as illustrated in the left panel of Fig.1.3. According to thermodynamics, the equi-

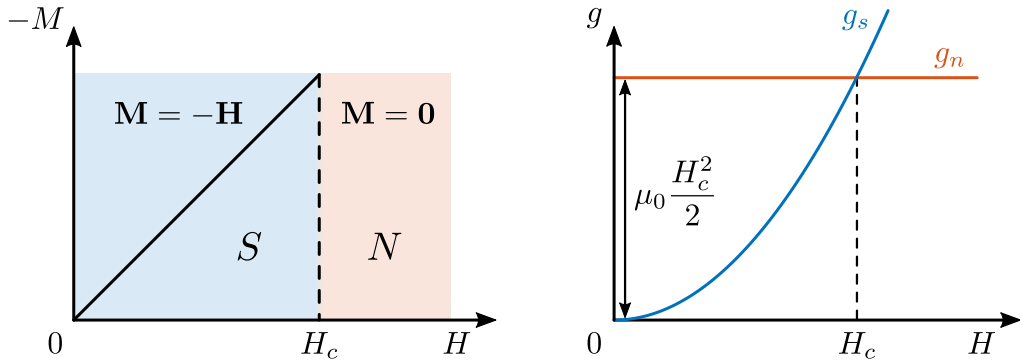


Figure 1.3 – State function of a type-I superconductor (left panel). Field dependence of the Gibbs free energy densities for the normal and superconducting state (right panel).

librium state of a system maintained at temperature T and subjected to a magnetic field H must minimize the *Gibbs free energy density* $g = u - Ts - \mu_0 MH^3$ [18]. Taking the differential $dg = -sdT - \mu_0 M dH$, we see that for each phase at temperature

¹Note that for pedagogical purposes, the importance of thermodynamics will be introduced by limiting ourselves to type I superconductors. More details are available in Ref.[17].

² $\mathbf{B} = \mu_0(\mathbf{H} + \mathbf{M})$ with \mathbf{H} the applied magnetic field and \mathbf{M} the magnetization.

³ u is the internal energy density and s is the entropy density.

T :

$$g(T, H) = g(T, 0) - \mu_0 \int_0^H M dH. \quad (1.18)$$

Particularizing the equation (1.18) with the states functions (1.16) and (1.17) gives the free energies for the superconducting state: $g_s(T, H) = g_s(T, 0) + \mu_0 H^2/2$, and for the normal state: $g_n(T, H) = g_n(T, 0)$. As can be seen in the right panel of Fig. 1.3, the intersection of these two curves at $H = H_c$ implies that $g_s[T, H_c(T)] = g_n[T, H_c(T)]$ which allows to determine the difference in energies for any values of the field:

$$g_s(T, H) - g_n(T, 0) = -\mu_0 \left[\frac{H_c^2(T)}{2} - \frac{H^2}{2} \right]. \quad (1.19)$$

For the particular case $T = 0$, the field

$$H_c = H_c(0) = \frac{2}{\mu_0} \sqrt{g_n(0, 0) - g_s(0, 0)} \quad (1.20)$$

is a measure of the energy difference between the normal and the superconducting states. For this reason, H_c is often called the *thermodynamic critical field* and is an important characteristic of the material.

The thermodynamic formalism of superconductivity, even if it does not provide a microscopic interpretation, allows to explain some of its properties. For example, measurements of the specific heat¹ in normal and superconducting phases show a discontinuous jump for $T = T_c$ [20] as shown in the left panel of Fig. 1.4. The specific heat is intrinsically linked to the free energy. In case of a constant field H , we have $C_H = -T (\partial^2 g / \partial T^2)_H$, which can be rewritten as:

$$C_s^{el} - C_n^{el} = -T \left(\frac{\partial^2 (g_s - g_n)}{\partial T^2} \right)_H = \mu_0 T \left[\left(\frac{\partial H_c(T)}{\partial T} \right)^2 + H_c(T) \left(\frac{\partial^2 H_c(T)}{\partial T^2} \right) \right], \quad (1.21)$$

using equation (1.19). The heat capacity difference at $T = T_c$ is thus given by:

$$(C_s^{el} - C_n^{el})_{T_c} = \mu_0 T_c \left(\frac{\partial H_c(T)}{\partial T} \right)_{T_c}^2. \quad (1.22)$$

Another strength of the thermodynamic approach is to specify the *order* of the superconducting transition whether a magnetic field is applied or not. The $H_c(T)$ curve in the right panel of Fig. 1.1 indicates the region of coexistence of the two phases S and N for which $g_s = g_n$. Thus, along $H_c(T)$ the energy variation between the two phases must be equal: $dg_s = dg_n$. From the expression of the differentials $dg_n = -s_n dT$, $dg_s = -s_s dT - \mu_0 M dH$ and the state function (1.16), we obtain the entropy difference:

$$s_s - s_n = \mu_0 H_c \frac{dH_c}{dT}, \quad (1.23)$$

¹The specific heat is in general the sum of two contributions. The first one is independent of the phase and comes from the vibrations of the crystal lattice (phonons) which increases as T^3 at low temperatures (Debye's model) and saturates at high temperatures (law of Dulong-Petit) [19]. Only the second contribution, from the electrons, is discussed in the text.

which allows us to determine the *latent heat* L_h for the S/N transition:

$$L_h = T(s_n - s_s) = -\mu_0 T H_c(T) \frac{dH_c(T)}{dT}. \quad (1.24)$$

Equations (1.23) and (1.24) particularized to the empirical case (1.1) are illustrated in the right panel of Fig. 1.4 and show a discontinuity of entropy ($s_s - s_n \neq 0$) for transitions under magnetic field and consequently that a heat input is necessary at the S/N transition. Since the discontinuity appears for the entropy, which is related to the first derivative of the free energy, the S/N transition under magnetic field is said to be of *first order*. At zero magnetic field, $s_n - s_s = 0$ and no heat is required. The discontinuity of the free energy carries over to the second derivative (equation (1.22)), which implies that the transition is of *second-order* which is a key element of the Ginzburg-Landau theory of the next section.

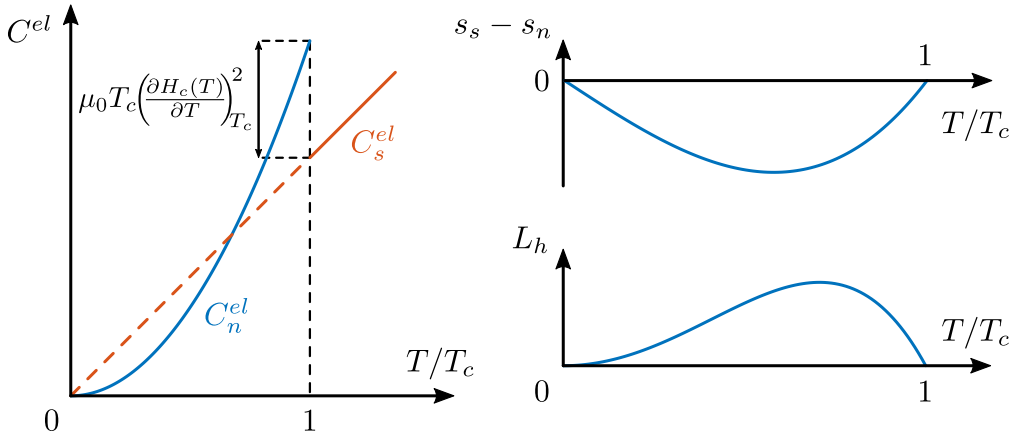


Figure 1.4 – Temperature dependence of the specific heat for a type-I superconductor. The discontinuity of C^{el} is the signature of a second order phase transition (left panel). Difference in entropy and latent heat as a function of temperature (right panel).

1.2.2.2 Ginzburg-Landau equations

In 1936, Landau published a general thermodynamic theory of second-order transitions [21] that can be applied to several phenomena such as the ferromagnetic transition at the Curie point, the superfluid transition of helium or superconductivity. This theory defines an *order parameter* η which measures the order of each phase. During the transition below the critical temperature T_c , a break of symmetry makes the system pass from a disordered state ($\eta = 0$) to an ordered state ($\eta > 0$). Since η is small for temperatures close to and below T_c , Landau's theory assumes that the Gibbs free energy density g can be expressed as a series expansion of the order parameter. In 1950, Ginzburg and Landau brilliantly assumed that the superconducting electron density (1.6) is an order parameter that can describe the superconducting transition (left panel of Fig. 1.5) [22]. In the case of a homogeneous

superconductor without applied magnetic field and no kinetic term we can write:

$$g_s(T) - g_n(T) = \alpha(T)|\Psi|^2 + \frac{\beta(T)}{2}|\Psi|^4 + \dots \quad (1.25)$$

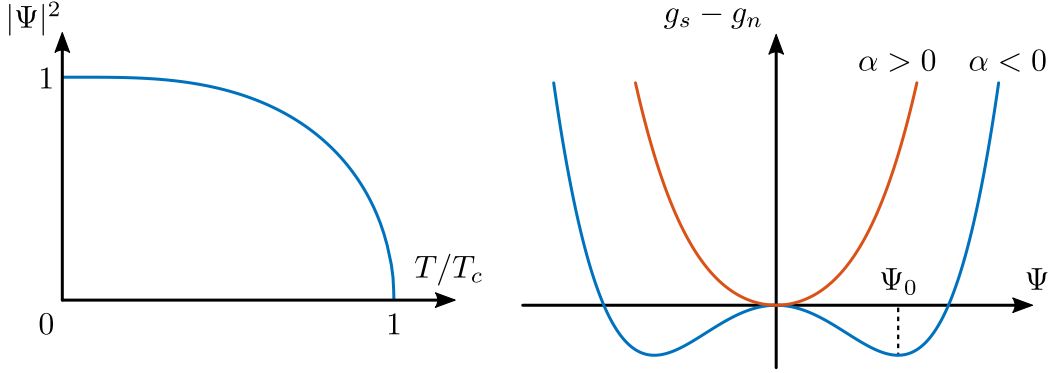


Figure 1.5 – Temperature evolution of the order parameter (left panel). Above T_c , $|\Psi| = 0$ resulting in the normal state. The right panel describes the difference of free energies as a function of Ψ . A minimum different from zero is only possible in the case of $\alpha < 0$.

The coefficients $\alpha(T)$ and $\beta(T)$ are phenomenological expansion parameters that depend on the material with the constraint that $\beta(T) > 0$ to allow the existence of a global minimum. The two situations corresponding to the possible signs of α are illustrated in the right panel of Fig. 1.5. For $T > T_c$, $\alpha(T) > 0$ and the normal state is always preferable to the superconducting state while below T_c , there exists a global minimum for $|\Psi|^2 = |\Psi_0|^2 = |\alpha(T)|/\beta(T)$ defined by $d(g_s - g_n)/d|\Psi|^2 = 0$. A complete discussion about the temperature dependence of α and β parameters is available in [23]. In presence of a magnetic field \mathbf{B}_0 applied to a inhomogeneous superconductor, a generalization of (1.25) gives:

$$g_s = g_n + \alpha|\Psi|^2 + \frac{\beta}{2}|\Psi|^4 + \frac{1}{2m_p} |(-i\hbar\nabla - q_p\mathbf{A})\Psi|^2 + \frac{(\nabla \times \mathbf{A} - \mathbf{B}_0)^2}{2\mu_0}, \quad (1.26)$$

where the first term takes into account the energy density of the normal state g_n , the second and third terms the condensation energy, the fourth term the kinetic energy and the last term the magnetic field shielding energy [24]. Minimizing the integral of (1.26) over the volume of the superconductor with respect to Ψ and \mathbf{A} results in the well-known *first Ginzburg-Landau equation*:

$$\alpha\Psi + \beta|\Psi|^2\Psi - \frac{1}{2m_p}(\hbar\nabla - iq_p\mathbf{A})^2\Psi = 0, \quad (1.27)$$

and *second Ginzburg-Landau equation*:

$$\mathbf{J}_s = \frac{q_p\hbar}{2m_pi}(\Psi^*\nabla\Psi - \Psi\nabla\Psi^*) - \frac{q_p^2}{m_p}|\Psi|^2\mathbf{A}. \quad (1.28)$$

The Ginzburg-Landau (GL) equations can be expressed in a more intuitive form by taking the definition of the London penetration depth λ_L (1.5) and by defining a second characteristic length called the *coherence length* (see left panel of Fig. 1.6):

$$\xi(T) = \sqrt{\frac{\hbar^2}{2m_p|\alpha(T)|}} = \frac{\xi(0)}{\sqrt{1 - T/T_c}}. \quad (1.29)$$

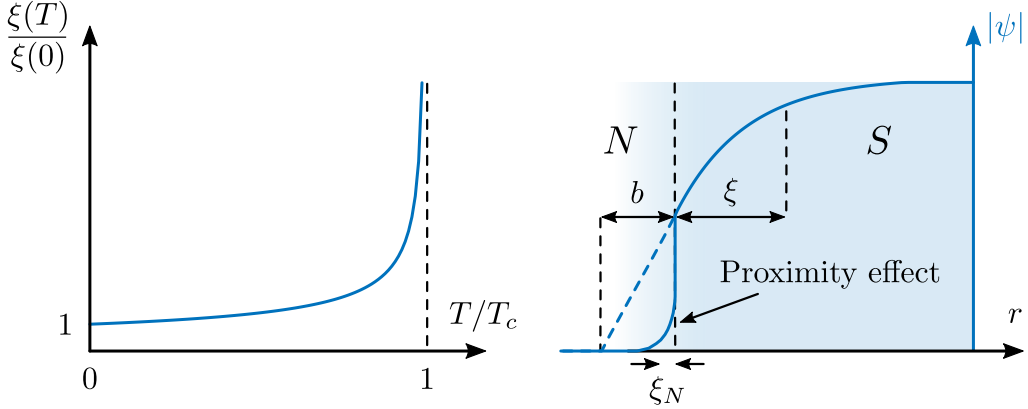


Figure 1.6 – Left panel: temperature dependence of the coherence length ξ . Right panel: evolution of the order parameter across an superconducting/normal metal (S/N) interface. The order parameter presents a discontinuity at the interface but penetrates the metal over a characteristic distance ξ_N (proximity effect). The value of the parameter b allows to consider an insulator ($b \rightarrow \infty$), a magnetic material ($b = 0$), $0 < b < \infty$ for a metal and $b < 0$ for another superconductor of lower T_c .

Expressing the order parameter as $\Psi = \psi \Psi_0 = \psi \sqrt{|\alpha|/\beta}$, the GL equations (1.27) and (1.28) are expressed using *dimensionless order parameter* ψ :

$$\xi^2 \left(\nabla + i \frac{2\pi}{\Phi_0} \mathbf{A} \right)^2 \psi + \psi - |\psi|^2 \psi = 0, \quad (1.30)$$

$$\mathbf{J}_s = -\frac{1}{\mu_0 \lambda_L^2} \left(\frac{\Phi_0}{2\pi} \nabla \theta + \mathbf{A} \right). \quad (1.31)$$

It is worth mentioning that equation (1.31) is exactly the same as equation (1.11) which means that the GL equations are a generalization of the London equations taking into account the quantum and non homogeneous character of ψ . The interpretation of ξ can be understood by considering the behavior of a superconductor in contact with a metal. Like all differential equations, the GL equations must be accompanied by appropriate boundary conditions that establish the magnetic field and/or currents at the interfaces of the superconductor. Without these conditions imposing constraints on the values and gradients of Ψ and \mathbf{A} , the solution to (1.28) and (1.27) would have the trivial solution $\Psi = \Psi_0$ everywhere. Using microscopic

theory, de Gennes showed that the general condition at the interface of a superconductor is given by [25]:

$$\mathbf{n} \cdot (-i\hbar\nabla + q_p\mathbf{A})\Psi = \frac{i\hbar}{b}\Psi, \quad (1.32)$$

where \mathbf{n} is a unit vector normal to the interface and b is a constant representing the extrapolated distance that Ψ would penetrate in the metal if the slope at the interface was maintained (see right panel of Fig. 1.6). The value of parameter b allows to consider in all generality several types of materials like an insulator ($b \rightarrow \infty$), a magnetic material ($b \rightarrow 0$), a metal ($0 < b < \infty$) or weaker superconductor ($b < 0$). The profile of the order parameter ψ along the direction perpendicular to the interface between a superconductor and a metal is obtained by solving (1.30), in the absence of a magnetic field ($\mathbf{A} = \mathbf{0}$), in both materials¹, by taking into account the boundary condition (1.32). The result is shown in the right panel of Fig. 1.6 and highlights two relevant results. First, the interpretation of the coherence length ξ which gives the characteristic length over which the order parameter returns to its equilibrium value following a perturbation (the interface with the metal in this case). Secondly, we see that the order parameter is reduced at the interface and extends over a certain distance ξ_N inside the metal. This penetration of the Coopers pairs inside the metal is called the *proximity effect*.

1.2.2.3 Type I versus type II superconductors

The response of a superconductor to a magnetic field distinguishes two categories of superconductors (see Fig. 1.7) which depend on the ratio of the two characteristic lengths expressed through the *Ginzburg-Landau parameter*:

$$\kappa_{GL} = \frac{\lambda_L}{\xi}. \quad (1.33)$$

According to (1.19), the thermodynamic approach informs us that the energy difference between the superconducting and normal states is the sum of two contributions. The first contribution $g^{cond} = -\mu_0 H_c^2/2$ is negative and represents the energy gain due to the condensation of Cooper pairs. The second contribution $g^{mag} = \mu_0 H^2/2$ is positive and accounts for the energy increase due to the presence of the magnetic field. These expressions of g^{cond} and g^{mag} are valid locally. In the case of a planar S/N interface the B and ψ profiles along the direction perpendicular to the interface have to be taken into account to obtain the surface energy G^{surf} . This energy corresponds to the formation of the interface. A simple model, involving approximate exponential profiles [17], is shown in Fig. 1.7 and gives:

$$G^{surf} = -\mu_0 \lambda_L \frac{H^2}{2} + \mu_0 \xi \frac{H_c^2}{2}. \quad (1.34)$$

¹Note that the equation (1.30) is only valid if the “metal” is in fact a superconductor with a lower T_c . In this case, the sign in front of the ψ term becomes negative due to the change of sign of α between the superconducting state ($\alpha < 0$) and the normal state ($\alpha > 0$). Even if the conclusion remains valid with a real metal ($T_{cn} = 0$), a satisfactory explanation can only be obtained in the framework of a microscopic theory of superconductivity.

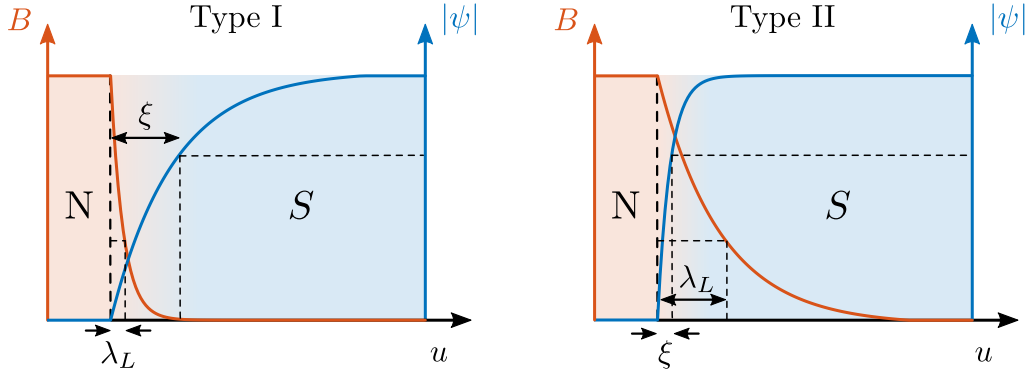


Figure 1.7 – Evolution of the magnetic field B and the order parameter ψ profiles at the superconductor/normal (S/N) interface for type I ($\lambda_L \ll \xi$, left panel) and type II ($\lambda_L \gg \xi$, right panel).

The equation (1.34) shows that, for a given applied field H , the formation of S/N interface is energetically favorable or unfavorable depending on the values of the two characteristic length λ_L and ξ and consequently to the parameter κ_{GL} . In 1957, A.A. Abrikosov showed that this energy minimization of a superconductor in a magnetic field is not done through large planar S/N interface but by the penetration of an object called a *vortex* which is a solution of the GL equations [26]. The structure of a vortex is shown in the left panel of Fig. 1.8 and consists of a normal core of radius ξ bearing a quantum of flux generated by a zone of screening currents of size λ_L . The corresponding equation of (1.34) for the creation of a vortex is given by:

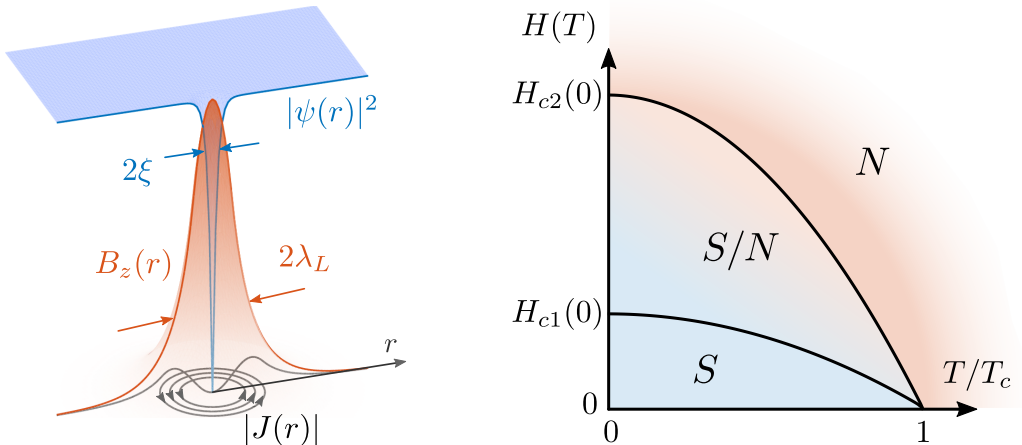


Figure 1.8 – The left panel shows the profile of a vortex at the center of which the Cooper pair density has a singularity while circular currents generate a flux quantum Φ_0 through the normal core. The right panel illustrates the phase diagram for a type II superconductor whose major difference with a type I superconductor is the mixte state (or Shubnikov state) characterized by the penetration of a large number of vortices in the superconductor.

$$G^{vortex} = 2\pi\mu_0(\xi^2 H_c^2 - \lambda_L^2 H^2). \quad (1.35)$$

The equation (1.35) is of great importance and shows the radically different behavior of the superconductor depending on the value of κ_{GL} ¹.

- Type I ($\xi > \lambda_L, \kappa_{GL} < 1$): G^{vortex} is never negative before reaching the critical field H_c and vortex formation is impossible. The line $H_c(T)$ delimits a sharp boundary between the S and N states (see right panel of Fig. 1.1).
- Type II ($\lambda_L > \xi, \kappa_{GL} > 1$): the vortex creation becomes favorable from the field $H_{c1} = (\xi/\lambda_L)H_c = H_c/\kappa_{GL} < H_c$ and the magnetic field partially penetrates inside the superconductor (S/N phase in the right panel of Fig. 1.8). The average magnetization $\langle \mathbf{M} \rangle$ is no longer exactly the opposite of \mathbf{H} (see Fig. 1.9). This is the *phase of Shubnikov* or the *mixed state*. The normal state is reached only at $H_{c2} > H_{c1}$.

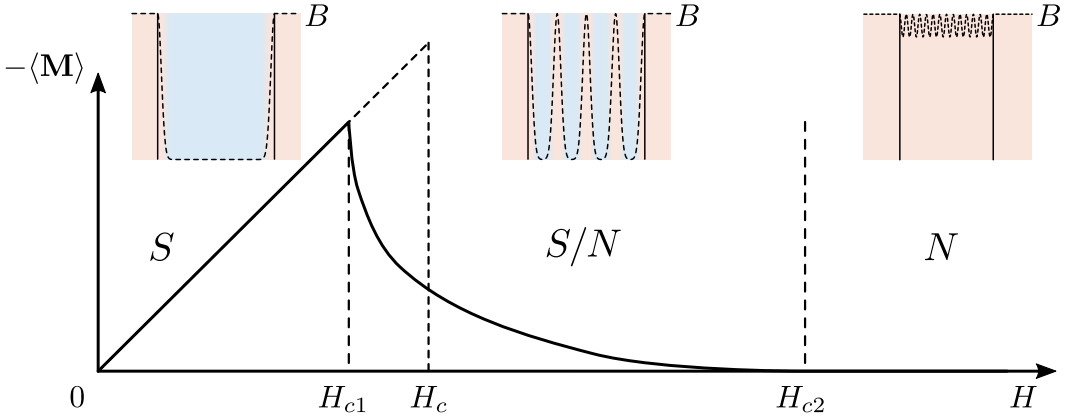


Figure 1.9 – Evolution of the magnetization for a type II superconductor. At the applied field $H \simeq H_{c1} < H_c$, the vortex penetration becomes energetically favorable. The vortex density increases until the value H_{c2} , at which the external field penetrates the whole superconductor.

1.2.3 BCS theory

Although GL's theory describes the behavior of a superconductor near T_c in a very satisfactory way, it does not provide any information on the nature and the microscopic origin of the charge carriers involved. The discovery of the isotope effect in 1950, which stipulates that the critical temperature of an element varies with the mass of its isotope, underlined the importance of phonons [28, 29]. It was not until 1957 that Bardeen, Cooper and Schrieffer (BCS) provided a microscopic theory of superconductivity [12]. The GL theory was derivated from the BCS theory by

¹The equation (1.35) is an approximation made by assuming an exponential profile for the expressions of B and ξ . A more detailed analysis based on the GL equations shows that the critical value that separates type I and II superconductors is $1/\sqrt{2}$ [27].

Gork'ov in 1959 [30]. One of the key points of the BCS theory was to understand that electrons, usually repelling each other via Coulomb interactions, can under certain conditions exhibit a weak attractive interaction through phonon coupling [31, 32]. This attraction involves two electrons and works intuitively as follows. A first electron propagating in the crystal lattice locally contracts the lattice by Coulomb interaction. This deformation creates a slight concentration of positive charge which attracts the next electron. This popularized vision can be interpreted more precisely as an exchange of virtual phonons between two electrons to form a pair: a *Cooper pair* [33]. The BCS theory shows that this interaction is only possible if the state of the two electrons are of the form $|\mathbf{k}_\uparrow, -\mathbf{k}_\downarrow\rangle$, *i.e.* of opposite momentum vectors and spins (left panel of Fig.1.10). Moreover, as the exchange of momentum is done through phonons, a Cooper pair can only be formed with electrons whose energy difference is lower than the maximum energy of the phonons $\hbar\omega_D$ (right panel of Fig.1.10).

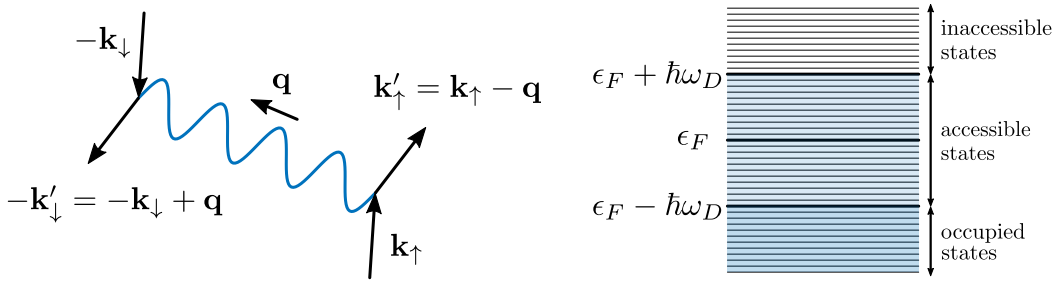


Figure 1.10 – The left panel shows the Feynman diagram illustrating the transfer of momentum through a phonon between two pair states $|\mathbf{k}_\uparrow, -\mathbf{k}_\downarrow\rangle$ and $|\mathbf{k}'_\uparrow, -\mathbf{k}'_\downarrow\rangle$. Occupied, accessible and forbidden states for a Cooper pair at 0 K (right panel).

It is obvious that independent electrons cannot form Cooper pairs and therefore an attractive term \hat{V} must be included in the Hamiltonian that accounts for the interaction between the electrons. The *simple BCS model* assumes that an attractive potential exists between all pair states of the form:

$$V_{\mathbf{k}', \mathbf{k}} = \langle \mathbf{k}'_\uparrow - \mathbf{k}'_\downarrow | \hat{V} | \mathbf{k}_\uparrow - \mathbf{k}_\downarrow \rangle = -V_{BCS}, \quad (1.36)$$

only for states within ϵ_F (Fermi energy) and $\epsilon_F + \hbar\omega_D$ (right panel of Fig.1.10). In the case of a single Cooper pair at 0 K, it can be shown that the Cooper pair will then sweep through the set of accessible energy states to lead to the formation of a lower energy state. The generalization of this problem considering a large number of Cooper pairs constitutes a complex version of the N-body problem. The conclusion also leads to the formation of a state whose energy lowering at 0 K, with respect to the Fermi energy, is called *superconducting gap*:

$$\Delta(0) = 2\hbar\omega_D e^{-\frac{1}{V_{BCS}G(\epsilon_F)}}, \quad (1.37)$$

with ω_D the Debye frequency, V_{BCS} the attractive potential between pair states and $G(\epsilon_F)$ the density of states at the Fermi energy. The BCS theory also proves a

direct link between the gap and T_c :

$$\Delta(0) \sim 1.76k_B T_c, \quad (1.38)$$

and its evolution with temperature. The temperature evolution of (1.38) is identical to the left panel of Fig. 1.5 ($|\Psi|^2$ to be replaced by $\Delta(T)/\Delta(0)$) showing therefore that the order parameter of the GL theory can also be interpreted as the local value of the gap [34]. The electrons not involved in the formation of Cooper pairs can, at $T \neq 0$ K, occupy some of the accessible energy levels of the Cooper pairs. This reduction of the accessible states increases the system's energy by an amount $\sqrt{\Delta^2 + (\epsilon_k - \epsilon_F)^2}$ and leads to the *dispersion relation*:

$$G(\epsilon) = G(\epsilon_F) \frac{|\epsilon_k - \epsilon_F|}{\sqrt{(\epsilon_k - \epsilon_F)^2 - \Delta^2}}, \quad (1.39)$$

where $G(\epsilon_F)$ is the density of state at the Fermi energy, is illustrated in Fig. 1.11. The existence of the superconducting gap in the quasiparticles spectrum gap was experimentally proven for the first time by Giaever in 1960 [35].

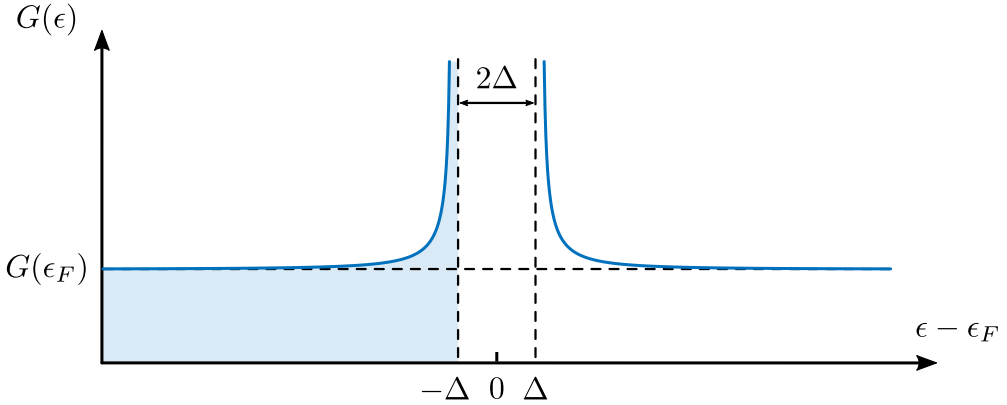


Figure 1.11 – Density of state of quasiparticles in a superconductor as a function of $\epsilon - \epsilon_F$.

1.3 The Josephson effect

In this section, we focus on the transport properties of different junctions. The Superconductor-Insulator-Superconductor (SIS) junction, being of great historical and technical importance, will be illustrated as an example. Superconductor-Constriction-Superconductor (SCS) junctions like the Dayem bridge (simple constriction), which are addressed in this thesis, will be developed later. A SIS junction consists of two superconducting reservoirs separated by a thin insulating layer as shown in the left panel of Fig. 1.12. In 1962, B. D. Josephson theoretically predicted that Cooper pairs can tunnel through the insulating layer [36] and that such a junction is governed by the following two equations:

$$I_s(\Theta) = I_c \sin \Theta, \quad (1.40)$$

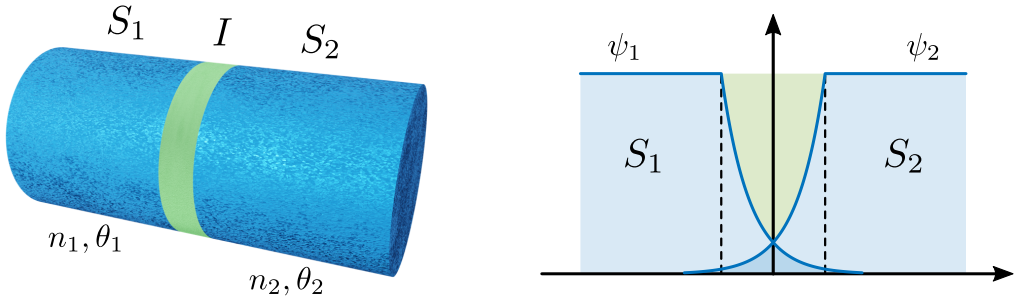


Figure 1.12 – SIS junction where two superconductors S_1 and S_2 are separated by a thin insulating layer I (left panel). Cooper pair density profile along the SIS junction. The overlap of the ψ functions in the insulator (dark blue area) indicates the existence of a Cooper pair current by tunneling effect (right panel).

$$\frac{d\Theta}{dt} = \frac{2\pi}{\Phi_0} V, \quad (1.41)$$

where I_s is the supercurrent, I_c the *critical current*, V the potential across the junction and

$$\Theta = \theta_1 - \theta_2 - \frac{2\pi}{\Phi_0} \int_1^2 \mathbf{A} \cdot d\mathbf{l} \quad (1.42)$$

the *gauge invariant phase difference*, where 1 and 2 denote points on either side of the junction [13]. In (1.42), the last term is only to be taken into account when magnetic fields are present and ensures that Θ is independent of the chosen gauge. A comprehensive demonstration of (1.42) can be found in [13]. The first equation (1.40), called current phase relationship (CPR) or direct current (DC) Josephson effect, implies a surprising result: a current can cross the junction in the absence of potential difference, only the phase difference matters¹. If the insulator layer is thin enough, see right panel of Fig.1.12, the wave functions of the two reservoirs can overlap and a non-zero Cooper pair density exists in the insulator and thus enable tunneling of Cooper pairs through the junction [37, 38]. The second equation (1.41), called the alternative current (AC) Josephson effect or *voltage-phase relation*, shows that applying a DC voltage V across the junction has the effect of linearly increasing the phase difference and therefore causing I_s to oscillate at the voltage dependent *Josephson frequency*:

$$\frac{f}{V} = \frac{1}{\Phi_0} \sim 483.597898 \frac{\text{MHz}}{\mu\text{V}}, \quad (1.43)$$

which produces frequencies close to 500 GHz for a voltage of 1 mV [39–42]. One year after B. Josephson’s result, Ambegaokar and Baratoff [43] (AB) generalize the SIS junction result for an arbitrary temperature, which in the symmetric case

¹Let us specify that the equation (1.40) does not mean that a SIS junction is a “source” of current but that the phase difference automatically adapts to the current imposed through the junction to verify the CPR.

$\Delta_1 = \Delta_2 = \Delta$, is given by:

$$I_s(\Theta, T) = \frac{\pi \Delta(T)}{2eR_N} \tanh\left(\frac{\Delta(T)}{2k_B T}\right) \sin \Theta. \quad (1.44)$$

Although the second Josephson equation (1.41) is general, this is not the case for (1.40). The CPR depends on the nature of the junction and it is therefore important to define when a current can be classified as a Josephson current. According to reviews [44, 45], a Josephson type current must satisfy the following condition:

1. The current can only flow if there is a phase difference between the two reservoirs.
2. It must be periodic: $I_s(\Theta) = I_s(\Theta + 2\pi)$.
3. The current is antisymmetric: $I_s(\Theta) = -I_s(-\Theta)$.
4. The current is zero for integer values of π : $I_s(k\pi) = 0$ (with k an integer).
5. The second Josephson equation (1.41) is verified.

The first four conditions have a general solution¹:

$$I_s(\Theta) = \sum_{n \geq 1} I_n \sin(n\Theta). \quad (1.45)$$

All junctions with a CPR of the type (1.45) are called *Josephson junctions* and the solution (1.40) related to the SIS junction, sometimes called a *conventional Josephson junction*, is a special case.

1.3.1 Different kinds of weak links

1.3.1.1 What is a weak link?

The insulating layer presented in the previous section is a particular case of a Weak-link (WL) between two superconducting reservoirs. Let us consider the case of two blocks of the same superconductor at the same temperature completely isolated from each other. We can describe the density of superelectrons in each of the blocks being described by equation (1.6) with an identical amplitude (same material and temperature), the phase being arbitrary. If we allow the two blocks to interact through a weak link, the two wave functions will then interfere to form a new wave function describing the global behavior of the two superconducting blocks. From this point of view, the Josephson effect can be seen, as well as the magnetic flux quantization, as a macroscopic manifestation of the interference of the wave functions describing the coherent behavior of the Cooper pairs [11].

A weak link, described by a given CPR, can be of very different natures [44, 45] and is defined as a region characterized by a critical current significantly lower

¹Note that in general, the sum should also contain a term $J_n \cos(n\Theta)$ [46].

than in the bulk [11]. This can be achieved, for example, by imposing to the current to pass through a material containing a lower density of Cooper pairs, which amounts to reduce the critical current density, as is the case for SIS junctions (left panel of Fig. 1.12 or panel (a) of Fig. 1.13). One can decrease the critical current density in a uniform superconducting film covered with a normal film (panel (b) of Fig. 1.13) or increase the density of Cooper pairs in a Superconductor-Normal metal-Superconductor (SNS) junction by proximity effect (panel (c) of Fig. 1.13). The critical current can be reduced by shrinking the cross-sectional area as in the case of a Dayem bridge (the one considered in this thesis, panel (d) of Fig. 1.13) or a junction of variable thickness (panel (e) of Fig. 1.13). Let us also mention the case of junctions using high T_c superconductors for which an abrupt change of orientation of the crystal lattice can be considered as a weak link because of their very short coherence lengths [47, 48].

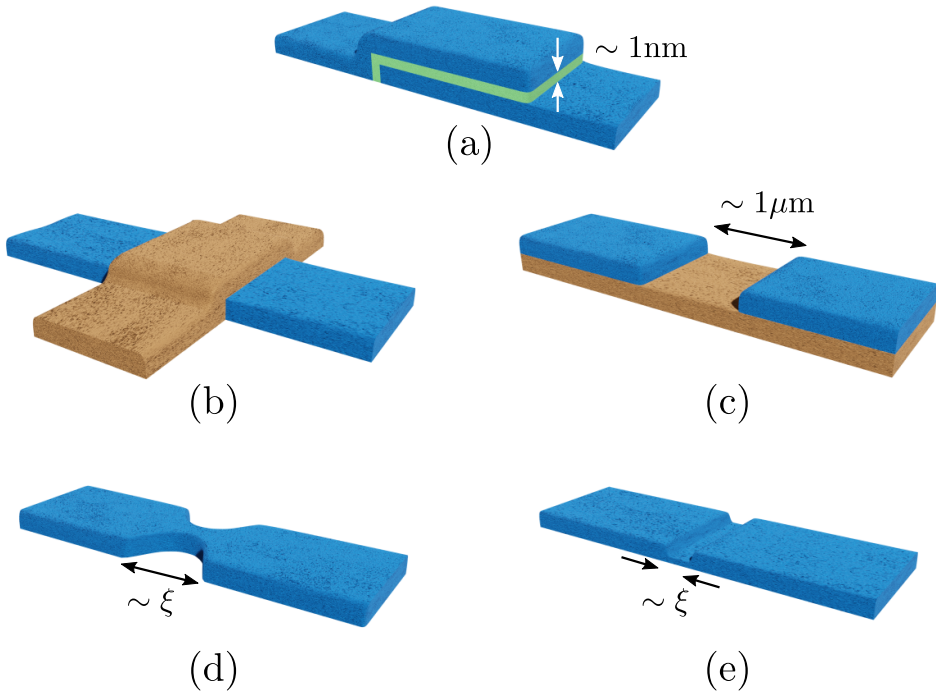


Figure 1.13 – Illustration of several weak-links configurations. Panel (a) shows the case of a SIS junction by superposition of superconducting (blue color) and insulating (green color) layers. Two examples of SNS junctions are given in panels (b) and (c) where the normal metal (brown color) affects the superconductor by the proximity effect. Junctions working on the principle of current concentration, are shown in panels (d) (Dayem bridge) and (e) (variable thickness junction).

1.3.1.2 Point contacts

In this section we briefly discuss CPR for junctions with high supercurrent concentration called *point contact* which, in addition to being a natural first approximation of SCS junctions, are also the simplest system that can exhibit characteristics of the Josephson effect. Further information is available in the two well-known reviews by Likharev [44] and Golubov *et.al.* [45]. Although not general, the Aslamasov-Larkin (AL) model has pedagogical interest.[49] This model, based on the GL theory, considers that the Josephson effect is a consequence of the overlap between the order parameters ψ from both superconducting blocks (see right panel of Fig. 1.12). The resulting current, valid only near T_c , is:

$$I_s(\Theta, T) = \frac{\pi \Delta_1(T) \Delta_2(T)}{4e R_N k_B T} \sin \Theta, \quad (1.46)$$

where Δ_i is the gap of block i and R_N is the junction normal resistance. The expression (1.46) does not depend on the electron mean free path l in the weak link and only requires the effective length d_{eff} ¹ of the junction to be well below the coherence length:

$$d_{eff} \ll \xi(T). \quad (1.47)$$

As $\xi(T)$ diverges for $T \rightarrow T_c$, (left panel of Fig. 1.6), the condition (1.47) is always verified close to T_c and the sinusoidal regime is the limiting case of all CPR. The generalization of the AL model for all temperatures was elaborated by Kulik-Omelyanchuk (KO) but requires to take into account the mean free path in the weak link. The First Kulik-Omelyanchuk model (KO-1) starts from the Usadel equations, which are valid in the dirty limit $l \ll \xi_0$ ², and having length $d_{eff} \ll \sqrt{\xi_0 l}$ [50]. Under these assumptions, the authors obtain in the $\Delta_1 = \Delta_2 = \Delta$ case:

$$I_s(\Theta, T) = \frac{4\pi k_B T}{e R_N} \sum_{\omega > 0} \frac{\Delta(T) \cos(\Theta/2)}{\delta(T)} \arctan \left(\frac{\Delta(T) \sin(\Theta/2)}{\delta(T)} \right), \quad (1.48)$$

where $\delta(T) = \sqrt{(\Delta(T)^2 \cos(\Theta/2))^2 + (\hbar\omega)^2}$ and $\hbar\omega = \pi k_B T (2n + 1)$. Later, the Second Kulik-Omelyanchuk model (KO-2) was developed for a small ($d_{eff} \ll \xi_0$) and clean ($d_{eff} \ll l$) WL by solving the Eilenberger equations to obtain [51]:

$$I_s(\Theta, T) = \frac{\pi \Delta(T)}{e R_N} \tanh \left(\frac{\Delta(T) \cos(\Theta/2)}{2k_B T} \right) \sin(\Theta/2). \quad (1.49)$$

In 1978 Haberkorn (H) generalized the two KO models by considering a tunnel barrier of arbitrary angle-averaged transmission probability \bar{D} in the constriction [52] and this model was further improved by Beenakeer (B) in 1991 by assuming

¹The effective length is defined by Likharev [44] as the distance over which the nonlinear effects in the weak link are localized. We always have $d_{eff} \geq d$ with d the “geometric” length of the link.

²As Likharev [44] carefully points out, one should not confuse the qualifiers “clean” and “dirty” which are used both for the general theory of superconductivity (l is then compared to the coherence length ξ_0) and for weak links (where l is compared to the effective length d_{eff}).

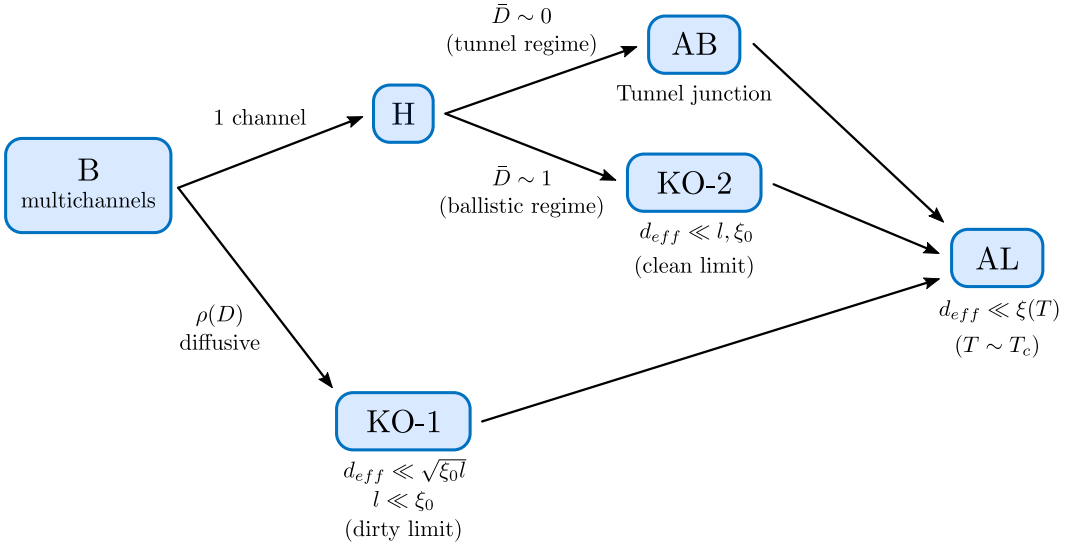


Figure 1.14 – Diagram representing the links between the different models for point contacts. All the presented models are special cases of the Beenakker multichannel model **B** and tend towards the results of **AL** when T is close to T_c .

the existence of a multitude of channels within the junction [53]. The connections between the different models is summarized in the diagram of Fig.1.14 and are developed in the appendix A where the details for the numerical determination of the CPR are provided. The evolution of the critical current as a function of temperature, determined from the CPR, is shown in the Fig.1.15 where the **AB** model is taken as reference. We observe that the differences between models are significant at low temperatures while all of them tend towards the sinusoidal regime of **AL** close to T_c .

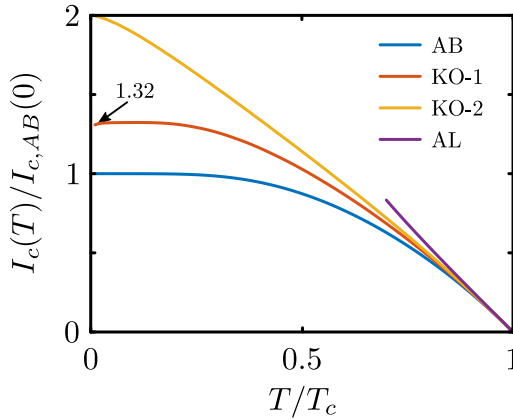


Figure 1.15 – Comparison of the temperature dependencies of the critical current for point-contact WL. The **AB** model is taken as reference. Figure adapted from [44].

1.3.1.3 Long junctions

The previous section showed that even for point contact junctions, the CPR exhibits a wide range of behaviors and tends towards the sinusoidal regime of tunnel junctions when $T \rightarrow T_c$. This section focuses on the influence of the junction length on the shape of the CPR. Likharev and Yakobson proposed in 1975 a simplified WL model called One Dimension Structure with Electrodes in Equilibrium (ODSEE), see left panel of Fig. 1.16) [54]. This model assumes that the cross-section of the junction w^2 is constant and sufficiently small ($w^2 \ll \lambda(T)^2$) so that the variables of the problem depend only on the coordinate along the junction's direction. It is also necessary for the two superconducting reservoirs at the junction terminals to be in equilibrium, such that the value of the order parameter at one end of the junction is equal to that of the adjacent electrode. The CPR is determined by solving the GL equations (1.30) and (1.31) without magnetic field to obtain the solutions illustrated on the right panel of the Fig. 1.16. We observe that for $\bar{d} = d/\xi(T) \rightarrow 0$,

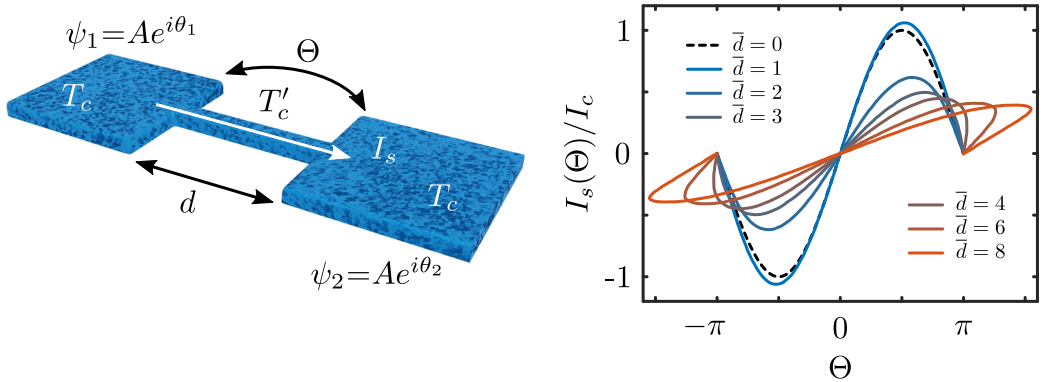


Figure 1.16 – Left panel: geometry of a long junction studied with the ODSEE model. The junction is characterized by the dimensionless parameter $\bar{d} = d/\xi(T)$ and the phase difference Θ at its boundaries. Right panel: evolution of the CPR with the length of the junction showing a significant deviation from the Josephson effect of tunnel junctions for $\bar{d} > 3.5$ where the CPR becomes multivalued. Panel adapted from [55].

the model reproduces the sinusoidal CPR of a short junction (black dotted line) with the critical current reached at the critical phase $\pi/2$. For reasonable junction lengths ($\bar{d} < \bar{d}_c \sim 3.5$) the CPR becomes distorted and the critical current decreases while shifting its critical phase to values higher than $\pi/2$. Beyond the length \bar{d}_c , the critical phase continues to increase to approach or exceed π , leading to a multivalued CPR for $\Theta \gtrsim \pi$ and a critical current tending to the depairing limit $I_s/I_c = 2/(3\sqrt{3})$ ¹. The multivalued critical current has been obtained more recently by other studies involving Superconducting QUantum Interference Device (SQUID)² [55–57]. Although the ODSEE is limited to temperatures close to T_c (GL assump-

¹The depairing mechanism occurs when the kinetic energy of the superconducting carriers becomes equal to their condensation energy leading to the breaking of the Cooper pair [13].

²See section 1.3.4.

tion), it is interesting to note that the ratio $d/\xi(T)$ increases as it approaches 0 K and it is tempting to apply the results of long junctions for short junctions at low temperature. In addition, some authors predict that the CPR of a thin wire at low temperatures must be linear [58, 59]. In 2017, Murphy and Bezryadin [60] successfully validated this hypothesis, reproducing SQUID oscillations at low temperatures with a CPR of the form:

$$I_s(\Theta) = I_c \frac{\Theta}{\Theta_c}, \quad (1.50)$$

where Θ_c is the *critical value* phase beyond which the junction switches to the normal state. The SQUID model of Murphy and Bezryadin is described in detail in section 1.3.4.2.

1.3.1.4 Weak link regimes

Left panel of Fig.1.17 summarizes the behavior of weak links in the dirty limit. Short junctions show a Josephson-like behavior (lower part) given by equation (1.45) and summarized in Fig.1.14. For long and narrow junctions (upper left part), the ODSEE model shows that above a critical length l_c the CPR becomes multivalued and that the critical current is caused by a break of the Cooper pairs following an increase of their kinetic energy (depairing limit). Finally, the top right quadrant relaxes the condition on the width of the junction. As soon as this width exceeds a few coherence lengths, the formation of vortices becomes possible and the dissipation generated by their displacement will dictate the value of the critical current of the junction [61].

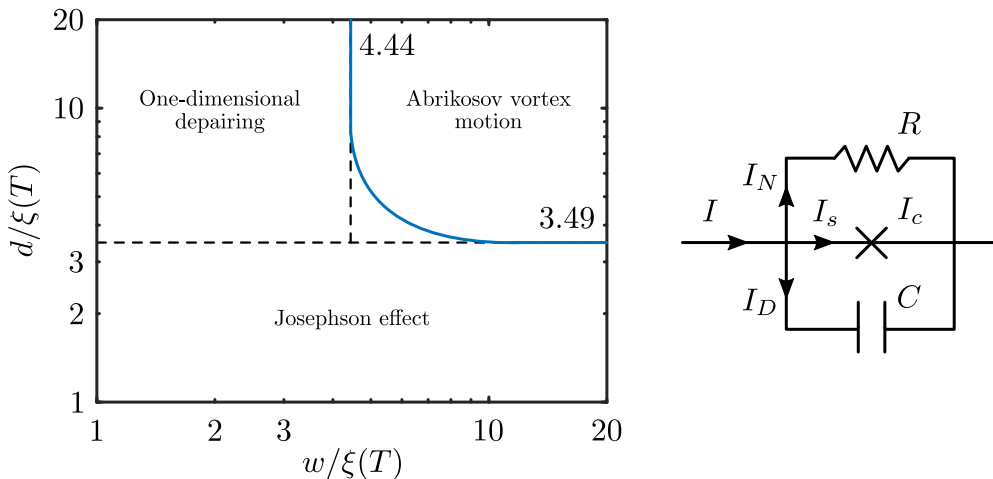


Figure 1.17 – Left panel: phase diagram for a weak link in the dirty limit showing that the physics dominating the junction, *i.e.* Josephson effect, depairing limit or vortex appearance, depends on its geometry. Figure adapted from [44]. Right panel: RCSJ lumped circuit.

1.3.2 The voltage state

Until now we have considered the zero voltage state, *i.e.* when $I \leq I_c$. For the sake of completeness, we consider here the case of a SIS junction biased by a current¹ $I > I_c$ in the framework of the Resistively and Capacitively Shunted Junction (RCSJ) model. This model equates a junction to a parallel circuit given in the right panel of Fig. 1.17 which directly states that the total current is given by:

$$I = I_s + I_N + I_D + I_F. \quad (1.51)$$

The current I_s is due to the Cooper pairs tunneling through a channel modeled by a perfect Josephson junction. It is the only channel used for $I \leq I_c$. The phase Θ then adjusts to satisfy equation (1.40) and the equation (1.41) imposes that $V = 0$. If $I > I_c$ a part of the current is provided by $I_N = V/R_N$, which models the transfer of quasiparticles, and by $I_C = CdV/dt$, coming from the displacement current due to the junction capacitance. These last two contributions necessarily imply $V \neq 0$ across the junction. The current I_F , which takes into account the noise due in part to the temperature, and is not discussed here. Given (1.41), the total current can be expressed as:

$$I = I_c \sin \Theta + \frac{\Phi_0}{2\pi R_N} \frac{d\Theta}{dt} + C \frac{\Phi_0}{2\pi} \frac{d^2\Theta}{dt^2}. \quad (1.52)$$

By defining the dimensionless variables $i = I/I_c$ and $\tau = t/\tau_c$ where

$$\tau_c = \Phi_0 / (2\pi I_c R_N), \quad (1.53)$$

and the *Stewart-McCumber parameter*:

$$\beta_c = \frac{2\pi C I_c R_N^2}{\Phi_0}, \quad (1.54)$$

the equation (1.52) takes the simplified form:

$$\beta_c \frac{d^2\Theta}{d\tau^2} + \frac{d\Theta}{d\tau} + \sin \Theta - i = 0. \quad (1.55)$$

Depending on junction size and material, the critical current generally ranges from a few nA to a few mA while normal resistances varies from a few Ω to several $k\Omega$. For non-extreme values of I_c and R_N , $\tau_c \in 10^{-12} - 10^{15}$ s. By imposing a current $i > 1$ in the junction, the equation (1.55) directly imposes that Θ is not constant and thus that the Cooper pairs current varies relentlessly. Consequently the currents of the resistive and capacitive channels will adapt to reach the imposed total current and it results a complicated dynamics of $i_s(\tau)$ and $v(\tau) = V(\tau)/(R_N I_c)$ whose result for some values of i are given in Fig. 1.18 in the *overdamped* case $\beta_c = 0$. The characteristic time (1.53) being very small, the oscillations are too fast to be observed and in practice only the temporal mean values of the potential $\langle v \rangle$ are

¹The case of voltage biased junctions will not be treated here. For more details see the references [14, 62].

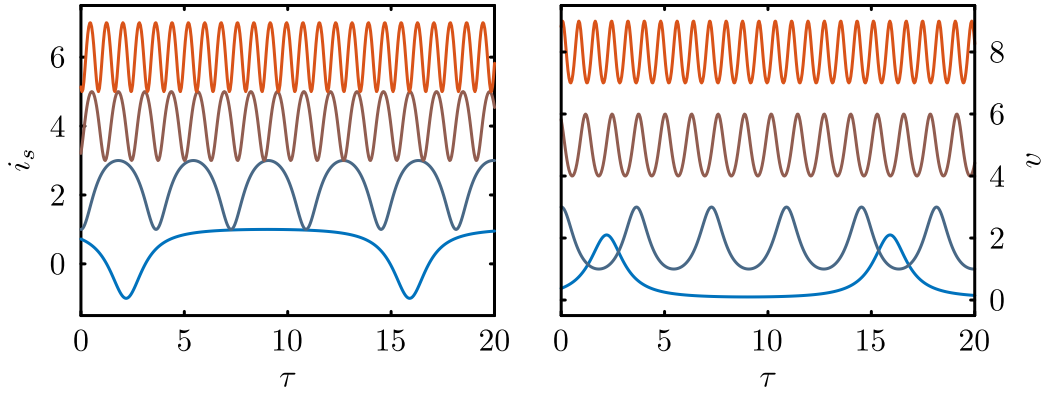


Figure 1.18 – Time evolution of the superconducting current (left panel) and voltage (right panel) for an overdamped ($\beta_c = 0$) junction for biased currents $i = 1.1, 2, 5, 8$ (respectively given by the blue to red curves). The top three curves of the left panel have been shifted vertically by 2, 4 and 6 for clarity.

measurable. The characteristic $\langle v \rangle(i)$ curve obtained for $\beta_c = 0$ is given by the blue curve¹ of the left panel of Fig. 1.19 and describes a reversible trajectory for positive and negative current sweeps characteristic of a overdamped junction. Increasing values of β_c (curves from light blue to red) lead to an irreversibility of the $\langle v \rangle(i)$. For all curves, the transition to the normal state occurs for $i = i_c = 1$ while the transition to the superconducting state occurs at $i_r < i_c$ and depends on β_c as illustrated in the right panel of Fig. 1.19. High values of β_c correspond to the limit case of *underdamped* junction where the $\langle v \rangle(i)$ curve tends to the ohmic behavior.

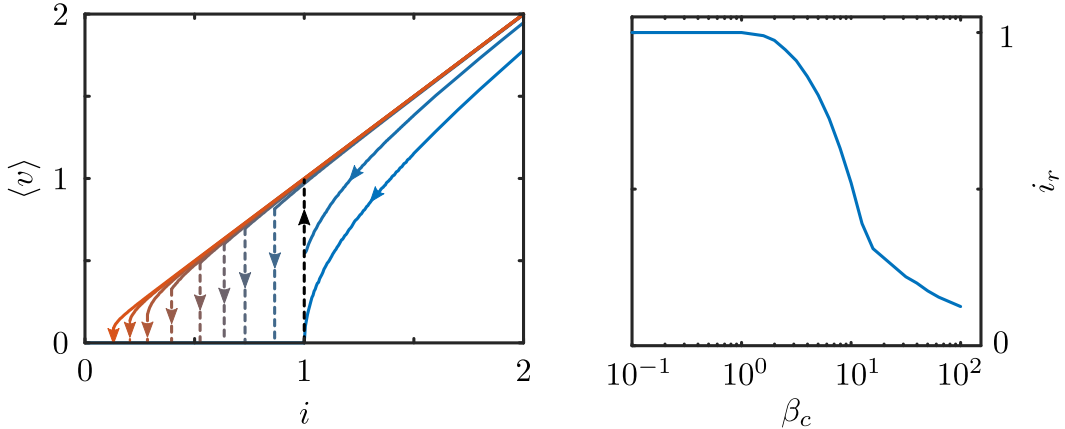


Figure 1.19 – Left panel: $\langle v \rangle(i)$ curves for β_c ranging from 0 (blue curve, overdamped junction) to 200 (red curve, underdamped junction). The transition to the normal state occurs at $i = i_c = 1$, independently of the value of β_c . The increase of β_c gives rise to an increase of the irreversible behavior of the junction. Right panel: evolution of the retrapping current i_r as a function of the parameter β_c .

¹Note that an analytical solution is available for this case and given by $\langle v \rangle = \sqrt{i^2 - 1}$ for $i > 1$.

1.3.3 Weak link in a magnetic field

Thus far, it was not necessary to take into account any inhomogeneity of Θ in the plane of the junction perpendicular to the direction of the current and the total current could be used in the first Josephson equation (1.40). To understand the behavior of a junction in a magnetic field, it is necessary to consider an extended junction with a local form:

$$J_s(y, z) = J_c \sin \Theta(y, z) \quad (1.56)$$

where $J_s(y, z)$ denotes the current density of Cooper pairs at any point on the junction (see left panel of Fig. 1.20) and J_c the local critical current density that we assume to be constant. Assuming that the magnetic field generated by the

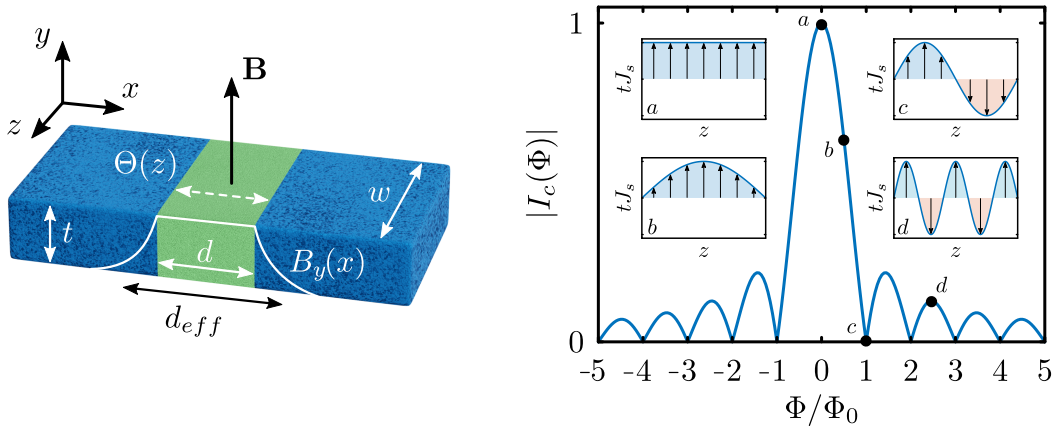


Figure 1.20 – Left panel: rectangular junction subjected to an out-of-plane magnetic field \mathbf{B} generating an inhomogeneity of the gauge invariant phase difference $\Theta(z)$. Right panel: evolution of the critical current as a function of the flux $\Phi = Bwd_{eff}$ which penetrates the junction. The oscillations of I_c are due to the variations imposed by B according to the equation (1.57). Examples of Josephson current distributions in the junction are given for the cases $\Phi = 0$, $\Phi_0/2$, Φ_0 and $2.5\Phi_0$ respectively labeled by the points a, b, c and d.

Josephson currents in the junction are negligible compared to the applied \mathbf{B}^1 , it can be shown [13] that the effect of a field \mathbf{B} in the y direction is to modulate the gauge invariant phase difference with respect to the z axis as follows:

$$\Theta(z) = \frac{2\pi}{\Phi_0} B d_{eff} z + \Theta_0 = Kz + \Theta_0, \quad (1.57)$$

where $d_{eff} = d + 2\lambda_L$ is the effective length of the junction which takes into account the penetration of the magnetic field $B_y(x)$ in both electrodes and Θ_0 an integration

¹This condition is equivalent to assuming that the dimensions of the cross-section of the junction are smaller than a characteristic length called the Josephson length λ_J , which can be seen as an analogue to the London length but for a junction. Since λ_J obeys a relation of the type (1.5), the small value of n_p inside the junction makes $\lambda_J \gg \lambda_L$.

constant. Since the phase Θ depends only on z , the equation (1.56) becomes:

$$J_s(z) = J_c \sin(Kz + \Theta_0). \quad (1.58)$$

The total current is obtained by integration of (1.58) over the section area:

$$I_s(B) = \int_{-t/2}^{t/2} dy \int_{-w/2}^{w/2} J_s(z) dz, \quad (1.59)$$

which can be seen as the Fourier transform of a gate function. The final result is:

$$I_s(\Phi) = I_c \frac{\sin\left(\pi \frac{\Phi}{\Phi_0}\right)}{\left(\pi \frac{\Phi}{\Phi_0}\right)}, \quad (1.60)$$

where $I_c = wtJ_c$. The absolute value of (1.60) is plotted in the right panel of Fig. 1.20.

The oscillations of the critical current can be understood more intuitively by considering some particular cases of the imposed flux. For $\Phi = 0$ (point a), the phase is identical over the whole width of the junction and therefore J_s is constant, this is the case where I_c reaches its maximum value. For $\Phi = \Phi_0/2$, the width of the junction corresponds to half a period of $\Theta(z)$, the current density cannot reach the critical value in the whole junction and so I_c is reduced (point b). For $\Phi = \Phi_0$ there is always as much positive as negative current and globally the total current is always zero and $I_c = 0$ (point c). A last case corresponding to $\Phi = 2.5 \Phi_0$ is given by point d. It is interesting to notice that in opposition to the RCSJ model of the previous section where the average voltage is due to a temporal interference of the wave function, here the critical current is due to a spatial interference of ψ .

1.3.4 The SQUID sensor

The acronym SQUID stands for Superconducting QUantum Interference Device and is one of the most sensitive magnetic field sensors in the world today [13, 63]. Its operation is based on the interference of the condensate wave function between two weak links in parallel in a superconducting loop, as shown in Fig. 1.21. In the following, we will recall the basic equations that describe the behavior of a general asymmetric SQUID [62]. The first is a direct consequence of Kirchhoff's law of current conservation:

$$I_s = I_{s_1} + I_{s_2} = I_{c_1} f_1(\Theta_1) + I_{c_2} f_2(\Theta_2), \quad (1.61)$$

where f_1 and f_2 describe the CPR of the two junctions in terms of the two gauge invariant phase differences Θ_1 and Θ_2 . Moreover, since the phase difference can vary by $2\pi n$ on a closed contour, the equation (1.13) evaluated counter-clockwise on the white dashed contour of the Fig. 1.21 gives:

$$(\theta_b - \theta_a) + (\theta_c - \theta_b) + (\theta_d - \theta_c) + (\theta_a - \theta_d) = 2\pi n. \quad (1.62)$$

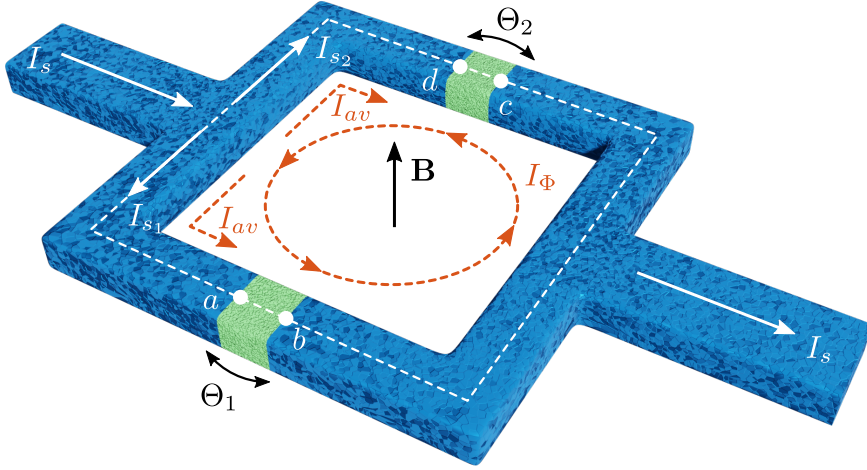


Figure 1.21 – Schematic representation of a SQUID formed by two weak links (green section) associated in parallel in a superconducting loop. The currents I_{s1} and I_{s2} (white solid arrows) can be seen as the sum of the average and circular currents I_{av} and I_{Φ} (red dotted arrows).

The first and third terms of (1.62) can be directly expressed as a function of the gauge invariant phase difference via (1.42) while the second and fourth terms are obtained by integrating the equation (1.11) over the $(b \rightarrow c)$ and $(d \rightarrow a)$ paths. We finally obtain¹:

$$\Theta_2 - \Theta_1 = 2\pi n + \frac{2\pi}{\Phi_0} \Phi + \frac{2\pi}{\Phi_0} \left(\int_b^c \mu_0 \lambda_L^2 \mathbf{J}_s \cdot d\mathbf{l} + \int_d^a \mu_0 \lambda_L^2 \mathbf{J}_s \cdot d\mathbf{l} \right), \quad (1.63)$$

where the magnetic flux Φ is defined as:

$$\Phi = \int_S \mathbf{B} \cdot d\mathbf{S}. \quad (1.64)$$

We can also express without loss of generality the two supercurrents as:

$$\begin{aligned} I_{s1} &= I_{av} + I_{\Phi} \\ I_{s2} &= I_{av} - I_{\Phi}, \end{aligned} \quad (1.65)$$

where,

$$\begin{aligned} I_{av} &= \frac{I_{s1} + I_{s2}}{2} \\ I_{\Phi} &= \frac{I_{s1} - I_{s2}}{2}, \end{aligned} \quad (1.66)$$

are respectively the average and circular currents and represented as red dotted arrows in Fig.1.21. This allows to express the total flux through the loop as the sum of two term:

$$\Phi = \Phi_{ext} + L_G I_{\Phi}, \quad (1.67)$$

¹ $\oint \mathbf{A} \cdot d\mathbf{l} = \int_S \nabla \times \mathbf{A} \cdot d\mathbf{S} = \int_S \mathbf{B} \cdot d\mathbf{S}.$

where Φ_{ext} the external applied magnetic flux and L_G is the geometric inductance of the SQUID. The last two terms in (1.63) can be expressed in a more concise form by defining the kinetic inductance L_K as¹:

$$L_K I = \int \mu_0 \lambda_L^2 \mathbf{J}_s \cdot d\mathbf{l}. \quad (1.68)$$

(1.67) and (1.68) incorporated in (1.63) reads:

$$\Theta_2 - \Theta_1 = 2\pi n + \frac{2\pi}{\Phi_0} (\Phi_{ext} + L_G I_\Phi + L_{K_1} I_{s_1} - L_{K_2} I_{s_2}). \quad (1.69)$$

Finally by using only the currents defined in (1.66), (1.69) becomes:

$$\Theta_2 - \Theta_1 = 2\pi n + \frac{2\pi}{\Phi_0} [\Phi_{ext} + (L_G + L_{K_1} + L_{K_2}) I_\Phi + (L_{K_1} - L_{K_2}) I_{av}]. \quad (1.70)$$

The system formed by the equations (1.61) and (1.70) describes the general behavior of a SQUID in the zero voltage state². Note that the equation (1.70) is independent of the nature of the junction while the equation (1.61) must be particularized for the specific weak links. For pedagogical purposes, we will first detail the behavior of the asymmetric SQUID in the case of SIS junctions, *i.e.* for which the CPR is given by (1.40). We will then study the case of a linear CPR (1.50) being closer to the situation experimentally addressed in this thesis.

1.3.4.1 Asymmetric model for SIS junctions

The equations to be solved can take an elegant and more concise form by defining some extra parameters. To begin with, the total inductance L of a SQUID, taking into account the geometrical and kinematic effects, is given by:

$$L = L_G + L_{K_1} + L_{K_2}. \quad (1.71)$$

We then assign to each arm, an inductance given by:

$$\begin{aligned} L_1 &= \frac{L_G}{2} + L_{K_1} = \frac{L}{2}(1 - \eta_L) \\ L_2 &= \frac{L_G}{2} + L_{K_2} = \frac{L}{2}(1 + \eta_L), \end{aligned} \quad (1.72)$$

with

$$\eta_L = \frac{L_2 - L_1}{L} = \frac{L_{K_2} - L_{K_1}}{L}, \quad (1.73)$$

¹The kinetic inductance can be interpreted as a measure of the inertia of the charge carrier pairs. The kinetic energy of the charges in a superconductor being $E_K = \int \frac{1}{2} n_p m_p v_p^2 dV = \int \frac{1}{2} \frac{m_p}{n_p q_p^2} J_s^2 dV = \frac{1}{2} L_K I^2$. It is easy to show that this last expression and equation (1.68) give the same result $L_K = \frac{m_p}{n_p q_p^2} \frac{l}{A}$ in the case of a homogeneous superconductor of length l and with a uniform cross section $A \ll \lambda_L^2$.

²State thus characterized by a time independent Θ as indicated by the second Josephson equation (1.41)

quantifying the asymmetry of the inductances.

The equivalent of (1.72) for the currents is:

$$\begin{aligned} I_{c1} &= I_{cav}(1 - \alpha_I) \\ I_{c2} &= I_{cav}(1 + \alpha_I), \end{aligned} \quad (1.74)$$

with

$$\alpha_I = \frac{I_{c2} - I_{c1}}{2I_{cav}}, \quad (1.75)$$

where

$$I_{cav} = \frac{I_{c1} + I_{c2}}{2}, \quad (1.76)$$

is the average critical current of the SQUID.

The parameter β_L quantifies the importance of the flux generated by I_{cav} compared to Φ_0 :

$$\beta_L = \frac{2LI_{cav}}{\Phi_0}. \quad (1.77)$$

Dividing all currents by I_{cav} and considering normalized fluxes as:

$$\phi = \frac{\Phi}{\Phi_0}, \quad (1.78)$$

we obtain the following three equations:

$$i_s = (1 - \alpha_I) \sin \Theta_1 + (1 + \alpha_I) \sin \Theta_2, \quad (1.79)$$

$$2i_\Phi = (1 - \alpha_I) \sin \Theta_1 - (1 + \alpha_I) \sin \Theta_2, \quad (1.80)$$

$$\Theta_2 - \Theta_1 = 2\pi n + 2\pi\phi_{ext} + \pi\beta_L \left(i_\Phi - \frac{\eta_L}{2} i_s \right), \quad (1.81)$$

allowing to obtain the three unknowns Θ_1 , Θ_2 and i_Φ for a given device (α_I , β_L and η_L known) biased with a current i_s and crossed by a flux ϕ_{ext} .

In general, the three equations (1.79), (1.80) and (1.81) must be solved numerically (see appendix B). Figure 1.22 first considers the simplified case without external flux ($\phi_{ext} = 0$) and for $n = 0$. The case exposed in panels (a) shows the evolution of the two phases Θ_1 and Θ_2 and of the three currents i_{s1} , i_{s2} and i_Φ as a function of the biased current i_s , which can vary between 0 and 2, in the full symmetrical case ($\alpha_I = \beta_L = \eta_L = 0$). The equation (1.81) imposes that $\Theta_1 = \Theta_2$ and the two currents are always equal. The critical current $i_c = 2$ naturally occurs when $\Theta_1 = \Theta_2 = \pi/2$ ¹ so when $i_{s1} = i_{s2} = 1$. Panel (b) considers the case of an asymmetry $\alpha_I = 0.5$ between the critical currents, we observe an identical evolution for the phases, each junction reaching its critical current $(1 - \alpha_I)$ and $(1 + \alpha_I)$ (horizontal dashed lines on the right Fig. of panel (b)) at the same time. The difference between i_{s1} and i_{s2} generates a circular current i_Φ but without contributing to the flux felt by the SQUID ($\beta_L = 0$). The case $\beta_L = 1$ and $\alpha_I = \eta_L = 0$ is redundant

¹In general, it is necessary that $\Theta_2 - \Theta_1 = k\pi$, k an integer, so that the critical current can reach the value $i_c = 2$.

with panel (a) because the equation (1.81) also leads to the result $\Theta_1 = \Theta_2$. Panel (c) illustrates a different evolution of Θ_1 and Θ_2 imposed by the term $\pi\beta_L i_\phi \neq 0$ of (1.81). The difference $\Theta_1 - \Theta_2$ being no longer zero, the current i_s saturates for a value $i_c < 2$ (see left panel of panel (c)). Panel (d) finally shows the case of an additional asymmetry for the inductance $\eta_L = 0.5$. In this case the term $-\pi\beta_L\eta_L i_s/2$ of (1.81) contributes additionally to the difference between the phases and the critical current i_c reached is even lower than for panel (c).

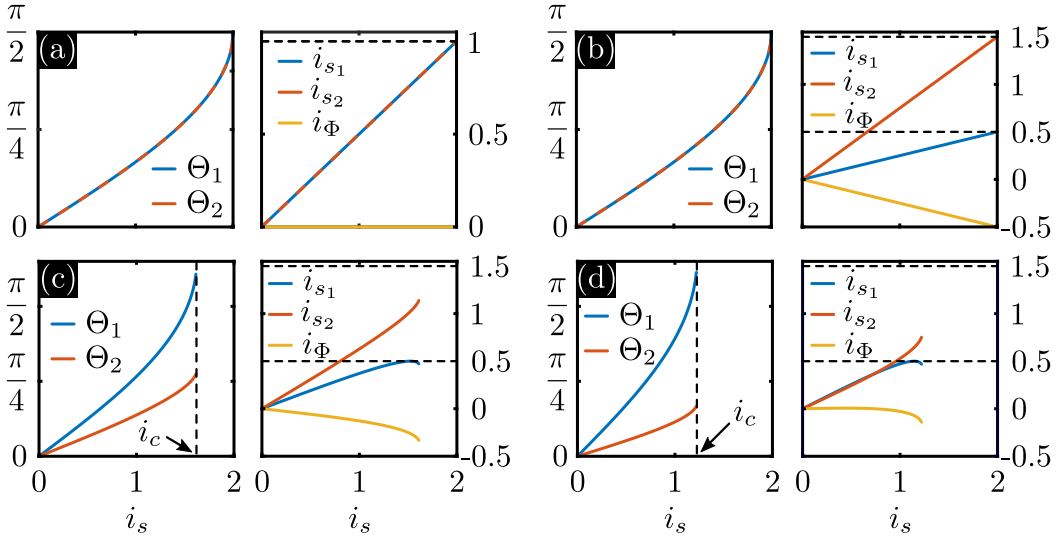


Figure 1.22 – Evolution of the phases Θ_1 , Θ_2 , currents i_1 , i_2 and i_Φ as a function of the applied current i_s in the zero voltage state with no external applied flux ($\phi_{ext} = 0$) and $n = 0$. Panel (a) is the full symmetric case $\alpha_I = \beta_L = \eta_L = 0$. Panel (b) considers a critical current asymmetry $\alpha_I = 0.5$. The last two panels also consider $\beta_L = 1$ and an inductance asymmetry $\eta_L = 0$ and $\eta_L = 0.5$ for (c) and (d) respectively.

Figure 1.23 now considers a non-zero applied flux. In order to avoid unnecessary complexity, only the fully symmetric case $\alpha_I = \beta_L = \eta_L = 0$ will be discussed. One can see directly that according to (1.81), the term $2\pi\phi_{ext}$ induces $\Theta_2 - \Theta_1 \neq 0$ as for the case $\phi_{ext} = 0.2$ of panel (a). Even for $i_s = 0$, a current $i_\phi \neq 0$ flows in the loop to exactly counterbalance the external flux. As for panel (c) of Fig. 1.22, the difference $\Theta_2 - \Theta_1$ induces a critical current $i_c < 2$. For a flux $\phi_{ext} = 0.4$ (panel(b)), the critical current is further reduced. The value $\phi_{ext} = 0.5$ is of great importance since then the equation (1.79) implies that $\Theta_2 - \Theta_1 = \pi$ and consequently that $i_s = 0$. This result can be generalized by stating that a symmetric SQUID has a zero critical current for any external flux equal to a half integer number of Φ_0 .¹ The critical current will then increase again for $0.5 < \phi_{ext} < 1$ as shown in panel (c). The roles of i_{s1} and i_{s2} are reversed between panels (a) and (c) due to the fact that their imposed fluxes are complementary. Panel (d) finally illustrates the case of one

¹Note that this does not indicate that the SQUID does not respect the flux quantization condition (1.14) thanks to the spontaneous appearance of the circulating currents i_ϕ .

flux quantum being imposed through the SQUID. The difference $\Theta_2 - \Theta_1 = 2\pi$ allows again to reach the maximum critical current $i_c = 2$.

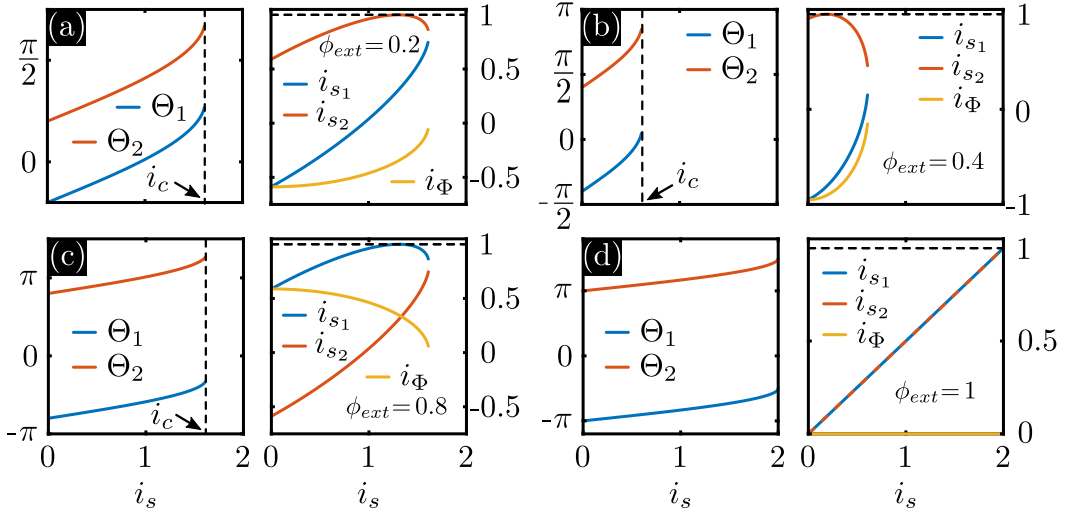


Figure 1.23 – Evolution of the phases Θ_1 , Θ_2 , currents i_1 , i_2 and i_Φ as a function of the applied current i_s in the zero voltage state with an applied external flux ($\phi_{ext} \neq 0$) in the fully symmetric case $\alpha_I = \beta_L = \eta_L = 0$. Panels (a), (b), (c) and (d) represent the cases of imposed flux $\phi_{ext} = 0.2, 0.4, 0.8$ and 1 respectively. The critical current i_s tends to zero when ϕ_{ext} is close to 0.5 .

As we have just shown, the evolution of the critical current is dictated by the properties of the SQUID and is determined by maximizing the current i_s given by (1.79) while taking into account the two constraints (1.80) and (1.81). Since the oscillations of i_c with the applied flux is a valuable indicator of the behavior of a SQUID, it is therefore useful to determine the influence of the parameters α_I , β_L and η_L on the $i_c(\phi)$ curves. Details concerning the calculations are available in the second part of the appendix B.

The influence of the critical current asymmetry α_I ($\beta_L = \eta_L = 0$) is illustrated in the left panel of the Fig. 1.24 for α_I values ranging from 0 (blue curve) to 1 (red curve) by steps of 0.1. An analytical solution exists for this case and is given by:

$$i_c(\phi_{ext}) = 2i_{c_{av}} \sqrt{\alpha_I^2 + (1 - \alpha_I^2) \cos^2(\pi\phi_{ext})}. \quad (1.82)$$

The result is a linear decrease of the modulation depth Δi_c (right panel) defined as:

$$\Delta i_c = i_{c,max} - i_{c,min}, \quad (1.83)$$

where $i_{c,max}$ and $i_{c,min}$ are respectively the maximum and minimum values of i_c .

A similar behavior is observed for β_L ($\alpha_I = \eta_L = 0$, left panel of Fig. 1.25) where a value $\beta_L \geq 1$ leads to a 50% reduction of the modulation depth (see right panel). According to (1.77), high values of β_L indicate that the flux coming from the inductance of the loop becomes much higher than Φ_0 and ϕ_{ext} , thus producing

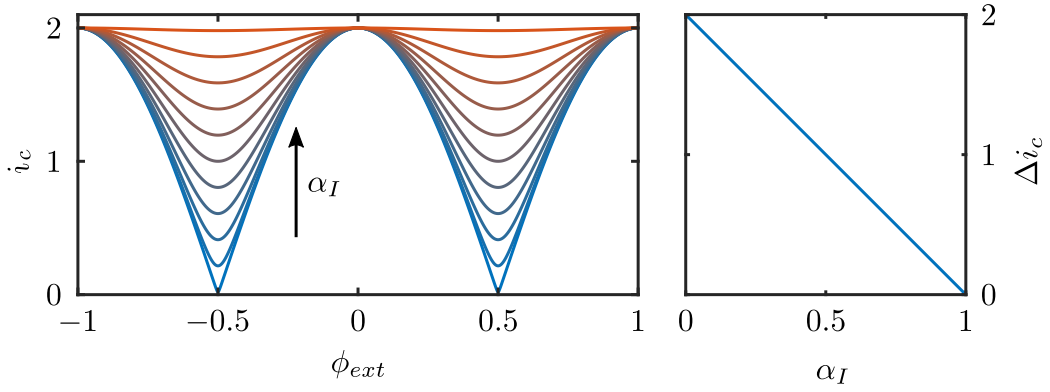


Figure 1.24 – Left panel: influence of the parameter α_I on the oscillations $i_c(\phi_{ext})$ for values ranging from 0 (blue curve) to 1 (red curve) by steps of 0.1. Right panel: linear evolution of the depth modulation Δi_c as a function of α_I .

an increasingly negligible influence of ϕ_{ext} on the SQUID oscillations ($\Delta i_c \rightarrow 0$). Taking into account the effect of noise, Tesche and Clarke[64] have shown that $\beta_L \simeq 1$ is necessary to optimize the SQUID's response.

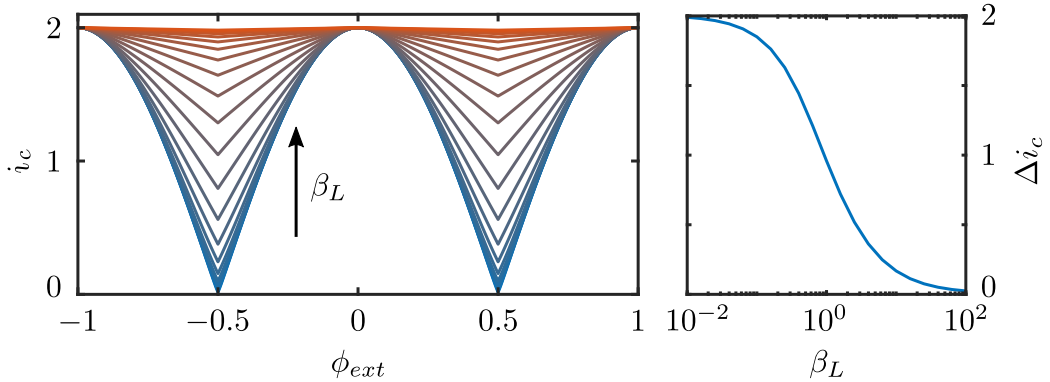


Figure 1.25 – Left panel: influence of the parameter β_L on the oscillations $i_c(\phi_{ext})$ for values ranging from 10^{-2} (blue curve) to 10^2 (red curve) by factors of $10^{0.2}$. Right panel: linear evolution of the depth modulation Δi_c as a function of β_L .

The last parameter η_L being important only if $\beta_L = 0$, the Fig. 1.26 shows the oscillations for the characteristic value $\beta_L = 1$. We observe that the effect of an asymmetry of the inductance η_L is a shift of the maximum critical current along horizontal axis without modification of the modulation depth. The latter being reached for $\Theta_1 = \Theta_2 = \pi/2$, the equations (1.79),(1.80) and (1.81) show that the flux giving $i_c = 2$ is:

$$\phi_{ext,max} = \beta_L \frac{(\alpha_I + \eta_L)}{2}, \quad (1.84)$$

which is therefore non-zero only if $\beta_L \neq 0$ with α_I and/or $\eta_L \neq 0$.

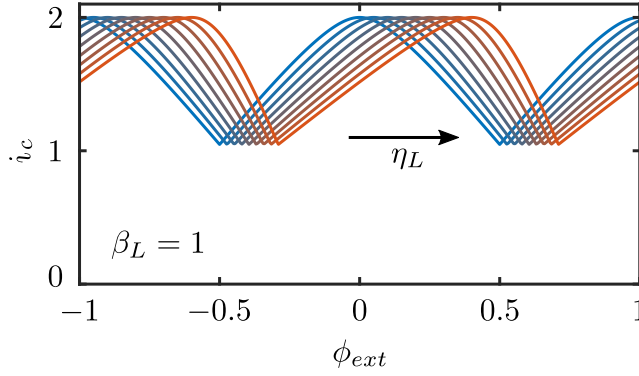


Figure 1.26 – Influence of the parameter η_L on the oscillations $i_c(\phi_{ext})$ for values ranging from 0 (blue curve) to 0.8 (red curve) by steps of 0.1. The value of $\beta_L = 1$ for all curves.

1.3.4.2 SQUID with linear CPR

In order to accurately model the devices investigated in this thesis, it is essential to consider of the junction length. Here we present a model proposed by Murphy and Bezryadin [60] and further developed in [65, 66] to reproduce SQUID oscillations at low temperatures. The junctions are assumed to be long (see Fig. 1.27) with a CPR given by (1.50). The equation (1.61) gives:

$$I_s = I_{c1} \frac{\Theta_1}{\Theta_{c1}} + I_{c2} \frac{\Theta_2}{\Theta_{c2}}, \quad (1.85)$$

with Θ_{c_i} the critical phase difference of the junction i . The constraint (1.62) on the phase variation along a closed contour cannot be directly applied here because a contribution from the electrode screening currents must be taken into account. Indeed, the generation of London currents in the electrodes due to the application of the field \mathbf{B} generates a phase variation along the paths $a \rightarrow b$ and $c \rightarrow d$ denoted respectively as $\delta_{a \rightarrow b}$ and $\delta_{c \rightarrow d}$. The equation (1.13) then takes the following form:

$$\delta_{a \rightarrow b} - \Theta_2 - \delta_{c \rightarrow d} + \Theta_1 = 2\pi n. \quad (1.86)$$

Assuming an identical geometry of the electrodes, symmetry considerations indicate that the two electrode contributions can be combined into a single term $2\delta(B)$ with $\delta(B) = \delta_{a \rightarrow b} = \int_a^b \nabla \theta \cdot d\mathbf{l}$. Since an increase in the magnetic field ΔB generating a variation of the contribution of the electrodes by a quantity $2\pi m$ (m an integer) leaves the amplitude of the wave function unchanged, one can intuitively impose that [57, 67, 68]:

$$2\delta(B) = 2\pi \frac{B}{\Delta B}, \quad (1.87)$$

where ΔB is the period of the $I_c(B)$ oscillations. Equation (1.86) can then be written as:

$$\Theta_1 - \Theta_2 + 2\pi \frac{B}{\Delta B} = 2\pi n. \quad (1.88)$$

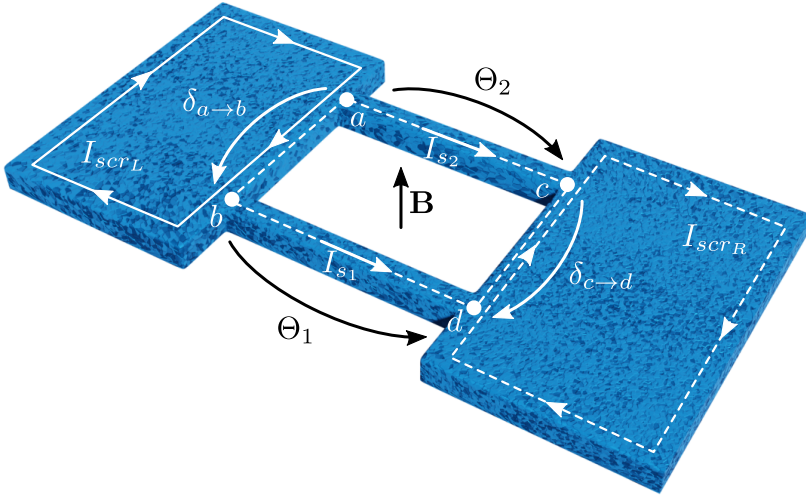


Figure 1.27 – Geometry of a SQUID in the case of long junction and large electrodes. The phase variations $\delta_{a \rightarrow b}$ and $\delta_{c \rightarrow d}$ are generated by the London spreading currents in both electrodes.

We still use α_I given by (1.74) as well as a similar parameter γ to take into account the asymmetry of the critical phases:

$$\begin{aligned}\Theta_{c1} &= \Theta_{cav}(1 - \gamma) \\ \Theta_{c2} &= \Theta_{cav}(1 + \gamma),\end{aligned}\tag{1.89}$$

with

$$\gamma = \frac{\Theta_{c2} - \Theta_{c1}}{2\Theta_{cav}},\tag{1.90}$$

where

$$\Theta_{cav} = \frac{\Theta_{c1} + \Theta_{c2}}{2},\tag{1.91}$$

is the average critical phase difference of the SQUID. Equation (1.85) becomes:

$$i_s = \frac{(1 - \alpha_I)}{(1 - \gamma)} \frac{\Theta_1}{\Theta_{cav}} + \frac{(1 + \alpha_I)}{(1 + \gamma)} \frac{\Theta_2}{\Theta_{cav}}.\tag{1.92}$$

The equations (1.88) and (1.92) allow to determine the variables Θ_1 and Θ_2 for given values of α_I , γ and n of the SQUID operated with a current i_s and in a perpendicular magnetic field B . The critical current is obtained when one of the junctions reaches a phase difference higher than its critical value. The influence of the parameters n , α_I and γ is shown for the $I_c(B)$ response in the Fig.1.28. As implied by the equation (1.88), a value $n \neq 0$ leads to a shift of the curve $i_c(B)$ along the horizontal axis. Panel (a) shows 7 curves corresponding to $-3 \leq n \leq 3$ with no asymmetries. For each value of n the maximum critical current being reached precisely when $B/\Delta B = n$. This shows that several vorticities are possible for a given value of B and consequently that the critical current can be multivalued.

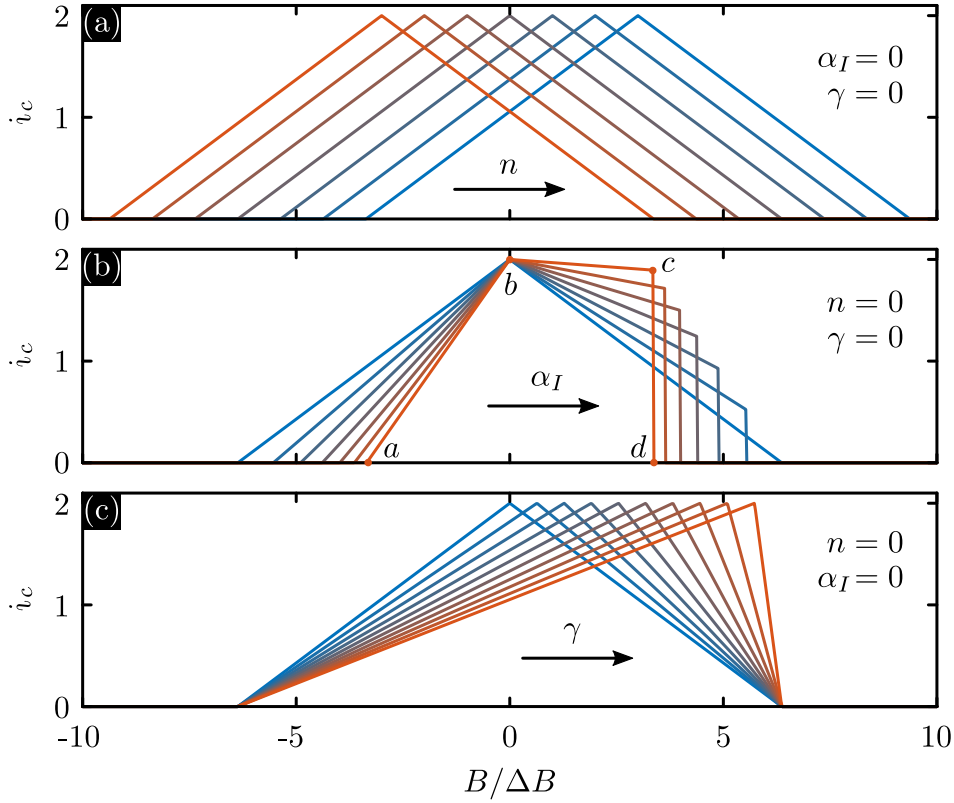


Figure 1.28 – Influence of the SQUID parameters on the magnetic field evolution of the critical current. Panel (a): $-3 \leq n \leq 3$ for $\alpha_I = \gamma = 0$. Panel (b): $\alpha_I \in [0, 0.9]$ by step of 0.15 for $n = \gamma = 0$. Panel (c): $\gamma \in [0, 0.9]$ by step of 0.1, $n = \alpha_I = 0$.

Hazra [69] showed that the most likely state is the one minimizing the energy of the system. The effect of the α_I asymmetry is illustrated in panel (b) for $n = \gamma = 0$ and highlights different behaviors for negative and positive values of B . Let's consider the case $\alpha_I = 0.9$ (red curve). For $B < 0$ ($a \rightarrow b$), (1.88) indicates that $\Theta_1 > \Theta_2$ and the SQUID is limited by junction 1. For $B > 0$, $\Theta_2 > \Theta_1$ and the SQUID is now bounded by junction 2 ($b \rightarrow c$). From point c , the SQUID is again bounded by the first junction. Indeed c and a being equidistant from $B = 0$, $\Theta_{1,a} = -\Theta_{1,d}$ and Θ_{c1} is thus reached again for junction 1, leading to the sharp decrease $c \rightarrow d$. Panel (c) shows the effect of an asymmetry of the critical phase. We notice that the effect of increasing γ is to shift the field for which the maximum critical current is reached. Since $i_c = 2$ is only possible if $\Theta_i = \Theta_{c_i}$, equation (1.88) immediately gives that the shift $B_{max,n}$ for a given value of n is:

$$B_{max,n} = \frac{\Delta B}{2\pi} (2\pi n + \Theta_{c_2} - \Theta_{c_1}) = \Delta B \left(n + \frac{\gamma \Theta_{c_{av}}}{\pi} \right). \quad (1.93)$$

1.3.4.3 The voltage state

In the same way as for the simple junction, the RCSJ model allows us to understand the behavior of a SQUID when it is operated at a current higher than its critical current [62]. A scheme of the SQUID is given in the inset of the left panel of Fig. 1.29. Assuming two SIS junctions and a symmetric SQUID, the equation of the RCSJ model (1.55) for each of the junctions gives:

$$\begin{aligned}\beta_c \frac{d^2 \Theta_1}{d\tau^2} + \frac{d\Theta_1}{d\tau} + \sin \Theta_1 - \frac{i}{2} - i_\Phi &= 0 \\ \beta_c \frac{d^2 \Theta_2}{d\tau^2} + \frac{d\Theta_2}{d\tau} + \sin \Theta_2 - \frac{i}{2} + i_\Phi &= 0,\end{aligned}\tag{1.94}$$

where β_c given by (1.54) and i is the dimensionless current. The relation (1.81) remains valid too:

$$\Theta_2 - \Theta_1 = 2\pi n + 2\pi\phi_{ext} + \pi\beta_L \left(i_\Phi - \frac{\eta_L}{2} i \right).\tag{1.95}$$

The last three equations must be solved numerically and the solution averaged to obtain the $v - i$ characteristic curve. The particular case of overdamped junctions ($\beta_c \ll 1$) and negligible inductance ($\beta_L \ll 1$) has the following analytical solution:

$$\langle v \rangle = \sqrt{\frac{i}{2} - \cos^2(\pi\phi_{ext})},\tag{1.96}$$

which is plotted in the left panel of Fig. 1.29 for the two extreme values 0 (bottom curve) and $\Phi_0/2$ (top curve) for the applied flux. Such a device operated at constant current $i > 2$ shows oscillations of its mean voltage as a function of the external flux

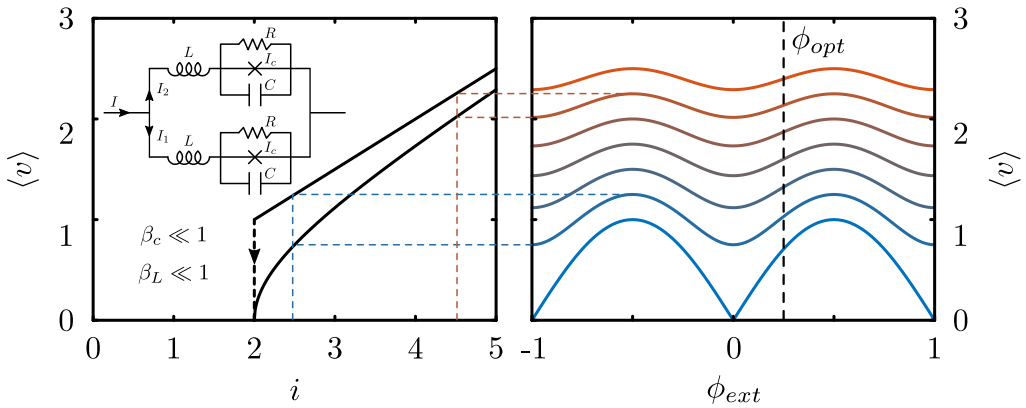


Figure 1.29 – Left panel: voltage current characteristics of a symmetric DC SQUID for $\beta_c \ll 1$ and $\beta_L \ll 1$. The bottom and top curves are obtained for an applied flux of 0 and $\Phi_0/2$ respectively. The inset schematizes the approximation of the SQUID by the RCSJ model. Right panel: voltage-current curves obtained by operating the SQUID with a current varying from $i = 2$ (blue curve) to 5 (red curve) by steps of 0.5.

ϕ_{ext} as shown in the right panel. We immediately observe that if the voltage increases with the applied current, the modulation of the oscillations decreases rapidly as soon as we move away from $i = 2$. The voltage across the SQUID being a periodic function of the flux quantum passing through it, it provides a natural extremely sensitive way to measure the magnetic field. However, its practical application requires specialized electronics to counterbalance some technical problems.

The first drawback to deal with is the non linearity of the SQUID response. To maximize sensitivity, the sensor is generally operated at $\phi_{opt} = \phi/4$, where the slope $\partial\langle v \rangle / \partial\phi_{ext}$ is maximized (see right panel of Fig.1.29). If the measured flux is low compared to Φ_0 , the SQUID response is almost linear and operational. Otherwise, the SQUID response needs to be linearized by using a Flux Blocked Loop (FBL) as shown in figure 1.30. In such a configuration, a current I_{opt} generates the constant flux ϕ_{opt} , while the SQUID is biased with a current I_{bias} slightly higher than its critical current. The voltage across the SQUID in this state is denoted V_0 . If then the SQUID picks up an external flux ϕ_{ext} , the voltage variation is integrated and converted into a current via resistor R_c to generate a feedback flux $\phi_{fb} = -\phi_{ext}$. With M_{fb} the mutual inductance between the feedback coil and the SQUID, the output voltage is then:

$$V_{out} = R_c I_{fb} = R_c \frac{\phi_{fb}}{M_{fb}} \propto \phi_{ext}, \quad (1.97)$$

which generates a response proportional to the external flux.

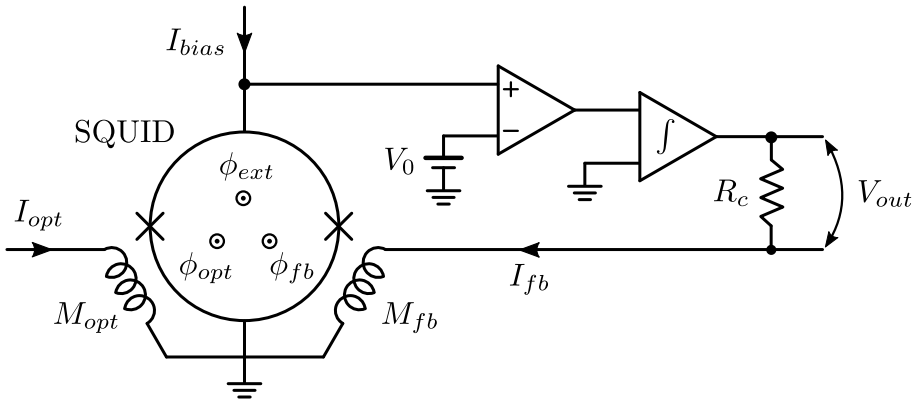


Figure 1.30 – The FBL linearizes the response of a SQUID sensor when the external flux is greater than Φ_0 . The voltage difference generated by ϕ_{ext} is integrated to generate a current I_{fb} which cancels the external flux and results in an output voltage $V_{out} \propto \phi_{ext}$.

Another problem arises from the fact that the $\langle v \rangle(i)$ curve may show irreversibility between the ramping up and down of the current. This hysteresis behavior has different origins depending on the nature of the junction, like hot spot formation in high critical currents Dayem bridges [70–72] or underdamped tunnel junctions [73, 74] (see left panel of Fig. 1.19).

Finally, thermal noise, white noise, or the ubiquitous $1/f$ noise limit the performance of the SQUID. The solution to all these problems involves technical considerations that are beyond the scope of this thesis and we refer the reader to specialized references [62, 75, 76].

1.3.4.4 Applications of SQUIDS

Despite the fact that they must be operated at cryogenic temperatures, the high sensitivity and the reduced size of SQUIDS devices have resulted in a wide range of applications. In biomagnetism, SQUIDS allow the measurement of weak magnetic fields in living organs [77] while they can also be used as a non-invasive evaluation tool in the search for defects on the surface of metals [78]. In imaging processes, the scanning SQUID microscopy (SSM) technique first invented by Black in 1993 allows to image the magnetic field distribution near the surface of a sample [79]. The first realizations of SSM suffered from a rather low resolution [80, 81] but has substantially improved by the realization of nanoSQUID on tip [82–84]. In cosmology, SQUIDS have also allowed to investigate the concept of cold dark matter [85, 86] and to detect gravitational waves [87]. The flow through a SQUID at the end of a superconducting waveguide allows to modify its boundary conditions and is useful in the study of the dynamic Casimir effect [88]. In the field of condensed matter, SSM has allowed the fundamental study of the order parameter for superconductors at high critical temperatures [89] as well as to detect the presence of Majorana fermions [90, 91]. For the study of nano-objects, loops of the order of 50 nm in radius are required. SQUIDS based on three-layer tunnel junctions are becoming unsuitable due to the difficulties of reducing their size below $1\,\mu\text{m}$ while having a sufficiently high critical current to guarantee acceptable sensitivity [92]. A good alternative lies in Dayem bridges which have a high critical current density and can be fabricated by a single lithography step with a resolution of a few tens of nm. These nanoSQUIDS based on Dayem bridges have as main application the study and manipulation of nanoparticles down to $\sim 5\,\text{nm}$ size [93–96]. The nanoSQUIDS have also been used to efficiently visualize vortex dynamics and vortex pinning centers in superconductors [84, 97–101]. The above examples are of course a short, non-exhaustive list of the large number of applications of SQUIDS. More details can be found in references [63, 75, 92, 102].

Chapter 2

Experimental techniques

This chapter details the experimental techniques which played an essential role in the accomplishment of this thesis. The method of sample fabrication by Electron Beam Lithography (EBL) is described in section 2.1. An important part of the measurements concerns transport properties at low temperatures carried out in a Physical Property Measurements System (PPMS) at the Katholieke Universiteit Leuven (KULeuven) and which is described in section 2.2. The section 2.3 introduces the Electromigration (EM) technique which is the founding pillar of this thesis. Finally, section 2.4 discusses the in-situ Scanning Electron Microscopy (SEM), Atomic Force Microscopy (AFM) and Kelvin Probe Force Microscopy (KPFM) as imaging tools to visualize the modifications induced by EM.

2.1 Sample fabrication

The samples investigated in this thesis are all made of Nb. Most of them were fabricated at the Néel Institute in Grenoble (France) either by Prof. Roman. B. G. Kramer or by Dr. Danial Majidi (under the supervision of Professor Clemens B. Winkelmann). The fabrication method is summarized in the Fig.2.1. Panel (a) shows the starting point with a substrate on which a thin layer of Nb of the desired thickness is deposited by electron-beam evaporation. A film of Poly(methyl methacrylate) (PMMA) resist is then formed by spin coating followed by a soft bake (panels (b,c)). The desired design is then successively patterned by EBL (panel (d)) and revealed after development (panel (e)). Panel (f) shows the deposition of the Al layer which will serve as a negative hard mask after lift-off procedure (panel (g)). Indeed, the Al serves as a protective layer for the Reactive Ion Etching (RIE) processing aimed at removing the uncovered Nb (panel (h)). The Al mask can then be dissolved by wet etching to give the final sample shown in panel (i). At this stage, the sample is ready for the bonding procedure under a strict protocol to avoid electrostatic discharge. Further details are available in section 3.4 of Ref.[103].

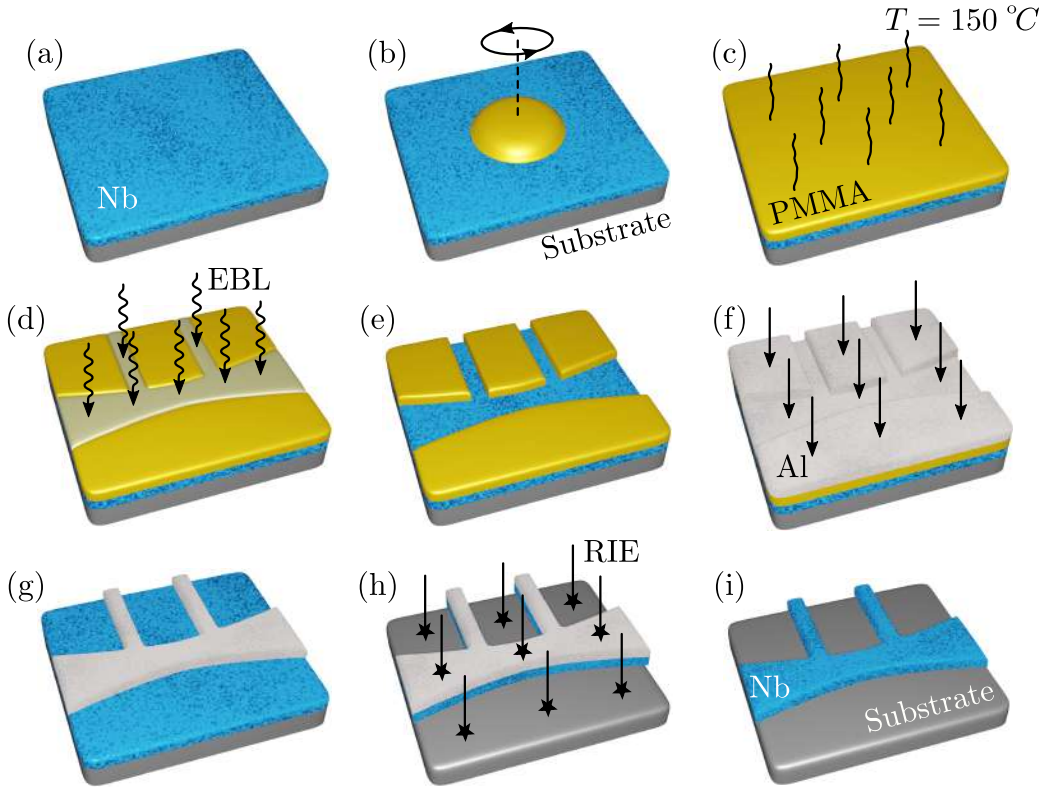


Figure 2.1 – Nanofabrication procedure for obtaining a Nb nanoconstriction. (a) Pristine Nb layer of desired thickness on substrate. (b,c) Resist layer formation. (d) EBL exposure of the resist. (e) Development step. (f) Al deposition. (g) Lift-off procedure. (h) RIE. (i) Final result.

2.2 Physical Property Measurement System

The low-temperature measurements were carried out in a Quantum Design PPMS model 6000 [104] equipped with a 7 T magnet available in the lab of Prof. J. Van de Vondel at the KULeuven. The PPMS is a cryostat using only liquid ^4He . It consists of a Dewar shown in the left panel of the Fig. 2.2 containing liquid ^4He in which the insert is immersed. Most of the relevant parts of the cryostat lie at the bottom of the stick, a zoomed-in view of which is shown in the right-hand panel of Fig. 2.2. The sample chamber, made of copper to promote uniform temperature, is at the center of the cryostat. It is surrounded by the cooling annulus which is connected to the liquid ^4He reservoir via the impedance assembly. The impedance assembly is composed of a tube (impedance) and a heater which warms up the impedance and its role is to control the flow of liquid ^4He towards the cooling annulus. The liquid or gaseous state of the ^4He in the cooling annulus then depends on the pressure in it. When the heater is switched on, a bubble forms inside the tube reducing the flow of liquid ^4He to zero. If the heater is switched off, the temperature of the tube drops

and allows the liquid ^4He to flow into the cooling annulus. The temperature range accessible by the PPMS can be divided into two regimes. For low temperatures ($T < 4.2\text{ K}$), the pressure in the cooling annulus is lowered once a quantity of liquid ^4He is accumulated. This technique allows to reduce the boiling temperature of helium to $T \simeq 1.9\text{ K}$. For the second regime (so-called high temperature regime), ^4He gas is stored in the cooling annulus which is then heated by two independent heaters located at the base of the puck contact and near the top of the sample chamber extending the accessible temperature of the PPMS to $T \simeq 400\text{ K}$. The vacuum space next to the cooling annulus contains reflective superinsulation to minimize radiative power loss into the helium bath.

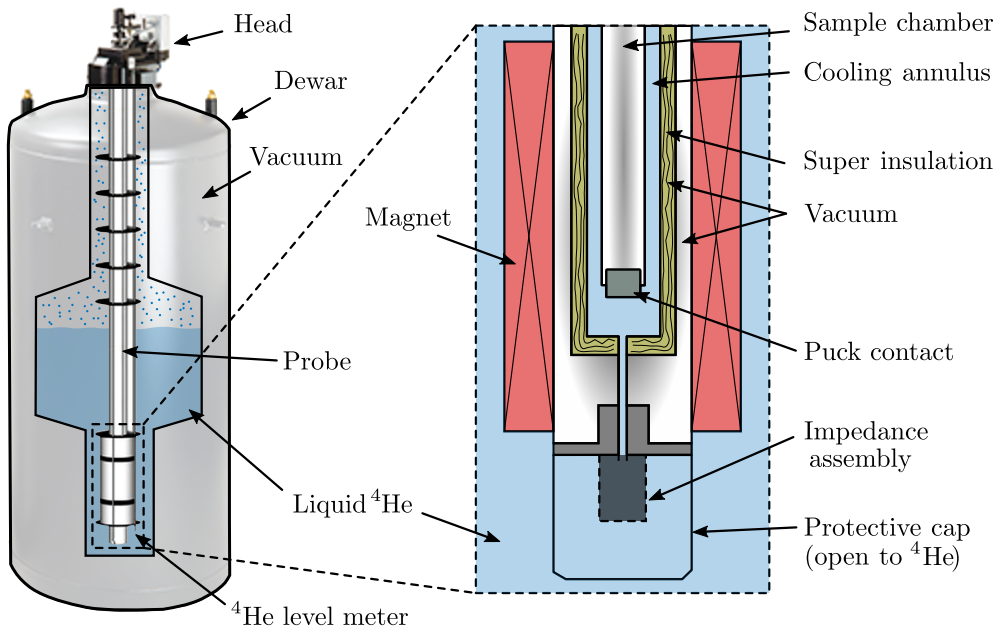


Figure 2.2 – Schematic representation of the PPMS for low temperature transport measurements. The left panel shows an overview of the cryostat, while the right panel shows the details of the insert.

2.3 Electromigration

This thesis is entirely based on the specific method of electrically induced atom migration called electromigration (EM), which requires the application of a large electric current density into metallic wires [105, 106]. This technique has been gradually mastered to take advantage of it as a nanofabrication tool. In the rest of this section, the evolution of this phenomenon is detailed, taking as a starting point its historical context. A theoretical approach to EM using the notion of electron wind force and the resulting mass transport will be discussed. The influencing factors for EM will be detailed with emphasis on the importance of defects of the

metal. Then, we will focus on EM as a way to modify the sample at the atomic scale.

2.3.1 Historical perspective

As soon as miniaturization of integrated circuits began in the late 60s, manufacturers were faced with a major problem [107]. Many electronic integrated circuits were returned to the manufacturers due to failure within a few weeks after being put into operation. As the optical microscope inspection showed no visible damage, the supposedly high reliability of these circuits was called into question. Electron scanning microscope inspection identified the problem. Tiny cracks, voids and hillocks, sometimes only a few nm long, were present along the metal lines and interconnects. The cause of these failures was attributed to the ever-increasing current density imposed by the miniaturization of electronic circuits and to the consequent electromigration occurring at its weakest points. In 1969, James Black summarized the problem by proposing an empirical law to describe the Median Time to Failure (MTF) due to EM of a series of identical device [108]:

$$\text{MTF} = \frac{A}{J^2} e^{\frac{E_a}{k_B T}}, \quad (2.1)$$

with E_a the activation energy of the defect causing the EM to be triggered, J the current density and A a constant depending on the geometry. Since then, EM has been a limiting factor in the miniaturization of circuits. However, understanding of the phenomenon has made it possible to limit its deleterious effects and to take advantage of its benefits. An introduction to this phenomenon is given in the next section.

2.3.2 Electron wind force theory and mass transport

In a perfect crystal at absolute zero temperature, independent electrons move without any resistance. This purely theoretical result, which has nothing to do with superconductivity, comes from the absence of perturbations in the solution of the Schrödinger equation that governs this system [19]. In a real metal, such perfect crystal does not exist and the resistivity of the material is then dominated by crystal defects (vacancies, impurities, boundary grains, dislocations) as well as temperature. The latter is responsible for the permanent agitation of the atoms at a Debye's frequency of $\simeq 10^{13}$ Hz and amplitude proportional to T which deforms the crystal lattice and causes incessant collisions with the electrons. In the absence of an applied current, the direction of the momentum transfers caused by the collisions is random and compensates on average. On the contrary, when the conductor is subjected to an electric field \mathbf{E} , the energy transmitted to an atom by an electron at each collision can be approximated by a simple classical calculation. Let us assume the electron is stopped after each collision and that the energy it acquires until the next collision is provided by the electric field. Noting l the mean free path, the averaged energy transmitted at each collision ϵ_{coll} is given by:

$$\epsilon_{coll} \simeq e E l = e \rho J l, \quad (2.2)$$

where the second equality is given by Ohm's law $E = \rho J$. For a typical good conductor used is everyday life $\rho = 10^{-8} \Omega\text{m}$, $J = 10^6 \text{ A/m}^2$ and $l \simeq 10 \text{ nm}$ and (2.2) gives $E_{\text{coll}} \simeq 10^{-10} \text{ eV}$. As this energy is very low, even compared to the thermal energy $k_B T_{\text{amb}} \simeq 3 \times 10^{-2} \text{ eV}$, EM does not happen in ordinary situations but only when considering a large number of collisions per second, i.e. by applying large current density. Another reason is that EM can only occur for low dimensional conductor. For a conductor of rectangular cross section S of thickness t in contact with a substrate at temperature T_0 , the dissipated heat density from Joule effect is:

$$p_{\text{Joule}} = \rho J^2, \quad (2.3)$$

while the evacuated heat to the substrate per unit volume is:

$$p_{\text{subst}} = \frac{\mathcal{H}(T - T_0)}{t}, \quad (2.4)$$

with \mathcal{H} the thermal conductivity to the substrate. The ratio of the two powers defines the Stekly parameter[109]:

$$\alpha_{\text{Stekly}} = \frac{p_{\text{Joule}}}{p_{\text{subst}}} = \frac{\rho J^2}{\mathcal{H}(T - T_0)} t, \quad (2.5)$$

and shows that the heat removal is favored when t is small. For arbitrary shape of the cross section with perimeter P , the Stekly parameter is $S/P \simeq \sqrt{S}$ and thus allowing larger current density in low dimensional conductor. For domestic electrical cables heat dissipation is too high compared to removal to the environment and the failure will then be caused by a melting of the metal for current densities of the order of 10^8 A/m^2 whereas EM only occurs at a 10^{10} to 10^{12} A/m^2 . The collision of several electrons with the crystal lattice is represented in the Fig.2.3 were \mathbf{F}_E is the Coulomb force and \mathbf{F}_w the average electron “wind” force resulting from the transfer of the electron momentum [110, 111]. According to (2.2), we see that F_w is proportional to the applied electric field E . The total force felt by an atom is therefore expressed as:

$$\mathbf{F} = \mathbf{F}_w + \mathbf{F}_E = Z_w e \mathbf{E} + Z e \mathbf{E} = Z^* e \rho \mathbf{J}, \quad (2.6)$$

where Z_w is the valence associated with the electron wind force and Z is the valence of the ion. The effective valence $Z^* = Z_w + Z$ represents the magnitude and direction of the momentum exchange [112] and its sign depends on the material. Although the semi-classical ballistic approach discussed here only justifies the negative sign of Z^* (the momentum transfer being in the direction of electron motion), a more general quantum approach shows that positive signs of the effective valence are also possible. The sign reversal of Z^* has been demonstrated experimentally in p- or n-types doped silicon polycrystallines [113].

Since the movement of an atom in the crystal lattice can be considered as highly overdamped, the drift velocity of the atoms \mathbf{v}_a is related to the force via:

$$\mathbf{v}_a = \mu \mathbf{F}, \quad (2.7)$$

with μ the mobility of the atoms. Combining (2.6) and (2.7) with Einstein's law $D = \mu k_B T$ for thermal diffusion phenomena, we obtain that the velocity of the atoms \mathbf{v}_a is given by:

$$\mathbf{v}_a = D \frac{Z^* e \rho \mathbf{J}}{k_B T}, \quad (2.8)$$

where D is the atomic diffusivity. The atomic flux \mathbf{J}_a is defined as:

$$\mathbf{J}_a = n_a \mathbf{v}_a = D \frac{n_a e \rho}{k_B T} Z^* \mathbf{J}, \quad (2.9)$$

with n_a the atomic density. The equation above is a simplified version taking into account only the effect of the electric field. Other contributions may have a significant influence on atom migration. A generalization of (2.9) is given by [114–116]:

$$\mathbf{J}_a = D \left(-\nabla n_a + \frac{n_a e \rho}{k_B T} Z^* \mathbf{J} - \frac{n_a \kappa}{k_B T^2} \nabla T - \frac{n_a f_R \Omega}{k_B T} \nabla \sigma \right). \quad (2.10)$$

where κ is the thermal conductivity, f_R is the vacancy relaxation factor, Ω the atomic volume and σ the mechanical stress. The phenomenon of atomic migration is in general of great complexity because of the interdependence of the different contributions. The case of a simple constriction with a bias current is illustrated in the Fig. 2.4. According to (2.9) it is likely that electromigration is triggered at the constriction because of current crowding. This approach is often used to impose the location to be modified by EM [117–119]. The transmission of the momentum of the charge carriers is then done in the $Z^* \mathbf{J}$ direction ($Z^* < 0$ in the present example) creating, if \mathbf{J} is sufficiently high, depleted zones in atoms (voids) and others with an excess of material (extrusion or hillocks). This density inhomogeneity is partially countered by the natural diffusion of atoms in the crystal lattice (first term of (2.10))

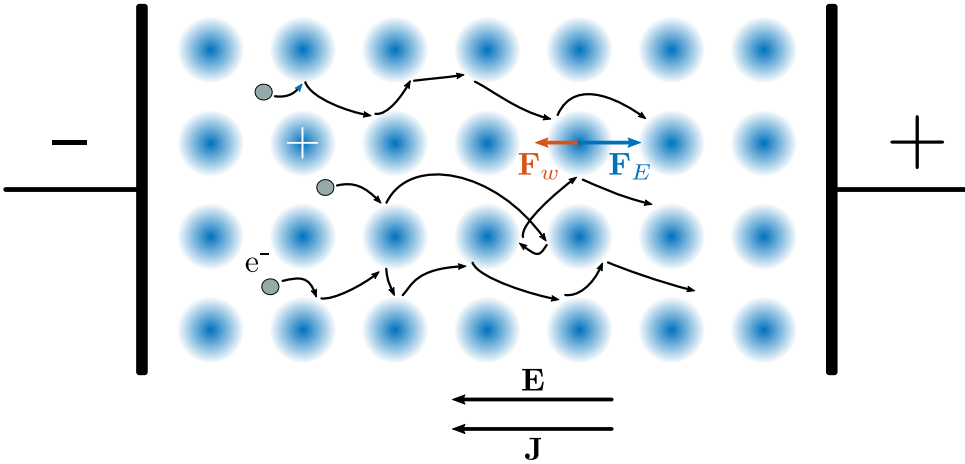


Figure 2.3 – Forces felt by the atoms in the crystal lattice. The momentum transfer of the electrons on the ions exert an averaged wind force \mathbf{F}_w while \mathbf{F}_E is the force exerted by the electric field. This is a sketchy representation assuming a mean free path comparable to the interatomic distance.

and by the stress gradient $\nabla\sigma$. Simultaneously, the power density ρJ^2 dissipated by Joule heating creates an inhomogeneous temperature distribution with a hot spot at the center of the constriction. The high kinetic energy of the ions in the center of the sample then migrate preferentially away from the constriction due to the temperature gradient ∇T . Note that the displacement of matter must respect a conservation equation:

$$\frac{\partial n_a}{\partial t} + \nabla \cdot \mathbf{J}_a = 0, \quad (2.11)$$

which shows that the formation of voids ($\partial n_a / \partial t < 0$) or extrusion ($\partial n_a / \partial t > 0$) is due to a divergence of the atomic flux, i.e. a difference between the matter that enters and leaves a given volume.

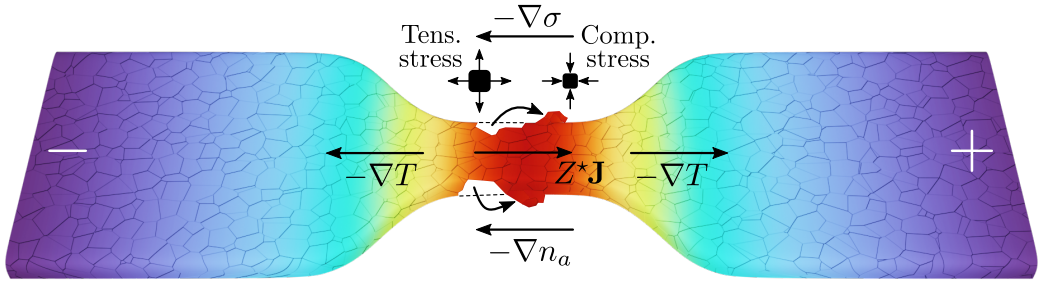


Figure 2.4 – Schematic representation of the phenomenon of atomic migration in a metallic constriction with the four contributions to the atomic flux (2.10) in the case where the electromigration term (2.9) is dominant and $Z^* < 0$. The divergence of the atomic flux (2.11) generates depleted zones (voids) and dense zones (extrusions or hillocks) which in turn accentuate or create stress, temperature and density gradients. For each contribution, the arrow indicates the direction in which the atoms are preferentially moved.

2.3.3 The grains structure

In addition to the interdependence and interplay of the above described mechanisms, the phenomenon of atomic migration is further complicated by the importance of the configuration of the grains structure. The diffusion parameter D in (2.10) is a function of the temperature:

$$D(T) = D_0 e^{-\frac{E_a}{k_B T}}, \quad (2.12)$$

but also depends on the presence of defects via the activation energy E_a . The diffusion path of an atom in the crystal is not completely random due to the activation energies associated with the different diffusion mechanisms. It is for example difficult for an atom to diffuse inside a grain while it is greatly facilitated along the grain boundaries or the outer surface of the crystal. To give an order of magnitude, the activation energy associated to the diffusion in a grain boundary or at the external surface is respectively two and three times lower than in the grain [112]. Therefore

the ratio between the grain size and the characteristic lengths of the sample are of great importance (see Fig. 2.5). Although feasible, the extreme amorphous and monocrystalline states are of minimal practical interest due to fabrication difficulties. The most likely configuration is the polycrystalline lattice where the abundance of grain boundaries makes it the dominant diffusion path. For larger grains, the near-bamboo configuration is a combination of diffusion along the grain boundaries and in the lattice while lattice diffusion dominates for the bamboo configuration.

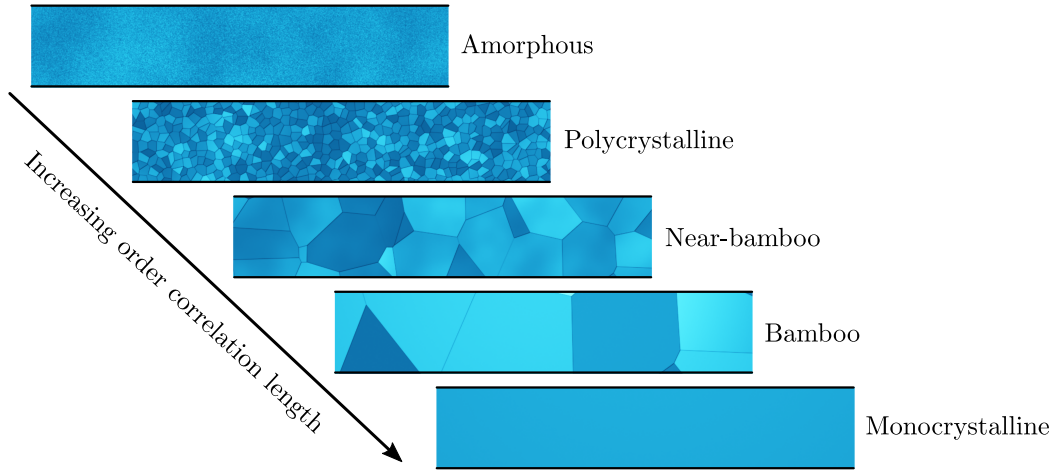


Figure 2.5 – Different possible grain structures in a conductor. The amorphous state is characterized by a very short order range in which the grains and grain boundaries are not clearly identifiable. For increasingly grain size to sample’s width ratio, the crystal can be successively qualified as polycrystalline, near-bamboo, bamboo and single crystal. Figure adapted from Ref. [116].

2.3.4 Controlled electromigration

EM is a complex phenomenon to tame because it accelerates uncontrollably after it is triggered. Let us consider the constriction shown in the Fig. 2.4 and suppose we measure its resistance $R(I)$ as a function of the applied current I (see left panel of Fig. 2.6). Starting from a resistance R_0 close to zero current (point A), a first plateau is generally observed at low currents where the dissipated heat is easily evacuated towards the substrate. Once point B is reached, the heat dissipation becomes significant and locally increases the temperature of the constriction. Therefore, $dR/dt \neq 0$ and the resistance is given by¹:

$$R(T) = R_0[1 + \alpha(T - T_0)], \quad (2.13)$$

with α the thermal coefficient of the material and T_0 the initial temperature. When the current density becomes sufficient to migrate atoms from the constriction (point

¹A more realistic formulation would obviously have to take into account an inhomogeneous temperature distribution as suggested in Fig. 2.4 and where (2.13) would then be valid only locally, i.e. for the resistivity $\rho(T)$. For simplicity, we will assume here that (2.13) is true.

B), which consequently forms voids, a positive feedback loop, given in the inset of the left panel of Fig. 2.6, is triggered. The formation of voids creates a local decrease in the cross section and thus an increase of both the resistance and the current density which increases the temperature of the constriction and accelerates the rate of change of the resistance to lead to more voids formation. This is a positive gain loop which results in a sudden increase in resistance symbolized by the red dotted line after point B and the destruction of the sample. An example of the thermal runaway caused by the positive feedback loop is represented in the right panel of Fig. 2.6 in the case of a Nb based SQUID where the failure of the top constriction created a crack in the substrate across the entire the sample.

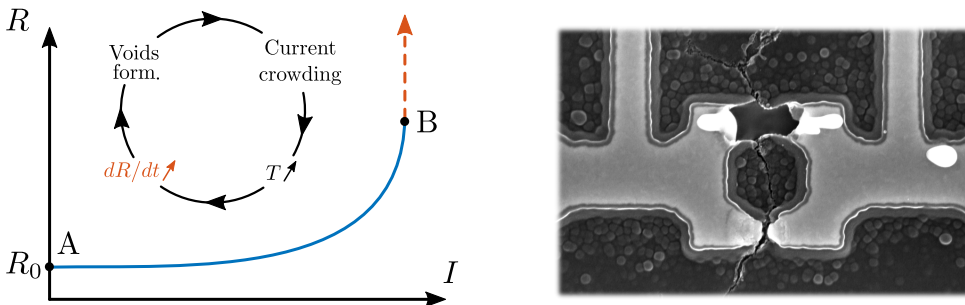


Figure 2.6 – Uncontrolled EM. Left panel: typical $R(I)$ curve composed of a parabolic Joule heating phase (A \rightarrow B) and the failure of the device after point B (red dotted line). The sudden resistance jump occurring after point B results from a positive gain feedback loop as described in the inset (adapted from [120]). Right panel: SEM image of a damaged SQUID device after an uncontrolled EM.

As EM cannot stabilize by itself, it is necessary to find a way to break the positive feedback loop to avoid the thermal runaway and obtain a new situation where the resistance does not suddenly increase (left panel of Fig. 2.7). One solution is to introduce a Proportional-Integral-Derivative (PID) controller into the feedback loop and is explained in details in the next section.

2.3.5 EM software

In this work, we use the software described in Ref. [103, 120] where the sample is modeled by the electrical diagram of the right panel of the Fig. 2.7 where R_j represents the resistance of the junction, i.e. the part of the constriction affected by the EM whereas the wires resistance R_w is not modified other than by the Joule effect (2.13). The lead resistance R_L models the remaining resistance of the circuit. The basic principle of the software represented in the Fig. 2.8 is to use a feedback loop which imposes a constant rate of change for the constriction resistance. To do so, we define a process variable p that measures the speed of the EM. The choice of p is somewhat arbitrary and several candidates like \dot{R} , \dot{R}/R , \dot{G} or P_R (dissipated power in the device) have been chosen in the literature [117, 121–125]. If the wire resistance R_w can be estimated, a wise choice is $p = -\dot{G}_j/G_j$ because it takes

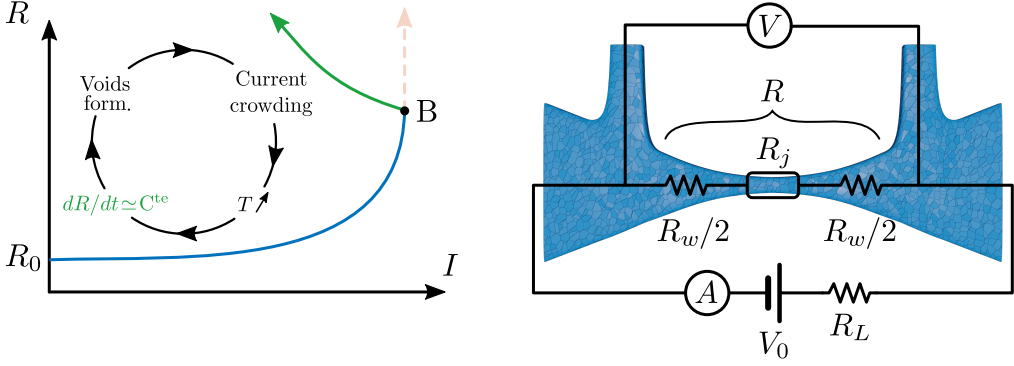


Figure 2.7 – Controlled EM. Left panel: typical $R(I)$ of a controlled EM. The main difference with a uncontrolled EM (Fig. 2.6) is after point B where the failure of the junction is avoided by the stabilization of a zero gain feedback loop. The time variation of the resistance is kept constant by a PID controller. Right panel shows a constriction with its electrical scheme. V_0 is the bias voltage, V is the voltage of the entire constriction, R_j , R_L and R_w are respectively the resistances of the junction, the leads and the wires between the voltage probes without R_j .

into account located damage in the junction. Most of the time, the estimation of R_w is rather difficult or need to make a first EM step and image the constriction to observe the affected area [120]. An easier choice is $p = -\dot{G}/G$ with $G = 1/R$ the conductance of the constriction¹. The EM software uses the bias voltage V_0 as a control variable and adapts its value every 20 ms in order to minimize the error $e(t) = p(t) - p_{setp}$ between the process variable p and its setpoint p_{setp} . The parameter p_{setp} is chosen by the experimenter and determines the speed at which the resistance changes and consequently the EM speed. At each iteration, the software measures the voltage V across the constriction and the current I to determine the conductance G_j of the junction. If G_j is lower than the threshold G_j^{Thr} the process is stopped. Otherwise, the algorithm proposes two conditional branches. The first one (blue cycle of Fig. 2.8) intervenes when the error is lower than $k\epsilon(t)$ with $\epsilon(t)$ the Root Mean square (RMS) noise and k a constant, the control variable is adapted with a PID function involving the proportional (P), integral (I) and derivative (D) of the error $e(t)$. This mechanism is involved when the resistance is dominated mainly by the Joule effect. When the heating and the current density are sufficient to migrate atoms, the formation of voids leads to resistance variations such that $e(t) > k\epsilon(t)$ and cannot be counterbalanced by the PID controller. At this moment the second mechanism (red cycle of Fig. 2.8) is engaged and the bias voltage is abruptly decreased by an amount $f_{nl} = -\delta V_0 \cdot a^N$ where δV_0 and a are constants and N an index incremented at each step. This non-linear response allows the control system to react quickly and avoid the EM runaway (green curve after the point B of the left panel of Fig. 2.7).

¹From now we will suppose that R_w is known and $p = -\dot{G}_j/G_j$.

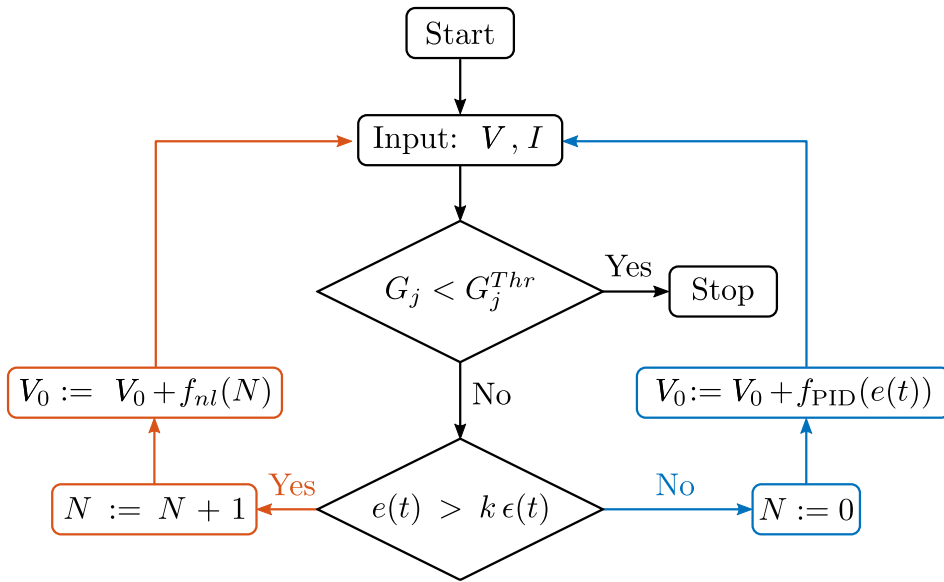


Figure 2.8 – Flow of chart of the EM control algorithm. The bias voltage V_0 is the control variable used to adjust the process variable p to its setpoint p_{setp} by minimizing the error $e(t) = p(t) - p_{setp}$. The PID response f_{PID} (blue cycle) is used when the error is small while the non-linear response f_{nl} (red cycle) reacts to sudden big variation of the resistance. The algorithm stops when the threshold conductance G_j^{Thr} is reached. Figure adapted from Ref. [120].

2.4 Imaging techniques

During an EM experiment, the damage is only observable through the evolution of the sample resistance. This measurement only gives a global idea of the changes undergone by the constriction. Several groups, including ours, have successfully tried to combine an EM experiment with an imaging technique. For example, a non-exhaustive list of EM experiments performed under electron microscopy (SEM, PID or Scanning Transmission Electron Microscopy (STEM)) includes nanobridges of Cu[126], Au[127], Al[128, 129], LCCO[129] or Pd-Pt[130] and in Nb-based SQUID[131]. In an AFM microscope, experiments were conducted mainly on gold microbridges[132–137]. In order to study the surface properties, the KPFM method, a variant of AFM allowing to measure locally the difference of work function¹ has been applied successfully on gold[133] and more recently on Yttrium Baryum Copper Oxide (YBCO)[138]. Within our group, the in-situ SEM observation platform of EM was developed in 2016 by X.A.D. Baumans and is documented in detail in Ref.[103]. In the following we will describe a recently developed in-situ AFM observation platform as well as the working principle of the AFM and KPFM techniques involved in this thesis.

¹See section 2.4.2.

2.4.1 In-situ Atomic Force Microscopy

Originally the AFM was designed to operate in a contact mode in which a thin metal tip is in permanent contact with the surface under examination[139]. Later on a second mode called non-contact or dynamic mode was developed in which a cantilever carrying the tip is oscillating at or near its resonant frequency of a few hundred of KHz and vibrates over the surface of the sample[140]. The second mode drastically reduces the interaction force between the tip and the surface and therefore allows a longer lifetime of the tip and a less invasive mode of the surface. For these reasons the dynamic mode is more widely used. The operating principle of an AFM in non-contact mode is sketched in the Fig.2.9. It consists of a xyz stage with piezo control on which the sample is placed, a cantilever with a fine tip mounted on a piezo scanner and a detection system. The latter is composed of a laser that reflects on the cantilever and detected by a photodiode that measures the amplitude and frequency of oscillation of the cantilever. The tip at the end of the cantilever is subject to a total force \mathbf{F}_t :

$$\mathbf{F}_t = \mathbf{F}_{ts} + \mathbf{F}_0 \cos(\omega_d t) \quad (2.14)$$

where \mathbf{F}_{ts} represents all the interactions between the tip and the surface and $\mathbf{F}_0 \cos(\omega_d t)$ is the exciting force from the piezo. First, the free oscillation amplitude of the system is measured when it is far from the surface ($\mathbf{F}_{ts} = \mathbf{0}$). As the tip approaches the surface, the interaction forces \mathbf{F}_{ts} change the resonance frequency and decrease the amplitude of the oscillations. As the tip moves over the surface, a feedback loop continuously adjusts the height of the cantilever to impose a setpoint amplitude of oscillations and thus a constant average distance between the tip and the sample surface. Therefore, the height of the cantilever gives the topography of the analyzed surface.

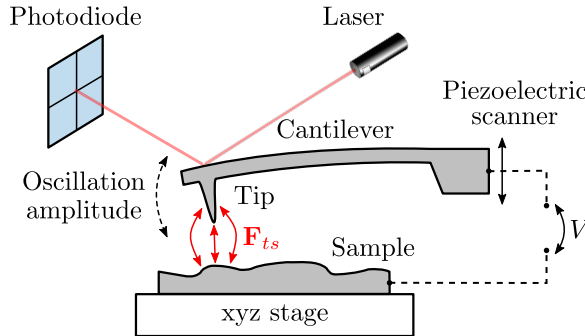


Figure 2.9 – Schematic representation of an AFM composed of a xyz stage and a tip on a cantilever. The cantilever is excited with a piezo at an amplitude measured by the reflected laser beam and the photodiode. A feedback loop ensures a constant average distance between the tip and the surface. By imposing a potential difference V between the sample and the cantilever (black dotted line), the dominant interaction is the electrostatic force and the AFM is converted to a KPFM.

A schematic representation of the in-situ AFM platform developed in the framework of this thesis is shown in Fig. 2.10. The sample is pasted and bonded on a specially designed sample holder to fit Bruker Nanoscope V AFM. The nanovoltmeter and the current source are driven via a General Purpose Interface Bus (GPIB) interface by a home-made EM software (see section 2.3.5). The outputs are connected to the sample via a Make Before Break (MBB) box which protects against electrostatic discharges¹. Two electrical configurations are used for the MBB box. The first one is used to perform the EM by connecting the instruments to the sample when the AFM tip is retracted. The second one is used during the AFM scan by leaving the sample connections in floating potential (the four terminals are connected to each other and not connected to ground). This prevents electric discharges between the AFM tip and the isolated sample. The MBB box allows to switch between these two configurations with minimum risk.

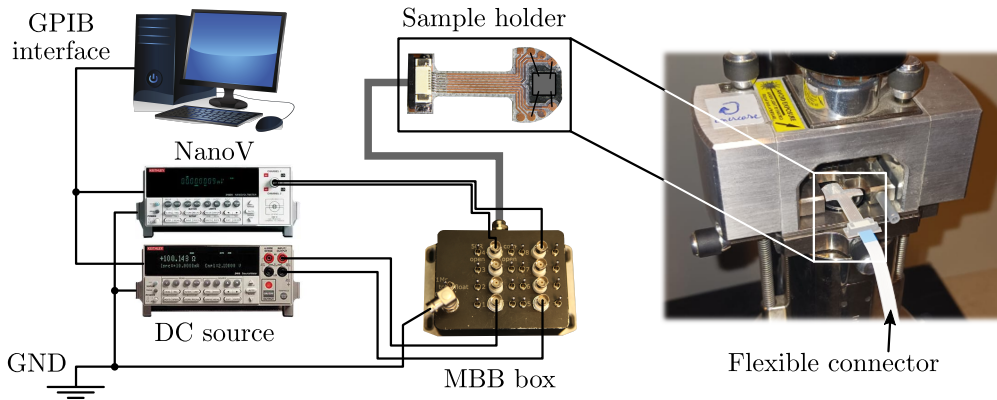


Figure 2.10 – Platform for in-situ EM under AFM inspection. A special sample holder has been designed to fit our Bruker Nanoscope V AFM. The MBB box connects the instruments driven by the EM software and the sample while preventing electrostatic discharges.

2.4.2 Kelvin Probe Force Microscopy

A KPFM experiment differs from conventional AFM only by the presence of an applied potential difference V between the sample and the tip (see black dotted line in Fig. 2.9). Under these conditions, the tip-sample system can be seen as a capacitor whose interaction force dominates the other forces and is of the form (in the vertical z direction):

$$F_{ts} \simeq F_{el} = \frac{1}{2} \frac{\partial C}{\partial z} V^2 \quad (2.15)$$

which depends on the capacitance gradient (and hence the sample-tip distance) and the potential V between the tip and the sample. V is the sum of three contributions: a constant term V_{dc} , a term coming from the difference of work function $\Delta\Phi/e =$

¹More details are available in Ref. [103] or in the supplementary information of Ref. [141]

$(\Phi_{sample} - \Phi_{tip})/e$ between the two materials which compose the tip and the surface, and a periodic excitation $V_{ac} \sin(\omega_{ac}t)$:

$$V = V_{dc} + \Delta\Phi/e + V_{ac} \sin(\omega_{ac}t) \quad (2.16)$$

The force (2.15) combined with the potential (2.16) generates a spectral response of the cantilever

$$F_{el} = F_{dc} + F_{\omega_{ac}} + F_{2\omega_{ac}}, \quad (2.17)$$

with

$$F_{dc} = \frac{\partial C}{\partial z} \left[\frac{1}{2} \left(V_{dc} - \frac{\Delta\Phi}{e} \right)^2 + \frac{V_{ac}^2}{4} \right] \quad (2.18)$$

$$F_{\omega_{ac}} = \frac{\partial C}{\partial z} \left(V_{dc} - \frac{\Delta\Phi}{e} \right) V_{ac} \sin(\omega_{ac}t) \quad (2.19)$$

$$F_{2\omega_{ac}} = -\frac{\partial C}{\partial z} \frac{V_{ac}^2}{4} \cos(2\omega_{ac}t) \quad (2.20)$$

The response to the frequency ω_{ac} is detected with a second lock-in and V_{dc} is permanently adapted by a feedback loop in order to cancel to obtain $F_{\omega_{ac}} = 0$. As a consequence, the applied dc signal is a measure of the difference in work function between the tip and the sample.

Chapter 3

Targeted modifications of monolithic multiterminal superconducting weak-links

This chapter is largely based on the following publication:

Collienne, S., Majidi, D., Van de Vondel, J., Winkelmann, C. B., and Silhanek, A. V., *Targeted modifications of monolithic multiterminal superconducting weak-links*, *Nanoscale* **14**, 5425 (2022).

3.1 Introduction

Nanoscale metallic multiterminal interconnects represent an ubiquitous layout in low dimensional electronic devices. On the technological side, for instance, on-chip power distribution networks and interconnects in clock grids normally involve multi-branched metal segments [142, 143]. The conventional and widely implemented four-probe and Hall electrical transport measurement configuration is yet another example where several voltage and current probes branch out from a transport bridge. Arguably, the most fervent interest on multiterminal devices can be found in superconducting electronics. In this context, a three-terminal device, so-called yTron, has been proposed as a sensor and readout of current-flow in a superconductor [144] whereas tunable superconducting weak links have been realized by injecting a normal current into the junction [145–155].

More recently, substantial theoretical [156–159] and experimental [160–164] efforts have been devoted to the investigation of multiterminal Josephson junctions, in part fueled by the possibility of developing topological Andreev bands in systems composed by multiple superconducting leads coupled through a central normal scattering region. Typically these devices require involved fabrication procedures (overlay lithography, shadow evaporation, multilayers, etc.) and although tunability of the junction properties has been demonstrated via gating, it requires significant effort to control each individual junction separately [165]. Therefore, developing new approaches with high efficiency and accurate tunability of individual junctions have a promising potential in superconductor science and technology.

In this chapter, we report on a simple and yet powerful EA technique to induce selective modification of conducting and superconducting multiterminal junctions by applying high electrical current density. A SEM image of a representative device is shown in Fig. 3.1(a,b) (see section 3.4 for fabrication details). The voltage contacts are placed at about $1.2\ \mu\text{m}$ away from the constrictions. In the EA process, a bias voltage across the device is slowly swept up while simultaneously monitoring the increase of resistance until reaching a pre-established value. Sudden increases of resistance leading to thermal runaway and eventually sample destruction are avoided by a reactive feedback loop [120] (see section 2.3.4). Unlike EM [141], EA is mainly driven (but not only) by the Joule heating produced by high current densities only achievable in refractory materials such as Nb. We have recently reported the successful implementation of this approach for producing targeted modifications of the superconducting properties in bow-tie Nb nanoconstrictions [61]. Here, this procedure is extended to three constrictions following the protocol described in Ref. [120]. Fig. 3.1(c) shows a typical evolution of the resistance measured between voltage pads 1-3 during the EA process. This curve exhibits an initial parabolic shape at low currents corresponding to Joule heating, followed by a sharp irreversible increase of resistance at high currents. After the bias voltage is set off, the addressed contact exhibits a resistance higher than the initial state. In three-terminal device we demonstrate the possibility to increase locally the resistance while simultaneously decreasing the critical current of a predefined junction without affecting the neighboring terminals. In this way, we are able to induce Fraunhofer-like critical

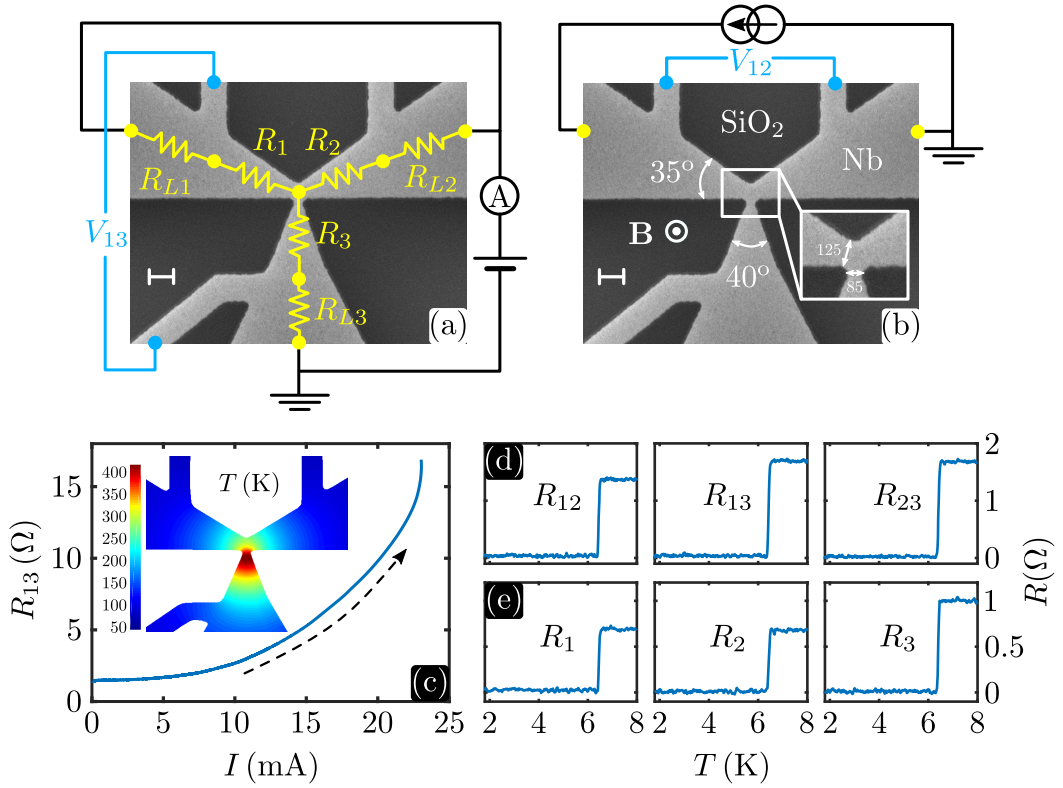


Figure 3.1 – SEM image of the pristine Nb three-terminal device (a,b). The white scale bar corresponds to 200 nm. As an example, the electrical connections to performed controlled Electroannealing (EA) of junction 3 is shown in panel (a) along with the star-shape equivalent lump circuit represented in yellow color. The resistances R_i are affected during the EA whereas the resistance R_{Li} of the leads remains undamaged. Panel (b) shows the configuration to measure the electrical response of junction formed by the terminals 1 and 2. The inset in panel (b) is a zoom in at the center of the device where the width of the junctions are given in nm. A representative resistance evolution during an EA process at 10 K is shown in panel (c). The inset in panel (c) shows the temperature distribution simulation for an intermediate current value 13 mA whose applied polarities lead to a localized temperature peak in the junction traversed by the highest current density. Panel (d) shows the actual measured temperature dependence of the resistance between two voltage contacts and panel (e) shows the calculated resistance of each junction.

current oscillation as a function of magnetic field in the selected junction. In other words, this technique permits to transform superconducting contacts in an otherwise monolithic sample into Josephson junctions by creating weak-links [44, 45] without the need to invoke complex multi-step fabrication processing. A somewhat similar method coined electroburning has been implemented to generate nano-gaps in a graphene three-terminal single-electron transistor [166].

3.2 Results

A unique advantage of multiterminal junctions with respect to a single junction [61] is the possibility to deduce the resistance of each individual junction to the central node. Indeed, the total resistance R_{ij} between two voltage contacts i and j , with $i, j = 1, 2, 3$ and $i \neq j$, can be considered as resulting from the resistance R_i associated to the zone between voltage contact i and the central point where the three terminals converge, plus the resistance R_j corresponding to the segment between the central point and voltage contact j . The equivalent lump circuit is illustrated in Fig. 3.1(a). The relation $R_{ij} = R_i + R_j$ represents a linear system of three equations with three unknowns which can be inverted to isolate each individual R_i . Note that the EA process does not modify the entire branch between the corresponding voltage contact and the central point, but rather a small region next to the central point where the current crowding leads to a high local temperature as confirmed by finite elements modelling (inset of Fig. 3.1(c), see section 3.5). As a first approximation, one can assume that the individual resistance R_i is inversely proportional to the width of the junction i . This approximation is more accurate if the opening angle of each branch is large. Fig. 3.1(d) shows the measured resistances R_{ij} as a function of temperature around the superconducting transition $T_c = 6.4$ K. Note that $R_{13} = R_{23} > R_{12}$ which is consistent with a mirror symmetric structure with a narrower junction 3, as shown in the SEM image of Fig. 3.1(b). In Fig. 3.1(e) we show the calculated resistances R_i corresponding to each junction confirming that $R_1 = R_2 < R_3$. Moreover, $R_3/R_1 \sim 1.42$ which is close to the ratio of constriction widths $w_1/w_3 \sim 1.47$.

Let us now explore the possibility to modify via EA process a predefined constriction, without affecting the other two neighboring terminals. In order to target junction i we ground the corresponding junction and feed the current from the remaining two. It is worth mentioning here that the polarity of the bias current plays a crucial role since it determines on which side of the constriction the material modification will take place (see AFM experiment in the section 3.3). Subsequently we measure $R_{ij}(T)$ and calculate the individual junction resistances $R_i(T)$. A selected set of these measurements are summarized in Fig. 3.2. The electric circuit used to electroanneal each of the three junctions is shown as inset in the rightmost column whereas each column shows the computed junction resistance $R_i(T)$ before and after modification by EA. We proceed chronologically, first modifying constriction 2 (upper row) up to more than doubling its resistance while junctions 1 and 3 remain intact. Then, in a next step, we aim to junction 1 on the same device (middle row). Finally, junction 3 is targeted (lower row) to achieve a final state in which the three junctions exhibit similar resistance values.

As we mentioned above, it is the opening angle of each branch which determines the spatial extent to the electroannealed region. In this particular study, we have purposely designed each branch with angles larger than 30° in such a way to guarantee modifications of the structure in a narrow region thus permitting phase coherent transport through the so created weak link [44, 45]. This effect is unambiguously demonstrated by measuring the critical current I_c^{ij} between two neighboring volt-

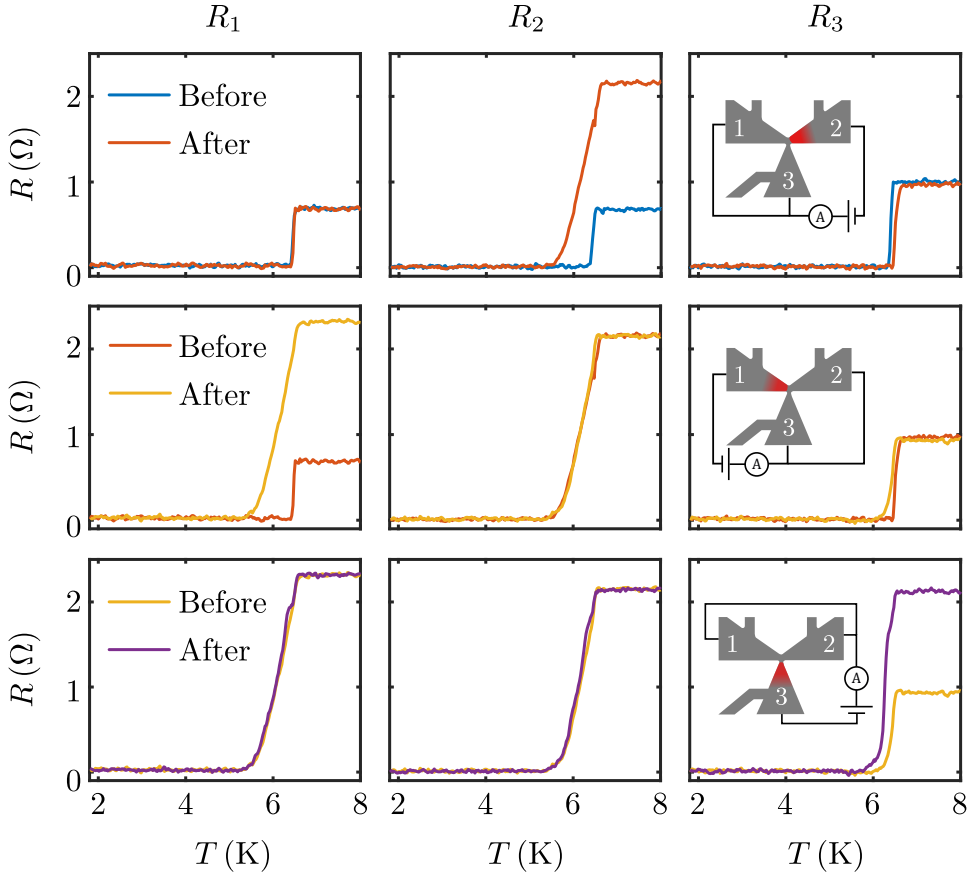


Figure 3.2 – Temperature dependence of the resistance associated to junction 1 (left column), junction 2 (middle column) and junction 3 (left column) before and after EA. In the upper, middle and lower rows, junctions 2, 1 and 3 have been respectively targeted using the circuits shown in the corresponding insets. In the upper row, the blue lines correspond to the pristine sample response. These curves have been measured with a bias current of $1 \mu\text{A}$ RMS at zero magnetic field.

age probes as a function of the magnetic field B applied normal to the plane of the device. In Fig. 3.3 we show the resulting $I_c^{ij}(B)$ curves, obtained with a $10 \mu\text{V}$ criterion at 1.8 K , for the same states described in Fig. 3.2. The blue datapoints in the upper row correspond to the pristine sample. Note that the zero-field critical current is larger for the I_{12} connection suggesting that the narrowest junction 3 limits the maximum critical current compared to the other two junctions.

Interestingly, all three curves show oscillations with a period $\Delta B \sim 190 \text{ mT}$ which could be associated to one flux quantum in a junction area of $0.0109 \mu\text{m}^2$ which is more than double the area of the central isosceles triangle formed by the converging terminals. This discrepancy is not surprising as already discussed in Ref.[61]. After modifying junction 2 (red data points), I_c^{13} remains invariant as expected, whereas both I_c^{12} and I_c^{23} decrease in amplitude. More importantly, the oscillation period in $I_c^{23}(B)$ is substantially reduced which could be associated to

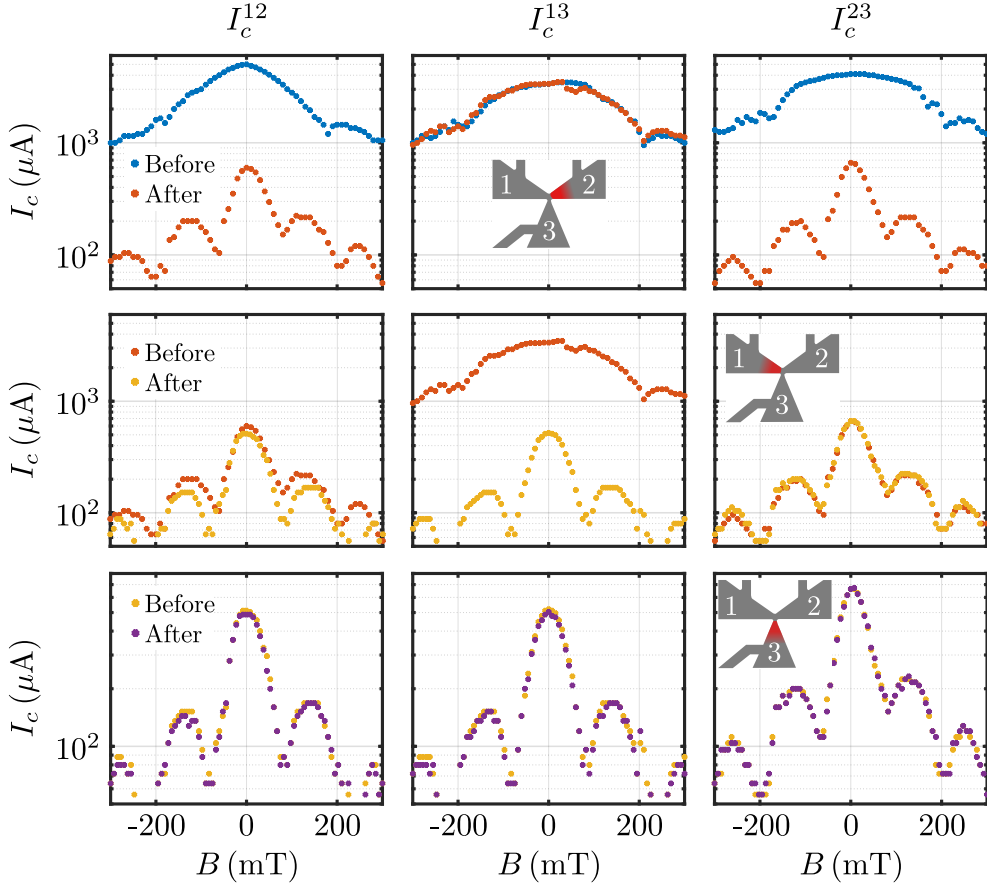


Figure 3.3 – Field-dependent critical currents obtained at 1.8 K through the junctions 1-2 (leftmost column), junctions 1-3 (central column) and junctions 2-3 (rightmost column) before and after EA. In the upper row, the blue dots correspond to the pristine sample and the red dots to the response after junction 2 has been modified by EA. In the middle row, junction 1 is addressed whereas in the lower row it is the junction 3 which is modified.

an increase of the effective junction area after EA. The fact that a modification of R_2 affects differently I_c^{12} and I_c^{23} is puzzling.

The middle row in Fig. 3.3 shows the evolution of the critical current when junction 1 is modified. In this case, I_c^{23} remains unchanged, whereas I_c^{12} and I_c^{13} decrease in amplitude and develop Fraunhofer-like oscillations [7]. In the lower row of Fig. 3.3, the EA of junction 3 does not lead to discernable changes in any of the critical currents thus indicating that the critical current remains dominated by the weaker links of junctions 1 and 2.

As we pointed out above, for the sake of clarity in Fig. 3.2 and 3.3 we have presented a selected set of three EA processes out of an ensemble of eight EA steps. The upper row of Fig. 3.4 shows the normal state resistance $R_N = R(10 \text{ K} > T_c)$ and the superconducting critical temperature T_c of each of the junctions as a function of

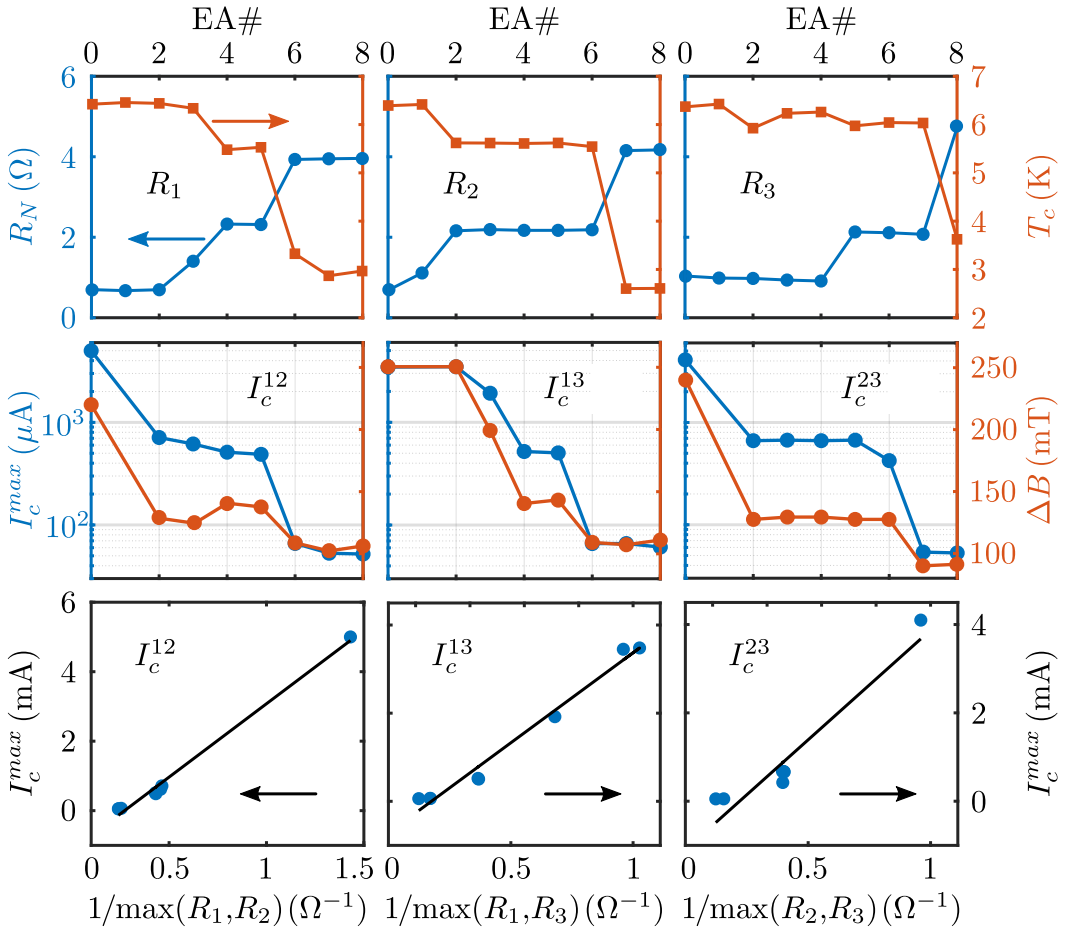


Figure 3.4 – Upper row: Computed normal state resistance R_N (blue symbols) and superconducting critical temperature T_c (red symbols) of each individual junction as a function of the EA step (EA#). Middle row: Maximum critical current (blue symbols) measured through a pair of terminals and magnetic field period of the Fraunhofer-like oscillation as a function of the EA step. Lower row: linear correlation between I_c^{ij} and $1/\max(R_i, R_j)$. The arrows indicate the corresponding ordinate axis.

the EA step (EA#). The R_N (blue symbols) shown in the upper row demonstrate full control of the targeted junction following the order EA1-EA2 junction 2 → EA3-EA4 junction 1 → EA5 junction 3 → EA6 junction 1 → EA7 junction 2 → EA8 junction 3. Local increase of R_i during EA tends to decrease the T_c of the targeted junction (red symbols, upper row).

The middle row of Fig. 3.4 shows the maximum critical current obtained at $B = 0$ and the period of the Fraunhofer-like pattern ΔB measured through a pair of terminals as a function of the EA step. The critical current I_c^{ij} is determined by the largest value between R_i and R_j . This is demonstrated by the linear correlation between I_c^{ij} and $1/\max(R_i, R_j)$ in the bottom row of Fig. 3.4 which could be used to extract the individual critical currents I_c^i as long as $R_i \neq R_j$. Although all the data

presented in this chapter has been acquired in one single device, the all-electrical control of the junction properties has been confirmed in one another similar sample and also at ambient temperature with AFM imaging as shown in section 3.3.

3.3 Atomic force microscopy imaging of the targeted structural modification

The high selectivity of the EA process demonstrated at low temperatures through electric measurements can be revealed by direct visualization under an atomic force microscope as shown in Fig. 3.5 (a complete description of the in situ AFM platform is available in section 2.4.1). These images were acquired in tapping mode and under ambient conditions. Panel (a) corresponds to the sample in its pristine state (i.e. before EA). For this initial state, each junction is characterized by a resistance $R_i \sim 9.1 \Omega$. Panel (b) shows the topography of the sample after targeted EA at junction #2 with a current ~ 14 mA. A clear bump develops in the target junction with no evident modification taking place in the neighboring junctions. This observation is consistent with an increase of the resistance $R_2 = 33.6 \Omega$ while the other resistances $R_1 \sim R_3 = 9.4 \Omega$ remain nearly unaffected. Panel (c) shows a subsequent further modification on terminal 2 with $R_2 = 80 \Omega$, with rather minor modifications on $R_1 = 9.4 \Omega$ and $R_3 = 10.2 \Omega$. It is worth noticing that in this second EA process, the propagating front of displaced matter does not advance further but instead hillocks appears on the sides of the junction # 2.

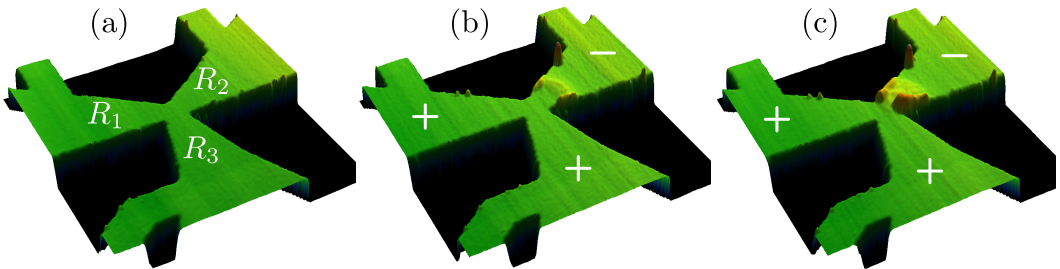


Figure 3.5 – AFM image of (a) the sample in its initial state, and after targeted modification of the terminal 2 following the first (b) and second (c) EA steps. The used polarities are indicated in the figure and are identical to that used at low temperatures.

3.4 Fabrication details

We fabricate the sample on a 2 inch double side polished sapphire substrate. Possessing a high thermal conductivity of sapphire, makes it highly suitable for our measurement where a fast thermal equilibrium is needed. First, a R-plane-oriented (1-102) sapphire substrate is transferred in the evaporation chamber of an Ultra High Vacuum (UHV) electron gun evaporator. Then, prior to 50 nm-thick Nb deposition, the substrate is heated at 660 °C to make oxygen contamination departing

	κ (WK ⁻¹ m ⁻¹)	ρ ($\mu\Omega$ cm)	α (K ⁻¹)
Nb	5	1.33	8×10^{-3}
Sapphire	3	/	/

Table 3.1 – Thermal conductivity, electrical resistivity and thermal coefficient as input parameters in COMSOL simulations.

from the sapphire substrate [167, 168]. The vacuum is kept lower than 10^{-9} Torr during Nb deposition. Eventually, in order to protect the Nb film from oxidation, a 5 nm-thick silicon capping layer is evaporated after letting the sample cool down below 80 °C in the same vacuum cycle. yTron devices are realized utilizing an Al hard mask on top of the Nb film by ebeam lithography and followed by lift-off procedure. The unprotected area of Nb with the Al mask is then removed by a reactive ion etching with a 20 W SF₆ plasma for 1 minute. Finally, the Al is removed by wet etching using the base developer MF319 for 3.5 minutes.

3.5 Finite elements model

In order to obtain the evolution of the temperature distribution during the reversible Joule heating regime, we performed finite element simulations. The model considers the sample as a thin film of 50 nm thickness whose exact geometry is obtained from SEM image. The spatial distributions of temperature and electric potential are calculated by solving the heat and continuity equations. The heat equation, is written :

$$\kappa \nabla^2 T + Q(T, \mathbf{r}) = 0 \quad (3.1)$$

with T the temperature in K and κ the thermal conductivity in WK⁻¹m⁻¹. The last term in (3.1) is determined by the Joule heating $Q(T, \mathbf{r}) = \rho(T) \mathbf{J}^2(\mathbf{r})$ with $\rho(T) = \rho_0[1 + \alpha(T - T_0)]$ the temperature dependent electrical resistivity in Ω m. The continuity equation is given by:

$$\nabla \cdot \mathbf{J} = 0 \quad (3.2)$$

where $\mathbf{J}(\mathbf{r})$ is the current density in Am⁻². Finally, the Ohm's law $\mathbf{E} = \rho(T) \mathbf{J}$ and the electrical field $\mathbf{E} = -\nabla V$ complete the system of equations. The parameters used in the simulations are summarized in Table 3.1.

The main panel of Fig. 3.6 shows the evolution of the resistance R as a function of the applied current I at the bath temperature $T_b = 10$ K. The observed parabolic profile typical of Joule heating is followed by a important resistance increase associated to structural modification caused by EA. It is precisely in this high-currents regime that permanent modifications of the junctions lead to the irreversible modifications of the normal state resistance and critical current of the device (see Fig. 3.4). The results of the simulations are represented by the red circles and allow us to estimate the temperature distribution in the sample for currents below 15 mA. The inset of Fig. 3.6 gives the temperature mapping for the special case $I = 14$ mA.

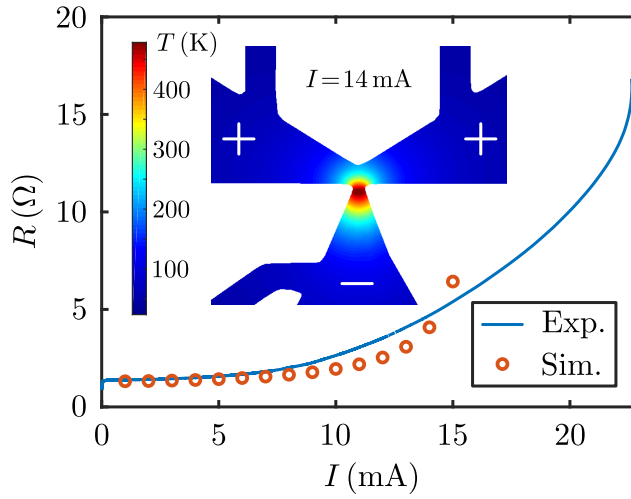


Figure 3.6 – Typical curve of an EA experiment (blue line) and the result of the finite element model for some values of bias current (red circles). The inset shows the obtained temperature map for $I = 14$ mA with the given polarities.

3.6 Conclusion

In brief, we have presented a technique particularly adapted to control individually the junction properties of each branch in a multiterminal device. The primary advantage of the proposed approach lies on its simplicity, offering full control of the material modifications and unprecedented high degree of selectivity. Although in the present study we focus on three terminal devices, the method can be extended to N-terminal devices or even several N-terminal devices interconnected. Two important parameters to consider are the terminal geometry and the polarity of the EA current. The exact nature of the Josephson junction created by EA is still uncertain, and may be either of the SNS type where N is a non-intrinsic superconductor or of the Superconductor-weaker superconductor-Superconductor (SS'S) type where S' denotes a superconductor of lower critical temperature, is another motivation for future work.

Chapter 4

Effect of moderated electropulsing on Nb multiterminal transport bridges

This chapter is largely based on the following publication:

Marinković, S., Abbey, E. A., Chaves, D. A. D., **Collienne, S.**, Fourneau, E., Jiang, L., Xue, C., Zhou, Y. H., Ortiz, W. A., Motta, M., Nguyen, N. D., Volodin, A., Van de Vondel, J., and Silhanek, A. V., *Effect of Moderate Electropulsing on Nb Multiterminal Transport Bridges*, Phys. Rev. Appl. **5**, 054009 (2023).

4.1 Introduction

Niobium is a material of choice for a variety of superconducting applications including Radio Frequency (RF) accelerator cavities [169–171], quantum interference devices [172–174], Josephson tunnel junctions and weak links [175, 176], superconducting resonators and filters [177–179], quantum bits [180–182], and flexible superconducting transmission lines [183, 184]. The reason behind this privileged position is manifold: it is the single element with the highest superconducting critical temperature, it develops stable dielectric oxide coatings (NbO , NbO_2 , Nb_2O_5) which protect the superconducting phase, Nb exhibits long-term stability under repeated thermal cycling, it can be nanostructured by additive or subtractive lithography, and it is malleable, ductile, and has low toxicity.

More importantly, the possibility to introduce surface treatments such as thermal etching, electropolishing, annealing in controlled atmosphere, and buffered chemical polishing, allows for further optimization of the properties of Nb, such as low microwave surface resistance desired for boosting the efficiency of RF cavities [185]. Naturally, these procedures are homogeneously applied to the entire sample/device and do not allow for spatial selectivity. An elegant approach able to overcome this limitation has been recently proposed based on local annealing of the sample by combined effects of Joule heating and EM [141]. This technique has been successfully implemented to tune the properties of Nb-based superconducting weak links [61], SQUIDS [131], multiterminal junctions [186], and for the fabrication of nanoheaters [187]. In the applications listed above, substantial resistance increase, even beyond the quantum of resistance of $25.8 \text{ k}\Omega$, was achieved by severe EM and the resulting structural modification as well as possible alloying were amply illustrated and discussed. In contrast to that, the consequences of mild EM on Nb has remained largely unexplored so far.

In this chapter, we provide experimental evidence on the origin of the material properties’ modifications induced by Electropulsing (EP) on Nb/Al. We focus particularly on the low stress regime corresponding to currents slightly above the onset of EA and giving rise to a few percent increase in resistance. The subtle induced change consists in a reduction of the work function in a targeted region likely associated to a local oxidation triggered by thermal effects, although no microstructural modifications are revealed. Comparing the spread and shape of the affected area with thermal maps computed through finite element modelling we are able to conclude that temperatures above $\sim 435 \text{ K}$ are needed to induce sizable modification in the material. Several funnel shaped constrictions with different angles were fabricated to demonstrate the possibility to control the extension of the affected area via geometry. The identification of the key parameters permitting to master the local modifications of Nb constrictions together with the understanding of the material’s properties affected by EP are relevant steps needed to achieve in situ superconducting weak links and normal leads, both individually tuned at will.

4.2 Experimental details

Resist patterns consisting of a double PMMA/co-PMMA layer were prepared by EBL on a Si/SiO₂ substrate ($750 \pm 50 \mu\text{m}$ Si, $300 \pm 25 \text{ nm}$ SiO₂) using the nanofabrication system Pioneer 2 from Raith GmbH. Subsequently, a Nb thin film ($\sim 50 \text{ nm}$) was deposited using RF magnetron sputtering in a chamber previously pumped down to 10^{-8} mbar with a deposition rate of 1 \AA/s at an Ar pressure of 5.3 mbar. Without breaking the vacuum, the sample was then capped with a 7 nm-thick Al layer by electron beam evaporation. The thickness of the Al capping layer has been chosen to be slightly thicker than the native oxide layer of Al [188], so it acts as a protective layer for Nb. The final structure is revealed after conventional lift-off process in warm acetone.

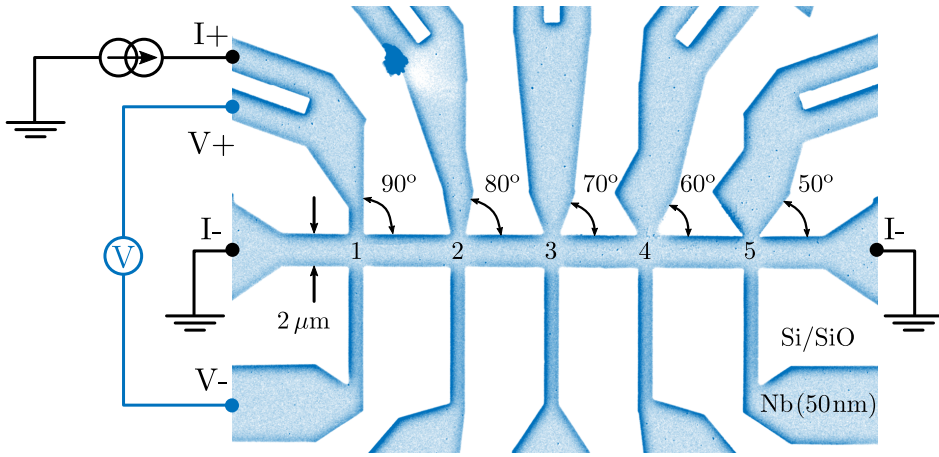


Figure 4.1 – False colored scanning electron microscopy image of one of the Nb multiterminal transport bridges. The circuitry and polarity of the current source are indicated for the case of EP junction 1.

Figure 4.1 shows the sample layout in which a $2 \mu\text{m}$ -wide central transport bridge is connected by ten terminals symmetrically placed with respect to the central axis of the bridge. All ten terminals are $1.25 \pm 0.05 \mu\text{m}$ wide at the point of contact (junction) with the bridge. In order to investigate the possible influence of the junction geometry on the properties of the zone affected by EP, the upper row of junctions labelled from 1 to 5 form different angles (respectively $\zeta = 90^\circ$ to 50° in steps of -10°) from the central axis of the bridge. We consider the complement of this angle to be the funnel angle $90^\circ - \zeta$. Junctions in the lower row are intended for the sole purpose of measuring the electric potential drop and will remain unaffected by the EP process.

In order to address a particular junction without affecting the neighboring junctions, the current is fed through the upper contact corresponding to that particular junction and the current sink is connected to the left and right extremes of the transport bridge. The voltage drop through the junction is measured between the upper and the opposing lower contact. For the sake of clarity, Fig. 4.1 shows the

polarity of current source and voltmeter for modifying junction 1. This strategy has been discussed in chapter 3 for the case of strongly modified Nb trijunctions [186]. The samples are contacted by needle probes while excited and probed by a dual-channel source-meter Keithley 2612B. The findings reported in this chapter were reproduced in five different samples.

Single-pass KPFM measurements [189] were conducted at ambient conditions on an Agilent Technologies 5500 Scanning Probe Microscope. The setup was equipped with conductive platinum silicide probes from Nanosensors (PtSi-FM) with a tip radius of curvature around 25 nm and nominal force constant of 2.8 N/m.

4.3 Electropulsing protocol and methodology

The EP protocol consists of applying current pulses during 1 s with linearly increasing amplitude. The resistance of the sample is probed during the pulse (R_{max}) as well as in between the pulses (R_{min}). The time between two consecutive electropulses is 25 s. This experiment is performed under ambient conditions. Figure 4.2 shows the resulting evolution of R_{max} (red symbols) and R_{min} (blue symbols) as a function of the pulsed current amplitude for each of the five junctions. The resistance $R_{max}(I)$ initially increases quadratically as a result of Joule heating and a finite temperature coefficient of resistance. At high current amplitudes, a sudden upturn indicates the onset of irreversible changes in the sample due to EP. A more convenient parameter able to separate the irreversible changes operating on the sample from the reversible Joule heating contribution, is R_{min} . Indeed, pulses of small amplitude lead to no modification of R_{min} as manifested by a nearly current independent resistance. Beyond a certain threshold current density, a slight decrease of resistivity is systematically observed. This effect can be linked to structural stress relieved during a mild Joule annealing process. This initial improvement of the sample is followed by a rapid increase of the resistance likely associated to irreversible oxidation of the Nb at the addressed junction. We have limited the excess resistance produced by this process to less than 10 % in each junction.

Note that even though the narrowest constriction of each junction has the same width ($\sim 1.25 \mu\text{m}$), the EP curve is not identical for different junctions. This observation may suggest that the modifications produced on the junctions are not solely dictated by the current crowding at the constriction but its funnel angle plays an important role as well. It is also interesting to observe that the maximum current amplitude I_{max} needed to induce the desired resistance increase varies non monotonically with the funnel angle, maximizing around $60 - 70^\circ$. This result has been reproduced in three different samples as shown in the inset of Fig. 4.2. A plausible explanation for this fact could be the unwanted residual Nb which tends to round the sharp corners in the junctions and which is apparent at intermediate funnel angles (see AFM images in section 4.6). Indeed, it is expected that current crowding in sharp bends [190] will tend to reduce the threshold applied current to trigger the EM process.

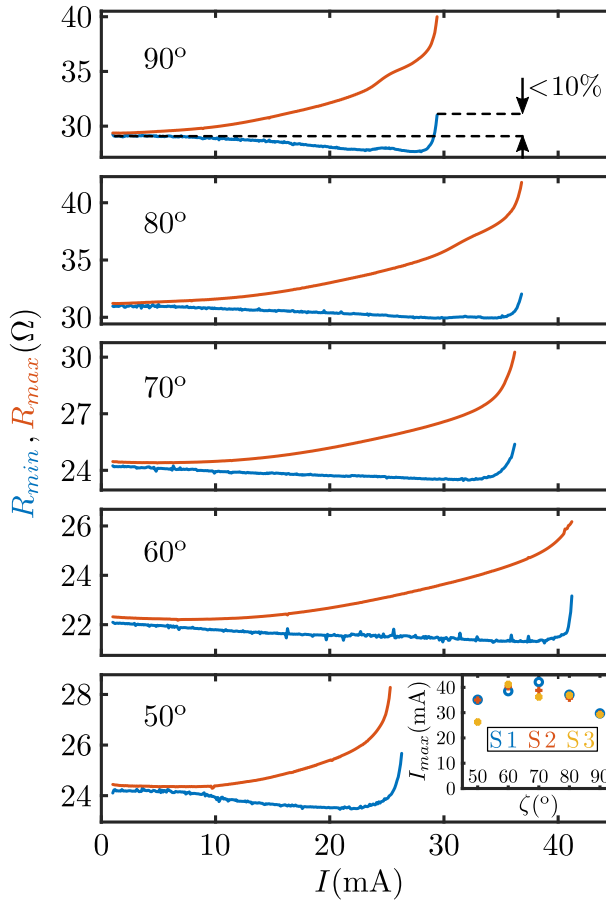


Figure 4.2 – Resistance probed during (R_{max}) and after (R_{min}) a current pulse of amplitude I for the five junctions shown in Fig. 4.1. The maximum current amplitude is set such that the initial resistance R_{min} increases by less than 10 %. Electropulsing is performed at ambient conditions and reproduced in three different devices, labelled S1, S2, and S3. The inset shows the maximum current I_{max} needed to attain 10 % increase in resistance for the three tested devices.

4.4 Visualization of the eletropulsing-induced junction's modification

Let us now analyse the induced modifications at each junction after the EP process described above. To that end we resort to several microscopy inspection techniques including AFM, SEM and KPFM. AFM measurements (shown in section 4.6) do not reveal any structural change after EP. Consistently, no hint of modifications are observed in the SEM images collected by an Everhart-Thornley (ET) detector shown in Fig. 4.3(a).

This detector collects mainly spatially spread type-2 Secondary Electron (SE2) and should be able to reveal nanoscale morphological changes on the sample's surface. In contrast to that, the in-lens image shown in Fig. 4.3(b) evidences a clear change

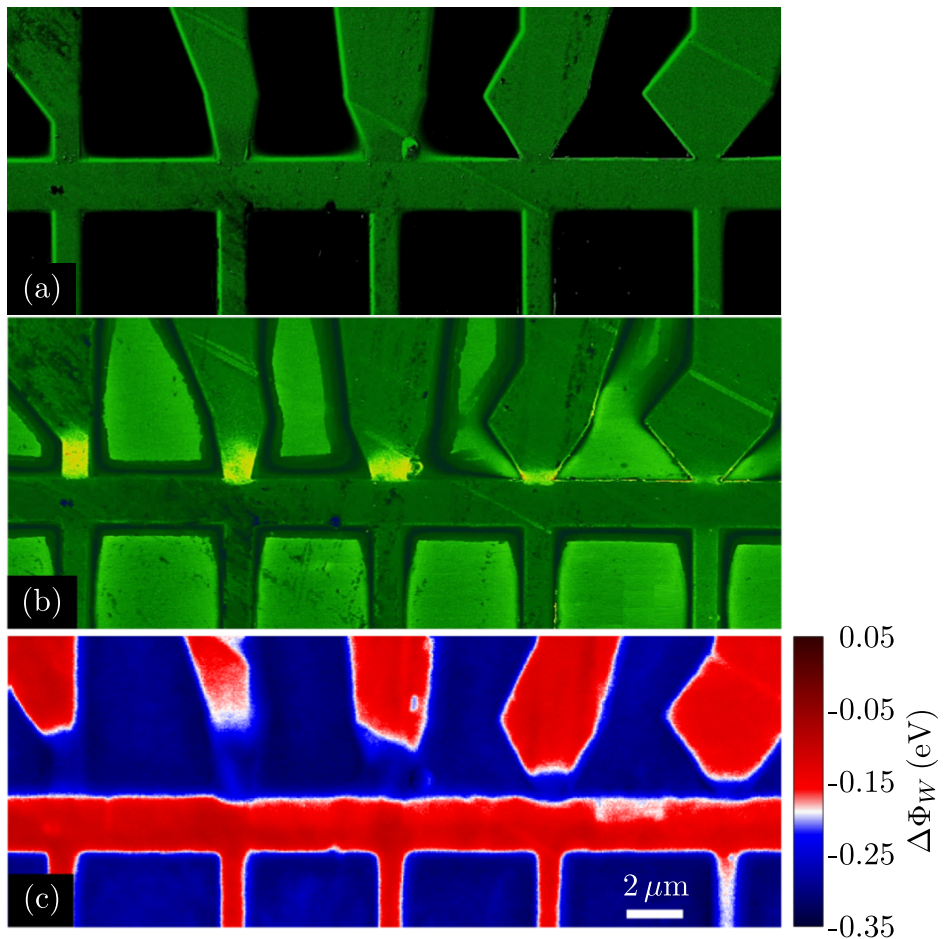


Figure 4.3 – Microscopy inspection of a Nb/Al device after the EP procedure shown in Fig. 4.2. (a) SEM images obtained by ET detector do not reveal any change that could be attributed to the EP process. (b) in-lens SEM image obtained at 2 kV demonstrates higher contrast in the junctions that have been electropulsed. (c) KPFM images of all junctions reveal a lower work function (in blue) in the regions that have been electropulsed.

of contrast in the electropulsed junctions. The in-lens detector collects mainly SE1 electrons generated near the upper region of the beam-sample interaction volume and therefore provides direct information on the sample's surface. These images have been acquired with an accelerating voltage of 2 kV which, according to Ref.[191], implies a penetration depth ~ 35 nm of the primary electrons into the Nb/Al bilayer. However, the primary factor determining the emission of secondary electrons (so called electron yield) is essentially the surface potential (work function). Indeed, the fact that the affected regions appear brighter than unaffected parts of the sample, implies a higher electron yield, associated to a lower work function in the affected area. In order to verify this hypothesis, we carried out KPFM measurements shown in Fig. 4.3(c). In this image, red (blue) color indicates

high (low) work function. There is a close correlation between the areas with high electron yield and those where the work function has been suppressed.

A possible explanation for the observed modification of the sample's surface after EP is local oxidation of the Al capping layer. Indeed, it has been recently shown that the SE emission is directly influenced by the oxidation of the aluminum surface [192]. In particular, for oxide layers thicker than 0.4 nm, the electron emission has been shown to increase (and therefore the work function to decrease). The work function of the oxide layer is also expected to be lower than that of the metallic aluminum [193]. More interestingly, in addition to oxidation, it has been shown that physis- and chemisorption of O and C strongly influence the work function and the secondary electron emission [194, 195]. These experimental findings have been lately confirmed by first-principle studies [196]. This phenomenon may also account for the observed decrease of the work function in the investigated Nb/Al junctions.

4.5 Finite element modelling

The oxygen diffusion is assisted by the local increase in temperature during the EP process and therefore, estimating the temperature profile in the junctions is of paramount importance to identify the extension of the affected area. An interesting feature observed in Fig. 4.3 is the fact that the affected region shrinks as the funnel angle increases. In order to understand the origin of this effect, we used the Finite Element Method (FEM) to take into account the exact geometry of the samples from the SEM image analysis. The thickness of the Nb/Al sample $t = 62$ nm, obtained from atomic force microscopy imaging (see section 4.6), is assumed uniform. Simulations considering a pure 62 nm thick Nb film or a bilayer Nb(55 nm)/Al(7 nm) give very similar results. The simulation solves the stationary heat equation:

$$\nabla \cdot \mathbf{q} = Q, \quad (4.1)$$

where $\mathbf{q} = -k\nabla T$ is the heat flux density in W/m² and $Q = \rho J^2$ is the local Joule heating, $\mathbf{J} = (1/\rho)\mathbf{E}$ being the current density in A/m² and $\mathbf{E} = -\nabla V$ the electric field in V/m. The average thermal conductivity for Nb/Al and Si were assigned to 54 W/(Km) and 130 W/(Km), respectively. The normal-state resistivity $\rho(T)$ of the sample exhibits an approximately linear temperature dependence $\rho(T) = \rho_0[1 + \alpha(T - 300)]$, where $\alpha = 2.5 \times 10^{-3} \text{ K}^{-1}$ is the thermal coefficient and ρ_0 is the resistivity at 300 K. The electric potential distribution for the Nb layer is obtained by solving Poisson's equation

$$\nabla^2 V = 0. \quad (4.2)$$

A boundary condition for (4.1) sets the temperature at the bottom of the substrate to room temperature (see inset of Fig. 4.4) while three conditions are needed for (4.2): one for the current input and two for the current output (as an example, see Fig. 4.1 for junction 1). The two equations (4.1) and (4.2) are coupled by the Joule heating term Q . The imperfect contact between Nb and Si imposes a thermal resistance R_{therm} which reduces the heat removal towards the substrate:

$$q_{int} = (T_{Nb} - T_{Si})/R_{therm}, \quad (4.3)$$

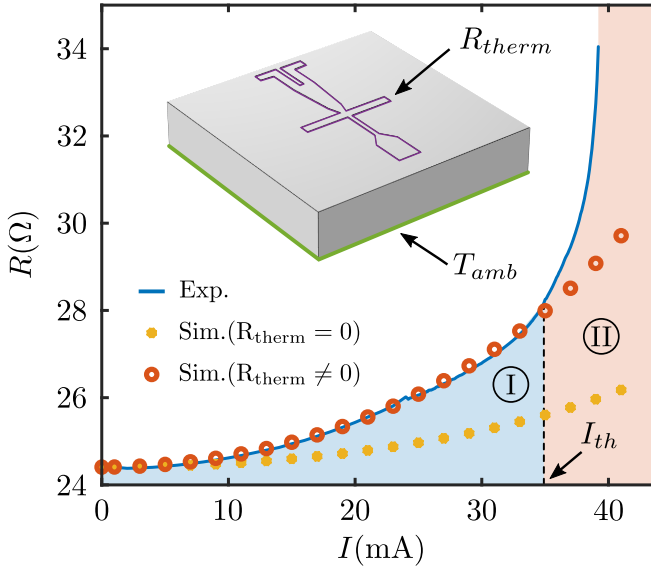


Figure 4.4 – Typical current resistance (blue curve) observed during an experiment of EP together with simulations without (yellow dots) and with (red circle) thermal resistance. The blue curve corresponds to $R_{max}(I)$ in Fig. 4.2. The simulations highlight the existence of zones I and II whose transition at the threshold current I_{th} means the appearance of irreversible alterations in the transport properties of the sample.

where q_{int} is the heat flux density at the interface between sample and substrate, R_{therm} is the thermal resistance in Km^2/W , T_{Nb} and T_{Si} the temperatures of the sample and the substrate, respectively. As an example, the junction 3 subjected to a succession of current pulses exhibits a resistance evolution represented by the blue curve in Fig. 4.4. Simulations without taking into account thermal resistance ($R_{therm} = 0$) are given by the yellow dots and show that the heating is insufficient to account for the experimentally observed resistance increase. The thermal resistance $R_{therm} = 2.61 \times 10^{-8} \text{Km}^2/\text{W}$ is determined by iteration until the early states of EP ($I < 20 \text{mA}$) are satisfactorily fitted (red circles). This value of R_{therm} is unique and the same for all junctions. The threshold current I_{th} , beyond which irreversible changes operate onto the junction, is defined as the current for which the modelling underestimates the experimental value of the resistance, which leads to the distinction between two zones. Zone I, for currents lower than the threshold current ($I < I_{th}$), presents a reversible parabolic profile characteristic of the Joule effect without structural modifications. The second zone ($I > I_{th}$), is characterized by a sudden increase of the resistance due to irreversible alterations of the material's properties.

The EP curves as well as simulations of the five junctions of the same sample are shown in the upper row of Fig. 4.5. An average resistivity $\rho_0 = 37 \pm 3 \mu\Omega\text{cm}$ has been determined to fit the value of the resistance at low current. The middle row of Fig. 4.5 shows the current density profiles for the applied current I_{th} . Independently of the total injected current, we observe that the current density becomes more in-

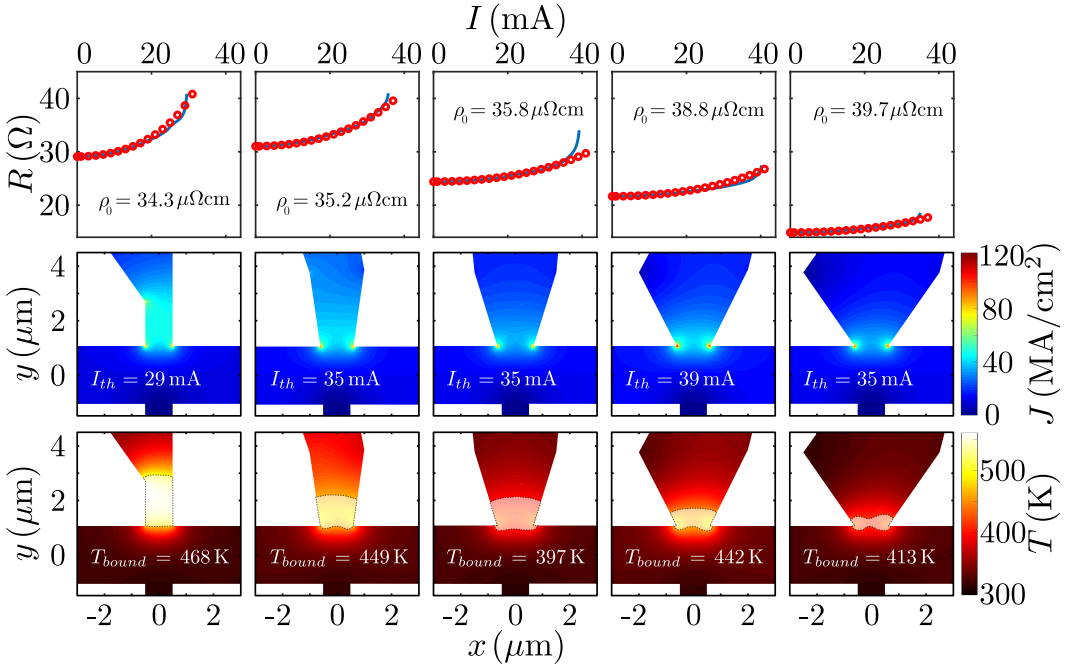


Figure 4.5 – Simulation results for the five junctions of the same sample. The EP measurements (blue curve) are given with simulations (red circles) in the first row. The current density maps corresponding to the current I_{th} are shown in the second row. The images of the third row illustrate the temperature distributions, with the dashed curve denoting the isothermal curve $T = T_{bound}$ surrounding the modified region of the work function.

homogeneous as the funnel angle increases, leading to a maximum current crowding in junction 5. The temperature maps, given in the bottom row, were compared to the affected areas of Fig. 4.3(b,c) to determine the temperature T_{bound} at the boundary of the affected area for which the work function is modified. These isothermal contours are plotted in dotted lines together with the corresponding threshold temperature, which can be estimated as $T_{bound} \sim 435 \pm 35$ K. This temperature is to be compared with the results reported in Ref.[197] concerning the growth kinetics of thin aluminum-oxide films formed by the dry thermal oxidation of a bare Al(431) substrate at a partial oxygen pressure of 1.33×10^{-4} Pa. These authors identified a threshold temperature of 573 K below which an amorphous Al oxide film develops that attains a limiting thickness, whereas above this threshold the growth of the Al oxide layer is not impeded at a limiting thickness. In the present chapter the partial oxygen pressure at atmospheric conditions is substantially higher thus likely reducing the threshold temperature needed for steady growing of the Al oxide layer.

In addition to the oxidation of the Al capping layer, there is a simultaneous process of Nb oxidation taking place at the vertical walls of the Nb structure which are not protected by the Al capping. Indeed, it is known that Nb and Nb_2O_5 exhibit low diffusivity below 400 K yielding good long-term stability including thermal cycling up to 400 K [198]. In other words, it is not surprising that the resistivity

increases at the loci where the local temperature exceeds 400 K. The numerical simulations also show a highly-inhomogeneous local temperature rise with a hot core reaching above 550 K. The fact that above 570 K the oxidation of Nb consists mainly in a exponential growth of diffusion-controlled oxygen uptake [198], suggests that the hottest part of the junction may undergo bulk modifications as well. This is indeed consistent with the development of a double step superconducting transition after EP as shown in section 4.7.

4.6 Atomic force microscopy profile

A line profile along the white dashed line of junction 1 obtained by Atomic Force Microscopy is given by the blue curve in the inset of the bottom right panel in Fig. 4.6. From this measurement we can extract a height $t_{Nb} \sim 62$ nm which includes the 7 nm thick Al capping layer. The red dashed line shows the profile used in the simulations in which the width w_{Nb} has been determined from the SEM image. Note that the AFM profile does not show vertical walls. This could in part be attributed to the tip-sample convolution effect [199].

Following EP, AFM analysis was conducted on all junctions. It is evident from the first row of Fig. 4.6 that there have been no significant structural modifications. The spikes observed in the AFM images result from residual resist traces after lift-off.

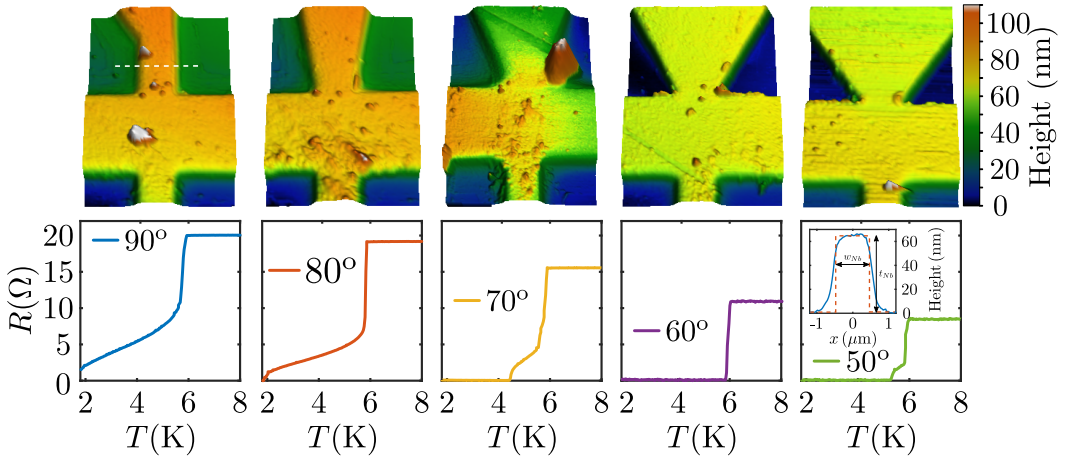


Figure 4.6 – After EP, AFM inspection is performed on all junctions (first row). As evidenced by the images obtained, there has been no structural change following EP. The second rows shows the corresponding $R(T)$ curves for all the junctions measured with an applied current $I = 1 \mu\text{A}$ after subsequent EP process. The height profile of the cross section along the white dotted line of junction 1 is given by the blue curve in the inset of the lower right panel. The red dotted line represents the section used in the simulations.

4.7 Superconducting transition of each junction after electropulsing

The resistance vs. temperature curves obtained for the addressed junctions (labelled as indicate in Fig. 4.1) after EP, are shown in the second row of Fig. 4.6. In most cases the EP leads to a two-step superconducting transition: as the temperature decreases, the first resistance drop occurs at about $T_c^0 = 5.8$ K, corresponding to the superconducting transition in part of the Nb bridge in between the voltage probes that remains unaffected by the EP. This is followed by a second drop to zero resistance at lower temperatures which corresponds to the affected area by the EP process. Note that the extension of the affected area is larger for junction 1 which explains the larger decrease of the superconducting critical temperature. The fact that the critical temperature is substantially reduced with respect to the bulk value (9.25 K) is a consequence of the fabrication method implying a lift-off procedure. Indeed, since Nb is a refractive material requiring high target temperatures, significant heating and outgassing of the resist leads to reduced critical temperatures [200].

4.8 Kelvin-probe Force Microscopy

The observations described in the main text were corroborated by KPFM measurements in similar devices, one of which is presented in Fig. 4.7. Although one constriction was damaged during EP, the comparison between in-lens SEM and KPFM images in panels (a) and (b) once more reveals a close correlation of the regions affected by the process. Furthermore, the work function variation ($\Delta\Phi_W$) profiles displayed in panel (c) unmistakably reveal that these regions experience a drop in work function.

4.9 Conclusion

In summary, we have demonstrated the possibility to change the properties of selected individual Nb junctions in a device with an arbitrary number of terminals through EP. This is an appealing approach by virtue of simplicity which permits nanofabrication without complex overlay processing and extra deposition steps. In addition, a large degree of selectivity is observed: unaddressed junctions remain intact and those targeted can be, to some extent, tuned by combining purposely predefined geometries and/or controlling the amplitude of the electropulsed current. As an illustration, this technique would allow us to transform a series of Nb contacts in SNS junctions or just normal contacts. The current chapter focuses on minor modifications of the material properties (low current amplitude) for which no structural change is revealed. In this limit, the affected area becomes apparent through in-lens imaging in a scanning electron microscope and as a contrast in Kelvin-probe force microscopy. Both characterization techniques point to a reduction of the work function and an enhancement of the secondary electrons

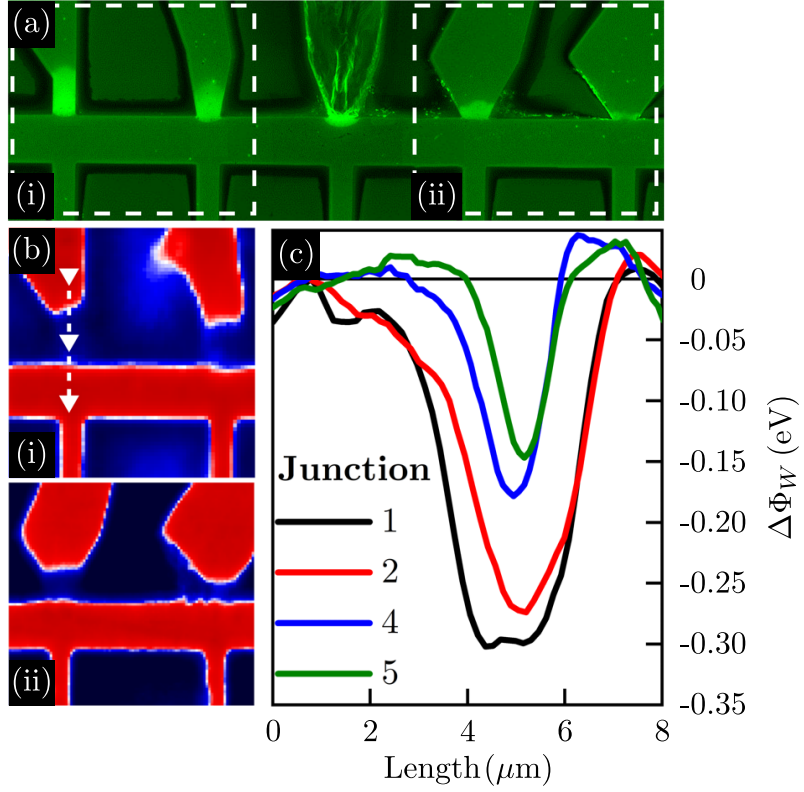


Figure 4.7 – (a) SEM in-lens image for Device B exhibiting a higher contrast close to the electropulsed constrictions. During the experiment, the middle junction was damaged and therefore is not considered in the analysis. (b) KPFM images are shown for junctions 1 and 2 – region highlighted by dashed rectangle (i) in panel (a) – and junctions 4 and 5 – rectangle (ii). As in the main text, red coloured regions are associated to higher values of the work function than blue coloured ones. This is explicitly shown in the profiles of panel (c), where the work function variation ($\Delta\Phi_W$) is plotted around each junction following the direction indicated by the white arrow across junction 1.

yield in the affected area. This phenomenon has been investigated in the past and can be attributed to physi- and chemisorption of O and C atoms. Complementary finite-element modelling using the exact geometry of the experimentally investigated samples suggests that the affected area is hotter than 435 K. The current blooming of Niobium-based superconducting devices together with the continuous progress on Nb thin films employed in transmon qubit architectures and the critical role played by oxygen vacancies as a decoherence mechanism, make the findings of this report timely by unveiling the severe implications of applying moderate currents in those devices.

Chapter 5

Nb-Based Nanoscale Superconducting Quantum Interference Devices Tuned by Electroannealing

This chapter is largely based on the following publication:

Collienne, S., Raes, B., Keijers, W., Linek, J., Koelle, D., Kleiner, R., Kramer, R. B. G., Van de Vondel, J., and Silhanek, A. V., *Nb-Based Nanoscale Superconducting Quantum Interference Devices Tuned by Electroannealing*, Phys. Rev. Appl. **15**, 034016 (2021).

5.1 Introduction

A dc-SQUID is composed of a superconducting loop interrupted by two Josephson junctions. The critical current of the device exhibits an oscillatory response as a function of magnetic field with a periodicity determined by the quantization of the magnetic flux threading the loop (see section 1.3.4). The microscopic size of a SQUID (usually combined with a suitable input circuit) enables one to realize sensitive magnetic field sensors [62], that are used in a large variety of applications [63]. With the advent of nanotechnology their range of application has been broadened [92] while their energy resolution approaches the ultimate quantum limit [201, 202]. During the last years, the interest to measure the magnetic response of nanoscale systems has launched a number of initiatives to miniaturize these devices [92, 203]. In this endeavour, conventional Josephson tunnel junctions with insulating barriers are less attractive since their low critical current density prevents them to achieve the optimum performance. With the goal to mitigate this drawback, a growing attention has been devoted to Dayem bridge junctions made of a high critical current density material such as Nb.

Although Nb Dayem bridge junctions can be nanostructured down to few tens of nm, the short coherence length of the material typically leads to a current-phase relation markedly different from the one measured in ideal Josephson junctions [44, 45]. This effect, in turn, manifests itself in triangular shaped critical current oscillations as a function of the applied magnetic field [71] which is detrimental to the SQUID performance, as it suppresses the critical current vs magnetic flux modulation depth [56, 204]. Furthermore, poor heat evacuation and high critical currents might lead to the development of self-heating hot spots when the device switches from the superconducting to the normal state. The resultant hysteretic current-voltage $V(I)$ characteristics prevent the SQUID from being operated in the dissipative regime (voltage mode) as phase coherence is often lost once the hot spots are formed.

Nowadays, the attention has shifted towards postfabrication tweaking of nanoscale SQUIDs in order to optimize their operation performance according to the specific needs. External adjustment of the as-fabricated Nb SQUIDs, addressing the critical current of the weak links, has been demonstrated to be a promising approach to achieve optimum performance. A non-exhaustive list of controllable junctions includes Nb/normal metal/Nb Josephson junction with two additional contacts into the normal region of the junction [154], Nb / semiconductor / Nb junctions modulated by current injection into the two-dimensional electron gas [205], hot-phonon controlled junctions [55], and a multi-port Nb weak-link design [155]. The above described approaches, although elegant and competitive, demand complex multistep nanofabrication procedures and they may become impractical for implementation in confined systems such as SQUID-on-tip devices [82].

In this chapter, we demonstrate that current-induced modifications of the structure of the weak links through an EA process provides a viable approach to tune the critical current of Nb nanoSQUIDs and to suppress their hysteretic response without compromising the operational temperature range of the devices. This pa-

per is organized as follows: in section 5.2 we briefly summarize the experimental methods. In section 5.3 we present and characterize the electric and magnetic response of the pristine Nb nanoSQUIDs. In particular, we demonstrate that the critical current oscillations as a function of magnetic field are well captured by a model assuming a linear CPR. This will be an important reference to compare with the electroannealed devices. Section 5.4 is devoted to the investigation of the physical modifications of the bridges caused by the EA process and its influence on the nanoSQUID's response. Although EA has the tendency to worsen the material properties, by further EA we witness an astonishing recovery allowing us to access a regime in which the SQUID can be operated in a non-hysteretic mode. The conclusion and perspectives for further developments are discussed in section 5.5.

5.2 Methods

5.2.1 Controlled EA

The EA process is achieved by software control with a feedback loop as described in Ref. [120]. It basically consists in the application of a voltage ramp to attain a constant conductance rate of $-2 G_0/s$, where G_0 is the quantum of conductance, while simultaneously monitoring the consequent resistance change. The software controlled feedback loop allows reacting upon abrupt resistance jumps and ensures a progressive evolution of the sample's resistance in time. The whole control algorithm is manually stopped either once a certain maximum current, so called the EA current I_{EA} , is achieved, or, for high annealing currents, if a given final resistance is reached. To prevent the sample from electrostatic discharges, a special mounting and connecting protocol as described in [103] is applied.

5.2.2 Cryogenic transport measurements

The EA has been carried out in a cryogenic environment with bath temperature $T_b \sim 10$ K above the superconducting critical temperature of Nb. Both, the electrical transport measurements and electro-migration process were carried out in a modified commercial Quantum Design-PPMS cryostat. The sample is mounted in a sealed chamber providing a temperature stability better than 1 mK in a He gas atmosphere at 20 mbar.

5.2.3 *In situ* SEM transport measurements

A specially designed platform permits us to perform EA runs and electrical measurements directly inside a scanning electron microscope. Each EA steps is followed by image acquisition. More details are given in [141].

5.3 Properties of the pristine Nb nanoSQUIDs

5.3.1 Fabrication and electrical characterization

The investigated samples consist of $t = 50$ nm-thick Nb films deposited by electron beam evaporation onto a Si substrate terminated with a 100 nm-thick SiO_2 layer. The evaporation is performed under UHV and the Nb film is subsequently capped with 5 nm of Si for protection. EBL has been carried out in a Nanobeam nB5 platform with an electron beam energy of 80 keV. Afterwards, an Al hard-mask is fabricated by e-beam evaporation, followed by a lift-off procedure. The Nb, unprotected by the Al mask, is removed by reactive ion etching with SF_6 gas during 10 s. Finally, the Al is removed by wet etching using the base developer MF-26A. In this study, five samples (labelled S1, S2, ..., S5) were characterized, all of them with nominal junction length of 100 nm and widths between 60 nm and 80 nm. A SEM image of a representative nanoSQUID is shown in Fig. 5.1(a). The voltage contacts are symmetrically placed at about $1\ \mu\text{m}$ away from the constrictions (Fig. 5.1(a)). Fig. 5.1(b) shows the superconducting transition of one prototypical device, with

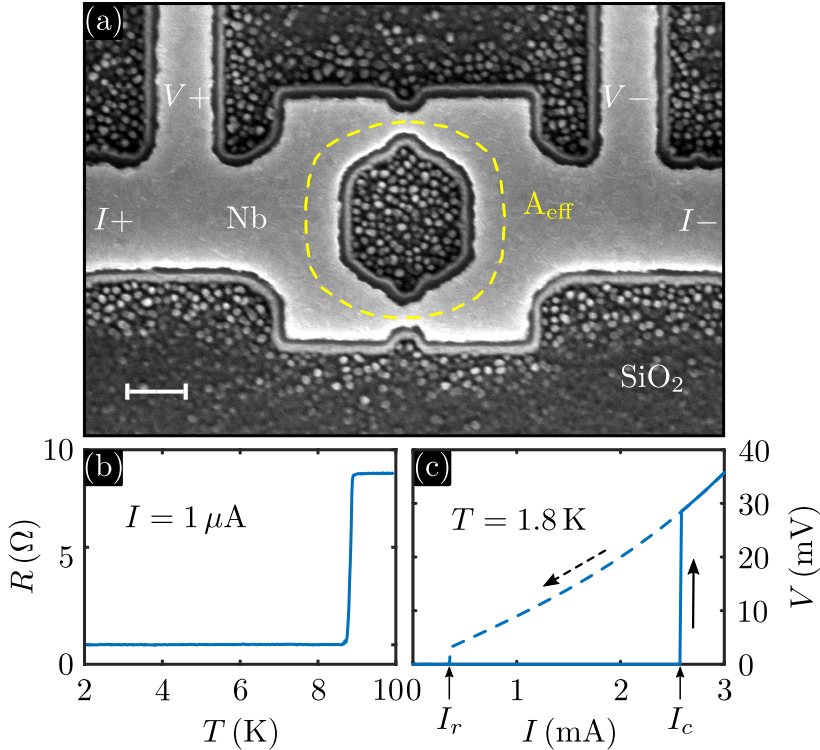


Figure 5.1 – SEM image of the pristine Nb nanoSQUID S1 (a). The scale bar corresponds to 200 nm. Panel (b) shows the superconducting transition of the device whereas in panel (c) the current-voltage characteristic at 1.8 K is shown. The arrows indicate the sweep direction of the bias current. In panel (a), the yellow dotted line indicates the effective area A_{eff} of the nanoSQUID.

resistance R , using a dc bias current of $1 \mu\text{A}$. The onset of the superconducting transition defined by the temperature T at which $R(T)/R_{10\text{K}} = 0.9$, with $R_{10\text{K}}$ the normal state resistance of the device at $T = 10 \text{ K}$, is located at $T_c = 8.87 \text{ K}$. A typical low temperature current-voltage characteristic $V(I)$ at zero magnetic field $B = 0 \text{ mT}$ and $T = 1.8 \text{ K}$ is shown in Fig. 5.1(c). As the current bias is gradually increased from zero, the voltage across the device is initially zero and switches abruptly to the resistive state at the critical current I_c . After a switching event, the device remains in the resistive state due to Joule heating. As the current is subsequently decreased the Joule heating is reduced and the device switches back to the zero-voltage state at the so called re-trapping current $I_r \leq I_c$.

The normal state resistance of the nanoSQUIDS exhibits an approximately linear temperature dependence with a thermal coefficient $\alpha = 8.5 \times 10^{-3} \text{ K}^{-1}$ between $T = 10 \text{ K}$ and $T = 300 \text{ K}$ with a Residual resistivity ratio (RRR) $RRR \approx 3.2 \pm 0.2$, and a resistivity $\rho(10 \text{ K}) = 9.7 \mu\Omega\text{cm}$. Using the relation $\rho\ell = 3.72 \times 10^{-6} \mu\Omega\text{cm}^2$ for Nb [206], we can estimate a mean free path $\ell = 3.9 \pm 0.1 \text{ nm}$. This allows us to calculate the superconducting coherence length at zero temperature using the dirty-limit expression[7] $\xi(0) = 0.855\sqrt{\xi_0\ell} = 10.5 \pm 0.5 \text{ nm}$, taking $\xi_0 = 39 \text{ nm}$. In the case of weak-coupling amorphous superconductors in the dirty-limit [207], the magnetic penetration depth can be estimated as $\lambda(0) = 1.05 \times 10^{-3} \sqrt{\rho/T_c} \sim 114 \text{ nm}$.

5.3.2 Magnetic field dependence of the critical current

Fig. 5.2 shows the dependence of the critical current of the nanoSQUID on the applied magnetic field $I_c(B)$, at four different temperatures. The value of the critical current is determined from the measured $V(I)$ characteristics as a function of the applied magnetic field B , using a $1 \mu\text{V}$ criterion. For the range of explored temperatures, the $I_c(B)$ curves show a clear quantum interference effect with a periodicity $\Delta B = 5.34 \text{ mT}$, from which an effective area $A_{\text{eff}} = 0.387 \mu\text{m}^2$ roughly twice as big as the actual geometrical area of the inner hole $A_h = 0.185 \mu\text{m}^2$ is obtained. Calculations with the simulation tool 3D-MLSI [208], which solves the London equations for two dimensional current sheets, results in an effective area $A_{\text{eff}}^{\text{sim}} = 0.363 \mu\text{m}^2$ for a SQUID with dimensions similar to those of Fig. 5.1(a) and considering ideal flux focusing [209].

By solving the GL equations, it has been shown that for nanobridges longer than $\sim 3.5\xi(T)$, the CPR becomes double valued and progressively more linear [55, 56] (see section 1.3.1.3). For the typical geometrical lengths of the Dayem bridges explored in this chapter ($d \sim 100 \text{ nm}$), a linear CPR represents a reasonable approximation in the temperature range $T < 0.9 T_c$ [69]. Although the GL formalism is strictly valid only close to T_c , an almost linear CPR has been predicted for thin and long wires even at $T = 0$ (see Ref. [60] and references therein).

The $I_c(B)$ curve is composed of approximately linear segments and is multivalued within certain field ranges for $T = 1.8 \text{ K}$ and 3 K . This linear dependence of the critical current on the magnetic field and the multivaluedness have been observed previously [55, 56] and can be accounted for by the model proposed in Ref.[60]. In

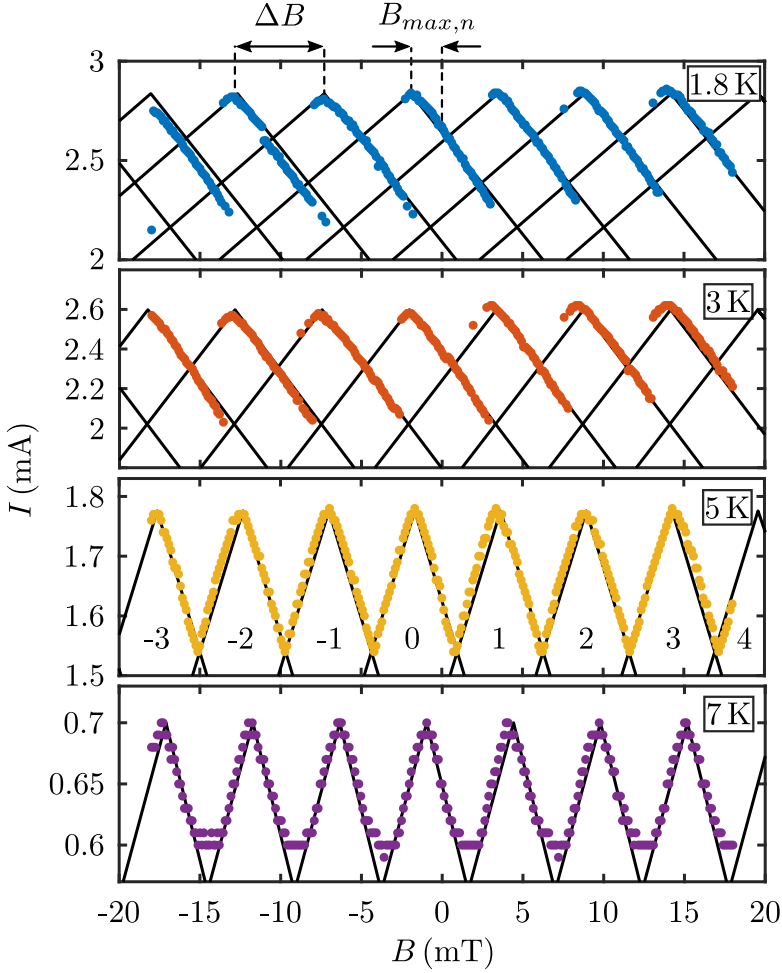


Figure 5.2 – Critical current of the pristine SQUID S1 as a function of the applied magnetic field for four different temperatures. Black lines correspond to the theoretical prediction assuming a linear current-phase relation according to the model described in Ref. [60]. The numbering from $n = -3$ to $+4$ in the panel corresponding to $T = 5$ K, indicate the vorticity. The fitting parameters obtained from the simulations are listed in Table. 5.1.

this model, we assume that each Dayem bridge can be described by a linear CPR:

$$I_j(\Theta_j) = I_{cj} \frac{\Theta_j}{\Theta_{cj}}, \quad (5.1)$$

where the index $j = 1$ or 2 indicates the Dayem bridge number, I_j is the corresponding supercurrent, I_{cj} is the critical current, and Θ_j is the gauge invariant phase difference of the macroscopic wavefunction taken between the end points of the j -th Dayem bridge. Further, Θ_{cj} is the critical phase difference at which the supercurrent reaches its maximum possible value and corresponds to the value above

which the Dayem bridge switches to the dissipative state. We additionally assume that the critical current of each Dayem bridge is independent of the magnetic field as expected for the small bridge area and consistent with the experimental observation that the critical current of our nanoSQUIDs oscillates with B around a field independent mean value. As the order parameter must be single valued, the total accumulated phase around the superconducting loop must be an integer multiple of 2π :

$$\Theta_1 - \Theta_2 + 2\pi \frac{B}{\Delta B} = 2\pi n, \quad (5.2)$$

where n is the vorticity (i.e. the winding number of the macroscopic wavefunction) of the SQUID loop.

The total critical current of the nanoSQUID, $I_c(B)$, is determined from Eq.(5.1)-(5.2) as the smallest total applied current $I = I_1 + I_2$ at which the phase difference across either bridge reaches its critical value $\Theta_j \geq \Theta_{cj}$. In addition to the approach presented in Ref. [60], we introduce two additional constraints allowing us to reduce the number of fitting parameters to only two (I_{c1} and Θ_{c1}) instead of four (I_{cj} and Θ_{cj} , $j = 1, 2$). Firstly, note that the maximum critical current of the nanoSQUID, given by $I_c = I_{c1} + I_{c2}$, takes place when both bridges reach their corresponding critical currents and critical phases. As we can determine I_c from the experimental data, this constraint allows us to eliminate one of the two critical currents as a fitting parameter. Secondly, the magnetic field value corresponding to the maximum of the $n = 0$ branch is given by:

$$B_{n=0} = \frac{\Delta B}{2\pi}(\Theta_{c2} - \Theta_{c1}), \quad (5.3)$$

(see Fig. 5.2). Eq.(5.3) allows us to eliminate one of the two critical phases differences as a fitting parameter. Note that Eq.(5.3) indicates that a shift of the $I_c(B)$ curves along the B -axis results from an asymmetry in Θ_{cj} for the two junctions. The results of the fitting procedure are depicted by solid black lines in Fig. 5.2 and the corresponding fitting parameters are shown in Table 5.1. The multivalued character of the $I_c(B)$ curve at low temperatures is properly captured by the model and results from the fact that different values of n gives rise to different critical current branches [60].

This model further assumes that the response is dominated by the kinetic inductance. A first order calculation of the geometric self-inductance of the loop gives ~ 0.7 pH [210]. For comparison, we can estimate the contribution of the kinetic inductance to be determined by $L_K = \mu_0 \lambda(0)^2 \int_{\Gamma} dr/A(r) \sim 1.9$ pH, where Γ is the curvilinear path with the coordinate r along one arm of the SQUID and $A(r)$ is the position dependent cross section of the conductor. Independently, $L_{Kj} = \frac{\Theta_{cj}\Phi_0}{I_{cj}2\pi}$, with $\Phi_0 \approx 2.0678$ mT μm^2 is the magnetic flux quantum, and therefore it can be deduced from the fitting parameters. The obtained values listed in Table 5.1 confirm that the kinetic energy indeed dominates the response of the nanoSQUID.

Table 5.1 shows that the asymmetry in critical current of the Dayem bridges $\alpha_I = |I_{c1} - I_{c2}|/(I_{c1} + I_{c2})$ is independent of temperature and remains around $\alpha_I \sim 0.05$ expected from geometrical inspection. The critical phase differences of

$T(\text{K})$	$I_{c1} \text{ (mA)}$	$\Theta_{c1} \text{ (rad)}$	$I_{c2} \text{ (mA)}$	$\Theta_{c2} \text{ (rad)}$
1.8	1.8 ± 0.5	20 ± 5	1.1 ± 0.5	18 ± 5
3	1.4 ± 0.2	15 ± 2	1.2 ± 0.2	13 ± 2
5	0.97 ± 0.08	12 ± 1	0.81 ± 0.08	11 ± 1
7	0.39 ± 0.03	8.5 ± 0.8	0.31 ± 0.03	7.4 ± 0.8

$T(\text{K})$	α_I	$L_{K1} \text{ (pH)}$	$L_{K2} \text{ (pH)}$
1.8	0.2 ± 0.3	3.7 ± 1.4	5.4 ± 2.9
3	0.1 ± 0.1	3.5 ± 0.7	3.6 ± 0.8
5	0.1 ± 0.1	4.1 ± 0.5	4.5 ± 0.6
7	0.1 ± 0.1	7.2 ± 0.9	7.9 ± 1.1

Table 5.1 – Fitting parameters for the $I_c(B)$ oscillations of the pristine state. The free fitting parameters are the critical current I_{c1} and phase Θ_{c1} of Dayem bridge 1. The values for Dayem bridge 2 are obtained from Eq.(5.2) and Eq.(5.3). $\alpha_I = |I_{c1} - I_{c2}|/(I_{c1} + I_{c2})$ indicates the asymmetry in critical currents and $L_{Kj} = \Theta_{cj}\Phi_0/(I_{cj}2\pi)$.

both nanobridges exceed the value of $\pi/2$ expected for tunnel junctions and decrease with increasing temperature. This observation is in agreement with the simulations carried out within the GL formalism by Hasselbach *et al.* [56]. Furthermore, according to [60], the effective length $d_{\text{eff}} \sim 4\xi\Theta_c/\pi > d$ for all temperatures. This result suggests an extended phase distribution spreading over a distance larger than the bridge's length [69].

5.4 Electroannealed devices

Let us now focus on the modification of the material properties at the constrictions by the controlled process of EA. Within this process, a bias voltage across the device is slowly swept up while simultaneously monitoring the decrease of conductivity until reaching a pre-established value. Sudden decreases of conductivity leading to a thermal runaway and eventually sample destruction are avoided by a reactive feedback loop [120]. Unlike EM [141], EA is mainly driven (but not only) by the Joule heating produced by high current densities only achievable in high melting-point materials such as Nb. We have recently reported the successful implementation of this approach [61] for producing targeted modifications of the superconducting properties in bow-tie Nb nanoconstrictions. In this chapter, this procedure is extended to two parallel constrictions following the protocol described in Ref.[120].

5.4.1 Targeted damage at the weak links

Performing the EA process at room temperature inside the chamber of a scanning electron microscope allows us to monitor *in situ* the structural changes occurring in the device under thermal stress. The upper left panel of Fig. 5.3 shows the values of the maximum resistance (R_{max}) obtained at a current I_{EA} and the minimum

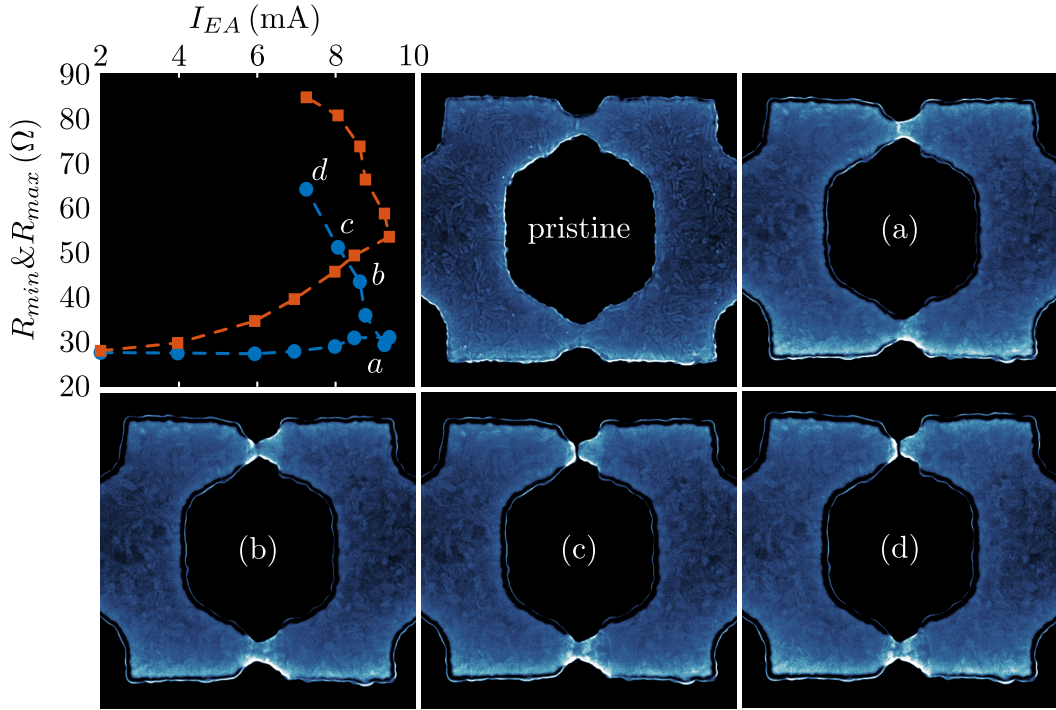


Figure 5.3 – SEM images obtained during the EA process for sample S3. The upper left panel shows the values of the maximum resistance (R_{max}) in red (squares) obtained at a current I_{EA} and the minimum resistance (R_{min}) in blue (dots) obtained after the current has been reduced to $1 \mu\text{A}$. The panels (a-d) show some selected SEM images after the device has been submitted to EA.

resistance (R_{min}) recorded after the current has been reduced to $1 \mu\text{A}$. For $I_{EA} \leq 8$ mA, the increase of R_{max} with increasing I_{EA} results primarily from Joule heating, as confirmed by the fact that no change of R_{min} is observed in this current range. The threshold beyond which irreversible modifications in the constrictions are induced corresponds to $I_{EA} = 8$ mA. For each EA step we have acquired SEM images immediately after the device has been submitted to thermal stress. A selected set of these images are shown in Fig. 5.3(a-d). The panel corresponding to the pristine sample, evidences a small asymmetry in the width of both bridges. Panel (a) shows that exceeding the 8 mA threshold current leads to clear material alteration localized at both bridges. These modifications are identified as significant brightness contrast in the SEM signal in comparison with the pristine state. The observed increased modifications on both bridges is directly correlated with an increase of the overall resistance of the device. Panel (b) shows the development of a nanogap in the narrower bridge, which becomes more apparent in panels (c-d). Additional data acquired from sample S2 confirm the observations and are available in appendix C.1. The fact that the gap is generated in the narrower constriction confirms previous findings [141] and indicates that the atomic migration regime driven by high

current density has been achieved. Clearly, during the EA process with the scope of tweaking the SQUID properties, the extreme situation of generating a gap in one of the weak links which would suppress the SQUID oscillations, is to be avoided.

An estimation of the local temperature in the weak links at the onset of EA of $T \sim 400 - 460$ K can be obtained from the $R(T)$ response of the sample and COMSOL simulations (see section 5.4.5). Interestingly this value does not seem to depend on the bath temperature. In other words, it is irrelevant whether the EA is performed under cryogenic conditions or at room temperature. Although Nb has an oxide coating consisting of amorphous and insulating Nb_2O_5 , which protects the superconductor against further oxidation from the atmosphere, above 400 K oxygen dissolves into Nb and deteriorates the superconducting properties [198, 211, 212], this can possibly explain the observed material alteration during the EA process. Additional AFM experiments are available for sample S5 in section 5.4.6 and confirm that the EA-induced changes are mostly localized at the two junctions of the SQUID.

5.4.2 Characterization of the superconducting properties of the weak links after EA

Fig. 5.4 shows the typical evolution of the normal state resistance and the superconducting transition temperature observed after subsequent EA processes carried out at 10 K. For the sake of clarity, a selected set of $R(T)$ curves measured with an applied current $I = 1 \mu\text{A}$ are shown in panel (a). The first observed effect after few initial EA steps (EA01 \rightarrow EA05, $I_{EA} \leq 8$ mA), consists in a modest improvement of the superconducting transition $\delta T_c \sim 150$ mK accompanied by a simultaneous decrease of the normal state resistance of the device (see region I in Fig. 5.4(b,c)). Although this effect is relatively weak, it is beyond the experimental error bar and consistently observed in all devices. It is worth noting that the improvement takes place in the whole device as indicated by a uniform shift of the entire $R(T)$ along the T -axis. A similar effect has been already reported in Ref. [61] and several possible reasons have been put forward such as degassing or thermally-induced stress-releasing. Further increasing the I_{EA} leads to the development of a second step in the $R(T)$ curve corresponding to the local modification of the critical temperature T'_c of the weak link (see region II in Fig. 5.4(b,c)). The observed deterioration in region II could be attributed to the high current density which deforms the constriction and induces local oxidation or alloying with the substrate. Adopting a criterion of 0.1Ω to determine T'_c , it is possible to track its evolution. The most striking result is a sudden improvement of the critical temperature (see region III in Fig. 5.4(b,c)) accompanied by a sharp decrease of the normal state resistance $R_{10\text{K}}$ for EA12 and EA13 (Fig. 5.4(c)). This behaviour has been carefully confirmed for sample S4 (see appendix C.2). We speculate that in this region, the Joule heating produced by the high current densities induces grain coalescence, grain growth and improved crystallinity. This in turn reduces the resistivity and enhances the mechanical properties (stress relaxation). As a consequence of this annealing process the critical current of the device decreases since the density of defects acting as pinning centers, decreases. Similar phenomena have been reported

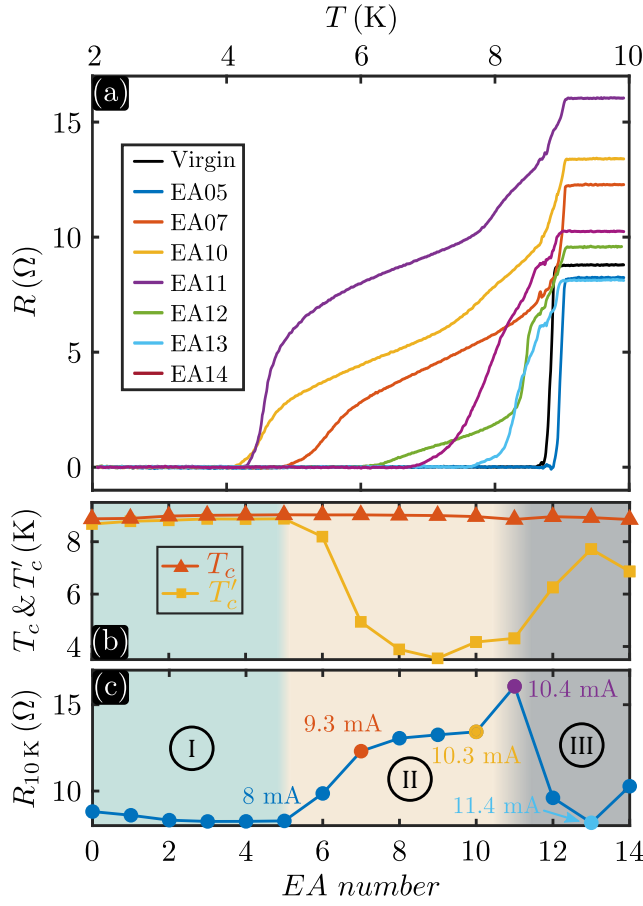


Figure 5.4 – (a) Selected set of $R(T)$ curves for sample S1 measured with an applied current $I = 1 \mu\text{A}$ after subsequent EA processes. (b) Evolution of the critical temperature of the weak link T'_c and the critical temperature of the arms of the SQUID T_c . (c) The normal state resistance R_{10K} as a function of the EA number. I_{EA} is given for some EA steps in the color corresponding to the panel (a). Regions I, II and III are described in the text.

in $\text{Mo}_6\text{S}_3\text{I}_6$ nanowires [213], Si microwires [214], and Cu microwires [215], and has been modelled numerically for the case of Pt nanowires [216]. What is particularly interesting in the present study is that rather minor changes in the mechanical and structural properties of Nb, have a sizeable impact on its superconducting properties. Further local material properties investigation (such as transmission electron microscopy or atom probe tomography [217]) are needed to confirm this interpretation. Eventually, further EA steps lead to a clear deterioration of the sample (see also sample S4 in the appendix C.2).

5.4.3 Critical current vs magnetic field oscillations after EA

Let us now analyse the SQUID critical current oscillations $I_c(B)$ when rendering the SQUID in different states using the EA process. Fig. 5.5 shows the $I_c(B)$ curves obtained after the last EA step (EA14) at three different temperatures together with the fits using the model described in section 5.3.2. The fitting parameters are shown in Table 5.2. After EA14, the asymmetry in critical currents increases with temperature and is comparable to the values obtained for the pristine nanoSQUID. In contrast to that, the critical phase differences are considerably smaller than those observed in the pristine SQUID, indicating a significant decrease of the effective length of the weak links [60]. Moreover, the critical phase differences for both Dayem bridge arms are almost identical, which is consistent with the observation that the $I_c(B)$ curves are centered around zero field as expected from Eq.5.3. Given the decrease in d_{eff} and that $L_K(T) = \mu_0 \lambda(T)^2 d_{\text{eff}} / A$, the significant increase in kinetic inductance implies, as expected, a reduced cross section of the constriction and a diminished density of superconducting carriers. It is worth noting that additional experiments have been undertaken on sample S4 to monitor the evolution of the coherence length over the EA steps (see section 5.4.7) which showed minor changes in ξ . By comparing Fig. 5.2 with Fig. 5.5, we observe that the global effect of EA is

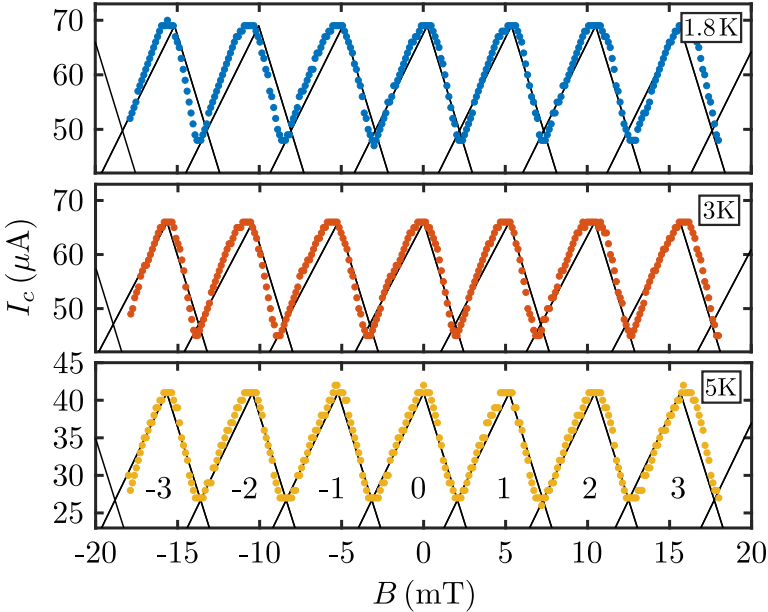


Figure 5.5 – Critical current of the SQUID as a function of the applied magnetic field for three different temperatures after EA14 (sample S1). The parameters of the simulations are listed in Table. 5.2. The numbering from $n = -3$ to $+3$ in the panel corresponding to $T = 5$ K, indicate the vorticity.

to significantly reduce the critical current and its oscillation amplitude with respect to magnetic field. Fig. 5.6 shows the evolution of the maximum value of the critical

current I_c^{max} along with the relative peak-to-peak modulation amplitude $\Delta I_c/I_c^{max}$ during successive EA steps for $T = 5$ K. We observe that during the first four EA steps the critical current of the SQUID exhibits a 2.5% rise concomitant with the slight resistance decrease and T'_C increase shown in Fig. 5.4. From the sixth

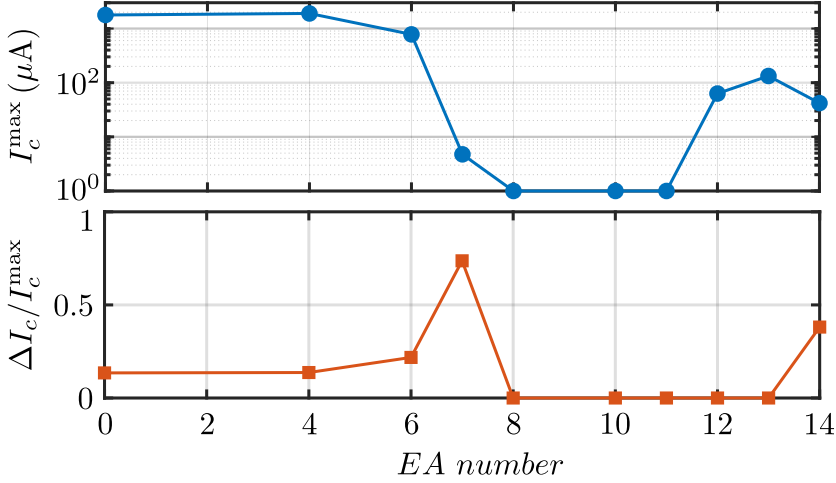


Figure 5.6 – Maximum value of the critical current I_c^{max} (a) along with the relative peak-to-peak amplitude oscillation $\Delta I_c/I_c^{max}$ (b), after each EA step for $T = 5$ K (sample S1). EA numbers with no data point correspond to situations with no measurements.

EA step the critical current displays a significant global reduction until reaching EA08 where both the critical current and its oscillations disappear. Thereafter, the critical current is restored to a significant value for EA12 to EA14 while the relative peak-to-peak modulation amplitude remains zero until before the last EA step. The fact that at EA13 the critical current has been substantially recovered without however exhibiting critical current oscillations, suggests that only one junction has resurrected.

T (K)	I_{c1} (μA)	Θ_{c1} (rad)	I_{c2} (μA)	Θ_{c2} (rad)
1.8	41 ± 5	5 ± 1	27 ± 5	6 ± 1
3	42 ± 5	5 ± 1	24 ± 5	5 ± 1
5	25 ± 3	4 ± 1	16 ± 3	4 ± 1
T (K)	α_I	L_{K1} (pH)	L_{K2} (pH)	
1.8	0.2 ± 0.1	40 ± 9	73 ± 18	
3	0.3 ± 0.1	39 ± 9	68 ± 20	
5	0.2 ± 0.1	53 ± 15	82 ± 26	

Table 5.2 – Fitting parameters for the $I_c(B)$ oscillations of the nanoSQUID after EA14. The parameters definitions are the same as in Table 5.1.

5.4.4 Thermal regimes and retrapping

As shown in Fig. 5.1(c) the pristine Nb nanoSQUIDS exhibit strongly hysteretic current-voltage characteristics. This is an unwanted feature limiting their flux resolution and operation speed. Unlike SQUIDS based on tunnel-barrier Josephson junctions, where the hysteresis results from the junction capacitance, in Dayem bridges the hysteresis arises from Joule heating. Fig. 5.7(a) shows the temperature dependence of the critical current $I_c(T)$ obtained by sweeping up the applied current, together with the retrapping current $I_r(T)$ obtained by sweeping down the

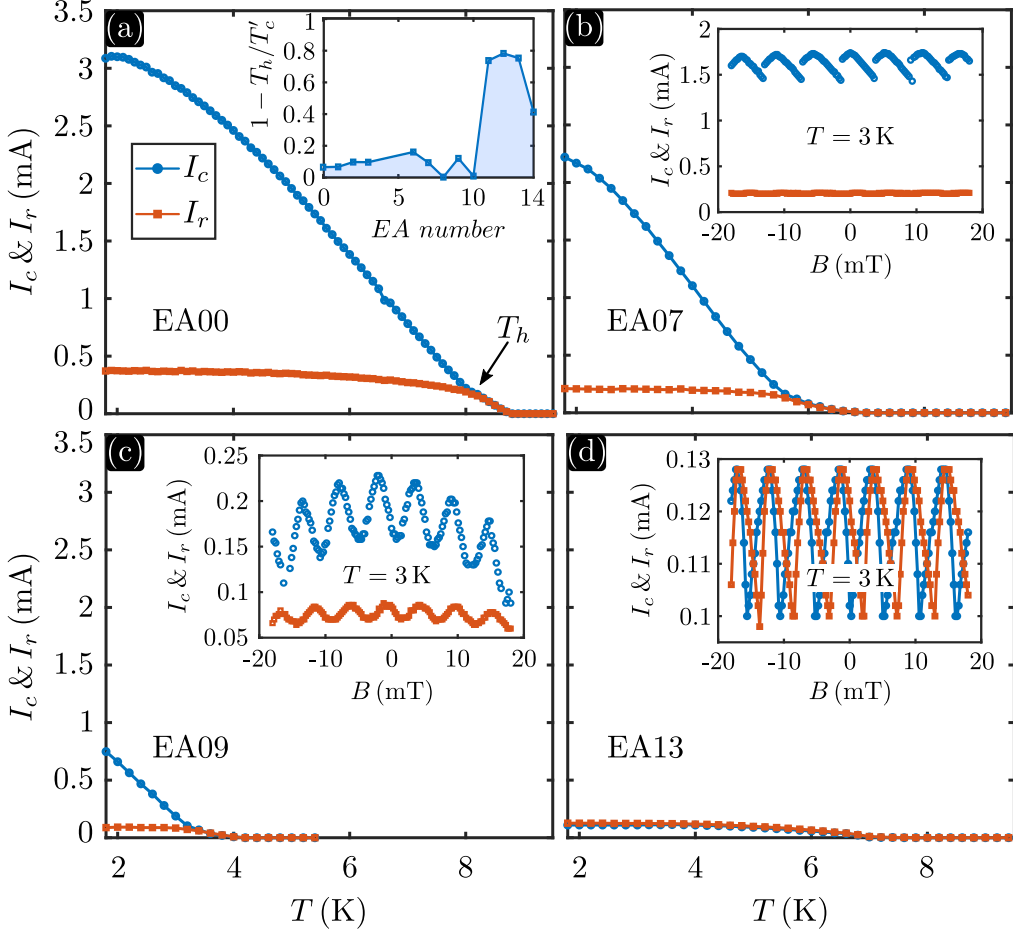


Figure 5.7 – Critical current I_c and retrapping current I_r of sample S4 as a function of temperature for the pristine sample (a), after EA07 (b), EA09 (c) and EA13 (d). The temperature above which the current-voltage characteristics become reversible, T_h , is indicated in panel (a). The blue coloured area in the inset of panel (a) shows that the range where the SQUID can be operated in the dissipative state is increased by EA process at expense of reducing I_c . The insets in panels (b-d) show $I_c(B)$ and $I_r(B)$ for the corresponding EA step.

applied current. There is a narrow temperature region $T_h < T < T_c$ where the $V(I)$ characteristic is nonhysteretic and the nanoSQUID can be operated in dissipative mode. By performing successive EA processes, it is possible to enhance the relative temperature range $1 - T_h/T'_c$ of nonhysteretic response, as shown by the blue coloured area in the inset of Fig. 5.7(a). This enlargement of the nonhysteretic regime comes at expense of reducing the critical current of the device. For the sake of illustration, panels (b-d) of Fig. 5.7 show the evolution of $I_c(T)$ and $I_r(T)$ at different EA steps (main panels) along with the SQUID oscillation at the indicated temperatures. Remarkably, no compromise is made on the critical temperature of the weak link T'_c which, on the contrary, is largely increased by the EA process compared to intermediate EA steps, as shown in Fig. 5.4(c). This is a truly striking and unique property of the electroannealed nanoSQUIDs. Note that SQUID oscillations are absent for the retrapping current in Fig. 5.7(b) indicating that the local temperature at the weak link is above T'_c due to the formation of a hot spot. However, clear SQUID oscillations of the retrapping current after EA09 indicate that the local temperature at the weak link does not exceed T'_c [204, 218]. Recently, a time dependent thermal model for a weak link made of a superconducting constriction was proposed by Gupta *et al.* [219]. The analysis of the $I_r(T)$ for our Nb

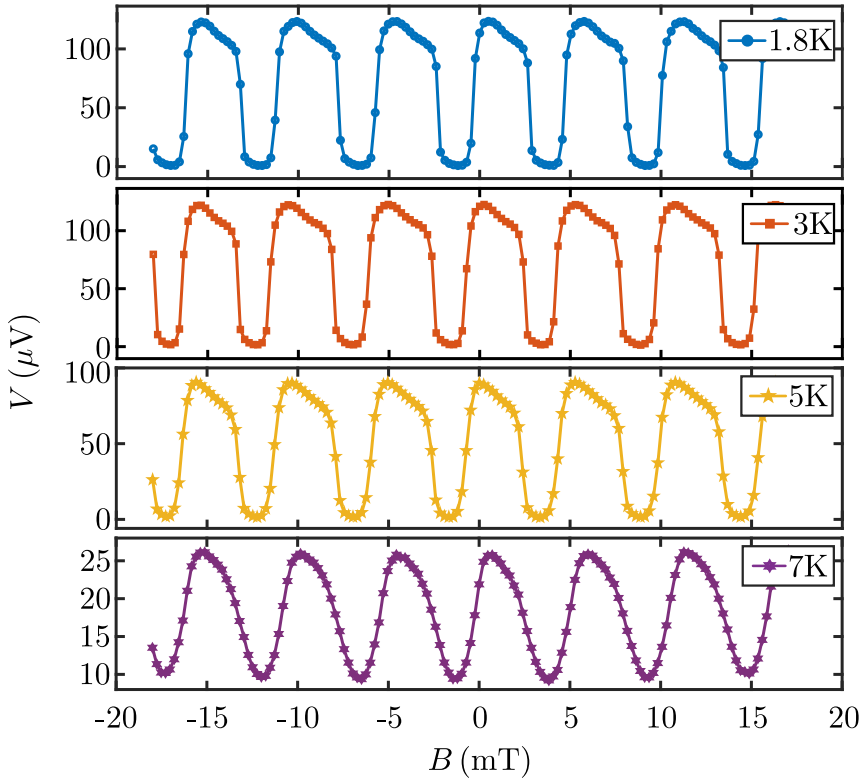


Figure 5.8 – Voltage oscillations observed for sample S4 after EA13. The bias currents are 132 μA , 130 μA , 104 μA and 30 μA for $T = 1.8$ K, 3 K, 5 K and 7 K, respectively.

nanoSQUIDS based on this model is discussed in section 5.4.8.

Practical SQUIDS are operated in the dissipative state as magnetic field sensor where the device produces an oscillating output voltage as function of the applied magnetic flux. In the early stages of EA, the fully resistive state generated by the high critical current and the hot spot formation prevent the device to present voltage oscillations. As a result of the EA process, the decrease of the critical current allows the SQUID interference to persist in the voltage state. Fig. 5.8 shows the voltage oscillations obtained after EA13. This result illustrates the potential of EA protocol to improve the properties of a SQUID and to switch from a hysteretic behaviour to a nonhysteretic nanoSQUID.

5.4.5 Finite Element Method simulation

Considering the non-trivial geometry of the system, the temperature inside the SQUID at low bath temperature for increasing current during the Joule heating regime has been estimated by the FEM based simulation software COMSOL [220]. The model assumes the 50 nm-thick Nb sample in contact with a 100 nm silicon oxide layer on top of a pure 100 x 100 x 30 μm^3 silicon wafer. The software resolves the heat transfer equation :

$$\rho_m C \frac{\partial T}{\partial t} = \kappa \nabla^2 T + Q \quad (5.4)$$

with ρ_m the density in kg/m^3 , C the specific heat capacity in $\text{J}/(\text{kgK})$, T the temperature in K and κ the thermal conductivity in $\text{W}/(\text{Km})$. The last term in 5.4 is determined by the Joule heating

$$Q = \mathbf{J} \cdot \mathbf{E} = \rho \mathbf{J}^2 \quad (5.5)$$

with ρ the electrical resistivity in Ωm . For the stationary solution, the left hand side term of 5.4 vanishes. The parameters used in the simulations are summarized in Table 5.3. The thermal conductivity for Nb is taken from the bulk properties of the material. Although this value probably overestimates the real thin film value of κ [221], the increase in temperature was rather insensitive to this parameter.

	κ [W/(mK)]	ρ [$\mu\Omega\text{cm}$]	α [K^{-1}]
Nb	54	9.57	8.5×10^{-3}
SiO ₂	1.4	10^{23}	/
Si	130	1.22×10^6	/

Table 5.3 – Thermal conductivity, electrical resistivity and thermal coefficient as input parameters in COMSOL simulations.

The model includes a thermal contact at two interfaces between all three layers by forcing heat fluxes to obey:

$$q_{int} = -\mathcal{H}(T)(T_2 - T_1) \quad (5.6)$$

where q_{int} is the heat flux in W/m^2 from medium 1 to medium 2 and $\mathcal{H}(T)$ the temperature-dependent heat transfer coefficient in $\text{W}/(\text{K}\text{m}^2)$.

The main panel of Fig. 5.9 plots the evolution of the resistance as a function of current at a bath temperature $T_b = 10$ K. At low bias current, thermal dissipation is low and the temperature throughout the SQUID is homogeneous and equal to T_b . At larger currents the heat generation cannot be evacuated fast enough hence leading to an inhomogeneous temperature distribution and higher resistance. Since the temperature increases by several hundred of Kelvins during the EA process, a temperature dependence of the heat transfer coefficient $\mathcal{H}(T) = a + bT^3$ where $a = 2.99 \times 10^6 \text{ W}/(\text{m}^2\text{K})$ and $b = 12.6 \text{ W}/(\text{m}^2\text{K}^4)$ are determined in order to reproduce the experimental results. The spatial distribution of temperature, given in the inset of Fig. 5.9 for $I = 9$ mA at the end of the reversible Joule heating regime, shows a substantial rise of temperature in the entire SQUID (~ 400 K) and not only in the bridges (~ 460 K).

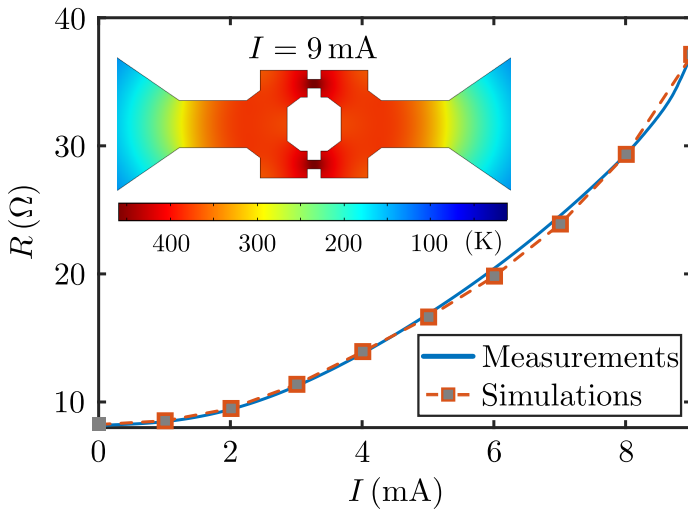


Figure 5.9 – Resistance rise as a function of increasing current (sample S1) for the current range where the $R(I)$ is solely affected by Joule heating. The blue curve represents the experimental data and red squares are results from FEM simulations. The inset shows the temperature profile in the bridge for $I = 9$ mA just before EA starts.

5.4.6 *In situ* atomic force microscopy

As can be seen in Fig. 5.3, the width of the lower bridge decreases from the pristine state to panel (c). This clear tendency to shrink leads us to believe that this phenomenon may be accompanied by overgrowth perpendicularly to the plane of the SQUID. In order to reveal these features, otherwise concealed by top-view SEM images, we used *in situ* AFM permitting a vertical resolution of 0.1 nm. Fig. 5.10 shows a set of AFM images acquired in tapping mode at ambient conditions and for

three consecutive stages of EA. As EA progresses and the resistance of the device increases, a clear overgrowth develops simultaneously in both junctions achieving a height excess of 17 nm. The observed overgrowth at the constrictions could also result from the formation of Nb_2O_5 since the AFM images were acquired at atmospheric condition unlike the SEM images presented in Fig. 5.3.

The AFM observations were carried out in a Multimode-8 atomic force microscope at room temperature and in air with standard silicon tapping mode probe with reflex aluminium coating on the detector side of the cantilever. A 10 nm radius of curvature tip with a cantilever of 42 N/m nominal spring constant was used with a lateral scan rate of 1 Hz at 512 lines.

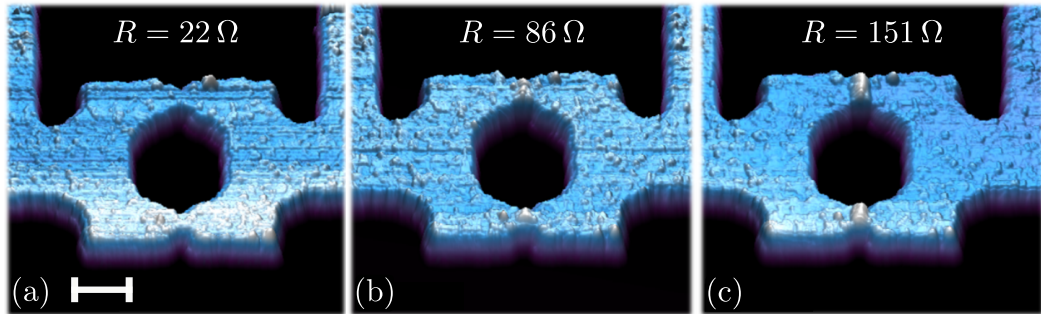


Figure 5.10 – AFM images taken after three consecutive stages of EA at room temperature (sample S5). The scale bar corresponds to 200 nm.

5.4.7 Coherence length evolution over EA

Since the EA process leads to a modification of the material properties as well as the geometry of the constrictions, it is important to know if the superconducting coherence length ξ at the weak links is also affected. In order to tackle this question, we measured the superconducting-normal phase boundary $B_{c2}(T)$ after each EA step. Fig. 5.11(a) shows the $R(B)$ curves measured at $T = 1.8$ K after four EA steps. Subsequent EA steps result in a reduced B_{c2} value of the weak link characterized by a kink in the $R(B)$ curves of EA08 and EA14 as indicated by the black arrows. This kink disappears for EA11, which corresponds to an EA step at almost maximum recovery, resulting in a $R(B)$ very close to the pristine state. A set of phase boundaries is shown in Fig. 5.11(b) together with the linear fits corresponding to $B_{c2}(T) = \Phi_0/(2\pi\xi(T)^2)$ with $\xi(T) = \xi(0)/\sqrt{1 - T/T_c}$ and $\Phi_0 \approx 2.0678 \text{ mT}\mu\text{m}^2$ is the magnetic flux quantum. Similarly as for the $R(T)$ curves, we used a criterion of $0.9R_N$ to determine B_{c2} of the SQUID arms and 0.1Ω for estimating B_{c2} at the weak links. Fig. 5.11(c) summarizes the results of the fitting and shows that the superconducting coherence length at the weak links $\xi'(0)$ remains nearly unaffected by the EA process up to EA10, whereas for further EA processes, $\xi'(0)$ tends to grow.

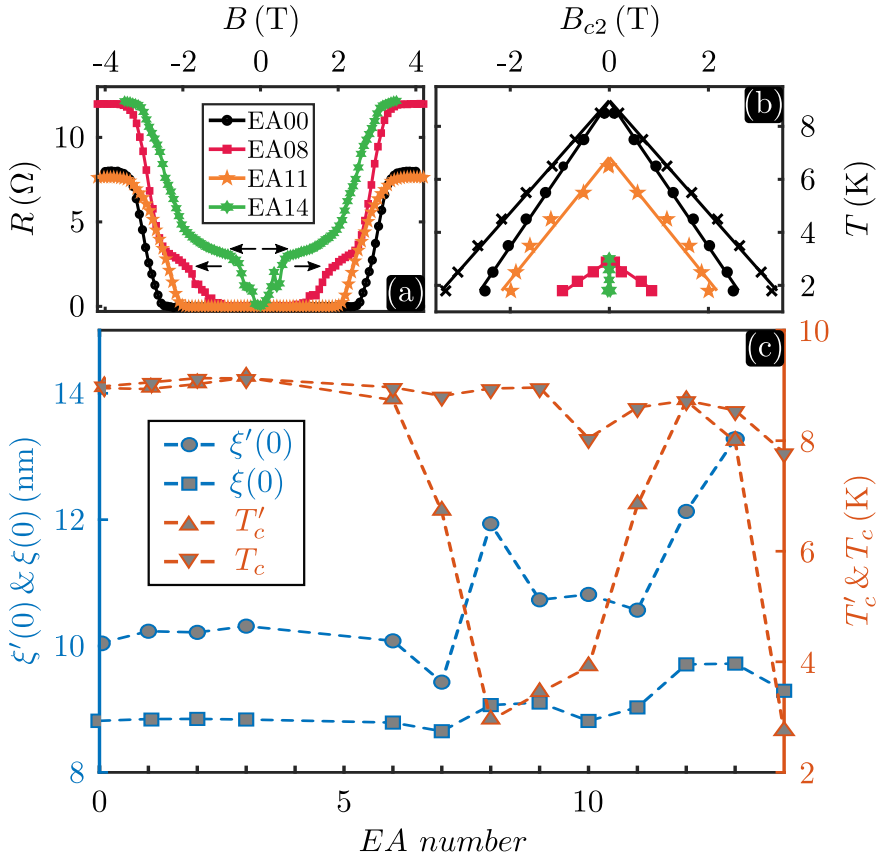


Figure 5.11 – (a) Resistance vs applied magnetic field B at $T = 1.8$ K and for four different stages of EA (sample S4). EA00 corresponds to the pristine state. (b) Phase boundaries $B_{c2}(T)$ for the SQUID arms (black crosses), the constriction in the pristine state (black circles), after EA08 (red squares), EA11 (orange stars) and EA14 (green stars). In panel (c) the critical temperature T'_c and the coherence length $\xi'(0)$ of the weak links are compared with those corresponding to the SQUID arms (T_c and $\xi(0)$) after each EA step.

5.4.8 Dynamic thermal model

Recently, a time dependent thermal model for a weak link made of a superconducting constriction was proposed by Gupta *et al.* [219]. The model describes several thermal regimes mainly determined by the heat evacuation efficiency. These authors identified a dynamic regime where a non-zero voltage exists across the weak link when its temperature stabilizes between the bath temperature and the superconductor's critical temperature. The model was successfully applied to Nb based nanoSQUIDs biased at different currents [204]. In this section we implement EA processing as a way to progressively affect the thermal properties of the weak link.

The thermal response of the system is ruled by a single parameter,

$$\beta_{DTM}(T_b) = \frac{R_N I_c^2(T_b)}{\mathcal{H}(T_c - T_b)}, \quad (5.7)$$

which quantifies the ratio between the Joule heating and the heat evacuation. In Eq.(5.7), R_N is the normal resistance of the two weak links in parallel, $I_c(T_b)$ is the critical current of the whole device at the bath temperature T_b and \mathcal{H} the heat loss coefficient in W/K from the weak link through the bulk electrodes and interfaces. Similar dimensionless parameters have been introduced in Ref.[109, 222]. For the case of a short weak link ($d \ll \xi$), and assuming a linear temperature dependence of the critical current and a temperature independent \mathcal{H} , the β_{DTM} parameter is linked to the retrapping current I_r and critical current I_c as follows [219]:

$$\left[\frac{I_r}{I_c} \right]^2 = \frac{\sqrt{1 + 4\beta_{DTM}^4} - 1}{2\beta_{DTM}^2}. \quad (5.8)$$

This equation allows us to determine β_{DTM} as a function of temperature as shown in Fig. 5.12(a). From the obtained $\beta_{DTM}(T_b)$ and the experimentally determined R_N , I_c and T_c , we can deduce \mathcal{H} .

The practical application of this model requires an estimation of the value of R_N . According to Ref.[72] the retrapping current $I_r(T) = 2\sqrt{2g(T)L_0T_c/R_N}$, with L_0 the Lorenz number, R_N the normal resistance of the two Josephson junctions in parallel and $g(T)$ a non-linear function of temperature related to the thermal conductivity in the superconducting state. Using only R_N as free fitting parameter we obtain $R_N \approx 6.2 \, \Omega$. Since EA modifies R_N , a new estimation needs to be done after each EA step. In order to do so, we assume, as confirmed by SEM and AFM measurements, that all EA modifications are located at the constrictions and that the affected area does not substantially change in size. The total normal resistance is simply given by $R = R_{\text{arms}} + R_N$ where R_{arms} is the resistance of the two arms of the SQUID in parallel. Under these assumptions, we are able to estimate the resistance of the arms from the pristine state: $R_{\text{arms}} = R_{\text{pristine}} - R_N = 1.72 \, \Omega$, which is assumed to remain invariant for subsequent EA processes. After each EA step, we measure R and deduce R_N as shown in the inset of Fig. 5.12(c). To obtain an estimation of the heat loss coefficient \mathcal{H} , we fit the experimental values of $\beta_{DTM}(T_b)$ with Eq.(5.7) using \mathcal{H} as single fitting parameter. Fitted curves assuming a temperature-independent \mathcal{H} are shown for EA00, EA07 and EA08 in Fig. 5.12(a), (b) and (c), respectively. For EA steps characterized by a high critical current (EA00 \rightarrow EA06), the model is unable to reproduce the $\beta_{DTM}(T_b)$ curve with a temperature-independent \mathcal{H} (Fig. 5.12(a)). The observed discrepancy between the theoretical model and the experimental data at low temperatures is likely due to the high value of the critical current which gives rise to substantial Joule heating for which the assumption of \mathcal{H} being temperature-independent is no longer valid. For EA07, the dynamic thermal model is able to capture already the main features of the $\beta_{DTM}(T_b)$ dependence using a temperature-independent \mathcal{H} parameter (Fig. 5.12(b)). From EA08 until EA10 the fitted curve perfectly overlaps the experimental values as

can be seen for EA08 in the main panel of Fig. 5.12(c) and the obtained $\mathcal{H}_{\text{opt}} = 11.9$ nW/K is of the same order of magnitude than the values reported by Biswas *et al.* [204] for Nb SQUIDS. After EA10, the sample becomes totally nonhysteretic and, according to Eq.(5.8), $\beta_{DTM} = 0$ for all temperatures, meaning that heat evacuation is always sufficient to avoid thermal runaway in the SQUID. As we will show below, the trend towards a nonhysteretic behavior is not caused by an improvement of \mathcal{H} but rather is a consequence of the rapid decrease of I_c . Assuming that the failure of the dynamic thermal model for the initial EA steps arises from the breakdown of the temperature independence of \mathcal{H} , we can instead calculate for each temperature and each EA steps, the value of $\mathcal{H}(T_b)$ directly given by eq.(5.7) (see Fig. 5.12(d)). The observed $\mathcal{H}(T_b)$ dependence indicates that the heat evacuation in the SQUIDS switches from a good heat evacuation regime before EA07 to a less effective one after EA07. Within these two regimes, $\mathcal{H}(T_b)$ seems to be rather independent of the EA number.

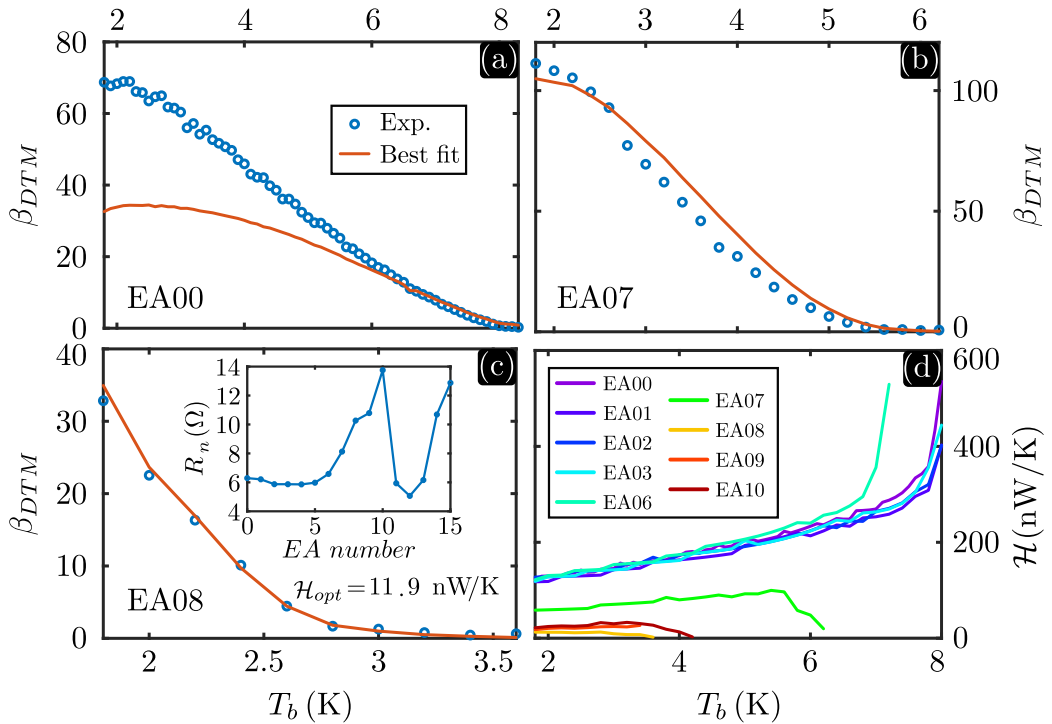


Figure 5.12 – Dynamic thermal model results for sample S4. (a), (b) and (c) give experimental values of β_{DTM} for EA00, EA07 and EA08 respectively and the corresponding optimum \mathcal{H}_{opt} . Inset of (c) indicates the evolution of the resistance of the two weak-links in parallel under the assumption cited in the text. (d) Evolution of $\mathcal{H}(T_b)$ for all EA steps. Note the green curve of EA07 that divide the EA steps in two distinguished thermal regimes.

5.5 Conclusion

In summary, we demonstrated the fabrication and *in situ* tuning of a nanoSQUID, by means of EA. We show that the EA process can be useful in a three-fold manner: (i) to improve the superconducting properties (higher T'_c , I_c and lower normal resistance) in the Josephson junctions for weak annealing currents, (ii) to suppress these superconducting properties of the weak links by intermediated applied currents, and (iii) to restore the superconducting properties with larger currents except for I_c which remain substantially lower than the value corresponding to the pristine state. We measured oscillations in the critical current as a function of magnetic field and demonstrated that the oscillation amplitude and asymmetry can be tuned over a broad range by successive EA processes. The overall tendency of EA to decrease the critical current makes it possible to modify the thermal behavior of a sample so as to reach a state with nonhysteretic current-voltage characteristics, while substantially preserving the critical temperature of the junctions T'_c . This property makes the EA technique particularly interesting and promising permitting easy adjustment and improvement of the properties of Nb SQUID sensors. We conclude that the proposed method is able to introduce modification and control of weak links at the nanoscale, with the possibility of adjusting its properties *in situ*, thus beyond the available state-of-the-art where weak links are either preformed and not tunable, or resulting from a rather involved nanofabrication procedure and further complex external control. The EA process should be applicable to refractory materials which can stand substantial heat, such as NbN and NbTi.

Chapter 6

Electroannealed four-branches devices

6.1 Introduction

Quantum computing has been a subject of intensive research for the past two decades. Several algorithms based on this technology have predicted resolution capabilities for certain problems that surpass solutions based on traditional computing [223–225]. The potential of this new technology was definitively proven in 2019 with the demonstration of the so called "quantum supremacy" [226]. The qubit, a fundamental unit of information manipulated by quantum computers, can be realized by numerous quantum systems such as cold atoms, trapped ions, or polarized photons. However, manipulation of such systems is complicated, and their properties, dictated by nature, are not modulable. On the contrary, current nanofabrication techniques using thin-film deposition allow for the design of superconducting circuits based on Josephson junctions whose energy levels are similar to those of an atom. As a result, these circuits are often referred to as artificial atoms [227], and represent a highly promising technology for current quantum computers. One of the major problems with qubits is their strong sensitivity to all sources of noise, leading to quantum decoherence. Minimizing noise sources is a technical and complex problem and strategies to mitigate them is of great importance [228]. Recently, it has been theoretically predicted that a particular superconducting system could host qubits while offering protection against quantum decoherence due to topological effects [157, 229]. These systems, called multiterminal Josephson Junctions, consist of $N > 2$ superconducting leads connected through a point-like normal scattering region, and the signature of the topological effect would be a quantification of conductance between the different terminals [158]. Since then, numerous attempts have been undertaken to demonstrate the presence of topological effects in multi-branched devices based on 2D Electron Gas (2DEG) [163, 165, 230] and graphene [162, 164, 231]. While promising, the fabrication steps required for creating such samples are involved and requiring sophisticated techniques. In this chapter, we propose the EA technique (see section 2.3) as a viable alternative for

creating normal scattering region in an initially homogeneous four-branches device. This technique is particularly appealing for its simplicity: requires conventional electronics, replaces involved multi-step overlay nanofabrication processing and offers a high degree of selectivity in narrow constrictions and junctions as shown in chapter 3.

As discussed in chapters 3, 4 and 5, the spatial extension of the affected volume can be revealed by AFM, SEM and KPFM. However these surface-sensitive techniques do not offer enough details of the inhomogeneous distribution of material's properties in the volume of the affected zone. In principle, this information is encoded in the resistive superconductive transition of the device and it could be extracted based on educated assumptions. In this chapter we reverse engineer resistance vs temperature curves obtained in four-terminal device to deduce the plausible distributions of resistivity and critical temperature throughout the entire device.

6.2 Electromigration of nanodevices

The investigated samples consist of Maltese cross shaped four-terminals junctions made of 50 nm-thick Nb on a sapphire (Sa) substrate. Details of the nanofabrication processing are the same as in section 3.4. A SEM image of one of the devices is shown in Fig. 6.1(a) along with the equivalent electrical diagram. The four arms of the cross are labeled 1 (west), 2 (north), 3 (east), and 4 (south). The total resistance of the i -th arm can be split in two contributions $R_i + R_{Li}$, with R_i representing the resistance between the center of the sample and the i -th voltage pad and R_{Li} is the remaining resistance of the i -th current lead. The circuitry shown in Fig. 6.1(a) corresponds to the particular case in which only R_1 is targeted for EA. Indeed, in this configuration, the voltage bias is connected in such a way to inject current through junctions 2, 3 and 4 and exiting it through junction 1. Due to current conservation (Kirchhoff's law) the current density is about three-times higher in junction 1 than in the other junctions thus permitting to modify the former without altering the latter. The voltage drop measured by the blue wiring in panel (a) will be able to witness eventual modifications of the resistance $R_{13} = R_1 + R_3$. Fig. 6.1(b) shows the evolution of the resistance R_{13} as a function of the current I flowing along the paths indicated by the white arrows in the inset. The increase of R_{13} as I increases has two origins, (i) a reversible contribution coming from the Joule heating combined with a finite resistance temperature coefficient, and (ii) an irreversible contribution arising from the material's properties modifications. It has been shown in chapter 3 that it is possible to isolate the individual junction resistances R_i by simple linear algebraic calculations. Fig. 6.1(c) shows the estimated R_i as a function of temperature for both the pristine state (EA00, blue curves) and after the first EA stage (EA01, red curves). The pristine state is characterized by a superconducting transition with a critical temperature $T_{c0} = 6.48 \pm 0.01$ K and a normal resistance $R_N = 0.58 \pm 0.03 \Omega$ for all the four junctions. Following the EA process, the resistance of junction 1 is increased by a factor of 7 whereas the other junctions remain intact. This finding

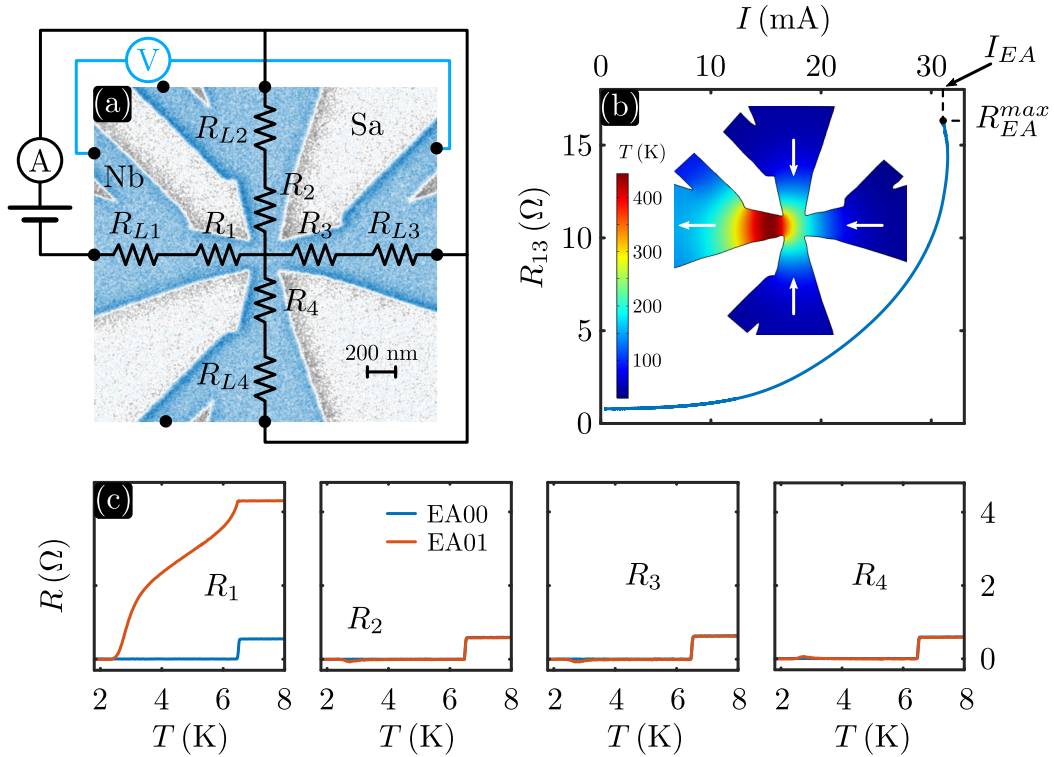


Figure 6.1 – (a) SEM image of one of the devices in pristine state EA00. The equivalent electrical lumped circuit represented by black lines corresponds to the wiring needed to target junction 1 via electroannealing. The resistance is measured between branches 1 and 3. A typical resistance evolution during EA is represented in (b) whose inset represent the spatial temperature distribution resulting from connections indicated in panel (a) for a current of 30 mA and starting at $T = 10$ K. The white arrows indicates the current direction in each terminal. The current crowding generates a significant increase of the temperature in junction 1 whose modification of the resistance R_1 is observable in the $R(T)$ measurements of the panel (c).

confirms the local character of the EA effect as well as its high degree of selectivity and control. Following the first EA step, the procedure is repeated three times for the remaining terminals 2 (EA02), 3 (EA03) and 4 (EA04) and these measurements will serve as input for the finite element modeling of the EA process.

6.3 Finite elements modeling

In this section, we describe plausible distributions of resistivity and critical temperature estimated from the $R(T)$ measurements. The model considers the Nb sample as a continuous medium of thickness 50 nm in contact with a sapphire substrate whose dimensions are given in Fig. 6.2(a). The geometry of the simulated system is obtained from a SEM image and is a reasonable approximation of the shape of the real devices. Since the temperature gradient is more pronounced in the center of the

sample due to current crowding, an accordingly denser mesh of nodes is chosen in the Nb layer (black framed insert in panel (a)) whereas a coarser mesh is introduced for the substrate (panel (a)). The simulation solves the stationary solution of the heat equation:

$$\nabla \cdot \mathbf{q} = Q, \quad (6.1)$$

where $\mathbf{q} = -\kappa \nabla T$ is the heat flux density in W/m^2 , κ is the thermal conductivity in $\text{W}/(\text{Km})$ and $Q = \mathbf{J} \cdot \mathbf{E}$ is the local Joule heating. $\mathbf{E} = -\nabla V = \rho \mathbf{J}$ is the electric field in V/m with \mathbf{J} the current density in A/m^2 . Equation (6.1) is solved for the substrate and the sample by considering a thermal conductivity $\kappa_{Sa} = 25 \text{ W}/(\text{Km})$ [232] and $\kappa_{Nb} = 54 \text{ W}/(\text{Km})$ [131] for sapphire and Nb, respectively. In view of the fact that the temperature variation of the sample is limited to a narrow range $300 - 550 \text{ K}$, it seems reasonable to assume these thermal conductivities as temperature-independent. Considering the fact that sapphire is a good insulator, the electric potential distribution is obtained only for the Nb layer by solving the continuity equation:

$$\nabla \cdot [(1/\rho)\mathbf{E}] = 0. \quad (6.2)$$

The sample exhibits an approximately linear temperature dependence of resistivity $\rho(x, y, T) = \rho(x, y, T_0)[1 + \alpha(T - T_0)]$, where $T_0 = 10 \text{ K}$, $\alpha = 56.2 \times 10^{-3} \text{ K}^{-1}$ is the experimentally determined resistance temperature coefficient and $\rho(x, y, T_0)$ is the EA dependent resistivity distribution in Ωm at 10 K . The boundary condition for eq. (6.1) sets the temperature at the bottom of the substrate to bath temperature T_{bath} while two conditions are needed for eq. (6.2), one concerning the current input $I_{in} = I_2 + I_3 + I_4$, and another for the current output $I_{out} = I_1$, as shown

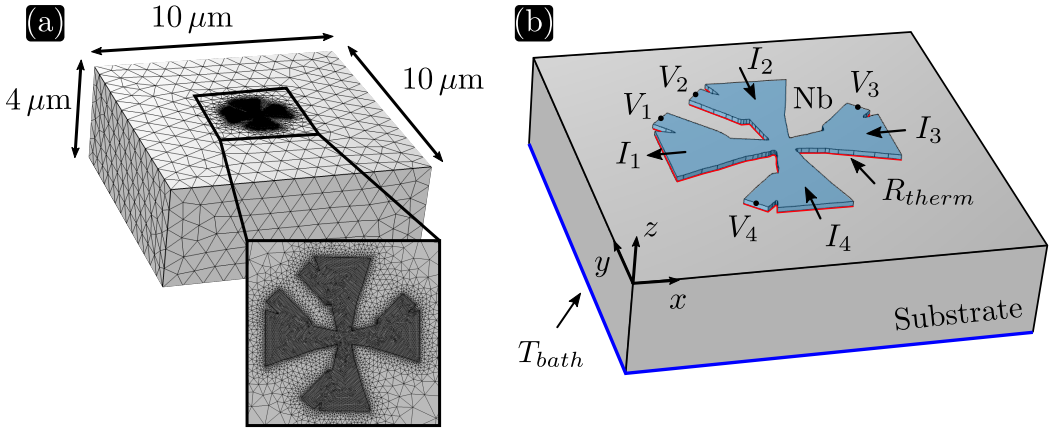


Figure 6.2 – (a) Dimensions of the geometry considered in the finite elements model. The substrate is modeled by a $10 \times 10 \times 4 \mu\text{m}^3$ box with a coarse mesh. The black frame shows a zoom of the Nb Maltese cross where a finer mesh is necessary. (b) The thermal resistance R_{therm} (red interface) takes into account the imperfect contact between the substrate (not to scale in this panel) and the Nb layer. A boundary condition specifies that the bottom of the substrate is at bath temperature T_{bath} (blue surface) while $I_{EA} = I_2 + I_3 + I_4 = I_1$ governs the EA process targeting junction 1.

in Fig. 6.2(b). The equations (6.1) and (6.2) are coupled by the Joule heating term Q and solved simultaneously. The imperfect contact between Nb and the substrate is taken into account through a temperature dependent thermal resistance $R_{therm}(T) = \Gamma/T$ [233] with a constant factor Γ , which hinders the heat removal towards the substrate. Thus, the heat flux density through the interface from the sample to the substrate q_{int} in W/m^2 can be expressed as:

$$q_{int} = (T_{Nb} - T_{Sa})/R_{therm}(T_{Nb}), \quad (6.3)$$

with R_{therm} in Km^2/W , and T_{Nb} and T_{Sa} are the temperatures of the sample and the substrate, respectively. As we have indicated in section 2.3, the structural modifications of the Nb film are mainly caused by the combined effect of Joule heating and current density. Therefore, we will assume in our model, that the current density $J_{EA}(x, y)$ and the temperature $T_{EA}(x, y)$ attained at certain point (x, y) during the EA process are the two parameters determining the local effective changes in resistivity and superconducting transition. Under this hypothesis, the $R(T)$ measurement obtained after an EA allows us to establish a relationship between the two $J_{EA}(x, y)$ and $T_{EA}(x, y)$ maps and both the resistivity $\rho(x, y)$ and the critical temperature $T_c(x, y)$ maps.

The implemented numerical algorithm is shown in Fig. 6.3 and proceeds as follows: at the first EA step, knowing the exact geometry of the device, the resistivity $\rho_{Nb} = 1.35 \mu\Omega\text{cm}$ of the sample in the pristine state is estimated based on its normal state resistance $R(10 \text{ K})$ (blue rectangle of Fig. 6.3). In this initial state, both the resistivity distribution $\rho(x, y) = \rho_{Nb}$ and the superconducting transition distribution $T_c(x, y) = T_{c0}$ are homogeneous. By adjusting the parameter R_{therm} (i.e. Γ) it would be possible to reproduce the experimental $R(I)$ curve within the reversible regime of the pristine sample [234]. However, a simpler approach consists in numerically applying the current I_{EA} corresponding to the maximum resistance R_{EA}^{max} reached during the EA step (see Fig. 6.1(b)) and determine the value of the new parameter R_{therm} in such a way that the temperature dependent resistance equals R_{EA}^{max} (yellow rectangle of Fig. 6.3). Note that at this stage the irreversible changes in the resistivity are not yet incorporated and all excess resistance is attributed to a change in the thermal contact. Having obtained R_{therm} we are now able to obtain the temperature distribution $T_{EA}(x, y)$ at $I = I_{EA}$ as shown for instance in the inset of Fig. 6.1(b). Since the degree of change on the material's properties depends on the local temperature $T_{EA}(x, y)$ reached during the EA, we assume that there is an inverse relationship between the temperature $T_{EA}(x, y)$ at $I = I_{EA}$ and the final local critical temperature distribution $T_c(x, y)$ that reproduces the experimental $R(T)$ curve after the EA process (purple rectangle of Fig. 6.3). The choice of the $R(T)$ curve will always be those of the junction experiencing the maximum current (i.e., the terminal undergoing the EA modifications). We make the assumption that the highest local temperature $T_{EA}(x, y)$ attained during the EA is associated to the largest depletion of the local critical temperature $T_c(x, y)$. For instance, for the experimental $R(T)$ curve shown in Fig. 6.4(b), the lowest critical temperature is labeled T_c^{min} and corresponds to the onset of the resistive state. At this temperature the entire device is superconducting but a singular region exhibiting a lower T_c ,

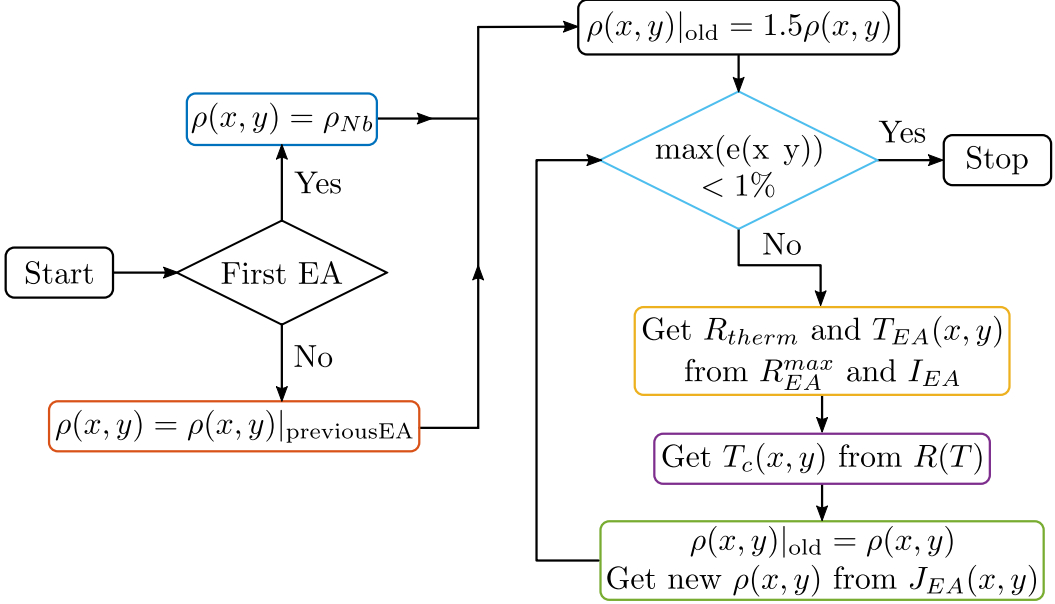


Figure 6.3 – Algorithm for determining the resistivity $\rho(x, y)$ and critical temperature $T_c(x, y)$ maps resulting from an EA step. The initialization of the resistivity map depends on the EA number. An iterative process (light blue diamond) modifies the resistivity map as long as the largest relative difference $\max(e(x, y))$ between two successive iterations for all (x, y) points exceeds 1%. The step providing the $T_c(x, y)$ map is detailed in Fig. 6.4.

which must naturally corresponds to the region where $T_{EA}(x, y)$ should have reached its maximum value T_{EA}^{max} . This is the initial point P in Fig. 6.4(c) from which we will be able to explicitly calculate the functional dependence $T_c = T_c(T_{EA})$.

In general, for an arbitrary annealing temperature $T_{EA}^* < T_{EA}^{max}$, we can identify the region A enclosed by the isothermal $T_{EA}(x, y) = T_{EA}^*$ (Fig. 6.4(a)), and knowing the resistivity distribution $\rho(x, y)$ calculate the resistance R^* associated to this region. From the computed R^* and using the experimental $R(T)$, we can hence determine the corresponding T_c^* at the border of the region A. In other words, the region outside A is superconducting ($T_c(x, y) > T_c^*$) and does not contribute to the dissipation where all the resistance come from the region A with $T_c(x, y) < T_c^*$. At the end of this iteration process we are able to faithfully reproduce the experimental $R(T)$ curve by assuming only changes in $T_c(x, y)$ but constant resistivity distribution $\rho(x, y) = \rho_{Nb}$. This is unrealistic and requires a subsequent modification of $\rho(x, y)$. To that end, we further assume that the resistivity is modified according to (green rectangle of Fig. 6.3):

$$\rho(x, y) = \rho_{Nb}[1 + c \Delta J(x, y)], \quad (6.4)$$

with $\Delta J(x, y) = J_{EA}(x, y) - J_{thres}$ if $J_{EA}(x, y) \geq J_{thres}$ and $\Delta J(x, y) = 0$ if $J_{EA}(x, y) < J_{thres}$, indicating that modifications in resistivity can only occur when

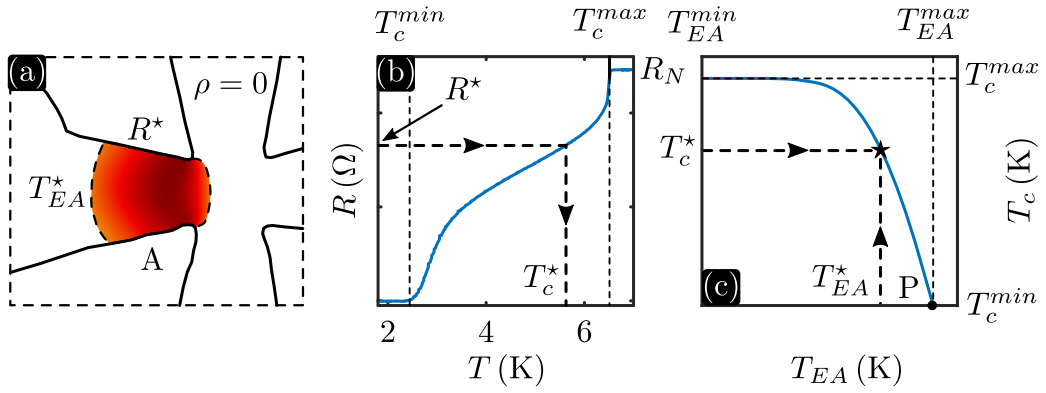


Figure 6.4 – (a) Spatial temperature distribution for $T(x, y) > T^*$ reached during the EA step. The red zone A contributes a resistance R^* to the total resistance by assuming zero resistivity in the white zone. (b) Measurement $R(T)$ used to establish the correspondence between R^* and the critical temperature T_c^* at the boundary of the zone A. (c) Relation between the temperature T reached during the EA and the local critical temperature T_c of the sample.

current density reaches a threshold current density J_{thres} . From the current density distribution at $I = I_{EA}$, J_{thres} can be estimated to be approximately equal to 2.2×10^{12} A/m² which is the value of the current density at the terminal biased by the total current I_{EA} . The parameter c is determined to fit the normal resistance $R(10\text{ K})$. Since the temperature estimation during EA, $T_{EA}(x, y)$, and critical temperature, $T_c(x, y)$, are dependent of the resistivity map, the complete procedure has to be repeated with the new resistivity. The iterative process repeats the complete step and stops once the error

$$e(x, y) = \frac{\rho(x, y) - \rho(x, y)|_{old}}{\rho(x, y)|_{old}} \quad (6.5)$$

between two successive iterations maps does not exceed 1 % (light blue diamond of Fig. 6.3) for any point (x, y) . Starting from the second EA step, the initial resistivity map is based on the result of the previous simulation (red rectangle of Fig. 6.3).

The results of the simulations for the first EA step are summarized in Fig. 6.5, where the resistivity and critical temperature maps are shown in panels (a) and (b), respectively. Due to current crowding, the edges of terminal 1 entrance are particularly affected (panel (a)), as evidenced by the local increase in resistivity by a factor of $\rho_{max}/\rho_{Nb} \simeq 80/1.35 = 59.3$. Note that the central region of the device remains really unaffected, while the damages extend approximately 150 nm inside junction 1. The distribution of T_c (panel (b)) follows a similar trend, but with less extensive variation compared to the resistivity. Although derived from a different geometry and performed under different conditions, the AFM measurements of section 3.3 show remarkable similarities with the simulated results, such as the localization of damages mostly on the edges of the electroannealed junction and the extension of damages further inside as one moves away from the center of

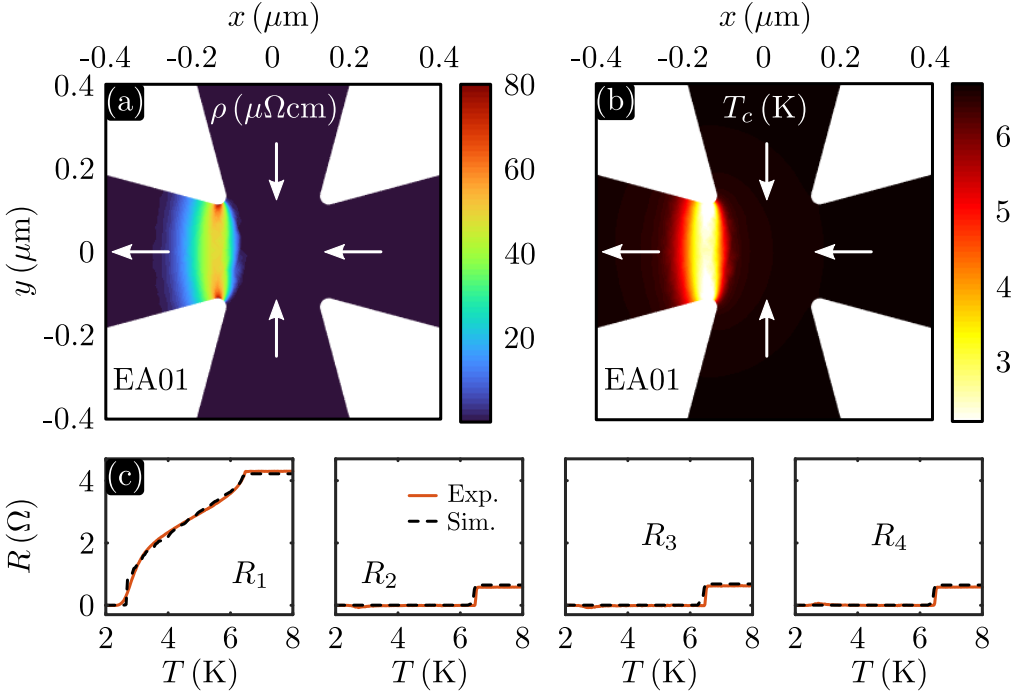


Figure 6.5 – Results of finite element simulations of the damages caused by the first EA step. The distributions of resistivity and critical temperature are shown in panels (a) and (b), respectively. The white arrows indicates the current direction in each terminal. Panel (c) displays the comparison between the experimental $R(T)$ measurements (red curves) and those obtained from the simulations (dotted black curves).

the device. Improving the model to consider the thermally activated nature of EA could enhance the accuracy of the simulations. Indeed, the hottest point in the temperature map during EA is located further inside the junction (see Fig. 6.1(b)), contrary to the current density, which necessarily reaches its maximum at the narrowest point of the targeted terminal. Nevertheless, the selectivity of the EA effects is well reproduced, as shown in panel (c) of Fig. 6.5, which shows the good agreement between the individual experimental $R(T)$ curves of each junction (red lines) with their counterparts from the simulation (dotted black lines). The results of the following three EA steps are shown in Fig. 6.6. For each EA step, the direction of the current in each terminal is indicated by the white arrows. The resistivity and critical temperature maps for EA02, targeting terminal 2, are depicted in panels (a) and (b) of Fig. 6.6, respectively. Here, weaker modifications are obtained due to a milder EA step compared to EA01, as shown in the $R_2(T)$ curve in panel (g) of Fig. 6.6. The resistivity is maximally increased by a factor of $50/1.35 = 37$, and the critical temperature of the terminal does not drop below 3.85 K. Additionally, we observe a propagation of modifications over a distance of ~ 70 nm, smaller than EA01, and the selectivity of the process according to the simulated damages is not as high as the one observed in the experimental results. Indeed inspecting $R_3(T)$

and $R_4(T)$ in panel (g) of Fig. 6.6, we notice that the normal resistances from the numerical results no longer perfectly overlap with the experimental measurements. This can be explained by modifications that affect the center of the device more

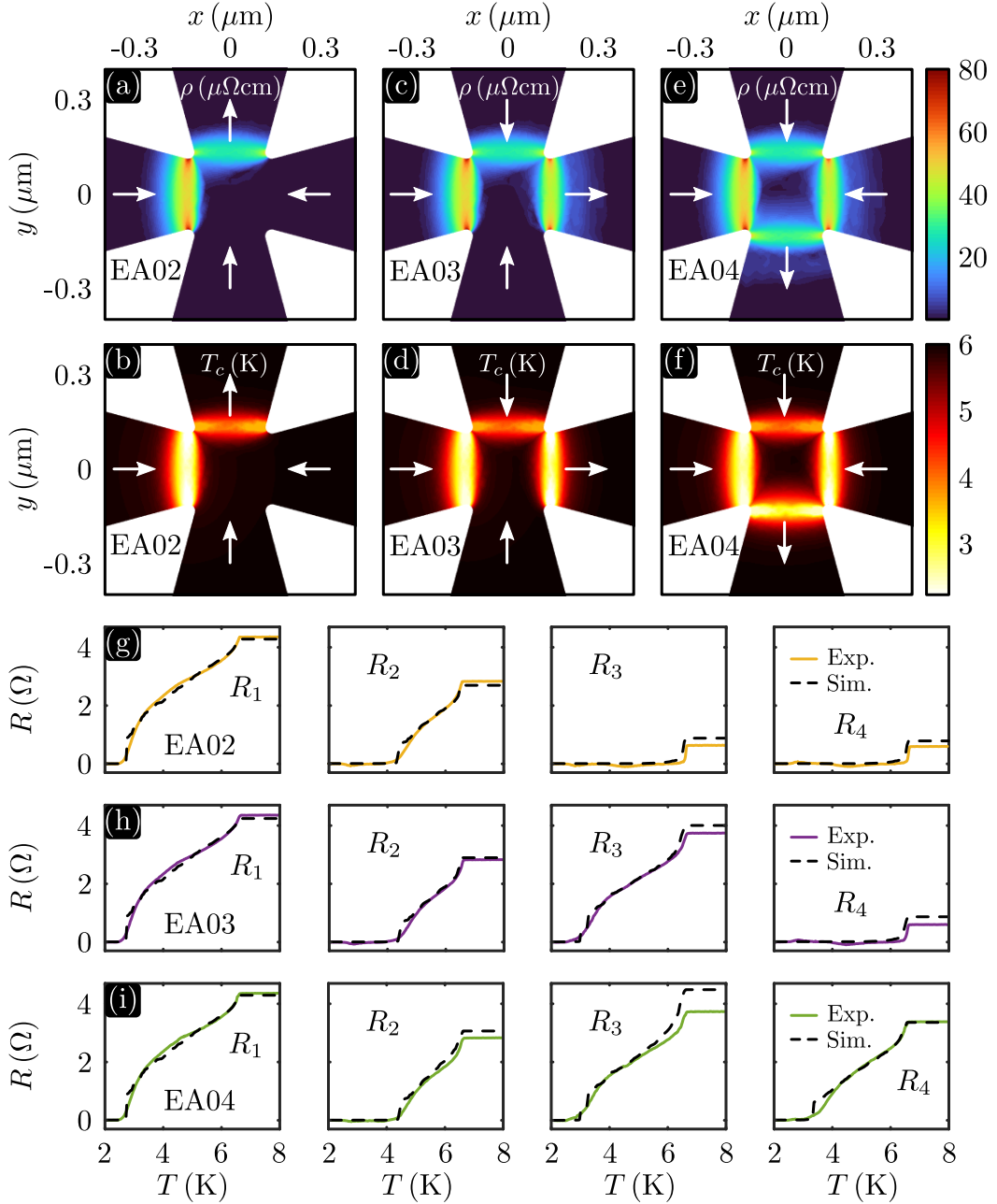


Figure 6.6 – Results of finite element simulations of the damages caused by the last three EA steps. Panels (a), (b), and (g) correspond to step EA02, panels (c), (d), and (h) correspond to step EA03, and panels (e), (f), and (i) correspond to step EA04.

than EA01, and as a consequence, they impact in the resistance of the other junctions. EA03 addressing terminal 3, and is presented in panels (c) and (d) based on the $R_3(T)$ curve in panel (h) of Fig. 6.6. The last step, EA04, is described in panels (e) and (f) of Fig. 6.6. As the EA steps progress, we observe increasingly significant modifications in the center of the device, thus impacting all terminals, as shown particularly in the $R_3(T)$ curve in panel (i). This is explained by the less homogeneous distribution of modifications as the EA steps proceed. The center of the device, being a better conductor than the terminals' entrances already modified by EA, has a higher current density than during EA01, where the current could distribute more uniformly.

6.4 Transport properties

In this section we present preliminary transport measurements for the same sample as the one considered in Fig. 6.5 and 6.6. Although a thorough understanding of these measurements is still lacking, they seem sufficiently stimulating to motivate further investigation. Transport properties are measured using the electrical diagram shown in panel (a) of the Fig. 6.7. Two independent perpendicular currents are chosen as positive from 1 to 3 for I_{13} and from 4 to 2 for I_{24} . Each current is

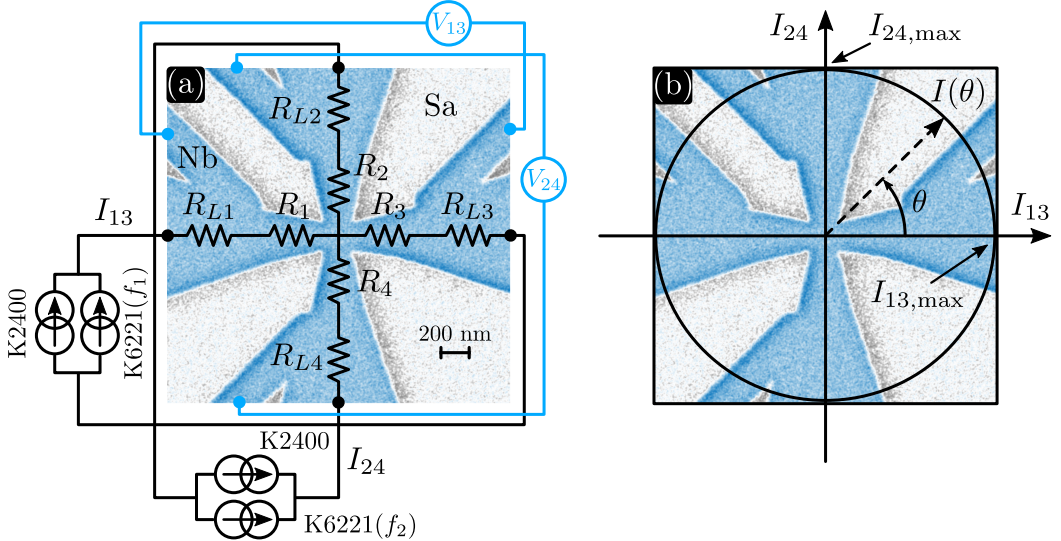


Figure 6.7 – (a) Configuration for measuring transport properties in a four-terminals device. Independent perpendicular currents I_{13} and I_{24} are each the sum of a DC contribution (K2400) and an AC contribution (K6221). Two different frequencies f_1 and f_2 are required to measure the differential resistance dV/dI independently across the voltage pads V_{13} and V_{24} (blue wiring). (b) Each current ramp starts at zero currents and follows a straight path in the (I_{13}, I_{24}) plane along a radius of length $I(\theta)$ and angle θ with respect to axis I_{13} . In general, $I_{13,max} \neq I_{24,max}$ and the explored current space is ellipsoidal.

the sum of DC and AC contributions for measurement of the differential resistance dV_{13}/dI_{13} and dV_{24}/dI_{24} by lock-in amplification using two frequencies $f_1 = 666$ Hz and $f_2 = 847$ Hz. We consider a current space (I_{13}, I_{24}) represented in panel (b) of Fig. 6.7 where each current ramp is a radius in current space oriented at an angle θ and of amplitude

$$I(\theta) = \frac{I_{13,\max} I_{24,\max}}{\sqrt{(I_{13,\max} \sin \theta)^2 + (I_{24,\max} \cos \theta)^2}} \quad (6.6)$$

which defines an ellipsoidal region in the current space. Unlike conventional hori-

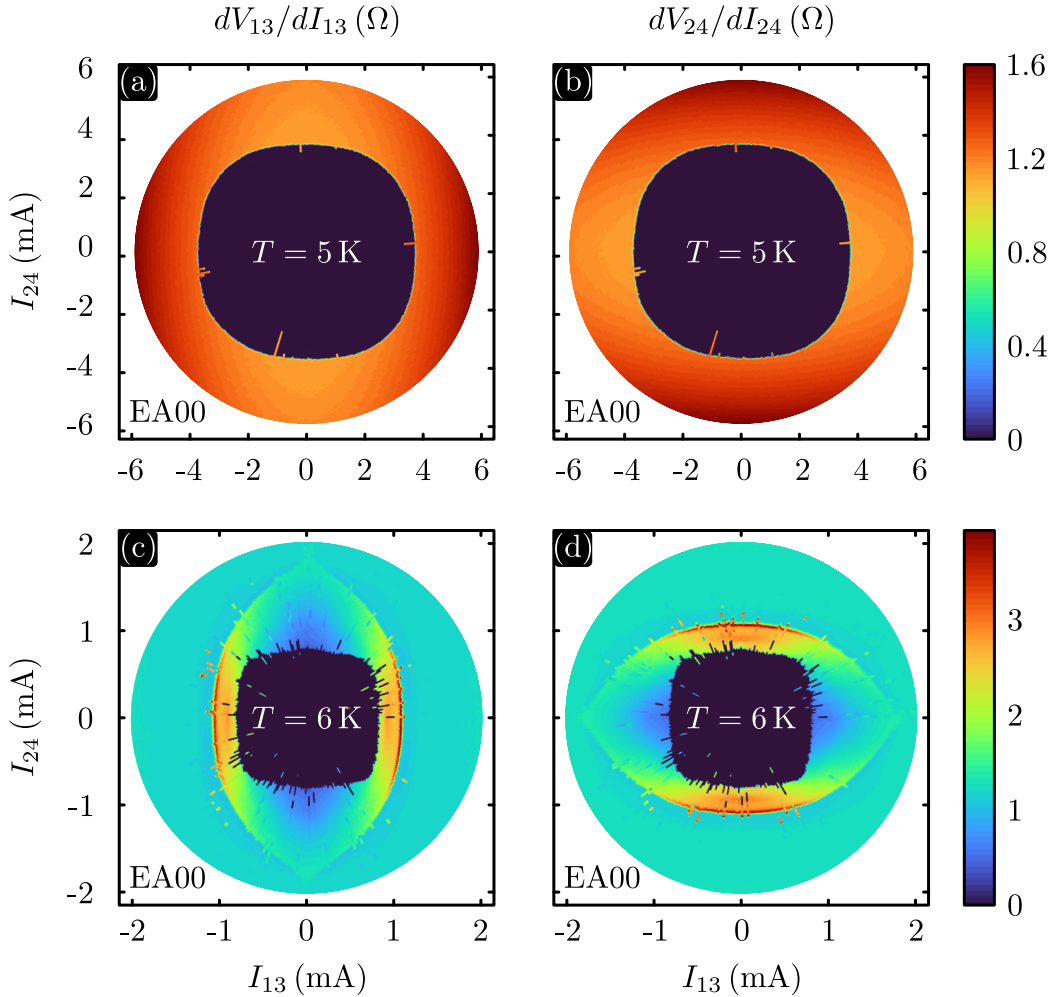


Figure 6.8 – Transport properties for the pristine state EA00. The maps show the differential resistance dV/dI at 5 K in the horizontal direction 13 (panel (a)) and in the vertical direction 24 (panel (b)). Panels (c,d) show similar measurements obtained at 6 K. Critical Current Contour (CCC)’s irregularity for panels (c) and (d) is due to slight cryostat’s temperature instability during measurement.

zontal or vertical scanning of the current space, the radial scanning mode systematically starts from the superconducting state in order to measure the critical current, which is much higher than the retrapping current due to the device's irreversibility. Pristine state EA00 measurements are shown in Fig. 6.8. Due to the high value of the critical current at $T = 1.8$ K ($I_c \sim 8.5$ mA), the bath temperature is set successively at 5 K (panels (a) and (b)) and 6 K (panels (c) and (d)) closer to the critical temperature $T_{c0} = 6.48$ K. To better understand the information contained in these graphs, Fig. 6.9 shows the dV_{13}/dI_{13} curve along the horizontal axis $I_{24} = 0$ from the origin to the maximum value $I_{13} = I_{13,\max}$ (blue curve, left axis) and its integral giving the voltage V_{13} (red curve, right axis). The two temperatures of Fig. 6.8(a,c) are considered in Fig. 6.9(a,b) respectively. At 5 K (panel (a) of Fig. 6.9), we observe

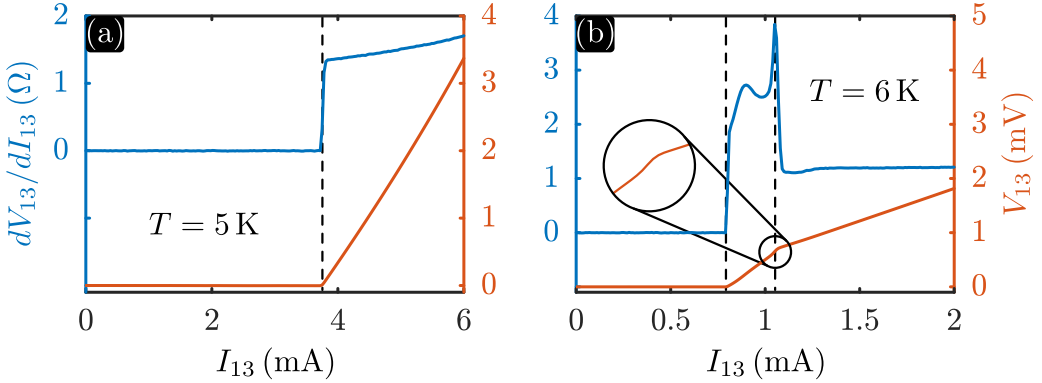


Figure 6.9 – Panel (a): dV_{13}/dI_{13} (blue curve, left axis) along the $I_{24} = 0$ axis of Fig. 6.8(a) from the origin to $I_{13} = I_{13,\max}$ and its integration V_{13} (red curve, right axis). Panel (b) shows the same curves, but for the Fig. 6.8(b). The circular zoom shows the increase in slope dV/dI as the whole device transitions to the normal state.

that after a sudden sharp increase around $I_{c,13} \sim 3.7$ mA (indicated by the dotted vertical line), the differential resistance increases permanently. As a result, the potential V_{13} (red curve) follows a parabolic behavior typical of Joule heating effect. Therefore, the two darker areas on the left and right of Fig. 6.8(a) can be understood as a consequence of the dominance of the device's thermal response. Note that these same areas are brighter in Fig. 6.8(b) indicating that the temperature increase along the $I_{24} = 0$ axis is mainly localized in terminals 1 and 3. Similar reasoning explains the behavior along the vertical axis $I_{13} = 0$ of Fig. 6.8(b), reflecting the device's 90° rotational symmetry. Globally, we note the absence of any abrupt variation in dV/dI outside the CCC. This suggests that the entire area measured by the four voltage pads is normal as soon as the CCC is crossed, and that the Joule heating effect is such that the temperature throughout the device is higher than the local T_c . The response of the device at 6 K in Fig. 6.8(c,d) shows a more complex behavior. Firstly, we see that the CCC, whose irregularity is due to a slight instability of the bath temperature, exhibits a squarish, indicating a weaker interdependence between the horizontal and vertical critical currents. As the superconducting zones

(inside the CCC) of Fig.6.8(c,d) are strictly identical, the critical current at 6 K is still sufficient to break the condensed state at the center of the device. However, we also observe the presence of a second jump in the differential resistance represented by the reptile iris like curve around the CCC, whose profile along the horizontal axis is shown in Fig. 6.9(b). The dotted line on the left indicates the critical current $I_{c,13} \sim 0.8$ mA while the second dotted line indicates the highest peak of dV_{13}/dI_{13} and a small jump of the voltage red curve as indicated by the circular zoom. Importantly, the current appears to be small enough to allow efficient heat dissipation, i.e. the differential resistance is constant after the right-hand peak. Consequently,

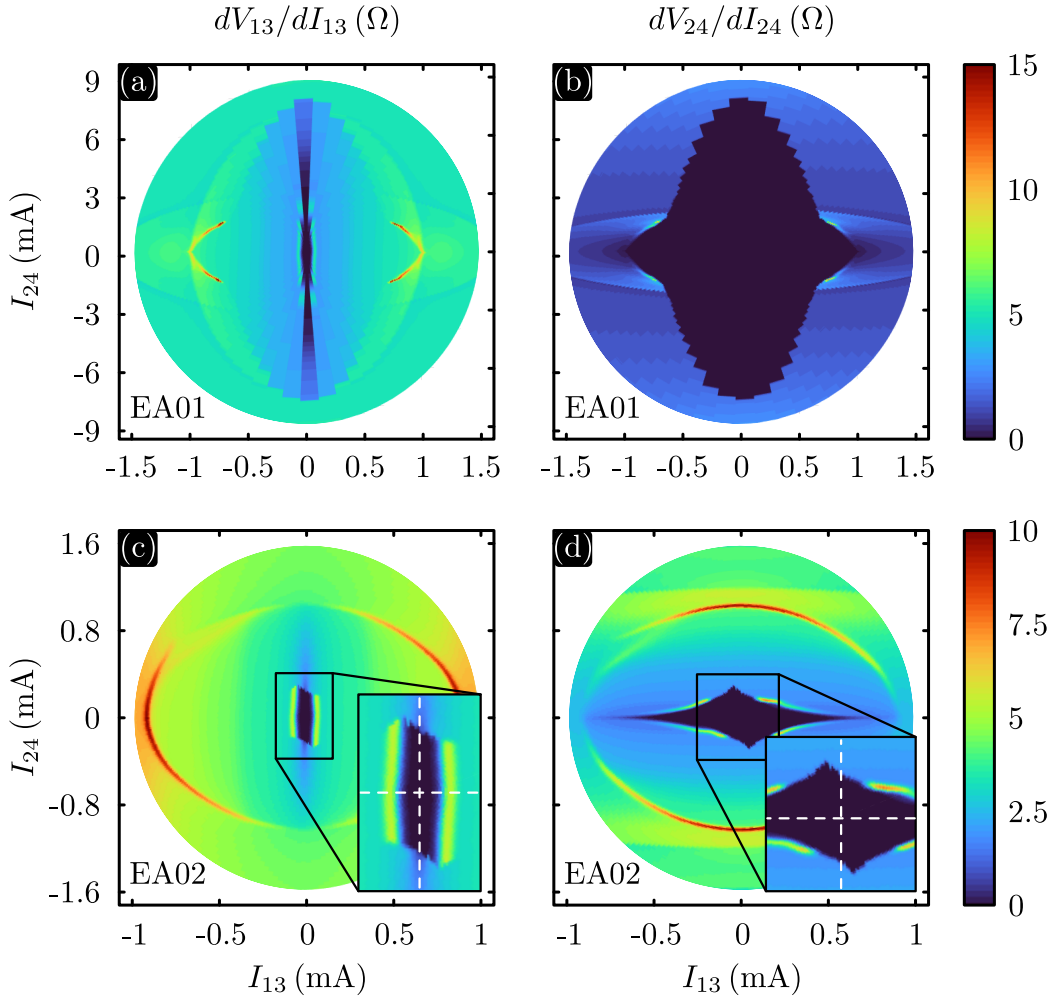


Figure 6.10 – Differential resistance for state EA01 (panels (a) and (b)) and state EA02 (panels (c) and (d)). The black boxes show a zoom of the central zone, where the intersection of the white dotted axes designates the origin of the current space. All measurements are made at $T = 1.8$ K. In contrast to Fig.6.8, note that $I_{13,\max} \neq I_{24,\max}$ and the current space is ellipsoidal.

the variations between the two vertical dotted lines cannot be attributed to the temperature coefficient α . The presence of such jump in the $V(I)$ characteristic in a long 1D junction in tin close to T_c was interpreted in Ref.[235] by the generation of phase slips inside the bridge. Using the $\rho l = 3.72 \times 10^{-6} \mu\Omega\text{cm}^2$ for Nb[206], and the resistivity $\rho_{Nb} = 1.35 \mu\Omega\text{cm}$ deduced from finite element simulations of section 6.3, we obtain an estimation of the mean free path $l \sim 27.6 \text{ nm}$. We then obtain an expression for the coherence length $\xi(6 \text{ K}) = 101 \text{ nm}$ where the coherence length at zero temperature is estimated in the dirty limit approximation[7] $\xi(0) = 0.855\sqrt{\xi_0 l}$, with $\xi_0 = 39 \text{ nm}$ the BCS coherence length for Nb. Therefore, our 200 nm wide bridge can be approximated to be in the 1D regime, and the second peak in the dV/dI curve is attributed to the presence of phase slips. The remainder of this section will therefore focus on the shape of the CCC, without paying much atten-

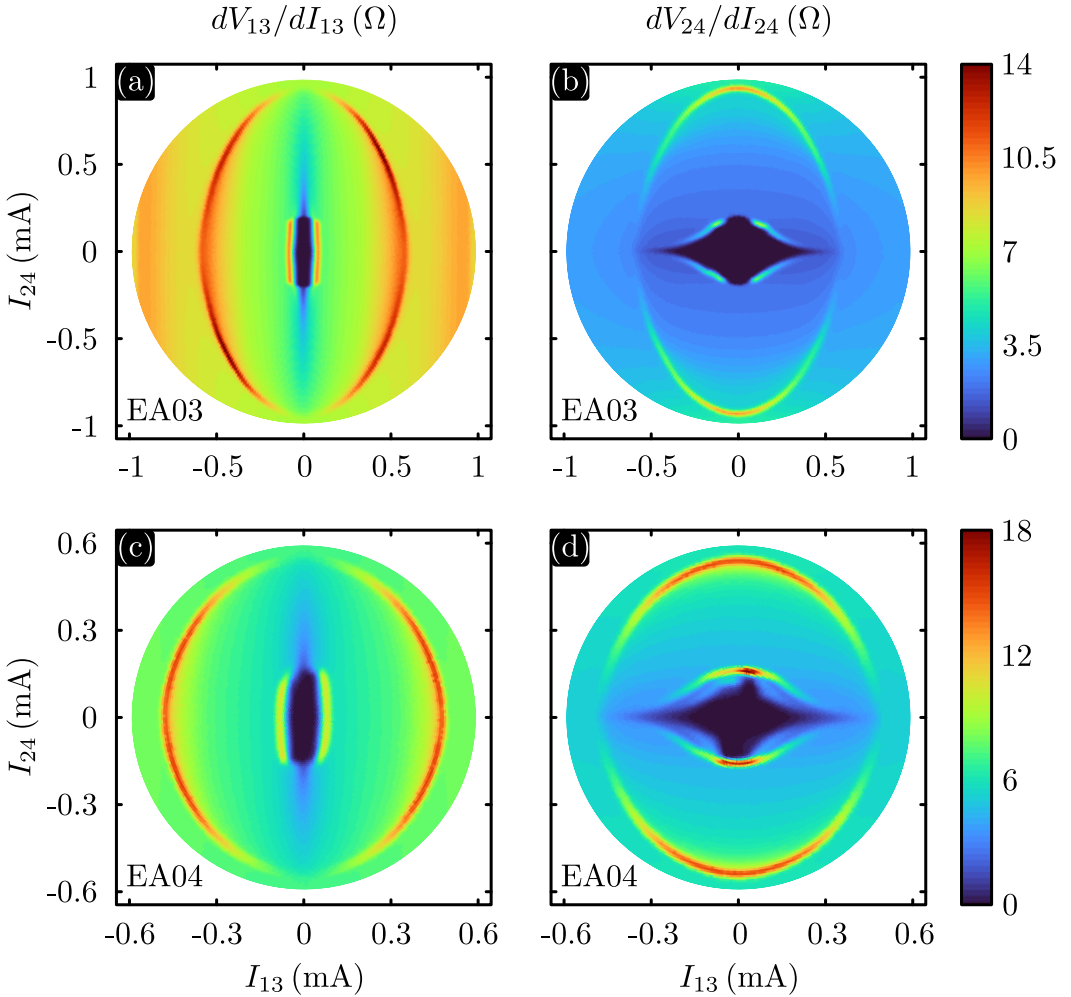


Figure 6.11 – Differential resistance for state EA03 (panels (a) and (b)) and state EA04 (panels (c) and (d)). All measurements are made at $T = 1.8 \text{ K}$.

tion to other features. After the first stage EA01 characterized by the alteration of terminal 1 as shown in Fig. 6.5(c), a strong asymmetry can be observed in the transport maps at $T = 1.8\text{K}$ of Fig. 6.10(a,b). Note that this asymmetry is reflected in a critical current $I_{c,13} \sim 25\text{ }\mu\text{A}$ significantly lower than $I_{c,24} \sim 8\text{ mA}$. The current space is therefore ellipsoidal and contracted along the vertical, generating a slight deformation. The low value of $I_{c,13}$ implies a substantial reduction of the heat dissipation, and we therefore observe different CCC between panels (a) and (b) in Fig. 6.10. The most interesting effect of EA modification on transport properties is observed at step EA02 (Fig. 6.6(g)) as shown in Fig. 6.10(c,d), where a surprising CCC is observed. In particular, the black box in panel (d) shows that the vertical critical currents are not reached on the vertical axis, but in the second and fourth quadrants of the current space, whose axes are given by the white dashed lines. This means that the critical current along direction 24 can be maximized or reduced to some extent by applying a current along direction 13.

For the sake of completeness, the results of steps EA03 (Fig. 6.6(h)) and EA04 (Fig. 6.6(i)) are respectively in panels (a,b) and (c,d) of Fig. 6.11. Surprisingly, the horizontal asymmetry of the CCC observed in Fig. 6.10(d) is not reproduced in Fig. 6.11(b) but appears to reappear in Fig. 6.11(d). Unfortunately, the mechanism explaining these observations is still missing and should motivate further investigations.

6.5 Ginzburg-Landau simulations

In an attempt to shed light on the origin of the above reported effect, we resort to time dependent GL simulations which are able to faithfully capture the microscopic behavior of the superconducting condensate. Let us start by briefly describing the extended generalized time-dependent Ginzburg-Landau (gTDGL) model, which is a generalized dimensionless version of the GL equations presented in section 1.2.2.2. This model takes into account the heat equation and is therefore a convincing candidate for describing the transport maps of section 6.4. Further information can be found in Ref.[24], from which the present section is inspired.

The gTDGL model [236, 237] that governs the dynamics of the complex order parameter $\psi(\mathbf{r}, t) = |\psi(\mathbf{r}, t)|e^{i\theta(\mathbf{r}, t)}$ consists of three coupled 2D partial differential equations for the amplitude $|\psi|$, the phase θ and local temperature \tilde{T} :

$$\begin{aligned} \frac{\bar{u}}{\sqrt{1 + \Gamma|\psi|^2}} \left(\frac{\partial}{\partial t} + iV + \frac{\Gamma^2}{2} \frac{\partial |\psi|^2}{\partial t} \right) \psi \\ = (f - g|\psi|^2)\psi + (\nabla - i\mathbf{A})^2\psi, \end{aligned} \quad (6.7)$$

$$\nabla \left(\frac{\partial \mathbf{A}}{\partial t} - \nabla V \right) = \nabla[|\psi|^2(\nabla\theta - \mathbf{A})], \quad (6.8)$$

$$c \frac{\partial \tilde{T}}{\partial t} = \kappa \nabla^2 \tilde{T} - \mathcal{H}(\tilde{T} - \tilde{T}0) + \left(\frac{\partial \mathbf{A}}{\partial t} - \nabla V \right)^2, \quad (6.9)$$

where $\bar{u} \simeq 5.79$ is the ratio of the relaxation times for the magnitude and the phase of the order parameter, $\Gamma = 10$ models the inelastic electron-phonon scattering, V is the electric potential, $f(T) = (T_c(\mathbf{r})^2 - T^2)/(T_c(\mathbf{r})^2 + T^2)$ and $g(T) = T_c(\mathbf{r})^4/(T_c(\mathbf{r})^2 + T^2)^2$ are thermal kernels extending gTDGL over a wider range of temperature [238], \mathcal{C} is the heat capacity, \mathcal{K} is the thermal conductivity, \mathcal{H} heat loss coefficient. Equations (6.7), (6.8) and (6.9) are written in dimensionless form where time is measured in units of the Ginzburg-Landau relaxation time at 0 K $\tau_{GL}(0) = \pi\hbar/8uk_BT_c$, distances are expressed in units of $\xi(0)$ and the order parameter is scaled with its bulk value, $\psi_{GL}(0) = 4\sqrt{\bar{u}}k_BT_c/\pi$. The electrostatic potential is expressed in units of $\varphi_{GL}(0) = \hbar/q_p\tau_{GL}(0)$ (q_p the charge of a Cooper pair), and the vector potential is expressed in units of $Q_{GL}(0) = B_{c2}(0)\xi(0)$, where $B_{c2}(0) = \hbar/q_p\xi(0)^2$ which is also used as unit for the magnetic field. The current density is expressed in $J_{GL}(0) = \sigma^{(0)}\varphi_{GL}(0)/\xi(0)$ with $\sigma^{(0)}$ the normal state conductivity. The temperature is normalized as $\tilde{T} = T/T_c$. Equation (6.8) is the current-conservation law with the normal current density $\mathbf{J}_n = \partial\mathbf{A}/\partial t - \nabla V$ and the supercurrent $\mathbf{J}_s = -|\psi|^2(\nabla\theta - \mathbf{A})$.

The model considers an idealized $2\mu\text{m}$ square geometry shown in Fig. 6.12(a). Two current densities J_{13} and J_{24} are imposed in the horizontal and vertical directions respectively. The equations (6.7),(6.8),(6.9) are discretized by finite differences with a 251×251 square mesh defining a unit cell of $\Delta x = \Delta y = 8\text{ nm}$. With the coherence length at 5 K estimated at $\xi(T = 5\text{ K}) \sim 58\text{ nm}$, the mesh is small enough ($\Delta x < 0.3\xi(T)$, $\Delta y < 0.3\xi(T)$) to ensure that the condensate dynamics are captured correctly. Subsequently, the current space is probed by 500 points as shown in Fig. 6.12(b). Each of these 500 blue points represents a complete simulation for

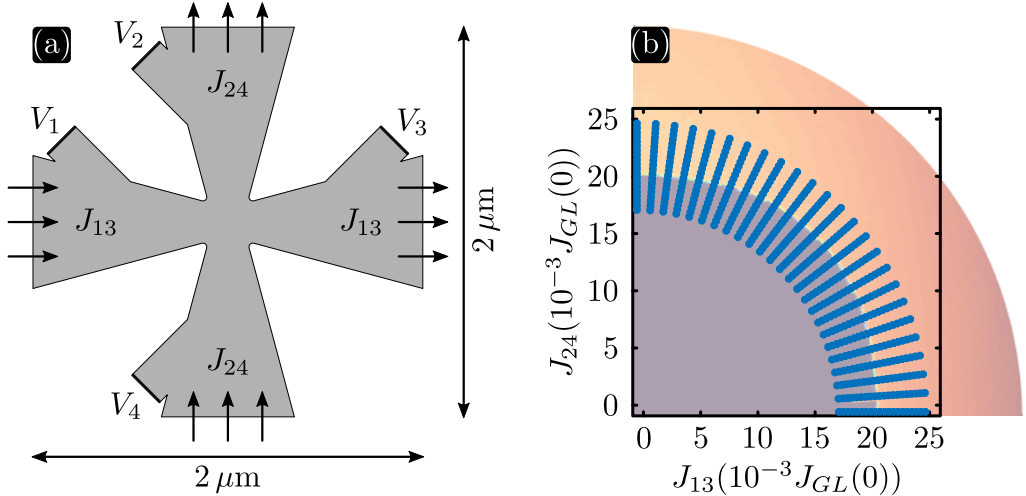


Figure 6.12 – Panel (a): idealized geometry considered for gTDGL simulations. Two independent current densities J_{13} and J_{24} are imposed in the horizontal and vertical directions respectively. Panel (b): discretization of the current space for the pristine EA00 state at $T = 5\text{ K}$. In view of the symmetry, only a quarter of the experimental current space is simulated.

which the equations (6.7),(6.8),(6.9) are solved from an initial homogeneous state $\psi = 1$ to a stationary (vortex-free) or periodic state (as a result of the creation and annihilation of vortex/anti-vortex pairs) depending on the amplitude of the applied currents. For the sake of illustration, the mechanism at the origin of dissipation is shown in Fig. 6.13 for the pristine state at 6 K when the system is fed by two equal horizontal (to the right) and vertical (upward) currents. If the current is high enough to locally exceed the depairing current, an oscillatory dynamic response characteristic of vortex dynamics is observed as shown in panel (g). The Cooper pair density $|\psi|^2$ and the supercurrent white streamlines for each of the labeled black points in this panel are presented by the panel with the same letter. The start of the dynamic phase is dictated by the moment when the current density reaches the

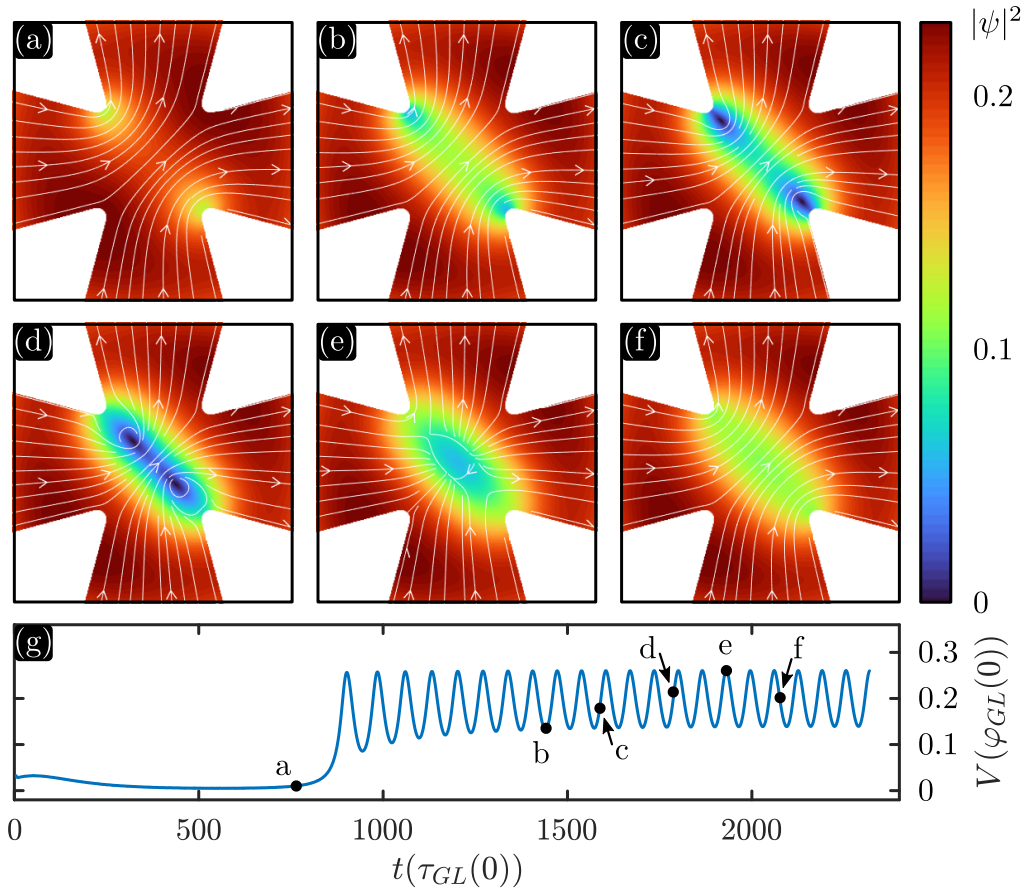


Figure 6.13 – Example of vortex dynamics at the onset of the dissipative state in a homogeneous four-terminal sample biased with equal horizontal and vertical currents at 6 K. Panels (a) to (f) illustrate the behavior of the superconducting condensate (Cooper pair density) together with the supercurrent (white streamlines) at points labeled as in panel (g). This last panel shows the evolution of voltage in both horizontal and vertical directions as a function of time.

depairing limit at current crowding spots. Due to the symmetries of the geometry and the imposed currents, the superconducting current density concentrates at the upper left and lower right corners, locally reducing the gap value (panel (a)). The magnetic field generated by the supercurrent then becomes sufficient to nucleate a vortex in the upper left corner and an anti-vortex in the lower right corner (panels (b) and (c)). Since vortices are subjected to a Lorentz-like force per unit length:

$$\mathbf{f}_\phi = \mathbf{J}_s \times \Phi_0 \mathbf{u}, \quad (6.10)$$

where \mathbf{u} is a unit vector in the direction of the flux quantum. The vortex/anti-vortex pair moves closer together (panel d) until it annihilates (panel (e) and (f)). The mechanism repeats itself endlessly giving rise to the dynamic behavior shown in panel (g), whereas the voltage measured corresponds to the time average of the oscillatory response.

The results of the virgin state EA00 simulations are given for $T = 5$ K and 6 K in panels (a,b) and (c,d) of Fig. 6.14 respectively. Note that the graphs in Fig. 6.14 give the value of the dimensionless resistance V/I , whereas the experimental results give the differential resistance dV/dI . This choice is justified by the low resolution of the simulated $V(I)$ curve, which generates a noisy dV/dI signal. Moreover, as dV/dI and $V(I)$ remain zero below the critical current (see Fig. 6.9), the shape of the CCC is not affected. Direct comparison of Fig. 6.14 with the experimental results in Fig. 6.8 shows that the same quasi-circular shape of the CCC indicated by the white dotted line is reproduced for measurements at 5 K (panels (a,b)). Likewise, the position of the highest resistance zones is naturally observed. On the other hand, the results at 6 K (panels (c,d)) do not reproduce the more pronounced squareness observed in the experimental CCC at 6 K (black dotted line), but seem to remain closer to the result at 5 K (white dotted line). This is undoubtedly due to improper estimation of thermal parameters, which underestimate heat losses to the substrate and systematically result in the formation of a large hot spot to the detriment of a gradual transition of the sample to the normal state.

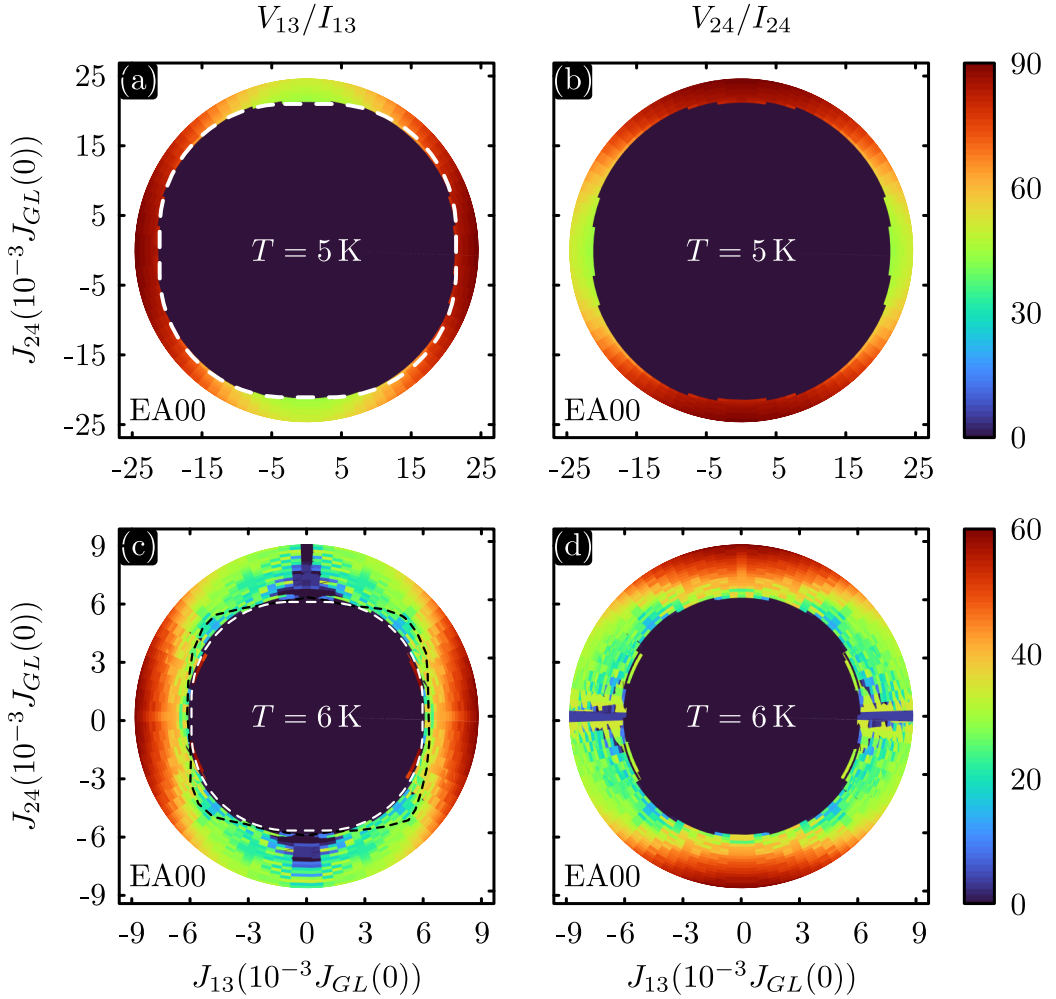


Figure 6.14 – Simulation results for the virgin EA00 state at $T = 5$, K (panels (a,b)) and at $T = 6$, K (panels (c,d)) with $\mathcal{C} = 0.01$, $\mathcal{K} = 0.24$ and $\mathcal{H} = 0.0024$. The experimental CCC at 5 K is highlighted by the white dotted line in panels (a,c) and at 6 K by the black dotted line in panel (c). These results are to be compared with measurements of Fig. 6.8.

6.6 Conclusion

In short, we have extended the conclusions of chapter 3 to the case of four-terminal devices, demonstrating the selectivity of the damage caused by EA. Based on measurements of $R(T)$ characteristics, we presented a finite-element model estimating plausible critical temperature and resistivity distributions resulting from high current density flow in a Nb device withstanding high temperature rises without significant mass migration. Simulations show a localized change at the point of smallest cross-section, with little propagation towards the voltage leads. Future experiments involving in-situ imaging techniques such as SEM or Scanning Thermal Microscopy (SThM) are required to validate this model. Transport properties have shown that it is possible to modify the initially quasi-circular CCC resulting in the formation of a hot spot in the normal state towards surprising non-monotonic shapes that are still not fully understood. An initial attempt to shed light on the phenomenon has been undertaken by the gTDGL model from which we were able to reproduce certain features of the pristine state. However, additional simulations taking into account the critical temperature and resistivity inhomogeneities of the finite element model, as well as improved estimation of the thermal parameters of the heat equation, are still required to reproduce the transport properties of EA states. It is worth noting that an explanation for the non-monotonic character of the zero-magnetic-field CCC was recently proposed in Ref.[239] in the case of four-terminal junctions connected by a normal central node and involve a quartet current (correlation between two Cooper pairs). In the present report, after EA of all junctions, the initially monolithic sample is modified to form a set of four SS'S junctions clustering around a superconducting central island, and deviates significantly from the configuration in Ref.[239]. In order to get closer to the theoretical conditions of Ref.[239], it would be necessary to fabricate an initial reversible sample with significantly narrower junctions while employing other polarities during EA or the thermomigration technique consisting in currents of alternative directions in order to localize the alterations at the center of the device.

Conclusions and perspectives

Throughout this thesis, we have investigated the effects of high current density on the properties of Nb-based superconducting samples with geometries other than the widely explored bow-tie configuration. Using the electroannealing technique, we demonstrated the possibility of inducing in situ inhomogeneities in the superconducting properties that are otherwise hardly achievable by conventional nanofabrication techniques. We considered multiterminal geometries with $N > 2$ current leads, allowing to operate as current divider and thus lessening the need for geometrical constriction. More specifically, we showed that the choice of polarity in a three-terminal or four-terminal sample allowed doubling or tripling respectively the current density in a specific targeted junction, permitting to introduce localized modifications of the critical temperature, normal resistance, and critical current while leaving other junctions unaffected. This unprecedented achievement demonstrated enhanced control over the localization of effects associated with EM/EA in samples compatible with multiterminal configuration and offered new perspectives in the design and control of SS'S or SNS type junction properties. The explored technique is particularly appealing in the quest for experimental evidence of quartet currents formed by the correlation of two Cooper pairs that assemble to form a four-electron quasiparticle. Indeed, recent theoretical considerations[239] have predicted that a four-branch multiterminal sample connected via a normal zone would exhibit a non-convex critical current contour at zero field, signature of the presence of quartet supercurrent.

We examined the modifications induced by weak EM/EA steps in multiterminal Al/Nb samples, resulting in resistance variations of less than 10%. We revealed that the surface electrical properties of the sample were modified through a local change of the work function. As this result was only investigated in a two-layer Al/Nb system, it would be interesting to explore its universality by testing other metallic materials, and to determine to what extent the change in the work function can be controlled. One could envisage the possibility to use this technique to increase the emission of electron guns without the need of coatings or faceted single crystal to lower the work function.

We discussed the effects of EM/EA on two parallel junctions in an Nb-based SQUID with Dayem bridge junctions. We demonstrated that successive EM/EA steps allowed adjusting the thermal behavior of the device. Following the extinction of the critical current at a high EM/EA step, the SQUID exhibited an astonishing

resurrection of critical temperature and critical current in the weak links which allows to re-establish coherence of the superconducting phase in the dissipative state. At the moment, the resurrection of superconducting properties remains currently unexplained. One possible explanation involves the formation of a conductive NbO oxide layer that acts as a shunted resistance, eliminating the irreversibility of the SQUID. Additional in-situ observation experiments or detailed analysis of the chemical composition of weak links via atom probe could potentially provide new insights. Furthermore, an in-depth analysis of the noise performance of the modified SQUID is still missing.

We presented a finite element model to obtain critical temperature and resistivity distributions in an Nb-based sample based on experimental $R(T)$ curves acquired for each junction. Although applied to a four-terminal sample, this model can potentially be extended to any geometry modified by EA and contributes to our understanding of the mechanisms associated with EA. Thermal scanning microscopy experiments providing the local temperature distribution at the sample surface would enable direct verification of the theoretical results, and would be the natural next step to validate our model.

In conclusion, this study delves into the intricate effects of electromigration and electroannealing in conductive materials, with a special focus on Nb and its potential applications in nanofabrication with atomic-scale resolution. Through exploration of complex geometries, we demonstrate the capability to achieve fine control over EM/EA effects, leading to tuning of the device's performance. Moreover, the novel insights gained through the finite element model contribute significantly to the advancement of superconducting materials and devices.

The findings from this thesis could have potential applications as an adjustment tool in superconducting qubits such as transmons, where energy levels are dependent on the properties of the Josephson junction or the SQUID that constitutes it. Additionally, these results could find utility in the broader field of superconducting electronics, where Nb compounds such as NbN and NbTiN are widely used.

Concerning future perspectives, the enhanced location control provided by multi-terminal geometry is not unique to Nb and could be applied to other conductors and superconductors. Specifically, it would be interesting to study the preferential EM of oxygen in multiterminal YBCO samples to enhance doping control.

Regarding the EM/EA techniques, several options can be explored to control its location more precisely. For example, considering polarities other than the one maximizing the current density in a single junction would be interesting. In the case of four-branch multi-terminals, providing two inputs and two outputs for the current could concentrate the effects of EA at the device's center instead of in a given terminal. Another approach would involve using EM/EA with alternative voltages, where the effects related to charge carrier momentum transfer are constantly compensated by alternating currents, leaving thermomigration as the dominant term.

Although the physics inherent in the EM/EA process is well understood, its

inherent stochastic character and the complexity of intertwined mechanism makes it a real challenge to master it. Nevertheless, there remain some very exciting new physics deserving further investigation. For example, a systematic study of three-terminal Nb-based samples showed that certain current polarities led to controlled EA at room temperature with localized changes in a single junction, or to complete and uncontrolled destruction at 10 K (all other parameters being unchanged). Identifying the hinge temperature(s) between these extreme behaviours and interpreting them, is one way of deepening our understanding of the EA phenomenon.

Appendices

Appendix A

CPR of point contacts

In what follows, the temperature evolution of the order parameter will be written as:

$$\Delta(t) = \Delta(0)f(t), \quad (\text{A.1})$$

where $t = T/T_c$ is the reduced temperature, $\Delta(0) = 1.76k_B T_c$ the gap at 0 K (1.38) and $f(t)$ the function illustrated in left panel of Fig.1.5. A 2% analytical approximation for $f(t)$ is given by:

$$f(t) \sim \tanh \left(1.74 \sqrt{\frac{1}{t} - 1} \right), \quad (\text{A.2})$$

which allows a direct analytical approximation of the CPR. The result of the substitution of (A.1) and (A.2) in the CPR relations of the section (1.3.1.2) is given directly for each case.

A.1 Ambegaokar-Baratoff (AB)

$$\frac{eR_N I_s(\Theta)}{2\pi k_B T_c} = \frac{1.76f(t)}{4} \tanh \left(\frac{1.76f(t)}{2t} \right) \sin \Theta. \quad (\text{A.3})$$

A.2 Aslamazov-Larkin (AL)

$$\frac{eR_N I_s(\Theta)}{2\pi k_B T_c} = \frac{1.76^2 f(t)^2}{8t} \sin \Theta. \quad (\text{A.4})$$

A.3 Kulik-Omelyanchuk - dirty limit (KO-1)

$$\frac{eR_N I_s(\Theta)}{2\pi k_B T_c} = 2t \sum_{n \geq 0} \frac{f(t) \cos(\Theta/2)}{\delta} \arctan \left(\frac{f(t) \sin(\Theta/2)}{\delta} \right), \quad (\text{A.5})$$

with

$$\delta = \sqrt{(f(t) \cos(\Theta/2))^2 + \left(\frac{\pi t(2n+1)}{1.76} \right)^2}. \quad (\text{A.6})$$

A.4 Kulik-Omelyanchuk - clean limit (KO-2)

$$\frac{eR_N I_s(\Theta)}{2\pi k_B T_c} = \left(\frac{1.76f(t)}{2} \right) \tanh \left(\frac{1.76f(t) \cos(\Theta/2)}{2t} \right) \sin(\Theta/2). \quad (\text{A.7})$$

The Fig.A.1 shows the CPR for the Ambegaokar-Baratoff (AB) (panel (a)), AL (panel (b)), KO-1 (panel (c)) and KO-2 (panel (d)) models at different temperatures. Since the AL model is only valid near T_c , temperatures only $T \geq 0.7T_c$ were considered.

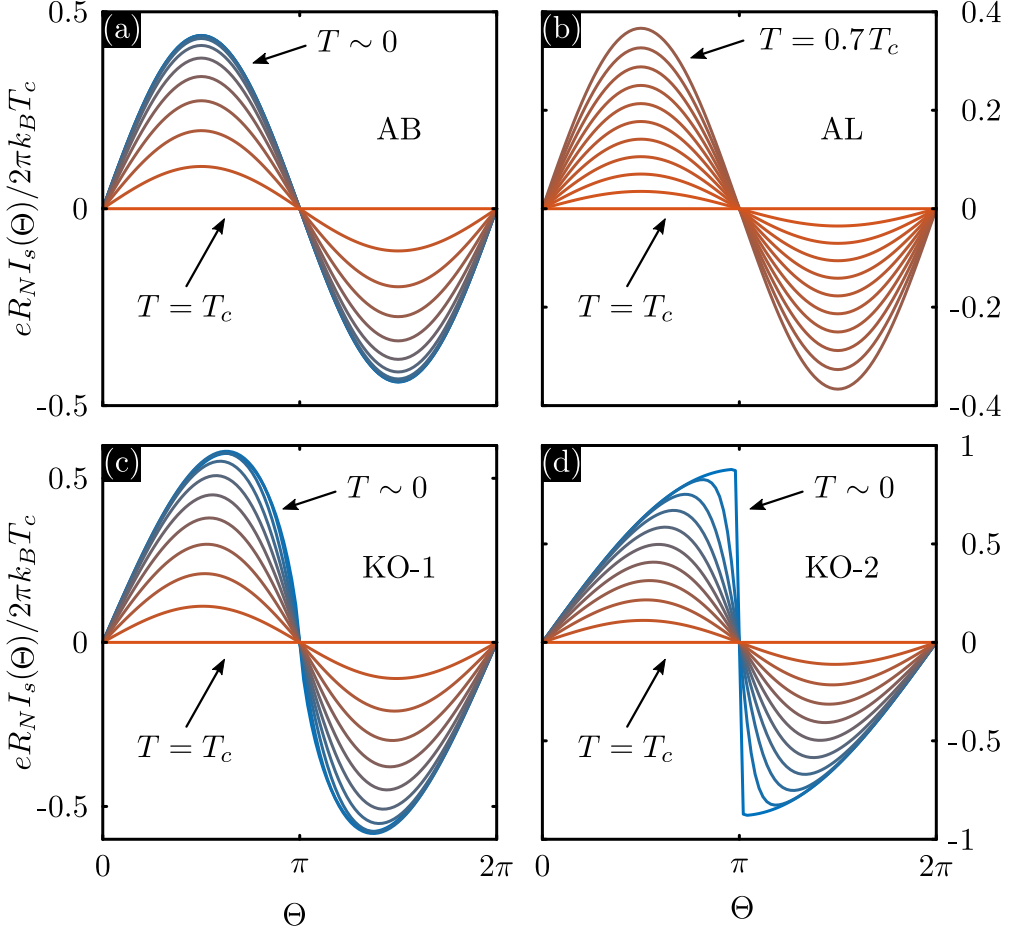


Figure A.1 – CPR of AB, AL, KO-1 and KO-2 models at different temperatures.

A.5 Haberkorn (H)

In the case of a average transparency \bar{D} of a tunnel barrier inserted in the constriction, H showed that the supercurrent is given by:

$$I_s(\Theta) = \frac{\pi \Delta(T)}{2eR_N} \frac{\sin \Theta}{\sqrt{1 - \bar{D} \sin^2(\Theta/2)}} \tanh \left(\frac{\Delta(T)}{2k_B T} \sqrt{1 - \bar{D} \sin^2(\Theta/2)} \right), \quad (\text{A.8})$$

which with (A.1) and (A.2) is the same as:

$$\frac{eR_N I_s(\Theta)}{2\pi k_B T_c} = \frac{1.76f(t)}{4} \frac{\sin \Theta}{\sqrt{1 - \bar{D} \sin^2(\Theta/2)}} \tanh \left(\frac{1.76f(t)}{2t} \sqrt{1 - \bar{D} \sin^2(\Theta/2)} \right). \quad (\text{A.9})$$

The equation (A.9) evaluated in the limit of the tunneling regime ($\bar{D} \sim 0$) gives the same result as AB while in the fully ballistic case ($\bar{D} \sim 1$) the result KO-2 is obtained.

A.6 Beenakeer (B)

In the multichannel case, B showed that (A.8) could be generalized by :

$$I_s(\Theta) = \frac{e\Delta(T)^2}{2\hbar} \sin \Theta \sum_{n=1}^N \frac{D_n}{E_n} \tanh \left(\frac{E_n}{2k_B T} \right), \quad (\text{A.10})$$

where D_n represents the transmission of the n^{th} energy channel

$$E_n = \Delta(T) \sqrt{1 - D_n \sin^2(\Theta/2)}, \quad (\text{A.11})$$

given by the eigenvalues of the transmission matrix. In the case of a continuous state distribution, as for a diffusive contact point, one has to take into account an eigenvalue density,

$$\rho(D) = \frac{\pi \hbar}{2e^2 R_N} \frac{1}{\sqrt{D(1-D)}}, \quad (\text{A.12})$$

In this case, (A.10) becomes:

$$I_s(\Theta) = \frac{e\Delta(T)^2}{2\hbar} \sin \Theta \int_0^1 \rho(D) \frac{D}{E(D)} \tanh \left(\frac{E(D)}{2k_B T} \right) dD, \quad (\text{A.13})$$

which is expressed via (A.1), (A.2), (A.11) and (A.12) as:

$$\begin{aligned} \frac{eR_N I_s(\Theta)}{2\pi k_B T_c} = & \frac{1.76f(t)}{8} \sin \Theta \int_0^1 \frac{\sqrt{D}}{\sqrt{1-D} \sqrt{1-D \sin^2(\Theta/2)}} \\ & \tanh \left(\frac{1.76f(t) \sqrt{1-D \sin^2(\Theta/2)}}{2t} \right) dD, \end{aligned} \quad (\text{A.14})$$

The integration of this last equation gives exactly the result KO-1.

Appendix B

The SQUID dynamics in the zero voltage state

B.1 Newton-Raphson method

Let be the series of equations:

$$\mathbf{f}(\mathbf{x}) = \mathbf{0}, \quad (\text{B.1})$$

With \mathbf{x} the vector with the n unknowns:

$$\mathbf{x} = \begin{pmatrix} x_1 \\ x_2 \\ \vdots \\ x_n \end{pmatrix}, \quad (\text{B.2})$$

and $\mathbf{f}(\mathbf{x})$ the n equations to solve:

$$\mathbf{x} = \begin{pmatrix} f_1(x_1, x_2, \dots, x_n) \\ f_2(x_1, x_2, \dots, x_n) \\ \vdots \\ f_n(x_1, x_2, \dots, x_n) \end{pmatrix}, \quad (\text{B.3})$$

The numerical solution can be estimated by iteration according to the following scheme:

$$\mathbf{x}^{(k+1)} = \mathbf{x}^{(k)} - \mathcal{J}^{-1}(\mathbf{x}^{(k)})\mathbf{f}(\mathbf{x}^{(k)}) \quad (\text{B.4})$$

where \mathcal{J} is the Jacobian matrix:

$$\mathcal{J} = \begin{pmatrix} \partial f_1/\partial x_1 & \partial f_1/\partial x_2 & \dots & \partial f_1/\partial x_n \\ \partial f_2/\partial x_1 & \partial f_2/\partial x_2 & \dots & \partial f_2/\partial x_n \\ \vdots & \vdots & \ddots & \vdots \\ \partial f_n/\partial x_1 & \partial f_n/\partial x_2 & \dots & \partial f_n/\partial x_n \end{pmatrix}. \quad (\text{B.5})$$

B.2 Current bellow critical current

The three equations governing the dynamic of a SQUID are (see section 1.3.4.1):

$$i_s = (1 - \alpha) \sin \Theta_1 + (1 + \alpha) \sin \Theta_2, \quad (\text{B.6})$$

$$2i_\Phi = (1 - \alpha) \sin \Theta_1 - (1 + \alpha) \sin \Theta_2, \quad (\text{B.7})$$

$$\Theta_2 - \Theta_1 = 2\pi n + 2\pi\phi_{ext} + \pi\beta_L \left(i_\Phi - \frac{\eta}{2} i_s \right). \quad (\text{B.8})$$

The three unknowns Θ_1 , Θ_2 and i_ϕ need to be determined for a given device (α , β_L and η known) biased with a current i_s and crossed by a flux ϕ_{ext} . The variable Θ_2 can be eliminated by combining (B.6) and (B.7) to obtain:

$$i_\phi(\Theta_1) = (1 - \alpha) \sin \Theta_1 - \frac{i_s}{2}. \quad (\text{B.9})$$

This last equation combined with (B.8) allows to establish a single equation between Θ_1 and Θ_2 :

$$\Theta_2(\Theta_1) = \Theta_1 + 2\pi n + 2\pi\phi_{ext} + \pi\beta_L(1 - \alpha) \sin \Theta_1 - \frac{\pi\beta_L}{2}(1 + \eta)i_s, \quad (\text{B.10})$$

which introduced in (B.6) gives a unique equation for Θ_1 :

$$i_s = (1 - \alpha) \sin \Theta_1 + (1 + \alpha) \sin(\Theta_2(\Theta_1)). \quad (\text{B.11})$$

The equation (B.11) is solved numerically by iteration by the Newton-Raphson method by considering $\mathbf{x} = (\Theta_1)$ and expressing (B.11) in the form (B.3):

$$f(\Theta_1) = i_s - (1 - \alpha) \sin \Theta_1 - (1 + \alpha) \sin(\Theta_2(\Theta_1)) = 0. \quad (\text{B.12})$$

The Jacobian matrix (B.5) reducing here to the single term:

$$\frac{\partial f(\Theta_1)}{\partial \Theta_1} = -(1 - \alpha) \cos \Theta_1 - (1 + \alpha)(1 + \pi\beta_L(1 - \alpha) \cos \Theta_1) \cos(\Theta_2(\Theta_1)) \quad (\text{B.13})$$

B.3 Critical current oscillations

Finding the critical current consists in maximizing i_s of (B.11) according to the unknown Θ_1 . The current i_s becomes the second unknown but an additional equation is provided by its extremity condition $\partial i_s / \partial \Theta_1 = 0$. This condition constitutes the second equation $f_2(i_s, \Theta_1) = 0$ to be respected and amounts to imposing (B.13) to zero while the first equation $f(i_s, \Theta_1) = 0$ remains identical to (B.12). Deriving f_1 and f_2 with respect to the two variables $\mathbf{x} = (i_s, \Theta_1)^T$, we obtain:

$$\frac{\partial f_1}{\partial i_s} = 1 - (1 + \alpha) \left(-\frac{\pi\beta_L}{2}(1 + \eta) \right) \cos(\Theta_2(\Theta_1)), \quad (\text{B.14})$$

$$\frac{\partial f_1}{\partial \Theta_1} = -(1 - \alpha) \cos \Theta_1 - (1 + \alpha)(1 + \pi\beta_L(1 - \alpha) \cos \Theta_1) \cos(\Theta_2(\Theta_1)), \quad (\text{B.15})$$

$$\frac{\partial f_2}{\partial i_s} = -(1 + \alpha)(1 + \pi\beta_L(1 - \alpha)\cos\Theta_1) \left(-\frac{\pi\beta_L}{2}(1 + \eta) \right), \quad (\text{B.16})$$

$$\begin{aligned} \frac{\partial f_2}{\partial \Theta_1} = & -(1 - \alpha)\sin\Theta_1 - (1 + \alpha)(\pi\beta_L(1 - \alpha)\sin\Theta_1)\cos(\Theta_2(\Theta_1)) \\ & - (1 + \alpha)(1 + \pi\beta_L(1 - \alpha)\cos\Theta_1)(1 + \pi\beta_L(1 - \alpha)\cos\Theta_1)\sin\Theta_2(\Theta_1). \end{aligned} \quad (\text{B.17})$$

For given value of α , β_L , η and n , the Newton-Raphson scheme (B.4) is then resolved for each value of the applied flux ϕ_{ext} to obtain the $i_c(\phi_{ext})$ oscillations plotted in Fig.1.24, 1.25 and 1.26.

Appendix C

Supplemental Material of chapter 6

C.1 In situ scanning electron microscopy of sample S2

Fig. C.1(a) shows the maximum resistance (R_{max}) obtained at a current I_{EA} and the minimum resistance (R_{min}) obtained after the current has been switched off for a supplementary sample. For $I_{EA} \leq 10$ mA, the increase of R_{max} with increasing I_{EA} results primarily from Joule heating, as confirmed by the fact that no change of R_{min} is observed in this current range. $I_{EA} = 10$ mA represents the threshold beyond which irreversible modifications in the constrictions are induced. For each EA step depicted in Fig. C.1(a), we have acquired SEM images after the device has been submitted to thermal stress. A selected set of these images are shown in Fig. C.1(b) to (e). Fig. C.1(f) and (g) show a zoom in of the two constrictions on Fig. C.1(e) where clear surface damage, preferentially occurring on the I^- side, can be observed. One can note that no apparent structural modification are revealed for $I_{EA} \approx 10$ mA whereas clear material alteration localized at both constrictions are seen after exceeding the threshold current. The affected area is about 4200 nm^2 and 6300 nm^2 for upper and lower constrictions, respectively.

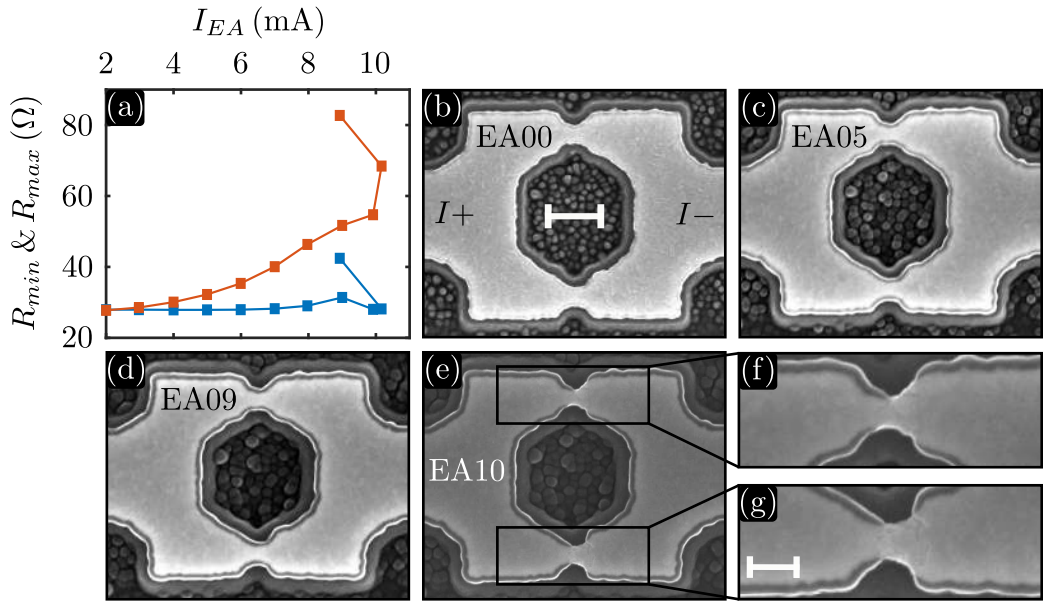


Figure C.1 – SEM images obtained during the EA process for sample S2. Panel (a) shows the values of the maximum resistance (R_{max}) in red color obtained at a current I_{EA} and the minimum resistance (R_{min}) in blue color obtained after the current has been switched off. Starting from pristine state (b) EA runs produce no apparent structural modification until reaching EA10 (e). Panels (f) and (g) show a zoom-in of both Dayem bridges in panel (e). Scales bars in (b) and (g) correspond to 200 nm and 100 nm, respectively.

C.2 Weak links superconducting properties

Fig. C.2(a) shows a selected set of $R(T)$ curves taken after various EA steps on sample S4. The measured normal resistance and critical temperatures are summarized in Fig. C.2(b) and present clear similarities with respect to the results shown in the main text for sample S1 (Fig. 4), demonstrating good reproducibility of the EA effects on sample behavior.

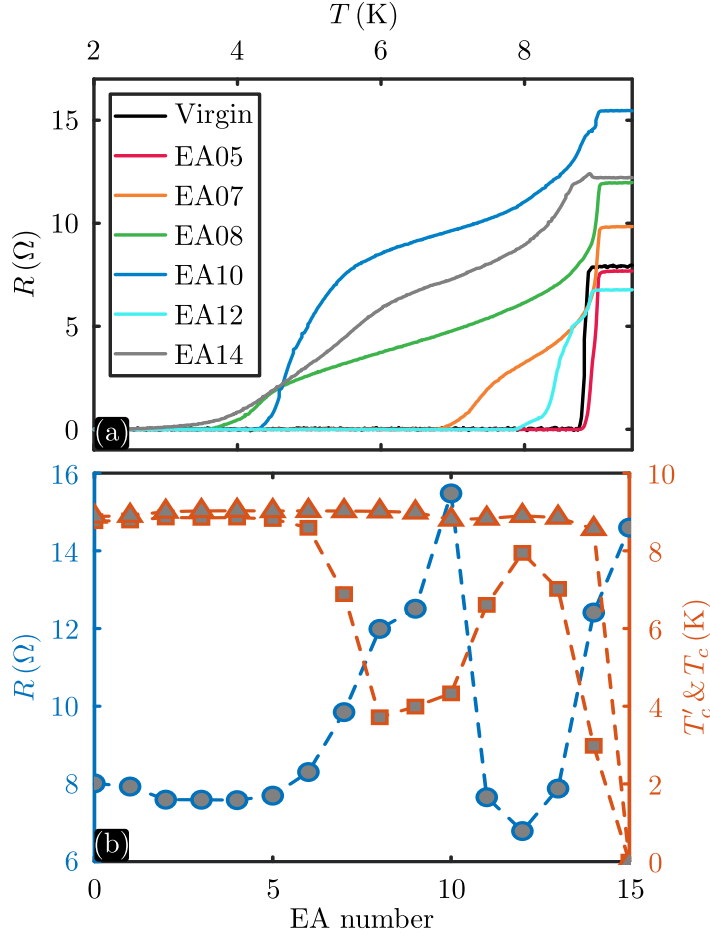


Figure C.2 – (a) $R(T)$ evolution for sample S4. (b) Resistance of the normal state and critical temperature taken for (a) and plotted as a function of EA number.

Bibliography

- ¹S. Blundell, *Superconductivity: A Very Short Introduction* (Oxford University Press, 2009).
- ²J. Matricon and G. Waysand, *La Guerre du froid. Une histoire de la supraconductivité*. (Seuil, 1994).
- ³A. Matthiessen and A. C. C. Vogt, *On the influence of temperature on the electric conducting-power of alloys*, Philos. Trans. R. Soc. **154**, 167–200 (1864).
- ⁴J. Dewar, *On Electric Resistance Thermometry at the Temperature of Boiling Hydrogen*, Proc. R. Soc. Lond. **73**, 244–251 (1904).
- ⁵L. Kelvin, XXIX. *Aepinus atomized*, Lond. Edinb. Dublin Philos. Mag. J. Sci. **3** (1902).
- ⁶H. K. Onnes, *The resistance of pure mercury at helium temperatures*, Commun. Phys. Univ. Leiden **120** (1911).
- ⁷M. Tinkham, *Introduction to Superconductivity*, 2nd (Dover Publications, Inc., 1996).
- ⁸W. Meissner and R. Ochsenfeld, *Ein neuer Effekt bei Eintritt der Supraleitfähigkeit*, Naturwissenschaften **21**, 787–788 (1933).
- ⁹F. London and H. London, *The electromagnetic equations of the superconductor*, Proc. Roy. Soc. A **149**, 71–88 (1935).
- ¹⁰C. J. Gorter and H. Casimir, *On supraconductivity I*, Physica **1**, 306–320 (1934).
- ¹¹V. V. Schmidt, *The Physics of Superconductors: Introduction to Fundamentals and Applications* (Springer Science, 1997).
- ¹²J. Bardeen, L. N. Cooper, and J. R. Schrieffer, *Theory of Superconductivity*, Phys. Rev. **108**, 1175–1204 (1957).
- ¹³T. P. Orlando and K. A. Delin, *Foundations of Applied Superconductivity* (Addison-Wesley, 1991).
- ¹⁴R. Gross and A. Marx, *Applied Superconductivity: Josephson Effect and Superconducting Electronics* (Walther-Meissner Institut, 2005).
- ¹⁵B. S. Deaver and W. M. Fairbank, *Experimental Evidence for Quantized Flux in Superconducting Cylinders*, Phys. Rev. Lett. **7**, 43–46 (1961).

- ¹⁶R. Doll and M. Näbauer, *Experimental Proof of Magnetic Flux Quantization in a Superconducting Ring*, Phys. Rev. Lett. **7**, 51–52 (1961).
- ¹⁷P. Mangin and R. Kahn, *Supraconductivité - Introduction* (EDP Sciences, Grenoble, 2013).
- ¹⁸F. Reif, *Fundamentals of statistical and thermal physics* (McGraw-Hill, Inc., 1965).
- ¹⁹S. Elliot, *The Physics and Chemistry of Solids* (WILEY, 1998).
- ²⁰N. E. Phillips, *Heat Capacity of Aluminum between 0.1 K and 4.0 K*, Phys. Rev. **114**, 676–685 (1959).
- ²¹L. D. Landau, *The Theory of Phase Transitions*, Nature **138**, 840–841 (1936).
- ²²V. L. Ginzburg and L. D. Landau, *On the theory of superconductivity*, Zh. Eksp. Teor. Fiz. **20**, 1064–1082 (1950).
- ²³A. R. Tilley and J. Tilley, *Superfluidity and Superconductivity* (IOP Publishing Ltd, 1990).
- ²⁴Ž. J. Jelić, *Emergent vortex phenomena in spatially and temporally modulated superconducting condensates*, PhD thesis (Universities of Liège/Antwerpen, 2017).
- ²⁵P. G. De Gennes, *Superconductivity of Metals and Alloys* (Benjamin, 1966).
- ²⁶A. A. Abrikosov, *On the magnetic properties of superconductors in the second group*, Sov. Phys. JETP **5**, 1174–1182 (1957).
- ²⁷D. Saint-James and G. Sarma, *Type II superconductivity* (Pergamon Press Ltd., 1969).
- ²⁸E. Maxwell, *Isotope Effect in the Superconductivity of Mercury*, Phys. Rev. **78**, 477–477 (1950).
- ²⁹C. A. Reynolds, B. Serin, W. H. Wright, and L. B. Nesbitt, *Superconductivity of Isotopes of Mercury*, Phys. Rev. **78**, 487–487 (1950).
- ³⁰L. P. Gor'kov, *Microscopic derivation of the Ginzburg-Landau equations in the theory of superconductivity*, Sov. Phys. JETP **36**, 1364 (1959).
- ³¹H. Fröhlich, *Theory of the Superconducting State. I. The Ground State at the Absolute Zero of Temperature*, Phys. Rev. **79**, 845–856 (1950).
- ³²H. Fröhlich, *Interaction of electrons with lattice vibrations*, Proc. R. Soc. Series A. Math. Phys. **215**, 291–298 (1952).
- ³³L. N. Cooper, *Bound Electron Pairs in a Degenerate Fermi Gas*, Phys. Rev. **104**, 1189–1190 (1956).
- ³⁴I. Giaever and K. Megerle, *Study of Superconductors by Electron Tunneling*, Phys. Rev. **122**, 1101–1111 (1961).
- ³⁵I. Giaever, *Energy Gap in Superconductors Measured by Electron Tunneling*, Phys. Rev. Lett. **5**, 147–148 (1960).
- ³⁶B. D. Josephson, *Possible new effects in superconductive tunnelling*, Phys. Lett. **1**, 251–253 (1962).

- ³⁷P. W. Anderson and J. M. Rowell, *Probable Observation of the Josephson Superconducting Tunneling Effect*, Phys. Rev. Lett. **10**, 230–232 (1963).
- ³⁸J. M. Rowell, *Magnetic Field Dependence of the Josephson Tunnel Current*, Phys. Rev. Lett. **11**, 200–202 (1963).
- ³⁹S. Shapiro, *Josephson Currents in Superconducting Tunneling: The Effect of Microwaves and Other Observations*, Phys. Rev. Lett. **11**, 80–82 (1963).
- ⁴⁰R. E. Eck, D. J. Scalapino, and B. N. Taylor, *Self-Detection of the ac Josephson Current*, Phys. Rev. Lett. **13**, 15–18 (1964).
- ⁴¹D. D. Coon and M. D. Fiske, *Josephson ac and Step Structure in the Supercurrent Tunneling Characteristic*, Phys. Rev. **138**, A744–A746 (1965).
- ⁴²I. Giaever, *Detection of the ac Josephson Effect*, Phys. Rev. Lett. **14**, 904–906 (1965).
- ⁴³V. Ambegaokar and A. Baratoff, *Tunneling Between Superconductors*, Phys. Rev. Lett. **10**, 486–489 (1963).
- ⁴⁴K. K. Likharev, *Superconducting weak links*, Rev. Mod. Phys. **51**, 101–159 (1979).
- ⁴⁵A. A. Golubov, M. Y. Kupriyanov, and E. Il’Ichev, *The current-phase relation in Josephson junctions*, Rev. Mod. Phys. **76**, 411–469 (2004).
- ⁴⁶Y. Tanaka and S. Kashiwaya, *Theory of Josephson effects in anisotropic superconductors*, Phys. Rev. B **56**, 892–912 (1997).
- ⁴⁷D. Dimos, P. Chaudhari, J. Mannhart, and F. K. LeGoues, *Orientation Dependence of Grain-Boundary Critical Currents in $YBa_2Cu_3O_{7-\delta}$ Bicrystals*, Phys. Rev. Lett. **61**, 219–222 (1988).
- ⁴⁸Z. G. Ivanov, P. Å. Nilsson, D. Winkler, J. A. Alarco, T. Claeson, E. A. Stepantsov, and A. Y. Tzalenchuk, *Weak links and dc SQUIDS on artificial nonsymmetric grain boundaries in $YBa_2Cu_3O_{7-\delta}$* , Appl. Phys. Lett. **59**, 3030–3032 (1991).
- ⁴⁹L. G. Aslamazov and A. I. Larkin, *Josephson effect in superconducting point contacts*, Pis’ma Zh. Eksp. Teor. Fiz. **9**, 150 (1969).
- ⁵⁰I. O. Kulik and A. N. Omel’yanchuk, *Contribution to the microscopic theory of the Josephson effect in superconducting bridges*, JETP Lett. **21**, 216 (1975).
- ⁵¹I. O. Kulik and A. N. Omel’yanchouk, *Properties of superconducting microbridges in the pure limit*, Sov. J. Low Temp. Phys. **3**, 459 (1977).
- ⁵²W. Haberkorn, H. Knauer, and J. Richter, *A theoretical study of the current-phase relation in Josephson contacts*, Phys. Status Solidi A **47**, K161 (1978).
- ⁵³C. W. J. Beenakker, *Universal limit of critical-current fluctuations in mesoscopic Josephson junctions*, Phys. Rev. Lett. **67**, 3836–3839 (1991).
- ⁵⁴K. K. Likharev and L. A. Yakobson, *Steady-state properties of superconducting bridges*, Zh. Tekh. Fiz. **45**, 1503–1509 (1975).
- ⁵⁵G. J. Podd, G. D. Hutchinson, D. A. Williams, and D. G. Hasko, *Micro-SQUIDS with controllable asymmetry via hot-phonon controlled junctions*, Phys. Rev. B **75**, 134501 (2007).

- ⁵⁶K. Hasselbach, D. Mailly, and J. R. Kirtley, *Micro-superconducting quantum interference device characteristics*, J. Appl. Phys. **91**, 4432–4437 (2002).
- ⁵⁷A. G. Sivakov, A. S. Pokhila, A. M. Glukhov, S. V. Kuplevakhsky, and A. N. Omel'yanchouk, *Oscillations of critical superconducting current in thin doubly-connected Sn films in an external perpendicular magnetic field*, Low Temp. Phys. **40**, 408–417 (2014).
- ⁵⁸J. Bardeen, *Critical Fields and Currents in Superconductors*, Rev. Mod. Phys. **34**, 667–681 (1962).
- ⁵⁹M. Y. Kupriyanov and V. Lukichev, *Temperature dependence of the pari-breaking current density in superconductors*, Sov. J. Low Temp. Phys. **6**, 210 (1980).
- ⁶⁰A. Murphy and A. Bezryadin, *Asymmetric nanowire SQUID: Linear current-phase relation, stochastic switching, and symmetries*, Phys. Rev. B **96**, 094507 (2017).
- ⁶¹J. Lombardo, Ž. L. Jelić, X. D. A. Baumans, J. E. Scheerder, J. P. Nacenta, V. V. Moshchalkov, J. Van de Vondel, R. B. G. Kramer, M. V. Milošević, and A. V. Silhanek, *In situ tailoring of superconducting junctions via electro-annealing*, Nanoscale **10**, 1987–1996 (2018).
- ⁶²J. Clarke and A. I. Braginski, *The SQUID Handbook. Vol. I: Fundamentals and Technology of SQUIDs and SQUID Systems* (WILEY-VCH Verlag GmbH & Co. KGaA, 2004).
- ⁶³J. Clarke and A. I. Braginski, *The SQUID Handbook. Vol. II: Applications of SQUIDs and SQUID Systems* (WILEY-VCH Verlag GmbH & Co. KGaA, 2006).
- ⁶⁴C. D. Tesche and J. Clarke, *DC SQUID: Noise and optimization*, J. Low Temp. Phys. **29**, 301–331 (1977).
- ⁶⁵H. Dausy, L. Nulens, B. Raes, M. J. Van Bael, and J. Van de Vondel, *Impact of Kinetic Inductance on the Critical-Current Oscillations of Nanobridge SQUIDs*, Phys. Rev. Applied **16**, 024013 (2021).
- ⁶⁶L. Nulens, H. Dausy, M. J. Wyszynski, B. Raes, M. J. Van Bael, M. V. Milošević, and J. Van de Vondel, *Metastable states and hidden phase slips in nanobridge SQUIDs*, Phys. Rev. B **106**, 134518 (2022).
- ⁶⁷D. S. Hopkins, D. Pekker, P. M. Goldbart, and A. Bezryadin, *Quantum Interference Device Made by DNA Templating of Superconducting Nanowires*, Science **308**, 1762–1765 (2005).
- ⁶⁸D. Pekker, A. Bezryadin, D. S. Hopkins, and P. M. Goldbart, *Operation of a superconducting nanowire quantum interference device with mesoscopic leads*, Phys. Rev. B **72**, 104517 (2005).
- ⁶⁹D. Hazra, *Nanobridge superconducting quantum interference devices: Beyond the Josephson limit*, Phys. Rev. B **99**, 144505 (2019).
- ⁷⁰W. J. Skocpol, M. R. Beasley, and M. Tinkham, *Self-heating hotspots in superconducting thin-film microbridges*, J. of Appl. Phys. **45**, 4054–4066 (1974).

- ⁷¹D. Hazra, J. Kirtley, and K. Hasselbach, *Nano-superconducting quantum interference devices with suspended junctions*, Appl. Phys. Lett. **104**, 152603 (2014).
- ⁷²D. Hazra, J. R. Kirtley, and K. Hasselbach, *Retrapping Current in Bridge-Type Nano-SQUIDs*, Phys. Rev. Applied **4**, 024021 (2015).
- ⁷³H. S. J. van der Zant, C. J. Muller, L. J. Geerligs, C. J. P. M. Harmans, and J. E. Mooij, *Coherent phase slip in arrays of underdamped Josephson tunnel junctions*, Phys. Rev. B **38**, 5154–5157 (1988).
- ⁷⁴H. S. J. van der Zant, F. C. Fritschy, T. P. Orlando, and J. E. Mooij, *Dynamics of vortices in underdamped Josephson-junction arrays*, Phys. Rev. Lett. **66**, 2531–2534 (1991).
- ⁷⁵R. L. Fagaly, *Superconducting quantum interference device instruments and applications*, Rev. of Sci. Instrum. **77**, 101101 (2006).
- ⁷⁶A. I. Braginski, *Superconductor Electronics: Status and Outlook*, J. Supercond. Nov. Magn. **32**, 23–44 (2019).
- ⁷⁷K. Sternickel and A. I. Braginski, *Biomagnetism using SQUIDs: status and perspectives*, Supercond. Sci. and Technol. **19**, S160 (2006).
- ⁷⁸W. Jenks, S. Sadeghi, and J. Wikswo Jr., *SQUIDs for nondestructive evaluation*, J. Phys. D **30**, 293–323 (1997).
- ⁷⁹R. C. Black, A. Mathai, F. C. Wellstood, E. Dantsker, A. H. Miklich, D. T. Nemeth, J. J. Kingston, and J. Clarke, *Magnetic microscopy using a liquid nitrogen cooled $YBa_2Cu_3O_7$ superconducting quantum interference device*, Appl. Phys. Lett. **62**, 2128–2130 (1993).
- ⁸⁰J. R. Kirtley and J. P. Wikswo, *Scanning Squid Microscopy*, Annu. Rev. Mater. Sci. **29**, 117–148 (1999).
- ⁸¹J. R. Kirtley, *Fundamental studies of superconductors using scanning magnetic imaging*, Rep. Prog. Phys. **73**, 126501 (2010).
- ⁸²A. Finkler, Y. Segev, Y. Myasoedov, M. L. Rappaport, L. Ne’eman, D. Vasyukov, E. Zeldov, M. E. Huber, J. Martin, and A. Yacoby, *Self-Aligned Nanoscale SQUID on a Tip*, Nano Lett. **10**, 1046–1049 (2010).
- ⁸³A. Finkler, D. Vasyukov, Y. Segev, L. Ne’eman, E. O. Lachman, M. L. Rappaport, Y. Myasoedov, E. Zeldov, and M. E. Huber, *Scanning superconducting quantum interference device on a tip for magnetic imaging of nanoscale phenomena*, Rev. of Sci. Instrum. **83**, 073702 (2012).
- ⁸⁴D. Vasyukov, Y. Anahory, L. Embon, D. Halbertal, J. Cuppens, L. Neeman, A. Finkler, Y. Segev, Y. Myasoedov, M. L. Rappaport, M. E. Huber, and E. Zeldov, *A scanning superconducting quantum interference device with single electron spin sensitivity*, Nat. Nanotechnol. **8**, 639–644 (2013).
- ⁸⁵D. Kinion and J. Clarke, *Superconducting quantum interference device as a near-quantum-limited amplifier for the axion dark-matter experiment*, Appl. Phys. Lett. **98**, 202503 (2011).

- ⁸⁶A. Wagner, G. Rybka, M. Hotz, L. J. Rosenberg, S. J. Asztalos, G. Carosi, C. Hagmann, D. Kinion, K. van Bibber, J. Hoskins, C. Martin, P. Sikivie, D. B. Tanner, R. Bradley, and J. Clarke, *Search for Hidden Sector Photons with the ADMX Detector*, Phys. Rev. Lett. **105**, 171801 (2010).
- ⁸⁷P. A. R. Ade, R. W. Aikin, D. Barkats, S. J. Benton, C. A. Bischoff, J. J. Bock, J. A. Brevik, I. Buder, E. Bullock, C. D. Dowell, L. Duband, J. P. Filippini, S. Fliescher, S. R. Golwala, M. Halpern, M. Hasselfield, S. R. Hildebrandt, G. C. Hilton, V. V. Hristov, K. D. Irwin, K. S. Karkare, J. P. Kaufman, B. G. Keating, S. A. Kernasovskiy, J. M. Kovac, C. L. Kuo, E. M. Leitch, M. Lueker, P. Mason, C. B. Netterfield, H. T. Nguyen, R. O'Brient, R. W. Ogburn, A. Orlando, C. Pryke, C. D. Reintsema, S. Richter, R. Schwarz, C. D. Sheehy, Z. K. Staniszewski, R. V. Sudiwala, G. P. Teply, J. E. Tolan, A. D. Turner, A. G. Viereg, C. L. Wong, and K. W. Yoon, *Detection of B-Mode Polarization at Degree Angular Scales by BICEP2*, Phys. Rev. Lett. **112**, 241101 (2014).
- ⁸⁸J. R. Johansson, G. Johansson, C. M. Wilson, and F. Nori, *Dynamical Casimir Effect in a Superconducting Coplanar Waveguide*, Phys. Rev. Lett. **103**, 147003 (2009).
- ⁸⁹J. R. Kirtley, *Probing the order parameter symmetry in the cuprate high temperature superconductors by SQUID microscopy*, C. R. Phys., Superconductivity of strongly correlated systems **12**, 436–445 (2011).
- ⁹⁰M. Veldhorst, C. G. Molenaar, C. J. M. Verwijs, H. Hilgenkamp, and A. Brinkman, *Optimizing the Majorana character of SQUIDs with topologically nontrivial barriers*, Phys. Rev. B **86**, 024509 (2012).
- ⁹¹C. Kurter, A. D. K. Finck, Y. S. Hor, and D. J. Van Harlingen, *Evidence for an anomalous current–phase relation in topological insulator Josephson junctions*, Nat. Commun. **6**, 7130 (2015).
- ⁹²C. Granata and A. Vettoliere, *Nano Superconducting Quantum Interference device: a powerful tool for nanoscale investigations*, Phy. Rep. **614**, 1–69 (2016).
- ⁹³W. Wernsdorfer, K. Hasselbach, D. Mailly, B. Barbara, A. Benoit, L. Thomas, and G. Suran, *DC-SQUID magnetization measurements of single magnetic particles*, J. Magn. Magn. Mater. **145**, 33–39 (1995).
- ⁹⁴E. Bonet, W. Wernsdorfer, B. Barbara, A. Benoît, D. Mailly, and A. Thiaville, *Three-Dimensional Magnetization Reversal Measurements in Nanoparticles*, Phys. Rev. Lett. **83**, 4188–4191 (1999).
- ⁹⁵C. Granata, R. Russo, E. Esposito, A. Vettoliere, M. Russo, A. Musinu, D. Peddis, and D. Fiorani, *Magnetic properties of iron oxide nanoparticles investigated by nanoSQUIDs*, EPJ B **86**, 272 (2013).
- ⁹⁶T. Schwarz, R. Wölbing, C. F. Reiche, B. Müller, M. J. Martínez-Pérez, T. Mühl, B. Büchner, R. Kleiner, and D. Koelle, *Low-Noise YBa₂Cu₃O₇ Nano-SQUIDs for Performing Magnetization-Reversal Measurements on Magnetic Nanoparticles*, Phys. Rev. Appl. **3**, 044011 (2015).

- ⁹⁷M. Jeffery, T. Van Duzer, J. R. Kirtley, and M. B. Ketchen, *Magnetic imaging of moat-guarded superconducting electronic circuits*, Appl. Phys. Lett. **67**, 1769–1771 (1995).
- ⁹⁸C. Veauvy, K. Hasselbach, and D. Mailly, *Micro-SQUID microscopy of vortices in a perforated superconducting Al film*, Phys. Rev. B **70**, 214513 (2004).
- ⁹⁹K. H. Kuit, J. R. Kirtley, W. van der Veur, C. G. Molenaar, F. J. G. Roesthuis, A. G. P. Troeman, J. R. Clem, H. Hilgenkamp, H. Rogalla, and J. Flokstra, *Vortex trapping and expulsion in thin-film $YBa_2Cu_3O_{7-\delta}$ strips*, Phys. Rev. B **77**, 134504 (2008).
- ¹⁰⁰F. Tafuri, J. R. Kirtley, P. G. Medaglia, P. Orgiani, and G. Balestrino, *Magnetic Imaging of Pearl Vortices in Artificially Layered $(Ba_{0.9}Nd_{0.1}CuO_{2+x})_m/(CaCuO_2)_n$ Systems*, Phys. Rev. Lett. **92**, 157006 (2004).
- ¹⁰¹L. Embon, Y. Anahory, A. Suhov, D. Halbertal, J. Cuppens, A. Yakovenko, A. Uri, Y. Myasoedov, M. L. Rappaport, M. E. Huber, A. Gurevich, and E. Zeldov, *Probing dynamics and pinning of single vortices in superconductors at nanometer scales*, Sci. Rep. **5**, 7598 (2015).
- ¹⁰²P. Seidel, *Applied Superconductivity: Handbook on Devices and Applications* (Wiley, Weinheim, 2015).
- ¹⁰³X. D. A. Baumans, *Nano-engineering superconducting junctions by atomic migration*, PhD thesis (Université de Liège, 2018).
- ¹⁰⁴*Physical Property Measurement System - Hardware Manual* (Quantum Design, 2008).
- ¹⁰⁵P. S. Ho and T. Kwok, *Electromigration in metals*, Rep. on Prog. Phys. **52**, 301 (1989).
- ¹⁰⁶R. Hoffmann-Vogel, *Electromigration and the structure of metallic nanocontacts*, Appl. Phys. Rev. **4**, 031302 (2017).
- ¹⁰⁷J. R. Lloyd, *Electromigration for Designers: An Introduction for the Non-Specialist*, (2002) <https://www.eetimes.com/electromigration-for-designers-an-introduction-for-the-non-specialist/>.
- ¹⁰⁸J. Black, *Electromigration—A brief survey and some recent results*, IEEE Transactions on Electron Devices **16**, 338–347 (1969).
- ¹⁰⁹A. V. Gurevich and R. G. Mints, *Self-heating in normal metals and superconductors*, Rev. Mod. Phys. **59**, 941–999 (1987).
- ¹¹⁰V. B. Fiks, Sov. Phys. Solid State **1**, 14 (1959).
- ¹¹¹H. B. Huntington and A. R. Grone, *Current-induced marker motion in gold wires*, J. Phys. Chem. Solids **20**, 76–87 (1961).
- ¹¹²J. R. Lloyd, *Electromigration in thin film conductors*, Semicond. Sci. Technol. **12**, 1177–1185 (1997).

- ¹¹³J. R. Lloyd, M. R. Polcari, and G. A. MacKenzie, *Observation of electromigration in heavily doped polycrystalline silicon thin films*, Appl. Phys. Lett. **36**, 428–430 (1980).
- ¹¹⁴M. E. Sarychev, Y. V. Zhitnikov, L. Borucki, C.-L. Liu, and T. M. Makhviladze, *General model for mechanical stress evolution during electromigration*, J. Appl. Phys. **86**, 3068–3075 (1999).
- ¹¹⁵R. L. de Orió, H. Ceric, and S. Selberherr, *Physically based models of electromigration: From Black’s equation to modern TCAD models*, **50**, 775–789 (2010).
- ¹¹⁶J. Lienig and M. Thiele, *Fundamentals of Electromigration-Aware Integrated Circuit Design* (Springer International Publishing, 2018).
- ¹¹⁷G. Esen and M. S. Fuhrer, *Temperature control of electromigration to form gold nanogap junctions*, Appl. Phys. Lett. **87**, 263101 (2005).
- ¹¹⁸M. L. Trouwborst, S. J. van der Molen, and B. J. van Wees, *The role of Joule heating in the formation of nanogaps by electromigration*, J. Appl. Phys. **99**, 114316 (2006).
- ¹¹⁹W. Jeong, K. Kim, Y. Kim, W. Lee, and P. Reddy, *Characterization of nanoscale temperature fields during electromigration of nanowires*, Sci. Rep. **4**, 4975 (2014).
- ¹²⁰V. S. Zharinov, X. D. A. Baumans, A. V. Silhanek, E. Janssens, and J. Van de Vondel, *Controlled electromigration protocol revised*, Rev. of Sci. Instrum. **89**, 043904 (2018).
- ¹²¹D. R. Strachan, D. E. Smith, D. E. Johnston, T.-H. Park, M. J. Therien, D. A. Bonnell, and A. T. Johnson, *Controlled fabrication of nanogaps in ambient environment for molecular electronics*, Appl. Phys. Lett. **86**, 043109 (2005).
- ¹²²O. Eliasson, G. Vasile, S. Ægir Jónsson, G. I. Gudjonsson, M. Arikan, and S. Ingvarsson, *Power regulation and electromigration in platinum microwires*, Rev. of Sci. Instrum. **85**, 114709 (2014).
- ¹²³H. B. Heersche, G. Lientschnig, K. O’Neill, H. S. J. van der Zant, and H. W. Zandbergen, *In situ imaging of electromigration-induced nanogap formation by transmission electron microscopy*, Appl. Phys. Lett. **91**, 072107 (2007).
- ¹²⁴J. M. Campbell and R. G. Knobel, *Feedback-controlled electromigration for the fabrication of point contacts*, Appl. Phys. Lett. **102**, 023105 (2013).
- ¹²⁵A. A. Houck, J. Labaziewicz, E. K. Chan, J. A. Folk, and I. L. Chuang, *Kondo Effect in Electromigrated Gold Break Junctions*, Nano Lett. **5**, 1685–1688 (2005).
- ¹²⁶S. Fujisawa, T. Kikkawa, and T. Kizuka, *Direct Observation of Electromigration and Induced Stress in Cu Nanowire*, Jpn. J. Appl. Phys. **42**, L1433–L1435 (2003).
- ¹²⁷T. Taychatanapat, K. I. Bolotin, F. Kuemmeth, and D. C. Ralph, *Imaging Electromigration during the Formation of Break Junctions*, Nano Lett. **7**, 652–656 (2007).

- ¹²⁸X. D. A. Baumans, D. Cerbu, O.-A. Adami, V. S. Zharinov, N. Verellen, G. Papari, J. E. Scheerder, G. Zhang, V. V. Moshchalkov, A. V. Silhanek, and J. Van de Vondel, *Thermal and quantum depletion of superconductivity in narrow junctions created by controlled electromigration*, Nat. Commun. **7**, 1–8 (2016).
- ¹²⁹X. D. A. Baumans, J. Lombardo, J. Brisbois, G. Shaw, V. S. Zharinov, G. He, H. Yu, J. Yuan, B. Zhu, K. Jin, R. B. G. Kramer, J. V. de Vondel, and A. V. Silhanek, *Healing Effect of Controlled Anti-Electromigration on Conventional and High-T_c Superconducting Nanowires*, Small **13**, 1700384 (2017).
- ¹³⁰T. Kozlova, M. Rudneva, and H. W. Zandbergen, *In situ TEM and STEM studies of reversible electromigration in thin palladium–platinum bridges*, Nanotechnology **24**, 505708 (2013).
- ¹³¹S. Collienne, B. Raes, W. Keijers, J. Linek, D. Koelle, R. Kleiner, R. B. Kramer, J. Van de Vondel, and A. V. Silhanek, *Nb-Based Nanoscale Superconducting Quantum Interference Devices Tuned by Electroannealing*, Phys. Rev. Appl. **15**, 034016 (2021).
- ¹³²M. Paniccia, R. Reifenberger, and P. Flinn, *In-situ observation of electromigration in Au using atomic force microscopy*, AIP Conf. Proc. **305**, 211–219 (1994).
- ¹³³S. Girod, J. Bubendorff, F. Montaigne, L. Simon, D. Lacour, and M. Hehn, *Real time atomic force microscopy imaging during nanogap formation by electromigration*, Nanotechnology **23**, 365302 (2012).
- ¹³⁴D. Arnold, M. Marz, S. Schneider, and R. Hoffmann-Vogel, *Structure and local charging of electromigrated Au nanocontacts*, Nanotechnology **28**, 055206 (2016).
- ¹³⁵M. Yagi, T. Saito, and J.-i. Shirakashi, *In situ atomic force microscopy imaging of structural changes in metal nanowires during feedback-controlled electromigration*, J. Vac. Sci. Technol. B **33**, 051806 (2015).
- ¹³⁶M. Yagi and J.-i. Shirakashi, *Evolution of local temperature in Au nanowires during feedback-controlled electromigration observed by atomic force microscopy*, Appl. Phys. Lett. **110**, 203105 (2017).
- ¹³⁷M. Yagi and J.-i. Shirakashi, *Quantifying Joule Heating and Mass Transport in Metal Nanowires during Controlled Electromigration*, Mater. **12**, 310 (2019).
- ¹³⁸E. Trabaldo, A. Kalaboukhov, R. Arpaia, E. Wahlberg, F. Lombardi, and T. Bauch, *Mapping the Phase Diagram of a YBa₂Cu₃O_{7-δ} Nanowire Through Electromigration*, Phys. Rev. Appl. **17**, 024021 (2022).
- ¹³⁹G. Binnig, C. F. Quate, and C. Gerber, *Atomic Force Microscope*, Phys. Rev. Lett. **56**, 930–933 (1986).
- ¹⁴⁰Y. Martin, C. C. Williams, and H. K. Wickramasinghe, *Atomic force microscope–force mapping and profiling on a sub 100-Å scale*, J. Appl. Phys. **61**, 4723–4729 (1987).

- ¹⁴¹W. Keijers, X. D. A. Baumans, R. Panghotra, J. Lombardo, V. S. Zharinov, R. B. G. Kramer, A. V. Silhanek, and J. Van de Vondel, *Nano-SQUIDs with controllable weak links created via current-induced atom migration*, *Nanoscale* **10**, 21475–21482 (2018).
- ¹⁴²H. Chen, S. X. D. Tan, V. Sukharev, X. Huang, and T. Kim, *Interconnect reliability modeling and analysis for multi-branch interconnect trees*, 52nd ACM / EDAC / IEEE Design Automation Conference (DAC), 1–6 (2015).
- ¹⁴³L. Chen, S. X. D. Tan, Z. Sun, S. Peng, M. Tang, and J. Mao, *Fast Analytic Electromigration Analysis for General Multisegment Interconnect Wires*, *IEEE Transactions on Very Large Scale Integration (VLSI) Systems* **28**, 421–432 (2020).
- ¹⁴⁴A. N. McCaughan, N. S. Abebe, Q. Y. Zhao, and K. K. Berggren, *Using Geometry To Sense Current*, *Nano Lett.* **16**, 7626–7631 (2016).
- ¹⁴⁵A. F. Volkov, *New Phenomena in Josephson SINIS Junctions*, *Phys. Rev. Lett.* **74**, 4730–4733 (1995).
- ¹⁴⁶R. de Bruyn Ouboter, A. N. Omel'yanchouk, and E. D. Vol, *Multi-terminal SQUID controlled by the transport current*, *Phys. B: Condens. Matter* **205**, 153–162 (1995).
- ¹⁴⁷A. F. Volkov and H. Takayanagi, *Long-range phase-coherent effects in the transport properties of mesoscopic superconductor–normal-metal structures*, *Phys. Rev. B* **56**, 11184–11194 (1997).
- ¹⁴⁸A. F. Morpurgo, T. M. Klapwijk, and B. J. van Wees, *Hot electron tunable supercurrent*, *Appl. Phys. Lett.* **72**, 966–968 (1998).
- ¹⁴⁹K. Neurohr, T. Schäpers, J. Malindretos, S. Lachenmann, A. I. Braginski, H. Lüth, M. Behet, G. Borghs, and A. A. Golubov, *Local suppression of Josephson currents in niobium/two-dimensional electron gas/niobium structures by an injection current*, *Phys. Rev. B* **59**, 11197–11200 (1999).
- ¹⁵⁰J. J. A. Baselmans, A. F. Morpurgo, B. J. van Wees, and T. M. Klapwijk, *Reversing the direction of the supercurrent in a controllable Josephson junction*, *Nature* **397**, 43–45 (1999).
- ¹⁵¹R. Shaikhaidarov, A. F. Volkov, H. Takayanagi, V. T. Petrashov, and P. Delsing, *Josephson effects in a superconductor–normal-metal mesoscopic structure with a dangling superconducting arm*, *Phys. Rev. B* **62**, R14649–R14652 (2000).
- ¹⁵²M. H. S. Amin, A. N. Omel'yanchouk, and A. M. Zagorskin, *DC SQUID based on the mesoscopic multiterminal Josephson junction*, *Phys. C: Supercond. Appl.* **372-376**, 178–180 (2002).
- ¹⁵³M. H. S. Amin, A. N. Omel'yanchouk, A. Blais, A. M. v. d. Brink, G. Rose, T. Duty, and A. M. Zagorskin, *Multi-terminal superconducting phase qubit*, *Phys. C: Supercond. Appl.* **368**, 310–314 (2002).
- ¹⁵⁴J. J. A. Baselmans, B. J. van Wees, and T. M. Klapwijk, *Direct demonstration of circulating currents in a controllable π -SQUID generated by a 0 to π transition of the weak links*, *Phys. Rev. B* **65**, 224513 (2002).

- ¹⁵⁵R. Winik, I. Holzman, E. G. Dalla Torre, E. Buks, and Y. Ivry, *Local tuning of the order parameter in superconducting weak links: A zero-inductance nanodevice*, Appl. Phys. Lett. **112**, 122601 (2018).
- ¹⁵⁶B. van Heck, S. Mi, and A. R. Akhmerov, *Single fermion manipulation via superconducting phase differences in multiterminal Josephson junctions*, Phys. Rev. B **90**, 155450 (2014).
- ¹⁵⁷R. P. Riwar, M. Houzet, J. S. Meyer, and Y. V. Nazarov, *Multi-terminal Josephson junctions as topological matter*, Nat. Commun. **7**, 11167 (2016).
- ¹⁵⁸J. S. Meyer and M. Houzet, *Conductance quantization in topological Josephson trijunctions*, Phys. Rev. B **103**, 174504 (2021).
- ¹⁵⁹L. Peralta Gavensky, G. Usaj, and C. A. Balseiro, *Topological phase diagram of a three-terminal Josephson junction: From the conventional to the Majorana regime*, Phys. Rev. B **100**, 014514 (2019).
- ¹⁶⁰A. Pfeffer, J. E. Duvauchelle, H. Courtois, R. Mélin, D. Feinberg, and F. Lefloch, *Subgap structure in the conductance of a three-terminal Josephson junction*, Phys. Rev. B **90**, 075401 (2014).
- ¹⁶¹Y. Cohen, Y. Ronen, J. H. Kang, M. Heiblum, D. Feinberg, R. Mélin, and H. Shtrikman, *Nonlocal supercurrent of quartets in a three-terminal Josephson junction*, Proc. Natl. Acad. Sci. U. S. A. **115**, 6991–6994 (2018).
- ¹⁶²A. W. Draelos, M. T. Wei, A. Seredinski, H. Li, Y. Mehta, K. Watanabe, T. Taniguchi, I. V. Borzenets, F. Amet, and G. Finkelstein, *Supercurrent Flow in Multiterminal Graphene Josephson Junctions*, Nano Lett. **19**, 1039–1043 (2019).
- ¹⁶³N. Pankratova, H. Lee, R. Kuzmin, K. Wickramasinghe, W. Mayer, J. Yuan, M. G. Vavilov, J. Shabani, and V. E. Manucharyan, *Multiterminal Josephson Effect*, Phys. Rev. X **10**, 031051 (2020).
- ¹⁶⁴E. G. Arnault, T. F. Q. Larson, A. Seredinski, L. Zhao, S. Idris, A. McConnell, K. Watanabe, T. Taniguchi, I. Borzenets, F. Amet, and G. Finkelstein, *Multiterminal Inverse AC Josephson Effect*, Nano Lett. **21**, 9668–9674 (2021).
- ¹⁶⁵G. V. Graziano, M. Gupta, M. Pendharkar, J. T. Dong, C. P. Dempsey, C. Palmstrøm, and V. S. Pribiag, *Selective control of conductance modes in multiterminal Josephson junctions*, Nature Commun. **13**, 5933 (2022).
- ¹⁶⁶P. Puczkarski, P. Gehring, C. S. Lau, J. Liu, A. Ardavan, J. H. Warner, G. A. D. Briggs, and J. A. Mol, *Three-terminal graphene single-electron transistor fabricated using feedback-controlled electroburning*, Appl. Phys. Lett. **107**, 133105 (2015).
- ¹⁶⁷C. Sürgers and H. v. Löhneysen, *Effect of oxygen segregation on the surface structure of single-crystalline niobium films on sapphire*, Appl. Phys. A **54**, 350–354 (1992).
- ¹⁶⁸G.-i. Oya, M. Koishi, and Y. Sawada, *High-quality single-crystal Nb films and influences of substrates on the epitaxial growth*, J. Appl. Phys. **60**, 1440–1446 (1986).

- ¹⁶⁹H. Padamsee, J. Knobloch, and T. Hays, *RF superconductivity for accelerators*, Vol. 2 (Wiley-VCH, 2008).
- ¹⁷⁰P. Bernard, D. Bloess, W. Hartung, C. Hauviller, W. Weingarten, P. Bosland, and J. Martignac, *Superconducting niobium sputter-coated copper cavities at 1500 MHz*, in 5th workshop on RF superconductivity (1991).
- ¹⁷¹D. Proch, *Reduction of multipacting in superconducting accelerator structures*, in Proc. conf. future possibilities for electron accelerators (1979), N1–N17.
- ¹⁷²S. K. H. Lam and D. L. Tilbrook, *Development of a niobium nanosuperconducting quantum interference device for the detection of small spin populations*, Appl. Phys. Lett. **82**, 1078 (2003).
- ¹⁷³R. Kleiner, D. Koelle, F. Ludwig, and J. Clarke, *Superconducting quantum interference devices: state of the art and applications*, Proc. IEEE **92**, 1534–1548 (2004).
- ¹⁷⁴M. Mück, M. O. André, J. Clarke, J. Gail, and C. Heiden, *Radio-frequency amplifier based on a niobium dc superconducting quantum interference device with microstrip input coupling*, Appl. Phys. Lett. **72**, 2885–2887 (1998).
- ¹⁷⁵V. Bouchiat, M. Faucher, C. Thirion, W. Wernsdorfer, T. Fournier, and B. Panetier, *Josephson junctions and superconducting quantum interference devices made by local oxidation of niobium ultrathin films*, Appl. Phys. Lett. **79**, 123 (2001).
- ¹⁷⁶C. J. Muller, J. M. Van Ruitenbeek, and L. J. De Jongh, *Experimental observation of the transition from weak link to tunnel junction*, Physica C **191**, 485–504 (1992).
- ¹⁷⁷D. E. Oates and G. F. Dionne, *Magnetically tunable superconducting resonators and filters*, IEEE Trans. Appl. Supercond. **9**, 4170–4175 (1999).
- ¹⁷⁸S. S. Attar, S. Setoodeh, P. D. Laforge, M. Bakri-Kassem, and R. R. Mansour, *Low temperature superconducting tunable bandstop resonator and filter using superconducting RF MEMS varactors*, IEEE Trans. Appl. Supercond. **24**, 150709 (2014).
- ¹⁷⁹S. H. Talisa, M. A. Janocko, C. Moskowitz, J. Talvacchio, J. F. Billing, R. Brown, D. C. Buck, K. Jones, B. R. McAvoy, G. R. Wagner, and D. H. Watt, *Low- and high-temperature superconducting microwave filters*, IEEE Trans. Microw. Theory Tech. **39**, 1448–1454 (1991).
- ¹⁸⁰M. Tanaka, H. Akaike, A. Fujimaki, Y. Yamanashi, N. Yoshikawa, S. Nagasawa, K. Takagi, and N. Takagi, *100-ghz single-flux-quantum bit-serial adder based on 10-kA/cm² niobium process*, IEEE Trans. Appl. Supercond. **21**, 792–796 (2011).
- ¹⁸¹M. Reagor, W. Pfaff, C. Axline, R. W. Heeres, N. Ofek, K. Sliwa, E. Holland, C. Wang, J. Blumoff, K. Chou, M. J. Hatridge, L. Frunzio, M. H. Devoret, L. Jiang, and R. J. Schoelkopf, *Quantum memory with millisecond coherence in circuit qed*, Phys. Rev. B **94**, 014506 (2016).

- ¹⁸²A. A. Murthy, P. M. Das, S. M. Ribet, C. Kopas, J. Lee, M. J. Reagor, L. Zhou, M. J. Kramer, M. C. Hersam, M. Checchin, A. Grassellino, R. dos Reis, V. P. Dravid, and A. Romanenko, *Developing a chemical and structural understanding of the surface oxide in a niobium superconducting qubit*, ACS Nano **16**, 17257–17262 (2022).
- ¹⁸³G. A. Hernandez, R. Bai, Y. C., J. A. Sellers, C. D. Ellis, D. B. Tuckerman, and M. C. Hamilton, *Microwave performance of niobium/kapton superconducting flexible cables*, IEEE Trans. Appl. Supercond. **27**, 1200104 (2017).
- ¹⁸⁴V. Gupta, B. Yelamanchili, S. Zou, T. Isaacs-Smith, J. A. Sellers, D. B. Tuckerman, and M. C. Hamilton, *Thin-film nb/polyimide superconducting stripline flexible cables*, **29**, 1501605 (2019).
- ¹⁸⁵P. V. Tyagi, M. Doleans, B. Hannah, R. Afanador, C. McMahan, S. Stewart, J. Mammosser, M. Howell, J. Saunders, B. Degraff, and S. H. Kim, *Improving the work function of the niobium surface of SRF cavities by plasma processing*, Appl. Surf. Sci. **369**, 29–35 (2016).
- ¹⁸⁶S. Collienne, D. Majidi, J. Van de Vondel, C. B. Winkelmann, and A. V. Silhanek, *Targeted modifications of monolithic multiterminal superconducting weak-links*, Nanoscale **14**, 5425–5429 (2022).
- ¹⁸⁷S. B. Alvarez, J. Brisbois, S. Melinte, R. B. G. Kramer, and A. V. Silhanek, *Statistics of thermomagnetic breakdown in nb superconducting films*, Sci. Rep. **9**, 3659 (2019).
- ¹⁸⁸J. Evertsson and et al., *The thickness of native oxides on aluminum alloys and single crystals*, Appl. Surf. Sci. **349**, 826–832 (2015).
- ¹⁸⁹G. Li, B. Mao, F. Lan, and L. Liu, *Practical aspects of single-pass scan kelvin probe force microscopy*, Rev. Sci. Inst. **83**, 113701 (2012).
- ¹⁹⁰F. B. Hagedorn and P. M. Hall, *Right-angle bends in thin strip conductors*, J. Appl. Phys. **34**, 128 (1963).
- ¹⁹¹K. Kanaya and S. Okayama, *Penetration and energy-loss theory of electrons in-solid targets*, J. Phys. D: Appl. Phys. **5**, 43 (1972).
- ¹⁹²J. Li, B. Hoekstra, Z.-B. Wang, J. Qiu, and Y.-K. Pu, *Secondary electron emission influenced by oxidation on the aluminum surface: the roles of the chemisorbed oxygen and the oxide layer*, Plasma Sources Sci. Technol. **27**, 044002 (2018).
- ¹⁹³T. T. Magkoev and G. G. Vladimirov, *Aluminium oxide ultrathin-film growth on the Mo(110) surface: a work-function study*, J. Phys. Condens. Matter **13**, L655–L661 (2001).
- ¹⁹⁴M. Grundner and J. Halbritter, *XPS and AES studies on oxide growth and oxide coatings on niobium*, J. Appl. Phys. **51**, 397–405 (1980).
- ¹⁹⁵S. Halas and T. Durakiewicz, *Is work function a surface or a bulk property?*, Vacuum **85**, 486–488 (2010).
- ¹⁹⁶Q. G. Wang and J. X. Shang, *First-principles study on the incipient oxidization of nb(110)*, J. Phys. Cond. Mat. **24**, 225005 (2012).

- ¹⁹⁷L. P. H. Jeuregns, W. G. Sloof, F. D. Tichelaar, and E. J. Mittemeijer, *Growth kinetics and mechanisms of aluminum-oxide films formed by thermal oxidation of aluminum*, J. Appl. Phys. **92**, 1649 (2002).
- ¹⁹⁸J. Halbritter, *On the oxidation and on the superconductivity of niobium*, Appl. Phys. A **43**, 1–28 (1987).
- ¹⁹⁹J. Canet-Ferrer, E. Coronado, A. Forment-Aliaga, and E. Pinilla-Cienfuegos, *Correction of the tip convolution effects in the imaging of nanostructures studied through scanning force microscopy*, Nanotechnology **25**, 395703 (2014).
- ²⁰⁰K. Ohnishi, T. Kimura, and Y. Otani, *Improvement of superconductive properties of mesoscopic Nb wires by Ti passivation layers*, Appl. Phys. Express **1**, 021701 (2008).
- ²⁰¹D. D. Awschalom, J. R. Rozen, M. B. Ketchen, W. J. Gallagher, A. W. Kleinsasser, R. L. Sandstrom, and B. Bumble, *Low-noise modular microsusceptometer using nearly quantum limited dc SQUIDs*, Appl. Phys. Lett. **53**, 2108–2110 (1988).
- ²⁰²M. Hatridge, R. Vijay, D. H. Slichter, J. Clarke, and I. Siddiqi, *Dispersive magnetometry with a quantum limited SQUID parametric amplifier*, Phys. Rev. B **83**, 134501 (2011).
- ²⁰³M. J. Martínez-Pérez and D. Koelle, *NanoSQUIDs: Basics & recent advances*, Phys. Sci. Rev. **2**, 20175001 (2017).
- ²⁰⁴S. Biswas, C. B. Winkelman, H. Courtois, and A. K. Gupta, *Josephson coupling in the dissipative state of a thermally hysteretic μ -SQUID*, Phys. Rev. B **98**, 174514 (2018).
- ²⁰⁵T. Schäpers, J. Malindretos, K. Neurohr, S. Lachenmann, A. van der Hart, G. Crecelius, H. Hardtdegen, H. Lüth, and A. A. Golubov, *Demonstration of a current-controlled three-terminal Nb-InxGa1-xAs/InP Josephson contact*, Appl. Phys. Lett. **73**, 2348–2350 (1998).
- ²⁰⁶A. F. Mayadas, R. B. Laibowitz, and J. J. Cuomo, *Electrical Characteristics of rf-Sputtered Single-Crystal Niobium Films*, J. Appl. Phys. **43**, 1287–1289 (1972).
- ²⁰⁷P. H. Kes and C. C. Tsuei, *Two-dimensional collective flux pinning, defects, and structural relaxation in amorphous superconducting films*, Phys. Rev. B **28**, 5126–5139 (1983).
- ²⁰⁸M. M. Khapaev, M. Y. Kupriyanov, E. Goldobin, and M. Siegel, *Current distribution simulation for superconducting multi-layered structures*, Supercond. Sci. Technol. **16**, 24–27 (2003).
- ²⁰⁹D. Drung, *Introduction to Nb-based SQUID Sensors*, IEEE/CSC and ESAS Superconductivity News Forum (global edition), 10.7567/APEX.6.077302 (2016).
- ²¹⁰J. Jaycox and M. Ketchen, *Planar coupling scheme for ultra low noise DC SQUIDs*, IEEE Trans. Magn. **17**, 400–403 (1981).
- ²¹¹W. DeSorbo, *Effect of Dissolved Gases on Some Superconducting Properties of Niobium*, Phys. Rev. **132**, 107–121 (1963).

- ²¹²C. C. Koch, J. O. Scarbrough, and D. M. Kroeger, *Effects of interstitial oxygen on the superconductivity of niobium*, Phys. Rev. B **9**, 888–897 (1974).
- ²¹³M. Hummelgård, R. Zhang, T. Carlberg, D. Vengust, D. Dvorsek, D. Mihailovic, and H. Olin, *Nanowire transformation and annealing by Joule heating*, Nanotechnology **21**, 165704 (2010).
- ²¹⁴G. Bakan, N. Khan, A. Cywar, K. Cil, M. Akbulut, A. Gokirmak, and H. Silva, *Self-heating of silicon microwires: Crystallization and thermoelectric effects*, J. Mater. Res. **26**, 1061–1071 (2011).
- ²¹⁵M. Tohmyoh and H. Ishihara, *Local Modification of Cu Microwires by Joule Heating*, Appl. Phys. Express, **5** (2013).
- ²¹⁶K. S. McGarrity, B. Gao, and J. M. Thijssen, *Simulation of Joule annealing in nanoscale Pt wires*, Comput. Mater. Sci. **50**, 3043–3049 (2011).
- ²¹⁷Y. Kim, R. Tao, R. F. Klie, and D. N. Seidman, *Direct Atomic-Scale Imaging of Hydrogen and Oxygen Interstitials in Pure Niobium Using Atom-Probe Tomography and Aberration-Corrected Scanning Transmission Electron Microscopy*, ACS Nano **7**, 732–739 (2013).
- ²¹⁸N. Kumar, T. Fournier, H. Courtois, C. Winkelmann, and A. K. Gupta, *Reversibility Of Superconducting Nb Weak Links Driven By The Proximity Effect In A Quantum Interference Device*, Phys. Rev. Lett. **114**, 157003 (2015).
- ²¹⁹A. K. Gupta, N. Kumar, and S. Biswas, *Temperature and phase dynamics in superconducting weak-link*, J. Appl. Phys. **116**, 173901 (2014).
- ²²⁰COMSOL Multiphysics® v. 5.4. COMSOL AB, Stockholm, Sweden (2018).
- ²²¹A. D. Avery, S. J. Mason, D. Bassett, D. Wesenberg, and B. L. Zink, *Thermal and electrical conductivity of approximately 100-nm permalloy, Ni, Co, Al, and Cu films and examination of the Wiedemann-Franz Law*, Phys. Rev. B **92** (2015).
- ²²²X. D. A. Baumans, V. S. Zharinov, E. Raymenants, S. Blanco Alvarez, J. E. Scheerder, J. Brisbois, D. Massarotti, R. Caruso, F. Tafuri, E. Janssens, V. V. Moshchalkov, J. Van de Vondel, and A. V. Silhanek, *Statistics of localized phase slips in tunable width planar point contacts*, Sci. Rep. **7**, 44569 (2017).
- ²²³P. Shor, *Algorithms for quantum computation: discrete logarithms and factoring*, in Proceedings 35th annual symposium on foundations of computer science (1994), pp. 124–134.
- ²²⁴L. K. Grover, *Quantum Mechanics Helps in Searching for a Needle in a Haystack*, Phys. Rev. Lett. **79**, 325–328 (1997).
- ²²⁵A. W. Harrow, A. Hassidim, and S. Lloyd, *Quantum Algorithm for Linear Systems of Equations*, Phys. Rev. Lett. **103**, 150502 (2009).
- ²²⁶F. Arute et al., *Quantum supremacy using a programmable superconducting processor*, Nature **574**, 505–510 (2019).

- ²²⁷A. F. Kockum and F. Nori, *Quantum Bits with Josephson Junctions*, in *Fundamentals and Frontiers of the Josephson Effect*, edited by F. Tafuri, Springer Series in Materials Science (Springer International Publishing, 2019), pp. 703–741.
- ²²⁸P. Krantz, M. Kjaergaard, F. Yan, T. P. Orlando, S. Gustavsson, and W. D. Oliver, *A Quantum Engineer's Guide to Superconducting Qubits*, Appl. Phys. Rev. **6**, 021318 (2019).
- ²²⁹J. S. Meyer and M. Houzet, *Nontrivial Chern Numbers in Three-Terminal Josephson Junctions*, Phys. Rev. Lett. **119**, 136807 (2017).
- ²³⁰G. V. Graziano, J. S. Lee, M. Pendharkar, C. J. Palmstrøm, and V. S. Pribiag, *Transport studies in a gate-tunable three-terminal Josephson junction*, Phys. Rev. B **101**, 054510 (2020).
- ²³¹K. F. Huang, Y. Ronen, R. Mélin, D. Feinberg, K. Watanabe, T. Taniguchi, and P. Kim, *Evidence for $4e$ charge of Cooper quartets in a biased multi-terminal graphene-based Josephson junction*, Nature Commun. **13**, 3032 (2022).
- ²³²D. G. Cahill, S.-M. Lee, and T. I. Selinder, *Thermal conductivity of κ - Al_2O_3 and α - Al_2O_3 wear-resistant coatings*, J. of Appl. Phys. **83**, 5783–5786 (1998).
- ²³³J. Ekin, *Experimental techniques for low-temperature measurements: cryostat design, material properties and superconductor critical-current testing*, 1st ed. (Oxford University Press/Oxford, 2006).
- ²³⁴S. Marinković, E. A. Abbey, D. A. D. Chaves, S. Collienne, E. Fourneau, L. Jiang, C. Xue, Y. H. Zhou, W. A. Ortiz, M. Motta, N. D. Nguyen, A. Volodin, J. Van de Vondel, and A. V. Silhanek, *Effect of Moderate Electropulsing on Nb Multiterminal Transport Bridges*, Phys. Rev. Appl. **19**, 054009 (2023).
- ²³⁵W. J. Skocpol, M. R. Beasley, and M. Tinkham, *Phase-slip centers and nonequilibrium processes in superconducting tin microbridges*, J. Low Temp. Phys. **16**, 145–167 (1974).
- ²³⁶L. Kramer and R. J. Watts-Tobin, *Theory of dissipative current-carrying states in superconducting filaments*, Phys. Rev. Lett. **40**, 1041–1044 (1978).
- ²³⁷R. J. Watts-Tobin, Y. Krähenbühl, and L. Kramer, *Nonequilibrium theory of dirty, current-carrying superconductors: phase-slip oscillators in narrow filaments near T_c* , J. Low Temp. Phys. **42**, 459–501 (1981).
- ²³⁸G. Stenuit, S. Michotte, J. Govaerts, and L. Piraux, *Temperature dependence of penetration and coherence lengths in lead nanowires*, Supercond. Sci. Technol. **18**, 174 (2004).
- ²³⁹R. Mélin, R. Danneau, and C. B. Winkelmann, *Proposal for detecting the π -shifted Cooper quartet supercurrent*, in Arxiv (2023).

Curriculum Vitae

Personal data

Name Simon Collienue
Birthdate June 17, 1989
Nationality Belgium (BE)
E-mail simoncollienue@gmail.com



Education

2018-2023 PhD student at the Physics Departement of University of Liège, Belgium. Group of Experimental Physics of Nanostructured Materials (EPNM)
2012-2014 Certified upper secondary education teacher, University of Liège, Belgium
2010-2012 Master in Physical Engineering, University of Liège, Belgium
2007-2010 Bachelor in Engineering, University of Liège, Belgium

List of publications

1. G. Zhang, **S. Collienue**, R. Zulkharnay, X. Ke, M. Liao, L. Liu, S. Li et al, *Reentrant Resistive State in Superconducting Diamond Nanowires*, to be submitted.
2. S. Marinkovic, E. A. Abbey, D. A. D. Chaves, **S. Collienue**, E. Fourneau, L. Jiang, C. Xue et al, *Effect of Moderate Electropulsing on Nb Multiterminal Transport Bridges*, Phys. Rev. Appl. **5**, 054009 (2023).
3. S. Marinkovic, E. Tralbaldo, **S. Collienue**, F. Lombardi, T. Bauch, and A.

- Silhanek, *Oxygen ordering in untwinned $YBa_2Cu_3O_{7-\delta}$ films driven by electrothermal stress*, Phys. Rev. B **107**, 014208 (2023).
4. G. Libeert, R. Murugesan, M. Guba, W. Keijers, **S. Collienne**, B. Raes, S. Brems et al, *Au β -Decorated graphene as a sensing platform for O_2 adsorption and desorption kinetics*, Nanoscale **14**, 12437-12446 (2022).
 5. **S. Collienne**, D. Majidi, J. Van de Vondel, C. B. Winkelmann, and A. Silhanek, *Targeted modifications of monolithic multiterminal superconducting weak-links*, Nanoscale **14**, 5425-5429 (2022)
 6. **S. Collienne**, S. Marinkovic, A. Fernández-Rodríguez, N. Mestres, A. Palau, and A. Silhanek, *Electrically-Driven Oxygen Vacancy Aggregation and Displacement in $YBa_2Cu_3O_{7-\delta}$ Films*, Adv. Electron. Mat., 2101290 (2022)
 7. **S. Collienne**, B. Raes, W. Keijers, J. Van de Vondel, J. Linek, D. Koelle, R. Kleiner, R. Kramer, and A. Silhanek, *Nb-based nanoscale superconducting quantum interference devices tuned by electroannealing*, Phys. Rev. Appl. **15**, 034016 (2021)
 8. S. Marinkovic, A. Fernandez-Rodriguez, **S. Collienne**, S. Blanco Alvarez, S. Melinte, B. Maiorov, G. Ruis et al, *Direct Visualization of Current-Stimulated Oxygen Migration in $YBa_2Cu_3O_{7-\delta}$ Thin Films*, ACS Nano **14**, 11765-11774 (2020)
 9. J. Lombardo, **S. Collienne**, A. Petrillo, E. Fourneau, N. D. Nguyen, and A. Silhanek, *Electromigration-induced resistance switching in indented Al microstrips*, New J. Phys., **21**, 113015 (2019)
 10. X. Baumans, A. Fernández-Rodríguez, N. Mestres, **S. Collienne**, J. Van de Vondel, A. Palau, and A. Silhanek, *Electromigration in the dissipative state of high temperature superconducting bridges*, Appl. Phys. Lett. **114**, 012601 (2019)
 11. S. Derochette, A. Mouithys-Mickalad, T. Franck, **S. Collienne**, J. Ceusters, G. Deby-Dupont, P. Neven, and D. Serteyn, *NDS27 combines the effect of curcumin lysinate and hydroxypropyl- β -cyclodextrin to inhibit equine PKC δ and NADPH oxidase involved in the oxidative burst of neutrophils*, FEBS Open Bio. **4**, 1021-1029 (2014)